Fundamental mechanisms in Li-air battery electrochemistry

Højberg, Jonathan; Vegge, Tejs; Norby, Poul; Johansen, Keld

Publication date:
2015

Document Version
Publisher's PDF, also known as Version of record

Jonathan Højberg

Fundamental mechanisms in Li-air battery electrochemistry

Submitted in candidacy for the degree Doctor of Philosophy

Supervisors
Prof. Tejs Vegge, DTU Energy
Senior scientist Poul Norby, DTU Energy
Senior scientist Keld Johansen, Haldor Topsøe A/S

March 24th, 2015

Title: Fundamental mechanisms in Li-air battery electrochemistry

Author
Jonathan Højberg
E-mail: jhoj@topsoe.dk

Supervisors
Prof. Tejs Vegge
Section for Atomic Scale Modeling and Materials
Department of Energy Conversion and Storage
Technical University of Denmark
E-mail: teve@dtu.dk

Senior scientist Poul Norby
Section for Atomic Scale Modeling and Materials
Department of Energy Conversion and Storage
Technical University of Denmark
E-mail: pnor@dtu.dk

Senior scientist Keld Johansen
Haldor Topsøe A/S
E-mail: kej@topsoe.dk

Technical University of Denmark
Section for Atomic Scale Modeling and Materials
Department of Energy Conversion and Storage
Technical University of Denmark
Frederiksborgvej 399
DK-4000 Roskilde
Denmark
www.ecs.dtu.dk
Tel: +45 46 77 58 00
E-mail: info@ecs.dtu.dk

Haldor Topsøe A/S
Nymøllevej 55
DK-2800 Kgs. Lyngby
Denmark
www.topsoe.com
Tel: +45 45 27 20 00
E-mail: topsoe@topsoe.dk

Release date: March 24th, 2015
1st revision: May 20th, 2015

Preface

This thesis is submitted in candidacy for the Ph.D. degree from the Technical University of Denmark (DTU). The work was carried out between January 2012 and March 2015 at the section for Atomic-scale Modeling and Materials, DTU Energy and at Haldor Topsøe A/S. A part of the work was also carried out in an external research stay at IBM Almaden Research Center, California, USA.

The project was supervised by Prof. Tejs Vegge, Head of Section at DTU Energy, Senior scientist Poul Norby at DTU Energy and Senior scientist Keld Johansen at Haldor Topsøe A/S. The project was financially supported by the ReLiable project (project nr. 11-116792) funded by the Danish Council for Strategic Research Program Commission on Sustainable Energy and Environment.

Abstract

The lithium-air (or Li-O_2) batteries have received wide attention as an enabling technology for a mass market entry of electric vehicles due to a potential capacity much higher than current Li-ion technology. The technology is a relatively new battery concept proposed in 1996, and the current research still focuses on developing an understanding of the reactions inside the battery. This thesis is dedicated to increase this understanding and use the knowledge to improve the performance of the battery, and the work span from detailed investigation of the atom positions to the proposal of a system used to manage a full size electric vehicle battery.

An automated differential electrochemical mass spectrometer (DEMS) was built to investigate the relationship between current and the consumption and release of gases, which is important to identify and quantify degradation reactions. The setup was used to characterize our carbon-based reference system as well as new ionic liquid-based electrolytes.

Electrochemical impedance spectroscopy (EIS) has been used extensively to describe reaction mechanisms inside the battery; the origin of the measured overpotentials; and the onset potential for electrochemical degradation. It was confirmed that the rapid potential loss near the end of discharge could be explained by an increase in the charge transport resistance; that the initial Li_2O_2 oxidation at 3.05 V was blocked by the formation of an SEI layer; and that the voltage increase during charge was primarily due to the formation of a mixed potential between competing oxidation reactions needed to maintain a constant current.

The knowledge about impedance spectroscopy was used to propose and investigate a novel battery management tool to estimate the state of charge and the state of health of a Li-O_2 battery system better than any other method available.

Finally, calculations were made to support that an open system configuration is a realistic option in terms of air purification, if H_2O and CO_2 levels at 1 ppm are allowed.

Resumé

Lithium-luft (eller Li-O_2) batterier har fået stor opmærksomhed, fordi de med en potentiel kapacitet mange gange større end nuværende Li-ion batterier, kan være med til at sikre et kommercielt gennembrud for elbiler. Li-O_2 batteriet er et relativt nyt koncept, der første gang blev demonstreret i 1996. Denne afhandling fokuserer på at udbygge forståelsen af hvad der sker inde i batteriet og anvende denne forståelse til at forbedre batteriet. Arbejdet spænder fra et detaljeret studie af de atomare positioner til udviklingen af et system, der kan bruges til at styre elbil-batterier i fuld skala.

I projektet blev der bygget et automatiseret differentielt elektrokemisk massespektrometer (DEMS) for at undersøge sammenhængen mellem den strøm, der løber fra batteriet og den mængde gas, der optages eller afgives. Dette er vigtigt for at kunne identificere og kvantificere eventuelle degraderingsreaktionerne i batteriet. Opstillingen blev brugt til at karakterisere vores kulstof-baserede reference system og nye elektrolytter baseret på ioniske væsker.

Elektrokemisk impedans spektroskopi (EIS) er blevet anvendt i vid udstrækning til at beskrive reaktionerne inde i batteriet; årsagen til det målte overpotentiale; og ved hvilket potentiale den elektriske degradering begynder. Det blev bekræftet at det hurtigt faldende potentiale i slutningen af afladningen kan forklares med en stigning af ladningsoverførselsmodstanden, at Li_2O_2 oxideringen starter ved 3.05 V, men blokkeres med det samme af et lag af kemiske degraderingsprodukter fra reaktioner mellem Li_2O_2 og elektrolytten, og at stigningen i spænding gennem opladningen primært skyldes et blandet potentiale mellem forskellige oxidative reaktioner, der aktiveres for at opretholde en konstant strøm i takt med at overfladen dækkes af degraderingsprodukter.

Den opbyggede viden om impedansspektroskopi blev brugt til at udvikle og teste en ny metode til at bestemme batteriets ladningstilstand og helbred. Metoden viste sig at være markant bedre end de eksisterende løsninger.

Endelig blev der foretaget en række beregninger, der viste, at et åbent Li-O_2 system til rensning af H_2O and CO_2 til et niveau under 1 ppm er et realistisk alternativ til at benytte en oxygen tank.

Acknowledgements

This thesis marks the end of three years of research. It has been a wonderful time with many memorial experiences and a lot of lovely people that I am grateful to have met. I would like to use this opportunity to thank all of you. My thanks go to:

My supervisor Prof. Tejs Vegge for invaluable academic discussions. For opening doors when needed, also some of the big ones with locks and chains, and otherwise letting me find my way.
Johan Hjelm and my co-supervisors Senior scientist Poul Norby and Senior scientist Keld Johansen for valuable input to my scientific work throughout the project.

A special thank goes to Assistant Prof. Bryan D. McCloskey and Prof. Alan Luntz for enabling the fantastic journey to California and the legendary IBM Almaden Reserach Center. I am grateful for the opportunity I had to have daily discussions in the lab and at the 4pm coffee break about Li-air battery chemistry, remodeling and the new software update in Winfrieds Tesla.

Prof. Søren Dahl for your support when needed and for putting me in contact with Senior scientist Poul Erik Højlund back in 2011, which led to this PhD project.

My fantastic colleagues at both Haldor Topsøe and DTU Energy. Invaluable help from LPHA, RTIR, LAFL and the rest of the characterization crew at Haldor Topsøe. Andreas and Mathias for a major help with the DEMS setup. Mike for always having time, always having a solution and never complaining when I have messed up you toolbox or tightened the Swagelok unions too much in a 7pm quick fix.

Ane for taking so good care of me when I started working with batteries and later, when I needed someone to share my PhD frustrations with. Kristian and Andreas for unforgettable moments in Denmark and in Crete, for Champagne bets, and an astonishing sprint in the end to ensure that our papers got submitted on time before my thesis deadline. Dr. Supti Das for a great collaboration on the DEMS measurements and a hectic effort to finish our paper. Jon for your continuous brainstorming. It has been a pleasure and an inspiration. And great fun to start up DBS, PCLF, COMX and all the other ones that didn't even get a name. Nice!

I would like to thank Merete for an overwhelming support in these final months even though you have been busy too.
And finally, I would like to express my gratitude of my beloved daughters Hedvig and Ingeborg. Now, I can finally say to you that I have finished my book.

Contents

List of Figures

Abbreviations

SoC	State of charge
SoD	State of discharge
SoH	State of health
BMS	Battery management system
OCV	Open circuit voltage
EIS	Electrochemical impedance spectroscopy
PEIS	Potentiostatic electrochemical impedance spectroscopy
GEIS	Galvanostatic electrochemical impedance spectroscopy
CPE	Constant phase element
AC	Alternating current
DC	Direct current
SEI	Solid-electrolyte interface
OER	Oxygen evolution reaction
ORR	Oxygen reduction reaction
DEMS	Differential electrochemical mass spectrometry
SAED	Selected area electron diffraction
EELS	Electron energy loss spectroscopy
TEM	Transmission electron microscopy
SEM	Scanning electron microscopy
EDS	Energy-dispersive X-ray spectroscopy
XRD	X-ray diffraction

To Hedvig and Ingeborg

Chapter 1

Introduction

1.1 Abandoning fossil fuels

Fossil fuels are still, by far, the most common source of energy in the world, constituting 79 % of the total energy production [1], but the renewable share of the energy production is increasing. The transition is motivated by two main factors: energy security and climate change mitigation. The dependence on oil and gas import has led to Chinese involvement in Sudan, American involvement in the Middle East and an escalation of the international crisis between Russia and the European countries. As the global energy demand is expected to increase by 1.1 % each year until 2040, there is a political incentive to decrease the amount of imported energy [2]. The latest IPCC report states that it is *extremely likely* that the increase in global temperature and sea-level is caused by the increase in CO_2 and other greenhouse gasses like CH_4 and N_2O, and that the costs of a business-as-usual approach will be severe - both in terms of finance and human well-being [3]. These combined factors result in large investments in renewable energy sources. 144 countries have defined policy targets to increase the share of renewable energy, and especially China has invested massively in renewable energy sources since 2011. The global amount of renewable energy sources amounted to 19 % of the total energy production in 2012, increasing by approximately 1 % each year [1].

Most renewable energy sources produce electricity from sun or wind energy. This means that energy is produced when the sun is shining and when the wind is blowing, and, as that does not necessarily match the demand of energy, this creates a massive storage need. A number of different storage methods exist with different advantages and disadvantages in terms of capacity, power, mobility and price. As an example, pumped hydro is the most cost-effective way of storing large amounts of electrical energy, but it requires

huge capital costs and the presence of appropriate geography. On the other hand, batteries are relatively expensive per stored kWh, but very useful for mobile applications as the energy density is high and the unit size is very flexible.

1.1.1 Non-fossil transportation

Today, much attention is being devoted to developing green transportation, as this accounts for 63.7 % of the global oil consumption (2012) [4]. Gasoline has a very high energy density of approximately 12.3 kWh/kg, and the challenge is to develop competitive energy storage methods with sufficiently high energy density. Different technologies like batteries, fuel cells and bio-diesel are currently being investigated. All technologies have benefits and drawbacks, and it is unlikely that any of the technologies will be able to solve the future challenge of non-fossil transportation alone. Looking at the use of batteries in transportation, Li-ion batteries have been implemented in different electric cars during the last 10 years. The driving ranges of economy cars lie between 80 km and 160 km, and it is forecasted that this driving range cannot improve by more than a factor of 2-3 using conventional battery technologies. This means that conventional battery technologies will not be able to match the driving range of gasoline cars, which is currently considered critical to enable a full transition to non-fossil transportation. The need for better mobile energy storage has strongly motivated research in other battery systems such as lithium-sulfur and lithium-oxygen batteries.

1.2 Batteries

A battery is an electrochemical cell that converts stored chemical energy into electrical energy. It was first invented by Alessandro Volta in 1800 and has since then become a common power source for many household and industrial applications. There are two types of batteries: primary batteries (disposable batteries), which are designed to be used once and discarded, and secondary batteries (rechargeable batteries), which are designed to be recharged and used multiple times. Batteries come in many sizes, from miniature cells used to power hearing aids and wristwatches to battery banks the size of buildings that provide backup power for telephone exchanges and data centers or act as frequency stabilization units in the power grid.

The wireless revolution that has dominated the western world in the late 00's has been powered by batteries, and especially the rechargeable lithium ion batteries. Lithium batteries were initially proposed by M. S. Whittingham [5] in the 1970s and important contributions have been made by John B. Goodenough among others [6]. The Li-ion

battery was commercialized by Sony in 1991 and many improvements have been made since then. The current state Li-ion battery has the largest capacity of all commercialized secondary batteries, and they are found everywhere. Globally, the annual production of battery cells is astonishing 20 billion cells. Tesla alone is expected to use 0.3 billion cells in 2015.

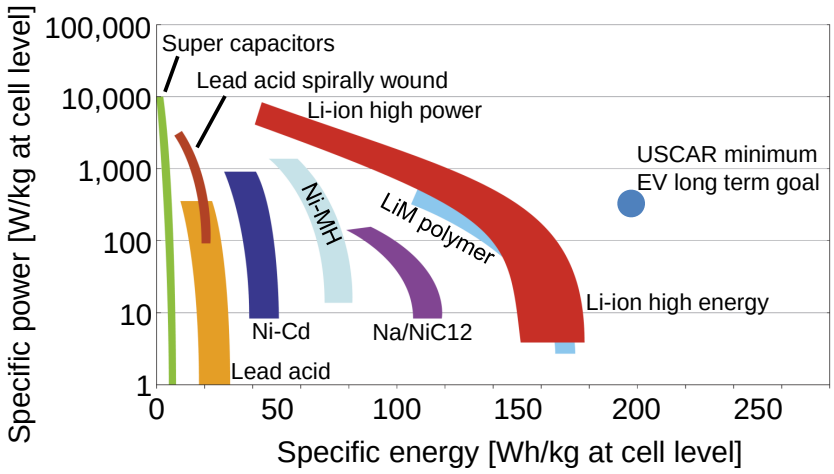

FIGURE 1.1: Ragone plot comparing the specific energy and specific power of different battery systems [7] and [8].

Many types of commercial secondary batteries exist. Figure 1.1 shows a Ragone plot of the most common chemistries like Lead-acid (Pb-H), Nickel Metalhydrate (NiMH) and different Li-ion based chemistries. Comparing with the 12.3 kWh/kg energy density of gasoline, it is clear that significant improvements are needed. The energy density can be improved in two ways: by increasing energy (potential) or by increasing capacity (decrease weight or volume per charge). The first strategy is exemplified by lithium nickel manganeseoxide (LNMO), where the potential is increased from 3.6 V to 4.7 V by substituting 25 % of the manganese with nickel, and the second strategy is exemplified by lithium nickel manganese cobaltoxide NMC, where more lithium can be extracted per transition metal. The Li-ion batteries are, however, limited by a heavy framework, and disruptive technologies are needed to obtain decisive improvements in energy density. Recently, the Li-air battery has been investigated heavily as such a disruptive technology.

1.2.1 Gold rush of the giant leap

The non-aqueous lithium-air (or Li-O_2) battery is a relatively new battery concept proposed by Abraham et al. in 1996 [9]. Compared with a lithium-ion battery, the lithium-air battery is an open system that allows oxygen from the atmosphere (or from an oxygen storage tank) to solute in the electrolyte and reduce at the positive cathode to form lithium peroxide (Li_2O_2) during discharge. This makes it possible to avoid

heavy transition metals in the cathode and use lighter elements like carbon instead, which reduces the total battery weight significantly. Theoretically, and disregarding support materials and electrolyte, the energy density of the Li-O_2 battery is 3.8-11.7 kWh/kg depending on whether the oxygen is included in the calculation or not [10]. This is comparable to gasoline and, if realizable, exceeding the improvements seen in the previous 150 years since Gaston Planté discovered the Lead-Acid battery in 1859.

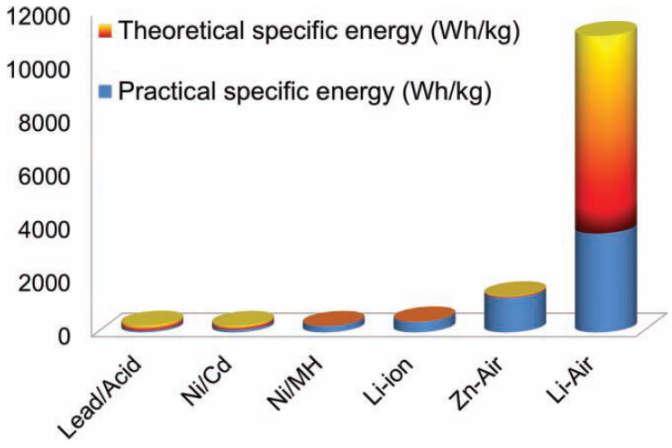

FIGURE 1.2: Comparison between the specific energy density of different battery technologies. It is seen that the theoretical energy density of the Li-air battery is significantly larger than all other rechargeable battery systems. The practical energy density is however somewhat smaller [11].

Figure 1.2 shows a comparison of the Li-O_2 chemistry with other battery technologies currently investigated. The Li-air battery received only little attention until Peter Bruce made experiments with his group demonstrating rechargeability [12]. This demonstration opened up the technology and initiated a competitive race in the scientific community to publish results as fast as possible. IBM started up the Battery 500 project to develop an EV Li-air battery with a driving range of 500 miles, and research groups all over the world started up Li-O_2 battery activities. Figure 1.3 shows an overview of the number of published scientific papers within Li-air batteries.

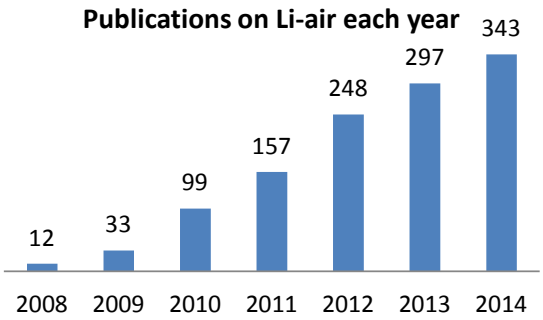

FIGURE 1.3: Number of publications on lithium-air batteries. The numbers are based on a Google Scholar search using *allintitle: (lithium-air OR Li-air OR lithium-O2 OR Li-O2).*

In early experiments using carbonate solvents in the electrolytes, it was observed that the cell voltage rose almost immediately to above 4 V during charge. This was incorrectly interpreted as a high Li-O_2 kinetic overpotential for charging, and has led to a strong focus on electrocatalysis in the literature. However, as will be pointed out in Chapter 4, this rapid rise was instead related to electrolyte decomposition that formed carbonate and carboxylate products rather than Li_2O_2 during discharge. Once formed, they do not oxidize electrochemically until 4 V.

In general, many publications within the field of Li-O_2 batteries are misinterpreted at best, because of an insufficient characterization of the involved mechanisms. Some of the most prominent results are the application of carbonate electrolytes, catalysts in the positive electrode and capacity limited cycling, and today many of these measurements and publications have been proven wrong.

A detailed review of the current state of research is found in the recent book *The Lithium Air Battery: Fundamentals* by Imanishi et al. [13] and a condensed version is presented in the excellent review by Luntz et al. [14] from 2014.

1.3 About this work

1.3.1 The aims of the project

Early in this project, it was clear that a careful study of the electrochemistry and fundamental reaction mechanisms was needed to ensure that we could distinguish the wanted electrochemistry from the unwanted. This changed my work from developing new cathode materials to developing a stable test system and reliable methods to characterize the fundamental electrochemical mechanisms inside the Li-O_2 battery. The focus has thus been to understand the formation and removal of Li_2O_2, and the undesired degradation reactions.

Today, no one knows if Li-O_2 batteries will ever be commercially viable because of the significant degradation, but as an employee at Haldor Topsøe A/S, it was also important to assess the viability in a system perspective, which has been done under the assumption that the challenge of degradation is solved or at least significantly reduced. The assessment focuses on air purification in an open Li-air battery system and battery management using an impedance based State-of-Charge (SoC) determination.

1.3.2 Outline of the thesis

The contents of this thesis are divided into seven chapters. The research results of the project are reported in Chapters 4, 5 and 6, and the work presented in those chapters has been carried out by me unless otherwise stated. This work resulted in two published peer-reviewed publications, two submitted publications and one publication draft. The five manuscripts are attached as appendices to the thesis. In addition to this, four appendices have been attached, including work that has been of significant importance to the project, without being a subject for publication. The thesis has been written as an independent work and the papers have been attached to support the discussions and conclusions presented.

2 Theory
This chapter focuses on the working principle of the Li-O_2 battery and a brief introduction to the theoretical foundation of electrochemical impedance spectroscopy (EIS).

3 Experimental
This chapter focuses on the manufacturing of cathodes, the basic working principles of the differential electrochemical mass spectrometry (DEMS) and electrochemical impedance spectroscopy.

4 Overpotentials and degradation
This chapter presents the work on explaining the fundamental reaction mechanisms in the Li-O_2 battery. Methods like EIS, DEMS, TEM and absorption measurements give important contributions to this work. This chapter is closely related to Paper I and Paper II.

5 Screening for new electrolytes
This chapter presents work on finding a new electrolyte by testing promising ionic liquids (IL) with DEMS. This chapter is closely related to Paper IV.

6 Commercializing Li-air batteries
This chapter presents a novel method to increase the accuracy of the state of charge determination in a Li-O_2 battery and work on air-purification of the inlet air in an open Li-air battery. This chapter is closely related to Paper III.

7 Summary and outlook
The four main results of the work are summed up and six suggestions to future work are presented.

List of included papers

Paper I

An electrochemical impedance spectroscopy investigation of the overpotentials in Li-O_2 batteries

Jonathan Højberg, Bryan D. McCloskey, Johan Hjelm, Tejs Vegge, Keld Johansen, Poul Norby and Alan C. Luntz

ACS Appl. Mater. Interfaces, 7, 4039–4047 (2015)

Paper II

Reactions and SEI formation during charging of Li-O_2 cells

Jonathan Højberg, Kristian B. Knudsen, Johan Hjelm and Tejs Vegge

ECS Electrochem. Lett., 4, A63–A66 (2015)

Paper III

Impedance-based battery management for metal-O_2 systems

Andreas E. Christensen, Jonathan Højberg, Poul Norby and Tejs Vegge

J. Pow. Sources. *Submitted* (2015)

Paper IV

Rechargeability of ionic liquids in Li-O_2 batteries

Supti Das, Jonathan Højberg, Kristian B. Knudsen, Poul Norby and Tejs Vegge

To be submitted

Paper V

The influence of CO_2 poisoning on overvoltages and discharge capacity in non-aqueous Li-air batteries

Yedilfana S. Mekonnen, Kristian B. Knudsen, Jon S. G. Mýrdal, Reza Younesi, Jonathan Højberg, Johan Hjelm, Poul Norby and Tejs Vegge

J. Chem. Phys., 140 (2014)

Chapter 2

Theory

2.1 The lithium-oxygen battery

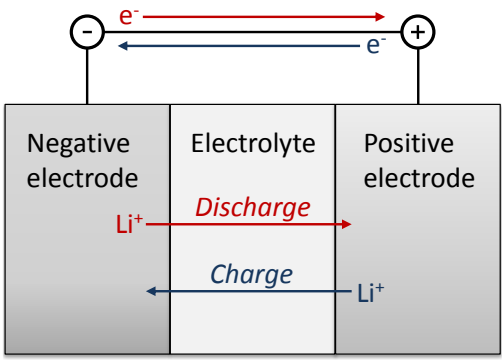

FIGURE 2.1: Schematic of the overall Li-battery working principle.

Figure 2.1 shows a highly simplified sketch of how lithium batteries work by moving Li^+ ions through the electrolyte from the negative electrode to the positive electrode during discharge and vice versa during charge. The two electrode materials absorb, store and release Li^+ ions at two different chemical potentials, and the difference between these chemical potentials gives the open circuit cell voltage (OCV)

$$\mathrm{OCV} = -\frac{\Delta G^{\ominus}}{zF} \tag{2.1}$$

where $\Delta G^{\ominus}$ is the change in Gibbs free energy of the reaction, z is the charge number (1 in Li-batteries), and F is the Faraday constant. The battery is discharged by connecting the two materials electrically through an external circuit. This allows electrons to move from the negative electrode to the positive electrode with an energy corresponding to the voltage difference multiplied by the elementary charge. The energy of the electrons can be used in the external circuit to power a laptop or another electrical device. The

battery is charged by applying a potential between the two electrodes greater than the equilibrium potential. This forces electrons to move from the cathode to the anode, which reverses the entire reaction. In Li-ion batteries the two electrode materials are crystaline intercalation materials, where lithium is stored inside the crystal. In Li-O_2 batteries, the electrodes are different, as both electrodes grow (shrink) during reduction (oxidation).

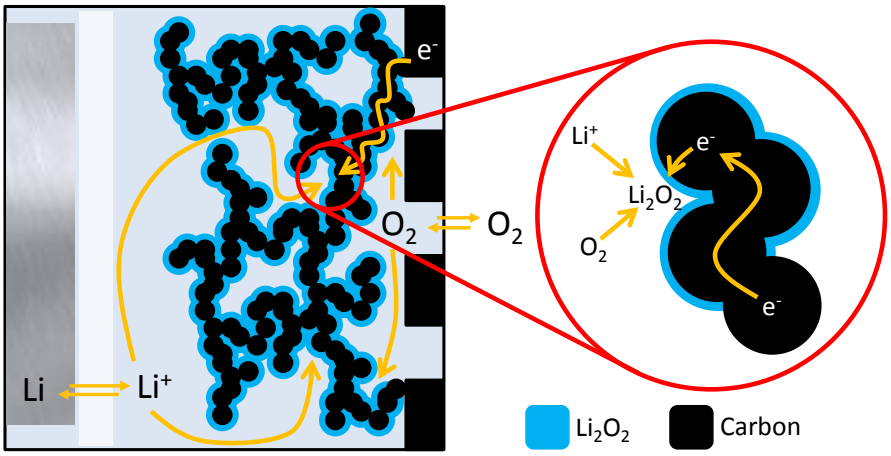

FIGURE 2.2: Li-air battery discharge electrochemistry.

The actual mechanism of the Li-O_2 battery depends on the choice of electrolyte. This can be aqueous, aprotic (water-free) or solid. The aprotic system has received most attention in literature due to the problems with ohmic losses, rechargeability and low energy density observed in the other systems. For this reason, only the aprotic system is considered in this work. Figure 2.2 shows the ideal electrochemistry of the aprotic Li-air battery. The battery is open to allow oxygen inside the battery. The oxygen diffuses to the positive electrode, where it is reduced to form Li_2O_2. During charge, the Li_2O_2 is oxidized and oxygen is released. The Li^+ ions move between the two electrodes to balance the charge and, on the negative electrode, lithium is soluted/plated to keep a constant number of Li^+ ions in the electrolyte.

2.1.1 New definitions for lithium-oxygen batteries

Rechargeability. The most important characteristic of the Li-O_2 battery at the current state is rechargeability, and because the system is fundamentally different from the Li-ion battery, the general definitions do not apply. In Li-ion batteries, the two electrodes are balanced such that any degradation involving either lithium or one of the electrode materials would directly affect the capacity of the battery. All current state Li-O_2 batteries use a massive excess of both lithium and electrolyte, which means

that electrochemical degradation can occur without being detected in the electrochemical measurements. This has led to the four definitions of rechargeability adapted from Luntz et al.[14]:

1. the yield of Li_2O_2 relative to that anticipated from the current and ideal cathode reaction $2(Li^+ + e^-) + O_2 \rightarrow Li_2O_2$ during discharge is $Y_{Li_2O_2} = 1.00$, i.e., no other products are formed during discharge either on the cathode or in the electrolyte, e.g., no LiOH, Li_2CO_3, LiF, carboxylates, etc
2. during discharge, the electrochemical current consumes only O_2, $(e^-/O_2)_{dis} = 2.00$, and during charge, all electrochemical current evolves O_2, $(e^-/O_2)_{cha} = 2.00$
3. no parasitic gas evolution (H_2, CO_2, etc.) occurs during the discharge-charge cycle
4. all O_2 consumed during discharge (ORR) is released during charge (OER) so that OER/ORR = 1.00

If all requirements are met, then the Li-O_2 battery is perfectly rechargeable. In addition, a long calendar life is necessary, and this requires that all thermal parasitic chemical reactions between components of the battery are minimal or at least self-limiting, e.g., between Li metal or Li_2O_2 and the electrolyte.

Normalization of battery capacity. Another important characteristic is the theoretical capacity and normalization. Li-O_2 batteries do not have a fundamental limit to the capacity in the same way as Li-ion batteries. Instead, the choice of normalization should be chosen such that it captures the limiting factor of the battery. It is generally accepted in the literature, that the growing, insulating Li_2O_2 layer causes cell death due to a blocking of electrons to the surface when the thickness reaches approximately 5 nm, and together with the BET area, this could give an estimate of the theoretical capacity. As suggested by Meini et al., this number should, however, be adjusted not to count in the micropore surface area, as they show that the capacity scales with the non-micropore surface area rather than the full BET area [15]. Reza et al. have likewise shown that the binder blocks the micropores [16].

Figure 2.3a shows the correlation between carbon loading and discharge capacity to 2.6 V using a current of 130 mA/g_C. The correlation is clear, which suggests a normalization to the carbon mass is appropriate for this system. Figure 2.3b shows how much electrochemical oxidation has occurred during charge at a given potential. The monotonic increase shows that a normalization to the mass is also appropriate during charge. The red points in the two graphs are the same measurements. They have been discarded due

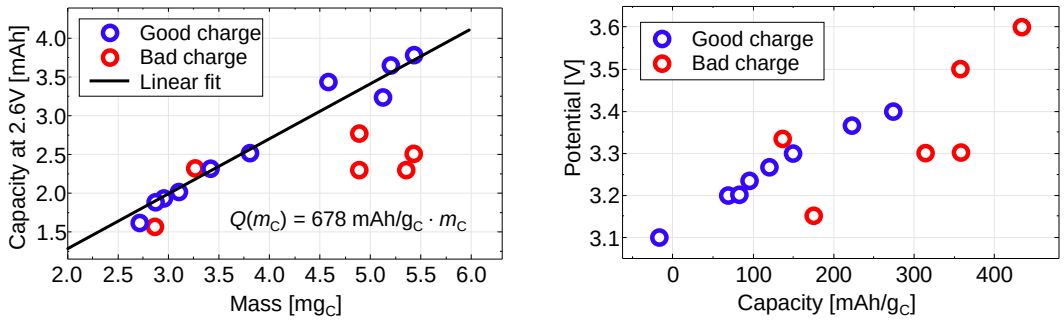

FIGURE 2.3: Left: Measurements of discharge capacity as a function of the carbon loading. Some cells started charging at potentials below 2.85 V indicating that degradation products formed during discharge are oxidized at these low potentials. Such cells are marked in red and are considered as outliers. The reason could be small leaks or insufficient drying of the cathodes or the Swagelok cells. A linear fit through (0,0) shows a capacity of 678 mAh/g_C, independent of the carbon loading. Right: The capacity of cells charged to different voltages compared to the average capacity of 678 mAh/g_C.

to differences in the discharge and charge curves that indicate the presence of impurities in the cathode.

2.2 Electrochemical impedance spectroscopy

Electrochemical impedance spectroscopy (EIS) is central in this thesis and is used extensively in Paper I, Paper II and Paper III. This section is used to highlight and explain the theory relevant to the Li-O_2 system, and a basic understanding of EIS is assumed. For additional information on the basic theory, the educational book chapter by Allen Bard [17] (Chapter 10) and the thorough book *Electrochemical Impedance Spectroscopy* by Mark Orazem and Bernard Tribollet [18] are recommended.

EIS has been used to describe the fundamental mechanisms of the Li-O_2 battery by a few other groups. The most thorough studies are presented by Adams et al. [19], Landa-Medrano et al. [20] and Bardenhagen et al. [21]. In addition to these publications, a number of groups have used EIS to characterize the capacity loss, hysteresis and pore clogging in Li-O_2 batteries among others [22–25] and Metha et al. have presented an initial modeling study presenting fundamental consideration, but without good experimental data to validate the model [26].

2.2.1 Correlation between overpotential and impedance

The ultimate goal of fundamental investigations such as EIS is to predict or improve certain performance parameters. It is therefore very interesting to relate the impedance

measurement to the change in overpotential. The impedance is defined as the derivative of the iv-curve:

$$Z(i) \quad = \quad \frac{\partial v}{\partial i} = \frac{\partial \eta}{\partial i}, \tag{2.2}$$

where v is the potential, i is the current density and η is the overpotential. Therefore, the impedance is linked closely to the Tafel plot, which has previously been used to describe reaction mechanisms in Li-O_2 batteries [27–30]. From the Tafel equation, the overpotential is seen to be proportional to $\log(i)$ at large overpotentials ($|\eta| \gg \mathrm{RT/nF}$), but as our batteries contain a porous cathode, this ideal behaviour is not valid. The consequences of a porous electrode have been investigated by Lasia [31] and show that the Tafel slope will increase at higher currents. This is in line with our measurements as well as previous Li-O_2 battery measurements by Viswanathan et al. [27] and Adams et al. [19] on porous electrodes. To describe the measurements better

$$\eta \quad = \quad |v - \mathrm{OCV}| = c_1 \cdot i^{c_2} \tag{2.3}$$

is applied as an empirical model, when Equation (2.2) is used to compare the measured impedance with the overpotential. OCV is the open circuit potential, and c_1 and c_2 are constants.

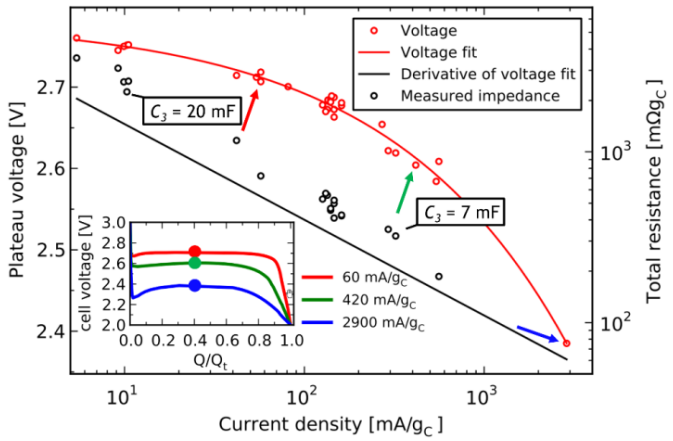

FIGURE 2.4: The plateau voltage dependence on current density (red dots) from 10 μA (9 μA/cm^2) to 5 mA (4.4 mA/cm^2). Equation (2.3) is fitted to the data (red line), which is then differentiated (black line) and compared with the total resistance (black dots) measured with impedance. Three representative discharge curves show how the plateau voltage is determined. The impedance and current density have been weighed by the carbon mass of each electrode. Reprint from Paper I.

Figure 2.4 from Paper I exemplifies the dependence between impedance and overpotential. The overpotential measurements are fitted to Equation (2.3) and differentiated according to Equation (2.2) to obtain the impedance. Comparing with the measured impedances, it is seen that the correspondence is not perfect in this system.

2.2.2 Modeling Li-O_2 battery impedance

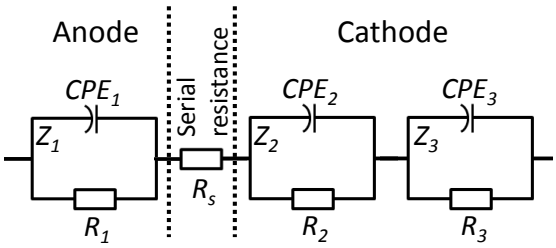

FIGURE 2.5: Equivalent circuit diagrams used to model most of the impedance measurements. It consists of three Voigt elements (parallel connected resistor with a constant phase element, CPE) and a serial resistance. The contributions to the impedance can be attributed to either the anode (Z_1) or the cathode (Z_2 and Z_3). The impedance is described in Equation (2.4). Reprint from Paper I.

The measured impedance response can, to a first approximation, be described using an equivalent circuit model consisting of three Voigt elements (parallel connected resistor with a constant phase element (CPE)) connected in series. The impedance of the Voigt elements is adopted from Hirschorn et al. [32], and the total impedance, $Z(\omega)$, is thus given by

$$Z(\omega) = R_s + \sum_{i=1..3} \frac{R_i}{1 + (j\omega)^{n_i} Q_i R_i}, \tag{2.4}$$

where ω is the angular frequency, and R_i, Q_i and n_i are parameters in Voigt element i. R is the DC resistance, and Q and n are parameters of the CPE. If $n = 1$, the CPE is a capacitor, and even if n is between 0.7 and 1, a pseudocapacitance, C^*, can be calculated. As discussed in detail by Jamnik et al. [33], this capacitance is typically a double layer capacitance related to the process, and by comparing with reference values, it is possible to estimate the surface area contributing to the process. The pseudocapacitance is calculated from the equivalent circuit parameters according to Hirschorn et al. [32]:

$$C^* = Q^{1/n} \left(\frac{R_\Omega R}{R_\Omega + R} \right)^{(1-n)/n}, \tag{2.5}$$

R_Ω is the DC resistance at the investigated frequency. As discussed by Zoltowski et al., the pseudocapacitance of a CPE element is not well defined [34], which means that the surface area obtained using C^* might vary slightly from the actual surface area, but the order of magnitude, and relative changes are still valid.

The surface area of the flat lithium anode and the porous cathode are in the range of 1 cm^2 and 1 m^2, respectively. The capacitance at the lithium metal surface in an organic electrolyte is typically 10-20 $\mu F/cm^2$ as reported by Aurbach et al. [35, 36] and the capacitance of XC72 is 12.6 F/g in an organic aprotic electrolyte as reported by

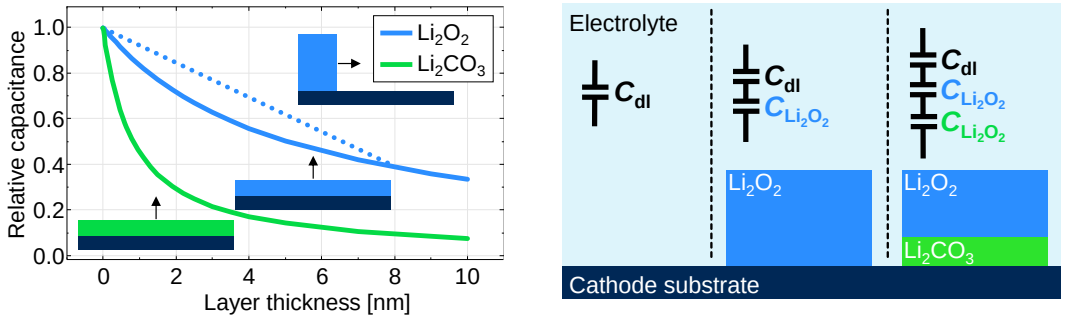

FIGURE 2.6: (a) The relative change of the cathode capacitance as a layer of Li_2O_2 or Li_2CO_3 is deposited. The dotted line represent a different scenario, where a 8 nm thick layer grows along the surface. In this case '8 nm' on the x-axis correspond to a full surface coverage. (b) Sketch of different relevant scenarios for the Li-O_2 battery and the equivalent capacitance.

Barbieri et al. [37]. From this, it is calculated that the capacitances should be in the range of 10 μF and 25 mF for the anode and cathode, respectively. Furthermore, the capacitance is expected to change during discharge as the dielectric Li_2O_2 is deposited. The relative permittivity ϵ_r of Li_2O_2 has been measured to be 30-35 by Gerbig et al. and Dunst et al. [38, 39]. Using a value of 30 to calculate the capacitance of the Li_2O_2 layer in series with a typical electrode-electrolyte capacitance of 20 mF, a Li_2O_2 layer of 5 nm will halve the cathode capacitance. This is shown in Figure 2.6a. A similar calculation has been made for the Li_2CO_3 interface layer between the cathode and the Li_2O_2. Using the relative permittivity of Li_2CO_3 of 4.9 measured by Young et al. [40], the capacitance will be halved with a layer thickness of 0.8 nm.

The analysis of the change in capacitance will be an important part of the discussions in Chapters 4 and 6, and, though simplified, the approach to growth of both Li_2O_2 and degradation products shown in Figure 2.6 serve as a good description of the actual change in capacitance during discharge and charge.

Chapter 3

Experimental methods

3.1 Cell configuration

Most of the work described in this work is performed using a specific combination of components as shown in Figure 3.1. It is, intentionally, made as close to the reference system used by McCloskey et al. described in [41] to enable a direct benchmarking and mutual exploitation of the results obtained in the two laboratories. The measurements

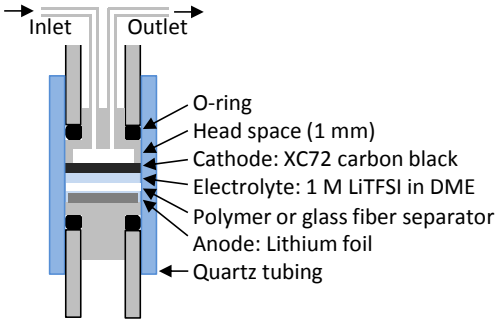

FIGURE 3.1: Schematic illustration of the reference system used in this thesis. The battery is made of a lithium metal anode, a polymer or glass fiber separator, a porous cathode made of XC72 carbon black and PTFE binder. The electrolyte is 1 M bis(trifluoromethane)sulfonimide lithium salt (LiTFSI) dissolved in 1,2-dimethoxyethane (DME). The Swagelok cell is described further in Section 3.1.1.

were made with an 11 mm diameter lithium metal anode (HongKong Wisdom Tech Company), two 12.7 mm diameter Celgard 2500 separators or one 12.7 mm Whatman glass fiber separator, a 10 mm diameter porous cathode made of XC72 carbon black and PTFE binder on a 316SS stainless steel 150 mesh, and 60-90 μL of 1 M LiTFSI in DME electrolyte depending on the choice of separator. Details of the cathode and the electrolyte are found in Sections 3.1.2 and 3.1.3, respectively.

3.1.1 The Swagelok cell

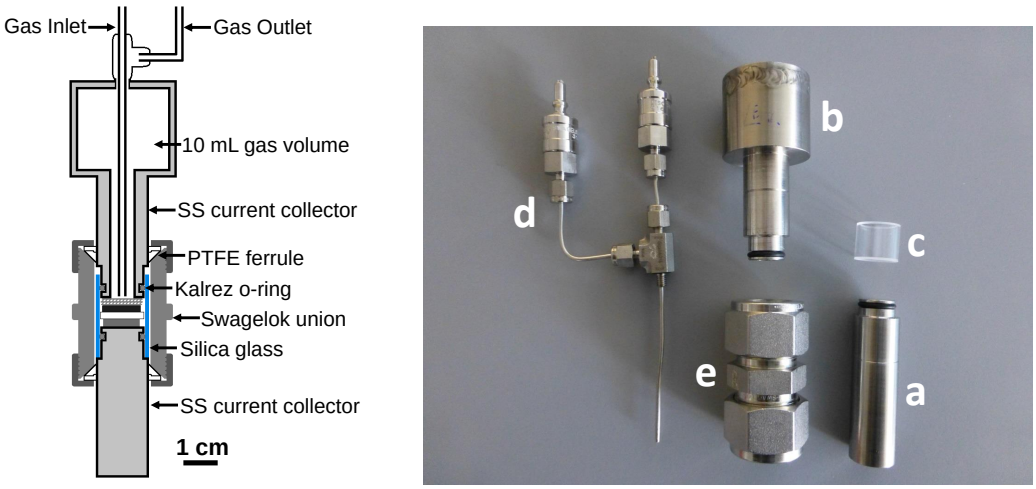

FIGURE 3.2: Left: Sketch of the 10 mL Swagelok cell. Right: Picture of the individual parts of the 10 mL Swagelok cell.

The cell configuration used to test Li-O_2 batteries was improved throughout the project. Pictures and descriptions of the four cell generations are found in Appendix A. Figure 3.2 shows the current generation; a Swagelok-type cell with a head-space volume of 10 mL. The volume has been chosen based on a maximum expected capacity of the tested batteries of 5 mAh, which corresponds to 2 mL O_2 at 1 bar, and as the initial head-space pressure was typically 1.8 bar, the change in oxygen partial pressure during discharge did not exceed 10 %. The battery components are stacked in the cell between 316SS anode and cathode tips that were sealed against a fused silica tube using FFKM Kalrez o-rings (KZ6375, M-Seals). A 1/16″ tee with M4 thread mounted on the cathode tip enabled connection of a gas inlet and a gas outlet to allow gases to be fed to and swept away from the cell. Two DESO quick connects ensured an easy connection to the gas system, while maintaining an airtight cell during the electrochemical test. The cell design has proven very robust, but it is important to stress that the precision requirements are significant, as the tolerance on the inner diameter of the glass tube is 50 μm. Typical leak rates was 0.2 - 20 mbar/h, with most leak rates in the range 5 - 10 mbar/h. This means that a 10 % change in pressure (180 mbar) from the leak alone is not reached until after at least 9 hours in all cells, which is sufficient for most measurements.
The gas inside the Swagelok cell can be changed between argon (purity 6.0, Air Liquid) and oxygen (purity 6.0, Air Liquid) using a Labview controlled automated setup described in Appendix A.

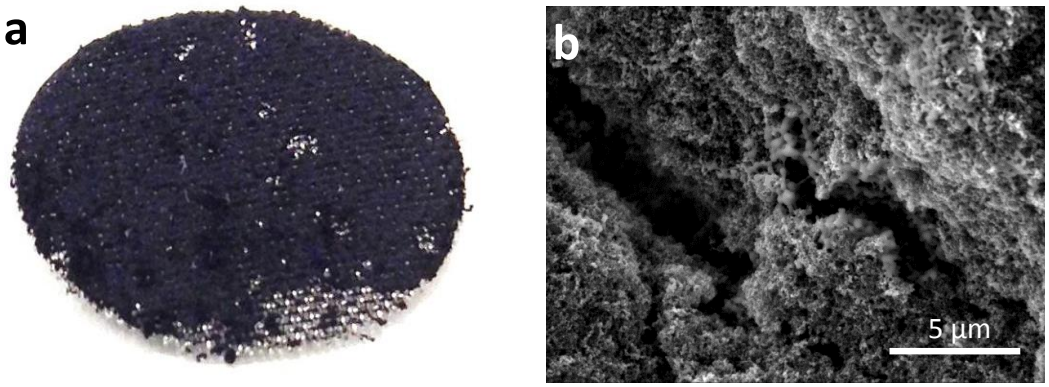

FIGURE 3.3: (a) Picture of an XC72 cathode. and SEM image of an XC72 cathode. (b) SEM image of the sprayed mixture of carbon and PTFE

3.1.2 The XC72 cathode

Figure 3.3 shows a picture of an XC72 cathode and a SEM image of the sprayed mixture of carbon and PTFE. The cathodes were prepared by air-spraying a carbon/PTFE dispersion onto a 316SS 150 mesh (WestCoast, Esbjerg, Denmark). The slurries were prepared by sonicating a carbon black powder (Vulcan XC72, Cabotcorp, GA) and PTFE (60 wt% dispersion in water, Sigma Aldrich) in a 3:1 wt/wt ratio in a 20:80 isopropanol/water mixture. Figure 3.4 shows how a Badger model 350 air-sprayer with a heavy nozzle was used to uniformly coat the dispersion onto the SS mesh. The SS mesh was rinsed in acetone several times prior to cathode preparation. Prior to cutting 10 mm diameter cathodes from the carbon-coated SS mesh with a Heavy Duty Disc Cutter (MTK-T-06, MTI Corporation), the mesh was allowed to air-dry for 3-4 h. All cathodes were dried 12 h in vacuum at 120 °C, washed twice in pure 1,2-dimethoxyethane (DME) inside a glovebox, followed by a second drying under vacuum for 10 min. Depending on the scope of the experiment, the carbon loading of each cathode was varied between 1 mg and 5.6 mg, but typical loadings were in the range 4.7 mg - 5.6 mg.

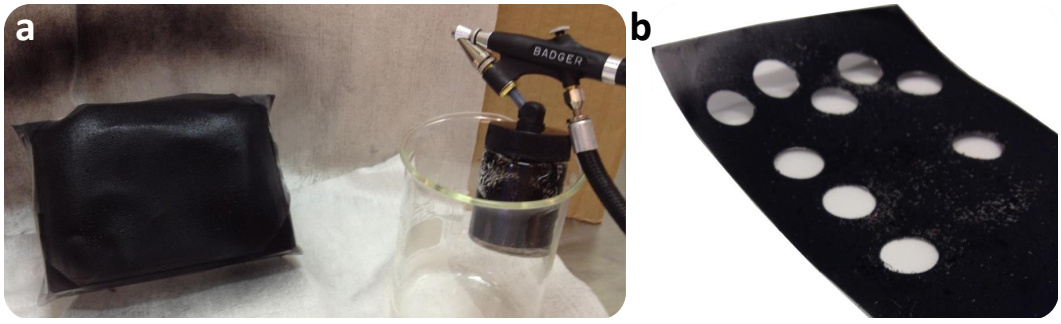

FIGURE 3.4: (a) Picture of air-sprayed carbon/PTFE dispersion on SS316 mesh and (b) the SS316 mesh after punching out air electrodes.

3.1.3 Electrolyte

1M LiTFSI in 1,2-dimethoxyethane. DME was purchased from Novolyte (Purolyte electrolyte grade) and LiTFSI (purity 99.9 %) was purchased at Sigma Aldrich. The electrolytes were mixed every 1-2 months to ensure a low level of water impurities. Prior to the mixing, the LiTFSI salt was dried under vacuum at 200 °C in 12 h and DME was dried using 4Å molecular sieves (Sigma Aldrich) for several days. The content of water was not measured directly, but the electrolyte was used in microelectrode experiments, were any water present would be detected immediately.

Ionic liquids. A total of six ionic liquids (IL) and the corresponding two lithium salts were tested as described in Paper IV. The ILs were purchased from Solvonic and Sigma Aldrich in purities between 98.5 % and 99.9 % and used as received from the suppliers. The electrolyte salts were dried prior to preparing the electrolye. LiTFSI (purity 99.9 %, Sigma Aldrich) was dried in vacuum for 12 h at 180 °C and Lithium bis(fluorosulfonyl) imide (LiFSI, purity 99.9 % Suzhou Fluolyte) was dried in vacuum for 12 h at 80 °C. Electrolytes with lithium salt concentrations of 0.3 M were prepared by mixing the appropriate ratio of salt and ionic liquid and stirring at room temperature in order to get homogenous electrolyte solution. Occasionally, the stirring was continued for several hours to ensure solution of the salt.

3.2 Differential electrochemical mass spectrometry

Differential electrochemical mass spectrometry (DEMS) is an essential measurement when characterizing the discharge and charge of Li-O_2 batteries, and metal-O_2 batteries in general, as the method is able to determine the e^-/O_2-ratio and the OER/ORR value, which are key in defining rechargeability as discussed in Section 2.1.1. The high sensitivity of the mass spectrometer enable detection of even small amounts of gas evolved and, by using a suitable setup, it is possible to get accurate quantitative measurements of the O_2 consumption (evolution) from the reduction of O_2 (oxidation of Li_2O_2) during discharge (charge) and CO_2 and H_2 from degradation reactions.

The method was originally proposed by Bruckenstein et al in 1971 [42]. They collected gaseous electrochemical reaction products in a vacuum system through a teflon membrane and detected the gases by mass spectrometry. Peter Bruce et al. reported measurements of the evolved oxygen gas during charge of a Li-O_2 battery using a similar setup in 2006 [12]. The setup was refined significantly for analysis of the gas consumption and release in lithium-oxygen batteries in 2011 by Bryan McCloskey and Alan Luntz

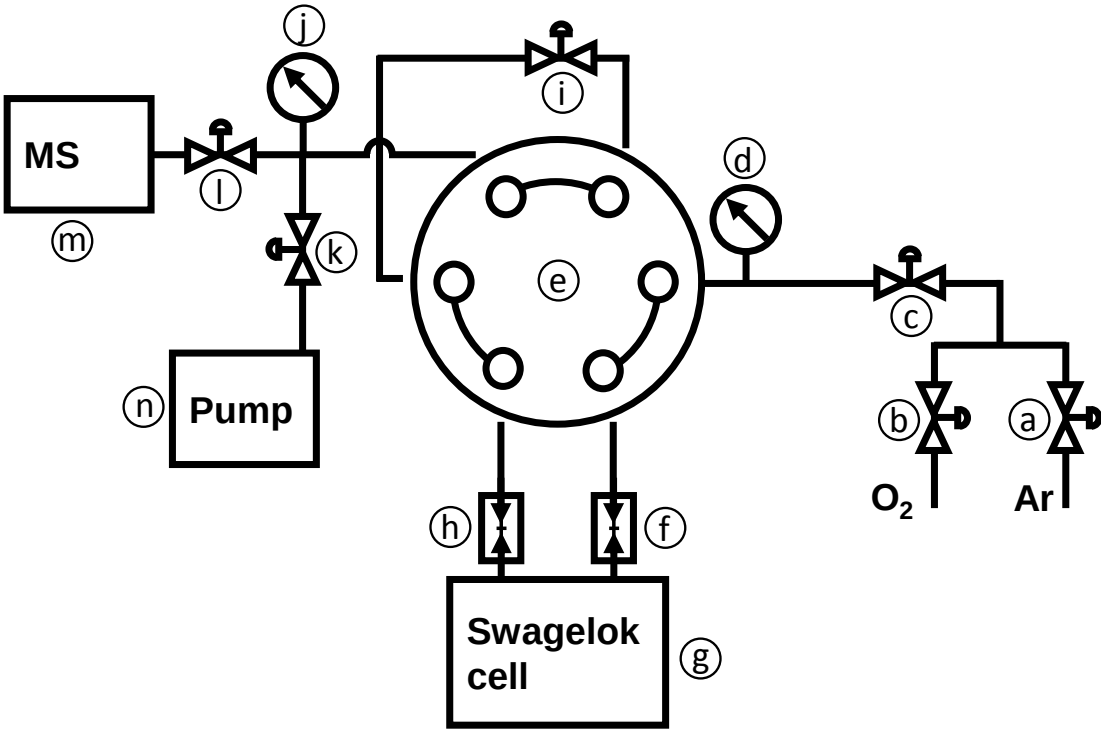

FIGURE 3.5: Schematic illustration of the DEMS setup. The circled letters are used to refer to specific parts of the setup in the text.

from the IBM group [41], and has provided important insight to the current understanding of the degradation in lithium-oxygen batteries. Since then, five to ten research groups have acknowledged the importance of this measurement and built a system in their own lab.

I have been responsible for building such a system in our lab. Of that reason, I have included pictures of the experimental setups I have constructed in Appendix A and details of calibrations and reference measurements are included in Appendix B. The DEMS system is illustrated in Figure 3.5. Six normally closed magnetic valves (SCG256A003NVMS 24VDC from OEM Automatic Klitsø A/S) (a), (b), (c), (i), (k) and (l) enable automatic control of how the gases are flowing, two pressure transducers (DMP 331i, BD Sensors) (d) and (j) monitor the pressure inside the setup, and (e) is an automatic 2-position 6-way valve (EHC6WE, VICI) that enable sampling from a special low-volume Swagelok cell (g). The Swagelok cell is easily attached to the setup using quick connects (SS-QM2-B-100 and SS-QM2-D-100, Swagelok) (f) and (h). The mass spectrometer (Omnistar GSD320-C, Pfeiffer Vacuum) (m) is used to analyze the gases from the Swagelok cell and the vacuum pump (n) is used to clean the system before each sample collection from the Swagelok cell.

3.2.1 Typical operation

As already discussed, the three important characteristics to look for in a DEMS measurement are the e^-/O_2-ratio, the OER/ORR value and the identification of other gases than oxygen. To obtain these results, two modes of operation are used:

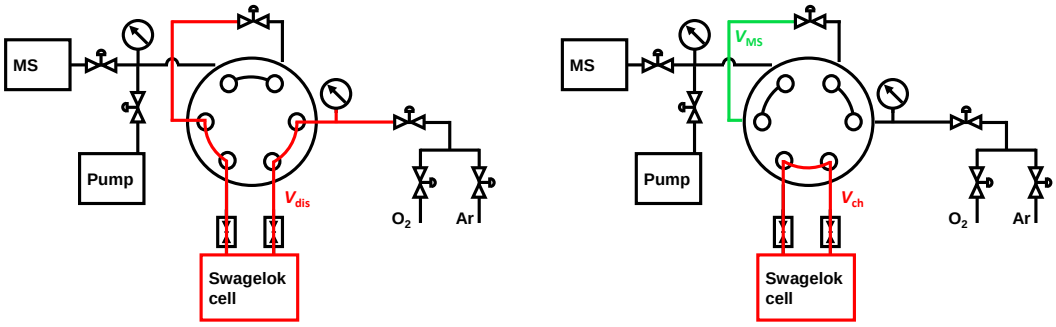

FIGURE 3.6: Schematic illustration of the DEMS setup in open (left) and closed (right) configuration. Volumes relevant for calculating the gas evolution and consumption are shown in red and green color.

Pressure mode. This method is always used in discharge, and in some cases during charge. The change in gas pressure is measured and related to the amount of oxygen consumed or released. This implies an assumption that oxygen is the only gas consumed or evolved. The pressure mode is performed in the configuration shown in Figure 3.6 (left).

DEMS. This method is primarily used during charge. Evolved gases are detected by flushing the Swagelok cell with argon, and collect the gas in a chamber V_{MS}, that is analyzed with the mass spectrometer. By comparing the M/Z intensity of the mass spectrum with reference measurements, it is possible to calculate the composition (and thereby the amount) of each gas. In the DEMS measurement, the cell is charging in the configuration shown in Figure 3.6 (right). In this period, the magnetic valves (c), (i) and (k) are open to remove all gases in the gas system. Just before sampling, (i) is closed and (a) is opened. The sampling is made by turning (e) to the open position and then back to the closed position. The charge continues while the sampled gas is analyzed with the mass spectrometer by opening (l). Only small amount of gas evolves between each sampling (0.1% - 1%), so the main content of the sampled gas is argon. The natural occurring ^{36}Ar isotope is used as a reference, as it constitute 0.333% of the argon gas, which is in the same range as the oxygen that needs to be detected through the charge.

3.3 Physical characterization

The cathode has been investigated using a number of physical characterization methods including transmission electron microscopy (TEM), scanning electron microscopy (SEM), BET, X-ray diffraction (XRD) and quantification of Li_2O_2 in the cathode using quantitative optical absorption spectroscopy. The project has focused mostly on the absorption technique and TEM characterization and the experimental section is therefore limited to these two measurement techniques.

3.3.1 Quantitative optical absorption spectroscopy

The amount of Li_2O_2 was determined at different stages of charge, using a spectrophotometric measurement. After electrochemical test of a Li-O_2 battery, the cell was purged with argon and transferred to a glovebox. The cell was carefully disassembled and the cathode was extracted. Each cathode was washed with 1,2-dimethoxyethane (BASF) dried using 4 Å molecular sieves (Sigma-Aldrich), and the cathodes were subsequently dried in vacuum. The cathodes were taken from the glovebox and immediately put into a 4 mL 0.063-0.07 % $TiOSO_4$ aqueous solution and the colored oxidized Ti-complex was seen immediately. The reactions occurring are

$$Li_2O_2 + 2H_2O \rightarrow 2LiOH + H_2O_2 \tag{3.1}$$

$$Ti(IV)OSO_4 + H_2O_2 + 2H_2O \rightarrow 4H^+ + H_2Ti(VI)O_4 + OSO_4^{4-} \tag{3.2}$$

$H_2Ti(VI)O_4$ absorbs strongly at 408 nm. The solutions were left to react for 15-30 min and to remove carbon particles, which otherwise would interfere with the spectrophotometric measurement, samples were centrifuged and the supernatant was extracted yielding a clear colored liquid that was characterized using a Shimadzu UV-3600 PharmaSpec with 1nm resolution and medium scan in absorbance mode. Further details on the model is found in Paper II.

3.3.2 TEM

The goal was to study the Li_2O_2 deposits in the discharged battery as well as the catalysts that most people thought would be necessary in 2011 [43–45]. As described in Section 1.3.1, it was subsequently found that catalysts only make things worse in Li-O_2 batteries because of an increased degradation rate in the battery, and the TEM studies shifted the focus almost entirely towards the Li_2O_2 morphology and growth. The literature contains very nice studies of this. The most prominent ones are the

identification of toroidal shaped Li_2O_2 particles made up of pancake like crystals [46], and the in situ charging of Li_2O_2 particles [47]. In addition to these publications, a few nice selected area electron diffraction (SAED) studies have been made to reveal the structural information on the nanometer scale [48–50].

The study of Li_2O_2 is challenging because it is both air- and beam-sensitive, and typical high-resolution techniques are not applicable. Furthermore, it has been shown by Aetukuri et al. that the large toroidal shaped particles are only formed in the presence of water impurities, and thus not interesting from a commercial point of view. This means that the challenge is to identify and investigate thin layers of Li_2O_2 with a thickness of only a few nanometers located on top of a carbon substrate. The experimental procedure is described below.

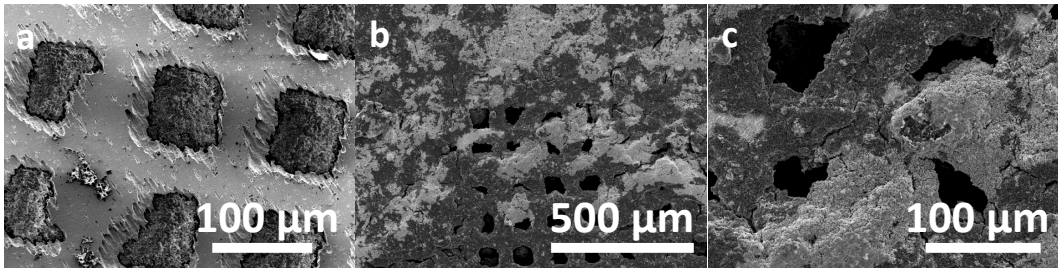

FIGURE 3.7: SEM images of (a) plain SS316 TEM grid and (b)-(c) two magnifications of SS316 TEM grid coated with XC72 carbon black and PTFE.

The TEM sample was made by spraying a stainless steel SS316 TEM grid in the same way as the ordinary cathodes, described in Section 3.1.2. Figure 3.7 shows SEM images of such a coat. The TEM grid was discharged galvanostatic together with an ordinary cathode with the typical current density of 130 mA/g_C. Comparing the discharge capacity with the cathode weight, approximately 20 wt% of Li_2O_2 is expected compared to carbon and PTFE binder.

The samples were examined in the FEI Tecnai G2 at DTU CEN in HR-TEM mode operated at 200kV. Imaging was performed at varies magnifications. The electron energy loss spectroscopy (EELS) acquisition was tuned by the Gatan tune and alignment software yielding an energy resolution of about 2.1eV measured as the FWHM of the zeroloss peak. The EELS was in this session only used as a qualitatively fingerprint in order to verify the presence of lithium in the sample. The samples were briefly screened at low magnification (for overview), and 3 areas were inspected further with EELS, selected area electron diffraction (SAED) and higher magnification.

3.4 Electrochemical impedance spectroscopy

The electrochemical characterization of the batteries has been a central part of the work presented in this thesis and in Paper I, Paper II and Paper III. Most measurements have been performed using Bio-Logic MPG-2 and VMP3 potentiostats with EIS capability. In the DEMS measurements, however, a Gamry Reference-600 was used. Several standard techniques like OCV mapping, galvanistatic and potentiostatic discharge and charge, and cyclic voltammetry have been used extensively and in a wide current and SoC window. Typically, only the first cycle is investigated, because subsequent cycles will be affected by the degradation occurring during the first cycle.

EIS measurements were conducted in galvanostatic (GEIS) and potentiostatic (PEIS) mode, and with and without a current load depending on the purpose of the measurement. More than five thousand spectra have been measured to continuously push the boundary of what was possible to probe with the technique. In Chapter 4, Paper I and Paper II, the focus is the discharge and charge mechanisms and thus it was beneficial to draw a current to investigate the processes under relevant conditions as discussed previously by Adams et al. [19]. In these measurements, the impedance was measured at currents between 15 μA (13 μA/cm^2) and 1 mA (0.88 mA/cm^2) with an alternating current (AC) amplitude of 10% of the direct current (DC) level. To investigate the charge with a rapid increase in potential, it was however necessary to use another approach. After charging to the desired potential in galvanostatic mode, the potential was kept an a 10 mV AC amplitude was superimposed in a PEIS measurement. This stabilized the system significantly and enabled the more detailed investigation of the charge impedance presented in Paper II. In Paper III, the focus is an accurate determination of the double layer capacitance of the air-electrode. Since gradients inside the battery will affect this measurement, it was desired to do these measurements at OCV. In general EIS measurements were performed at frequencies between 10 mHz and 20 kHz, and in some cases a wider interval. 15 points per decade is used to enable a proper fitting of the data using equivalent circuit fitting.

Three electrode measurements were performed in the group using an EL-CELL to confirm the assumptions of which processes belonged to which electrode, but the majority of measurements were performed in simple 2-electrode Swagelok cells. In the 2-electrode cell, variations to the battery was used to identify the electrode specific reactions. Among these tests were: (i) measuring impedance at open-circuit voltage (OCV) in argon atmosphere to prevent the oxygen reduction/oxidation, (ii) using a symmetrical cell of two pre-discharged cathodes, and (iii) testing a different cathode. In the symmetrical cell, the anode/cathode reactions are oxidation/reduction of Li_2O_2 which remove any lithium metal-related contributions from the EIS measurement. Both cathodes in the

symmetrical cell initially discharged 0.25 mAh in separate cells before they were combined in a new cell. The cathodes were rinsed with DME after the individual discharge to remove the electrolyte-salt before the cathodes were used in the symmetrical cell. The symmetrical cell was tested in O_2 gas and was made without exposing the cathodes to air at any point.

The equivalent circuit fits are made using the scipy optimizer fmin_slsqp using the software package RAVDAV 0.9.7 [51].

Chapter 4

Overpotentials and degradation

This chapter focuses on the reference system with an XC72 cathode and is closely related to Paper I and Paper II. A number of physical and electrochemical measurements will be presented to qualify the discussion of the discharge and charge mechanisms and how they affect the overpotential. All measurements were performed using a system with an XC72 carbon black cathode, DME/LiTFSI electrolyte and lithium anode as described in Section 3.1. The system has been chosen because it is widely studied and show low degradation compared to other Li-O_2 systems. It has been characterized extensively in previous publications from 2011 to 2013 by McCloskey et al. [28, 41, 52–56], and these measurements will be used to supplement the discussion. The measurements have been conducted at DTU Energy and Haldor Topsøe A/S in Denmark and at IBM Almaden Research Center in California.

4.1 Physical characterization

4.1.1 X-ray diffraction

X-ray diffraction provides a simple identification of Li_2O_2 in the discharged cathode. The method has mistakenly been used in literature to prove the absence of degradation product, which is not possible, since the degradation products are not necessarily crystalline. In our group we have primarily used the method to study the growth of Li_2O_2. Figure 4.1 (left) shows an XRD spectrum of a discharged XC72 cathode. The six major Li_2O_2 peaks and the peaks from the PTFE binder are clearly visible and indicate that the primary reaction is the formation of Li_2O_2. Figure 4.1 (right) shows an in-situ study of an XC72 cathode in a capillary cell performed by Storm et al. [57]. In this study, they were able to observe a linear increase in the peak area of the 100 diffraction peak during

discharge with low uncertainty and thereby assess the amount of crystalline Li_2O_2 in the sample to supplement measurements like the absorption measurements described in Section 3.3.1.

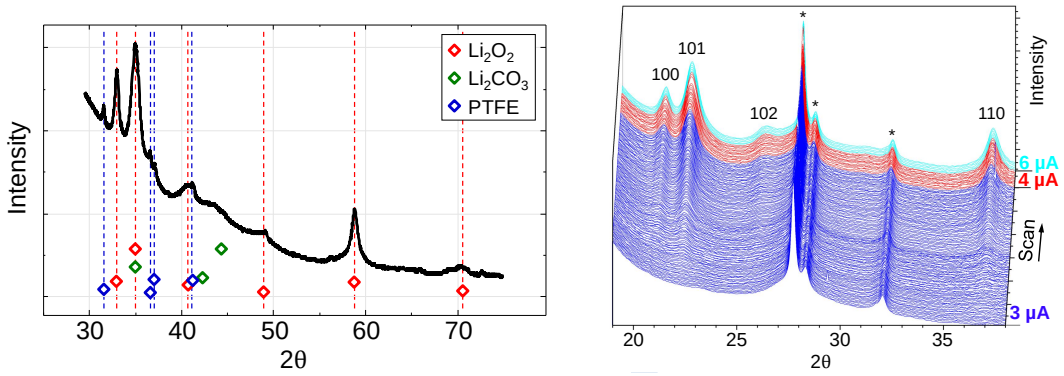

FIGURE 4.1: (Left) Ex-situ XRD measurement performed by sealing powder from a discharged cathode in a 0.7 mm diameter capillary inside the glovebox without exposing the powder to ambient air. The data is acquired using a Regaku Advance X-ray Diffractometer with Cu-Kα radiation (λ =0.15418 nm). (Right) In-situ diffraction patterns for the discharge of a capillary battery showing the appearance of four diffraction peaks of Li_2O_2 and the ones of the SS wire (*). The current density changes through the measurement from 3 μA (blue) to 4 μA (red) and 6 μA (light blue). Adapted from [57] with permission.

4.1.2 Differential electrochemical mass spectrometry

As already discussed in Section 2.1.1, it is important to quantify the consumption and release of oxygen and other gases during discharge and charge, and the DEMS systems at DTU Energy and at IBM Almaden research laboratory has been essential to the presented work. The measurements shown in this section has been conducted at DTU Energy.

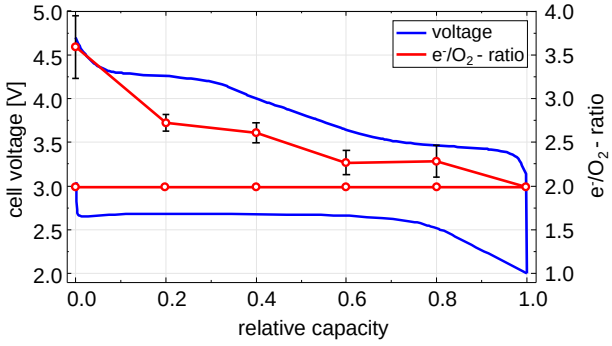

FIGURE 4.2: The SoC dependence of the e^-/O_2-ratio during discharge and charge. The values are averages of six batteries tested at currents in the range of 100-200 mA/g carbon.

Figure 4.2 shows how the e^-/O_2-ratio depends on SoC. The values are averages of six measurements like the ones presented in Figure B.5 in Appendix B and the error-bars indicate one standard deviation. During discharge, the error-bars are small and hidden behind the symbols. It is seen that the process is a 2.0 e^-/O_2 process during the entire discharge with very small deviations. During charge, however, the e^-/O_2-ratio increases during the entire charge ending at 3.5 e^-/O_2 at the end of charge. It is also noted that the standard deviation of the e^-/O_2-ratio increases significantly in charge-mode, indicating that the exact electrochemistry may change between measurements depending on small variations in current density or other parameters. The e^-/O_2-ratio during discharge and charge and the OER/ORR value based on the performed measurements are shown in Table 4.1 with the corresponding values obtained by McCloskey et al. [56]. It is seen that all key parameters are well within one standard deviation.

	OER/ORR	$(e^-/O_2)_{dis}$	$(e^-/O_2)_{cha}$
DTU	0.78 ± 0.05	1.99 ± 0.02	2.62 ± 0.12
IBM, [56]	0.78	2.01	2.59

TABLE 4.1: Comparison between DEMS measurements performed at the setup built at DTU Energy and values reported by McCloskey et al. at IBM [56].

A wider current range from 5 $\mu A/g_C$ to 2.5 mA/g_C is explored in Paper I, and it is found that the e^-/O_2-ratio and OER/ORR-ratio are rather independent of the applied current density at currents above 25 $\mu A/g_C$.

4.1.3 Absorption measurements

The amount of Li_2O_2 remaining in the cathode during discharge and charge was quantified using absorption measurements of a Ti-complex oxidized by H_2O_2 formed when submerging the tested cathodes with Li_2O_2 (and possibly LiO_2) in an aqueous solution as described in Section 3.3.1 and in Paper II.

Figure 4.3a shows the oxygen evolution (blue line) and the Li_2O_2 removal (red line) as the cathode is charged. The oxygen evolution is determined based on the DEMS measurements presented in Figure 4.2 and the Li_2O_2 removal is based on the optical absorption measurements. The O_2 evolution and, in particular, the deviation from the theoretical value is in accordance with measurements presented by McCloskey et al. [52], and suggests the presence of electrochemical degradation reactions, especially at potentials above 3.5 V. The Li_2O_2 is, however, disappearing more rapid than expected from the electrochemistry, suggesting a significant chemical degradation. Figure 4.3b shows the amount of chemical and electrochemical reactions in different potential intervals, and it is clear that the chemical degradation is most significant in the potential

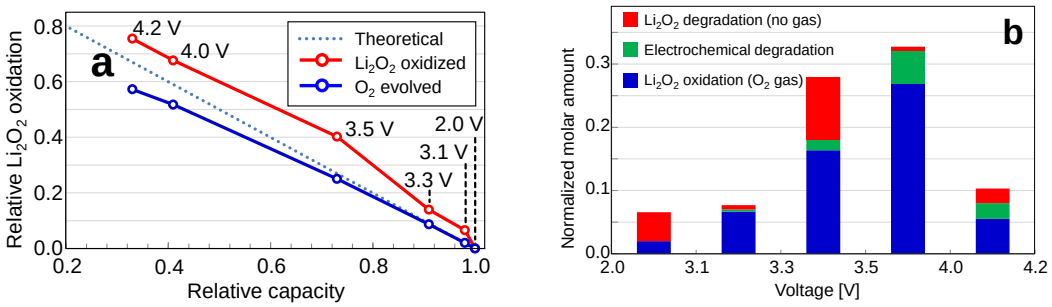

FIGURE 4.3: (a) Measurement of O_2 evolution using DEMS (blue) and Li_2O_2 removal (either chemical or electrochemical) using absorption measurements (red). The dotted line correspond to a pure 2 e^-/O_2 oxidation of Li_2O_2 with no chemical degradation. (b) The amount of Li_2O_2 oxidation with and without gas evolution and electrochemical degradation. Values are normalized such that the sum of the electrochemical reactions (Blue and green) equals the relative change in capacity in each interval and sum up to 1 for a full charge.

ranges 2 V – 3.1 V and 3.3 V – 3.5 V. This effect is somewhat more pronounced than previously reported [52].

4.1.4 Scanning electron microscopy

Scanning electron microscopy (SEM) was performed primarily as a preparation for the TEM measurements, as it is a quick and easy way to get an overview of the sample. A poor coating was used for this measurement to expose both carbon and stainless steel.

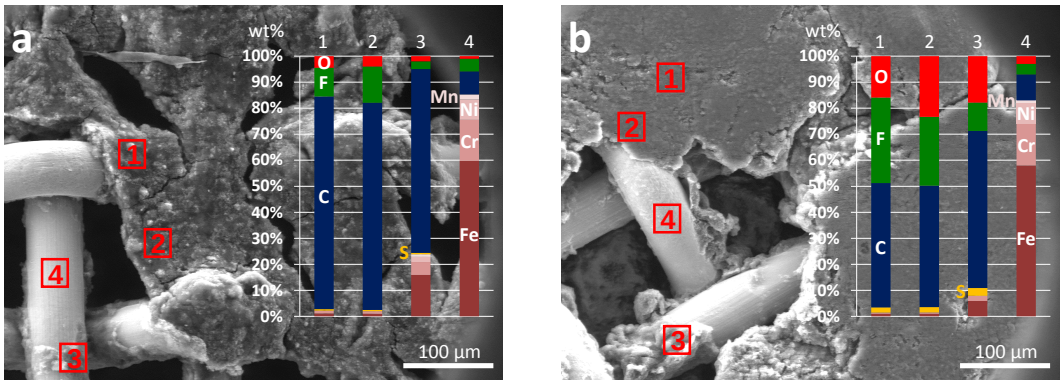

FIGURE 4.4: SEM images and EDS spectra of (a) a pristine and (b) a discharged cathode. Low vacuum mode was used to prevent charging of the samples.

Figure 4.4 shows low magnification SEM images and EDS analysis of a pristine and a discharged cathode. The structure of the cathode material was very different on the two samples, which is probably because the discharged cathode has been pressed inside the battery. The EDS-analysis showed clear differences between the two samples. First, the discharged cathode contained more oxygen than the pristine cathode, which is expected in a discharged cathode containing Li_2O_2. Second, the tested cathode showed a higher

ratio of fluorine and sulfur, which is probably due to a slight amount of residual LiTFSI salt, that was not washed out completely. The ratio between Fe, Cr, Ni and Mn matches the content of the 316 stainless steel mesh used as support for the carbon powder.

The EDS-analysis is associated with significant uncertain since carbon and oxygen are only emitting low energy x-rays that are easily reabsorbed before reaching the surface, and, in addition to this, the structure is very irregular. This means that the EDS analysis should be seen as a qualitative method rather than a quantitative one. Knowing this, it is, however, still interesting to consider the numbers briefly and compare them with the expected amounts of Li_2O_2. The EDS measurements detects 20 wt% of oxygen and 2 wt% of sulfur in the discharged cathode, as seen in Figure 4.4b. Oxygen is only expected from the LiTFSI salt and Li_2O_2, and both oxygen and sulfur constitutes 22 wt% of the LiTFSI salt. According to the EDS data, this means that the sample contain of 18 wt% of Li_2O_2 (as 2 wt% is in the LiTFSI) and 9 wt% LiTFSI (2 wt% LiTFSI divided by 22 wt% sulfur in LiTFSI). This is very close to the expected value of 20 wt% Li_2O_2 in the discharged cathode.

4.1.5 Transmission electron microscopy

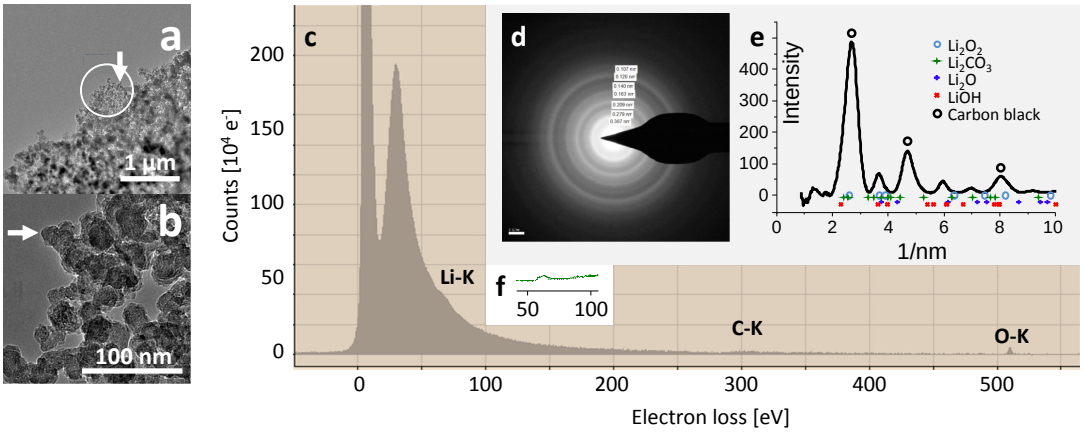

FIGURE 4.5: TEM measurements performed on a discharged TEM grid prepared with XC72 carbon black as described in Section 3.3.2. The measurements were performed at Tecnai G2 at the Technical University of Denmark, operated in TEM mode at 200kV.

Figure 4.5a and 4.5b show TEM images in two magnifications of a specimen in a discharged cathode prepared directly on a TEM grid as described in Section 3.3.2. Figure 4.5c shows an EELS spectrum of this area and Figure 4.5d shows the measured SAED pattern of this area. Figure 4.5e shows the analysis of the diffractogram and reveals three large peaks marked with black circles which correspond to scattering of carbon black, as identified in Figure C.2 in Appendix C. In addition to this, smaller peaks are clearly revealed, which are expected to be related to Li-structures. No bulk Li-phase was

identified, but it is important to note that the exact position of the peaks may deviate significantly from the bulk phases when the crystals are in the nano-scale. The presence of Li-phases is further substantiated by the EELS spectrum, where the lithium, carbon and oxygen signals are all identified. Figure 4.5f shows the spectrum of the lithium peak after subtraction of an exponential background estimation made just before the peak. In conclusion, lithium-species and carbon were detected both by EELS and electron diffraction in three investigated areas having particle morphologies resembling carbon black particles, i.e. particles of about 20-50 nm. This means that the lithium-species must be located within the carbon particles, and this is an indication of the expected layer-growth of Li_2O_2. It is also noted that we did not see any big particles in the sample, and even though the absence of particles is not a proof, it is a good indication that our system does not contain water impurities, as discussed by Aetukuri et al. [58]. We have further measurements in preparation using an optimized EELS/EFTEM method, described in Ref. [59], to pinpoint the location of Li-species to confirm or reject the presence of the expected Li_2O_2 layer of only a few nanometers on the carbon black particles.

4.2 Electrochemical characterization of the system

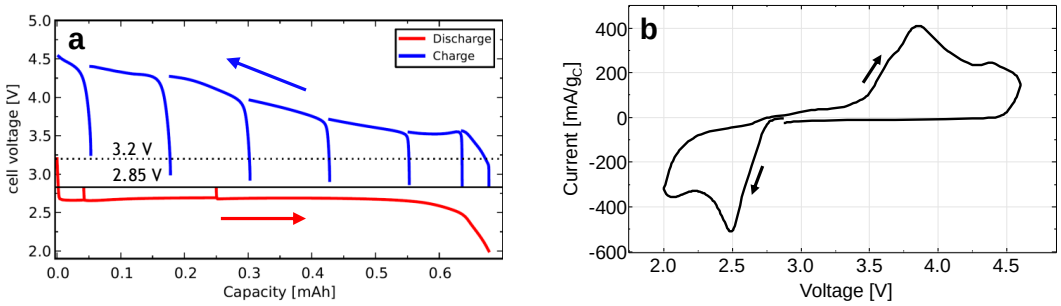

FIGURE 4.6: (a) Measurement of OCV through a 250 μA (220 μA/cm^2) discharge and charge. The steep voltage transients occur when the battery is allowed to relax at OCV. Reprint from Paper I. (b) Cyclic voltammetry between 2.0 V and 4.6 V with a scan rate of 0.5 mV/s.

Figure 4.6a shows the OCV measured as a function of the state of charge in a full discharge-charge cycle at 250 μA (220 μA/cm^2, 130 mA/g$_C$). The battery was allowed to relax to OCV by interruption of the current a number of times during both discharge and charge, which is seen as steep voltage transients in Figure 4.6a. The relaxation criteria was a change in cell voltage of less than 1 mV/h or a relaxation time of 15 h. The initial OCV was 3.2 V. The OCV decreased to 2.85 V after a short period of discharge and stayed at this value during the entire discharge - also after reaching the 2.0 V cutoff at sudden death. During charge, the OCV was 2.85 V, but it increased

slightly toward the end of charge where it reached 3.2 V. Figure 4.6b shows a cyclic voltammogram between 2.0 V and 4.6 V with a scan rate of 0.5 mV/s. The first thing to notice is the asymmetry of the measurement, suggesting that the discharge and charge mechanism is not a single reversible redox reaction. It seems like two processes occur during discharge with onset potentials of 2.75 V and 2.3 V respectively. During charge, a small peak is identified at around 3.1 V and several bumps are found in the curve as the potential is increased further. The measurement agree with previous results published by McCloskey et al.[41].

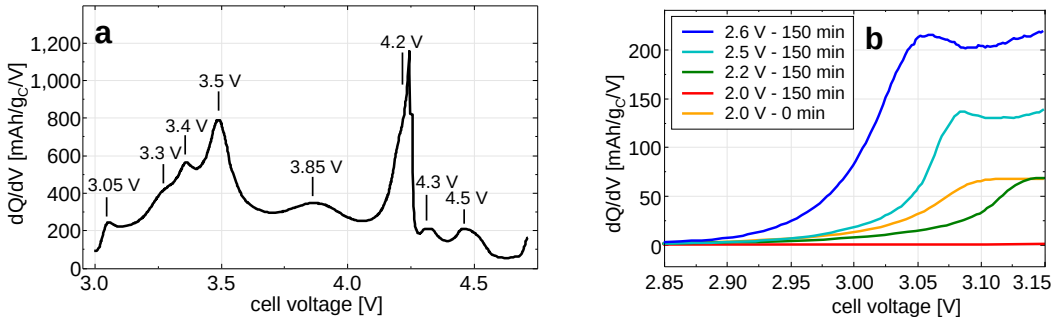

FIGURE 4.7: (a) Differential capacity plot (dQ/dV) of a typical charge. Each peak represents an electrochemical reaction. Reprint from Paper II. (b) Differential capacity plot of the initial part of the charge following a constant current of 130 mA/g_C discharge to 2.0 V, 2.2 V, 2.5 V or 2.6 V, which was maintained at 150 min before charging. The measurement labeled *2.0 V – 0 min* was charged immediately after reaching 2.0 V. Reprint from Paper II.

Figure 4.7a shows a differential capacity plot (dQ/dV) of a typical charge curve. The peaks correspond to voltage plateaus in the charge curve and thereby different processes. This is in line with the cyclic voltammetry measurement shown in Figure 4.6b, and from the differential capacity, eight electrochemical processes can be identified at 3.05 V, 3.3 V, 3.4 V, 3.5 V, 3.85 V, 4.2 V, 4.3 V and 4.5 V. Figure 4.7b shows how the onset potential of the process at around 3.05 V increases with the depth of discharge and the exposure time at low potentials. Analysis of 10 charge measurements following a discharge to 2.6 V show a capacity corresponding to 540 ± 80 $\mu mol_{Li_2O_2}/g_C$ below 3.15 V. This corresponds to 4.3 % of the total discharge capacity or approximately one monolayer as calculated in Paper II.

4.3 Electrochemical impedance spectroscopy

The results presented in this section are selected among more than five thousand impedance spectra. A wide range of current densities, potentials and techniques have been investigated and the measurements included are chosen to substantiate the discussion of the discharge and charge mechanisms presented in Section 4.4, 4.5 and 4.6.

4.3.1 Discharge to sudden death at 250 μA

EIS measurements from the first discharge at 250 μA (220 μA/cm^2) are shown in Figure 4.8a-d. The spectra were measured while drawing a current, which means that the SoDs shown in Figure 4.8 and Table 4.2 are approximate values. Three arcs are distinguished in the Nyquist plot in Figure 4.8a. They were almost constant in the first part of the discharge but changed as the potential decreased near the end of discharge. The three identified impedance contributions are labeled Z_1, Z_2, and Z_3, and, on the basis of a fit to the equivalent circuit given in Equation (2.4), the corresponding peak frequencies, resistances and pseudocapacitances are given in Table 4.2 from two of these measurements.

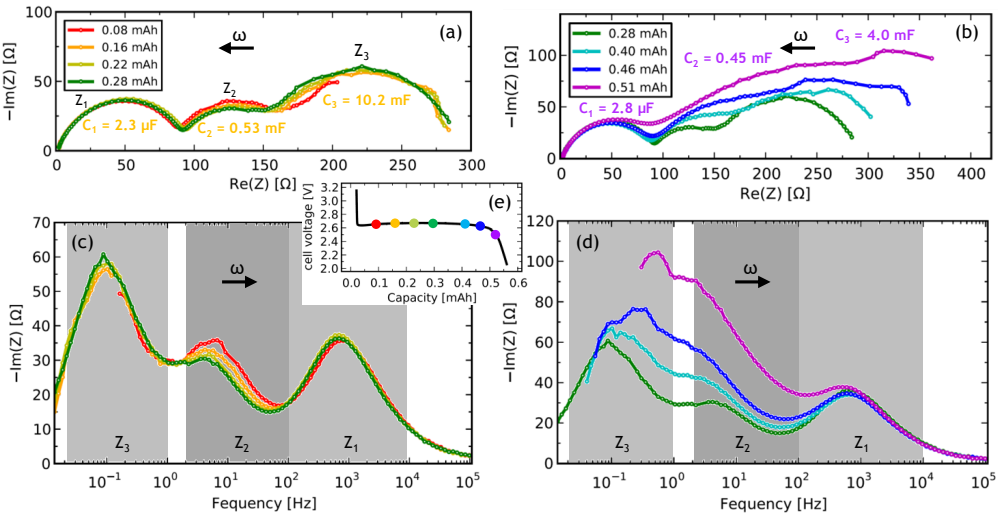

FIGURE 4.8: Nyquist-plot (a and b) and Bode-like plot (c and d) of impedance measurements during a 250 μA (220 μA/cm^2) constant current discharge. The approximate SoDs are shown in (e) and in the legend of (a and b). Three processes are identified and named Z_1, Z_2, and Z_3. The three corresponding peak frequencies are within the grey intervals marked in (c and d) at all current densities and SoDs investigated. Reprint from Paper I.

It is seen that R_1 is constant through the discharge, whereas R_2 and R_3 increase, and C_3^* decreases. The decrease of C_3^* and increase of R_3 through the discharge, could be a blocking of the cathode surface. The magnitudes of the pseudocapacitances indicate that Z_1 originates from an anode process, and Z_2 and Z_3 originate from cathode processes. The cathode blocking and identification of reaction processes in the impedance spectra are discussed further in Section 4.4.

The peak frequencies changed between different current densities and close to sudden death. In all of our measurements, however, f_1 was between 100 Hz and 10 kHz, f_2 was between 2 Hz and 100 Hz, and f_3 was between 20 mHz and 1 Hz. These intervals are

shown in Figure 4.8b and 4.8d, and the clear separation helps in identifying the different impedance contributions.

4.3.2 Discharge to sudden death at 20 μA

We decreased the discharge current to 20 μA (18 μA/cm^2) to increase the stability of the system during the impedance measurements, see Figure 4.9. When comparing this with the previous discharge at 250 μA presented in Figure 4.8, it is important to note that both the capacity and the polarization resistance are significantly larger in the 20 μA discharge.

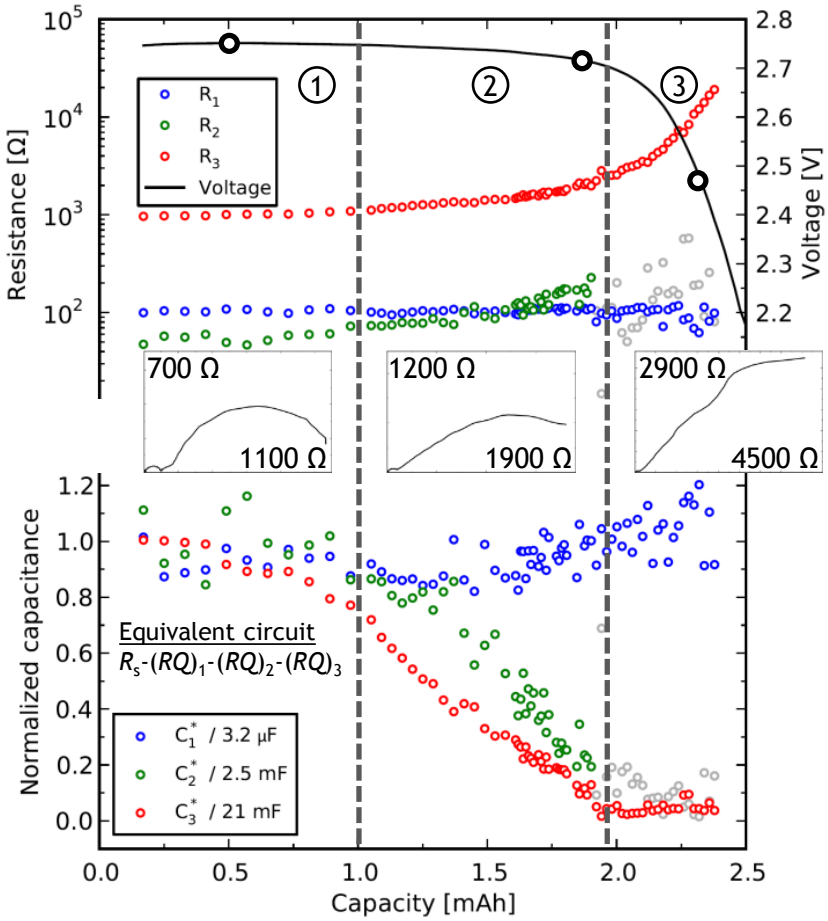

FIGURE 4.9: Resistances and normalized pseudocapacitances determined from EIS measurements in a 20 μA (18 μA/cm^2) constant current discharge to 2.2 V using Equation (2.4). Nyquist plots are shown at three representative stages and the corresponding SoDs are marked with circles on the voltage profile. R_2 and C_2^* could not be determined well at the end of discharge and are thus greyed out. Reprint from Paper I.

On the basis of a fit using Equation (2.4), the resistance and pseudocapacitance parameters of Z_1, Z_2, and Z_3 are presented in Figure 4.9 and summarized in Table 4.2. The

parameters of Z_1 were constant through the entire discharge, and the change of parameters related to Z_2 and Z_3 are divided into three parts as indicated in Figure 4.9: (1) At 0% - 40% SoD, only negligible change was observed, (2) at 40% - 80% SoD, R_2 and R_3 increased 2-3 times, and C_2^* and C_3^* decreased by 95%, and (3) at 80% - 100% SoD, R_3 increased to 14.1 kΩ (more than 10 times the initial value), the pseudocapacitances stayed at 5% of the initial value, and the voltage dropped. Parameters related to Z_2 could not be determined in the last part of the discharge because of the overlap with Z_3.

At 20 μA, the average relative Kramers-Kronig deviation at frequencies from 1 mHz to 10 Hz was typically 0.5% at the plateau, increasing near sudden death to 2% at 2.2 V.

4.3.3 Supporting EIS measurements

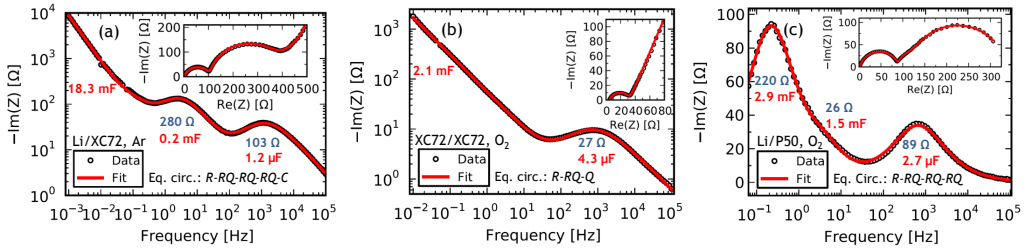

FIGURE 4.10: Bode-plot and Nyquist-plot of supporting EIS measurements. All measurements are fitted to the equivalent circuit listed in the plot and the fitted parameters are listed in the plot (resistance in blue and pseudocapacitance in red). Left: Potentiostatic EIS measurement at OCV of a cell in Argon atmosphere. Middle: Potentiostatic EIS measurement of a symmetrical cell at 0 V with an amplitude of 5 mV. The cell is made of two cathodes that have been discharged in separate cells with a lithium anode at 250 μA (220 μA/cm^2). Right: Galvanostatic EIS measurement from a 250 μA (220 μA/cm^2) discharge with an AvCarb P50 carbon cathode. Adapted from Paper I.

Figure 4.10 shows three supporting EIS measurements; An EIS measurement at OCV of a cell in argon atmosphere, an EIS measurement a cell with a different carbon cathode and an EIS measurement of a symmetrical cathode-cathode cell at 0 V. All measurements are fitted to the equivalent circuit listed in each plot and the fitted parameters are also listed in the plot (resistance in blue and pseudocapacitance in red).

Figure 4.10 (left) shows a potentiostatic EIS measurement at OCV with 5 mV amplitude of a fresh battery in argon atmosphere before exposure to oxygen. The purpose was to investigate reactions not related to oxygen reduction, and it is seen that Z_1 and Z_2 were also present in the absence of oxygen. The low frequency tail could be modeled with a capacitor, C_3, which means that no charge transfer reaction is present for this process. The spectrum was modeled with the equivalent circuit *R-RQ-RQ-RQ-C*. The capacitance C_3 was 18.3 mF, and the pseudocapacitances C_1^* and C_2^* were 1.2 μF and

0.2 mF, respectively. The presence of Z_2 suggests that this process is not related to oxygen reduction.

Figure 4.10 (middle) shows a potentiostatic EIS measurement of a symmetrical cell at OCV with 5 mV amplitude. The purpose was to eliminate contributions from the lithium anode in the EIS spectrum. The cell was made of two cathodes that had been discharged 1 hour in separate cells with a lithium anode at 250 μA (220 μA/cm^2). The spectrum was modeled with a *R-RQ-Q* circuit. The CPE element was chosen instead of a capacitor to describe the low frequency tail, because the slope was -0.74 in the Bode plot, rather than -1 in the case of a capacitor. The pseudo-capacitance of the low frequency tail was 2.1 mF and the resistance and pseudo-capacitance of the *RQ* circuit was 27 Ω and 4.3 μF, respectively.

Figure 4.10 (right) shows a GEIS measurement on a cell with an AvCarb P50 carbon paper cathode prepared as described in [54]. The purpose was to investigate cathode specific contributions to the impedance. Both Z_1 and Z_3 had similar parameter values compared to XC72, whereas Z_2 was very small.

4.3.4 Charge at 250 μA

In Figure 4.11, we present typical EIS measurements during a charge. To limit the complexity of the analysis, impedance measurements are only made at voltages below 4.2 V to avoid the major decomposition reactions observed at higher potentials using DEMS. In this measurement, the 4.2 V limit corresponded to 60% SoC.

Three impedance contributions are identified. The parameters obtained using equivalent circuit fitting on the green (0.03 mAh) and black (0.42 mAh) spectra with Equation (2.4)

	f_1 [Hz]	f_2 [Hz]	f_3 [Hz]	R_1 [Ω]	R_2 [Ω]	R_3 [Ω]	C_1^* [mF]	C_2^* [mF]	C_3^* [mF]
Discharge at 250 μA									
0.16 mAh	733	5.4	$93{\cdot}10^{-3}$	96	56	145	$2.3{\cdot}10^{-3}$	0.53	10.2
0.51 mAh	605	3.4	$184{\cdot}10^{-3}$	94	92	188	$2.8{\cdot}10^{-3}$	0.45	4.0
Discharge at 20 μA									
0.5 mAh	470	1.15	$5.5{\cdot}10^{-3}$	109	50	1007	$3.1{\cdot}10^{-3}$	2.8	19.3
1.9 mAh	464	1.12	$9.9{\cdot}10^{-3}$	107	158	2131	$3.2{\cdot}10^{-3}$	0.6	2.0
2.3 mAh	479		$1.1{\cdot}10^{-3}$	114		14097	$2.9{\cdot}10^{-3}$		0.8
Charge at 250 μA									
0.03 mAh	678	9.6	$267{\cdot}10^{-3}$	65	166	497	$3.6{\cdot}10^{-3}$	$76{\cdot}10^{-3}$	1.0
0.42 mAh	983	14.0	$19{\cdot}10^{-3}$	255	105	700	$0.6{\cdot}10^{-3}$	$99{\cdot}10^{-3}$	9.0

TABLE 4.2: Peak frequencies, resistances and pseudo-capacitances from selected impedance fit. The expected capacitances for the full anode and cathode are 10 μF and 25 mF, respectively. Typical values of n are $n_1 = 0.77$, $n_2 = 0.86$ and $n_3 = 0.78$.

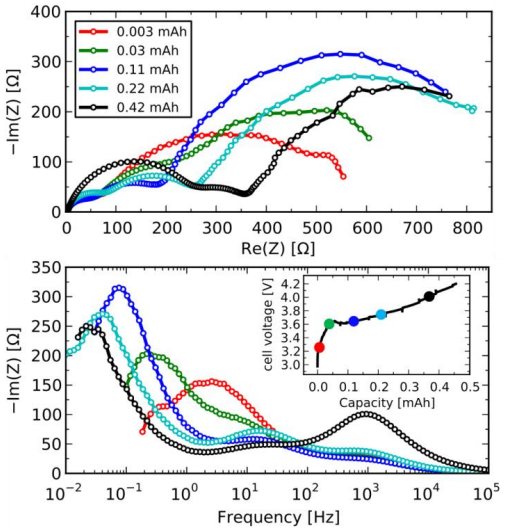

FIGURE 4.11: Nyquist (top) and Bode-like (bottom) plots of EIS measurements made during a 250 μA (220 μA/cm^2) constant current charge. The charge followed a discharge similar to that shown in figure 4.8e with a discharge resistance extrapolated to 3 kΩ at 2.0V. The SoCs are shown as circles in the inset graph with the voltage profile. The 0.03 mAh and 0.42 mAh measurement were modeled using (2.4) and the obtained parameters are found in Table 4.2. Reprint from Paper I.

are given in Table 4.2. The three contributions are in the same frequency ranges as seen during discharge. The polarization resistance ($R_1 + R_2 + R_3$) was almost constant in the range 500 Ω - 1000 Ω, but the peak frequencies and the relative magnitude of the different impedance-contributions changed. Looking at the pseudocapacitances, C_1^* decreased from 3.6 μF to 0.6 μF, and C_3^* increased from 1.0 mF to 9.0 mF. This suggests that the active cathode area is increasing and that the active area of the anode is decreasing during charge. It is further noted that C_3^* is almost the same in the end of charge and in the beginning of the discharge (10.2 mF). Finally, it is noted that R_1 was almost constant until 3.7 V, after which it suddenly increased. This supports that the lithium anode surface is deactivated by the formation of the solid electrolyte interface (SEI) layer - possibly due to oxygen crossover.

To investigate the charge process further, EIS was measured at 11 different potentials during the initial charge from 3.10 V to 3.60 V. Figure S5 in the Supporting Information of Paper II shows a typical measurement, with the equivalent circuit fit and the determination of the resistance, $R_{Li_2O_2}$, and the pseudocapacitance. Both parameters are related to the charge transfer through Li_2O_2 and Li_2O_2 oxidation. Figure 4.12a shows the cathode resistance at selected voltages during charge, as determined by EIS. It is seen that the resistance increases from 3.10 V to 3.30 V, decreases at 3.33 V, increases until 3.50 V, and decreases again at 3.60 V. The resistance and corresponding pseudocapacitances at the marked cross section are shown in Figure 4.12b for all 11

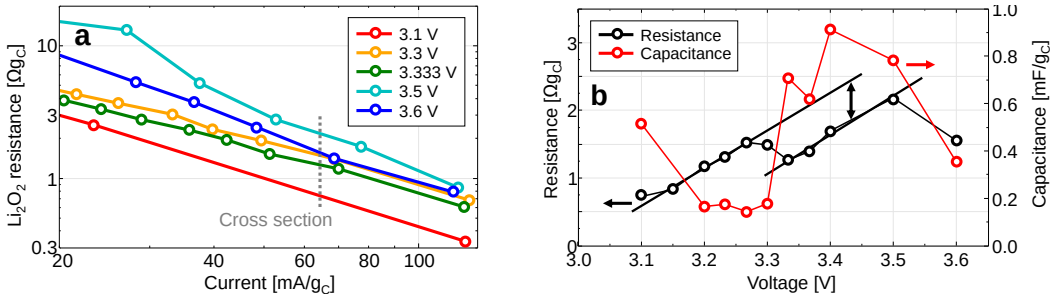

FIGURE 4.12: (a) The resistance related to Li_2O_2 oxidation and charge transfer through Li_2O_2, determined using EIS at different potentials. The current decreases during the measurement. Reprint from Paper II. (b) Resistance and capacitance from charge after the current has decreased to 50 % of the initial current. Guide lines have been inserted to illustrate the stepwise increases in the resistance. Reprint from Paper II.

potentials. It is seen that both the resistance and the pseudocapacitance change stepwise as a function of potential. The resistance increases monotonic until 2.27 V, then it drops and continues a second monotonic increase from 3.33V to 3.50 V after which it drops. The pseudocapacitance is high at 3.10 V, decreases at 3.20 V, increases at 3.33 V and decreases again at 3.60 V. When keeping the potential at 3.10 V, it was observed that the capacitance decreased 60 % from 0.7 mF/g_C to 0.28 mF/g_C. During this EIS measurement, the current decreased and Li_2O_2 is removed, and as both changes are expected to increase the capacitance, it clearly suggests that compounds are deposited during this initial charge, which is in line with the absorption measurements presented in Section 4.1.3.

4.4 Identification of processes during discharge

From Sections 4.3 and 4.2, it is seen that three impedance contributions were present during discharge and they are referred to as Z_1, Z_2 and Z_3. The five key findings were that (i) the impedance did not change at the discharge plateau, (ii) Z_2 and Z_3 increased near sudden death, (iii) C_3^* decreased significantly just before sudden death, (iv) pseudocapacitances related to Z_1, Z_2 and Z_3 were typically 3 μF for C_1^*, 0.1-3 mF for C_2^*, and 1-20 mF for C_3^*, and (v) the OCV was always 2.85V during discharge.

The results support previous findings by Adams et al. and Landa-Medrano et al. [19, 20] that Z_1 originates from the anode and that Z_2 and Z_3 originate from the cathode. In addition to this, our results show that Z_3 is a combination of the charge transfer reaction of oxygen reduction and the electronic transport through the Li_2O_2, whereas Z_2 is a cathode-specific process that is not related to the oxygen reduction. The assignment of anode and cathode features in the EIS is substantiated by the following three observations.

First, the full capacitance at the lithium anode surface is expected to be in the range of 10 μF as discussed in Section 3.4, whereas the capacitance of the XC72 electrode is expected to be 25 mF. If only part of an electrode is active during the EIS measurement, the capacitance will be lower. As reported, C_1 was typically 3 μF, whereas C_2^* and C_3^* were in the range of 0.1 mF - 20 mF. Furthermore, the cathode capacitance per active surface area calculated by Adams et al. was in the same range as C_3^* [19].

Second, the careful parameter study performed by Adams et al. [19] shows that relevant cathode processes have peak frequencies below 10 Hz, which correspond with f_2 and f_3 in our study, whereas the peak frequency of the anode process is 1 kHz, which corresponds to f_1 in our study.

Third, Z_1 did not change during discharge, whereas Z_2 and Z_3 increased significantly close to sudden death. Both electrodes change during the measurement. On the lithium anode, Younesi et al. have previously shown that an SEI layer is forming in a combination of chemical and electrochemical reactions [60], but as shown by McCloskey et al. [27] this is affecting neither the electrochemistry nor the measured impedance. On the other hand, the cathode is covered with an insulating layer of mainly Li_2O_2 during discharge, and an increase in charge transfer resistance is typically captured in EIS measurements.

Ascribing Z_3 to oxygen reduction and electronic transport through Li_2O_2 is based on two observations: (i) Z_3 is the only process related to oxygen reduction, as both Z_1 and Z_2 are present in argon, and (ii) R_3 was the largest resistance during the entire discharge, both when the cathode was limited by reaction kinetics at the discharge plateau and by electronic conduction at sudden death.

The process related to Z_2 is cathode specific and not related to oxygen reduction, as it was present in argon, but almost absent in a measurement with P50 carbon paper. As P50 is binder-free, this could indicate a degradation effect related to the PTFE binder. A little surprising, Z_2 was not present in the symmetrical cell measurement. This could indicate that the parasitic reaction was chemically passivated during handling when assembling the symmetrical cell.

The *iv*-curve presented in Figure 2.4 was made to ensure that all electrochemical processes were captured in the impedance spectrum. This was indeed the case, since the total impedance could account for the changes in the overpotential. Actually, the measured impedance seemed to overestimate the slope of the *iv*-curve, and the reason is most likely a result of lower Li_2O_2 formation yields, and therefore more heterogeneous discharge electrodeposits, at lower current densities as shown in a previous publication [52]. Lastra et al. and Mekonnen et al. [61, 62] have shown that an increase of

Li_2CO_3-like inclusions in the Li_2O_2 layer can change the electrical conductivity using DFT calculations, and such changes would also change the current dependence of the impedance and explain the deviation.

4.5 Analysis of the overpotential during discharge

The measurements show that the electrochemistry was unchanged during the entire discharge and they support the general understanding of tunneling being the dominant charge transport mechanism through the Li_2O_2 layer at relevant current densities and temperatures, which was initially proposed by Albertus et al. [29] and confirmed by Luntz et al. [63] Furthermore, the discharge was initially occurring in the entire cathode, whereas the increasing electronic transport through the growing Li_2O_2-layer passivated large parts of the cathode during discharge.

The tunneling mechanism is supported by two observations. First, the impedance contribution Z_3 related to oxygen reduction and electronic conduction through Li_2O_2 was constant at the discharge plateau and increased rapidly near sudden death, which is characteristic for the tunneling barrier that depends exponentially on the Li_2O_2 layer thickness, and second, the electrochemistry was unchanged during the discharge, as shown by a constant 2 e^-/O_2 process and identification of the same three processes in the impedance spectra at all SoDs.

The passivation of the cathode is observed in the pseudocapacitance C_3^*. At 20 μA, the initial value is 21 mF. This is the expected value of the entire cathode, which means that Li_2O_2 deposition is occurring in the entire cathode. The decrease in stage 1, as defined in Figure 4.9, reflects Li_2O_2 formation, because the introduction of a dielectric material in a capacitor changes the capacitance. In stage 2, the decrease is significant and cannot be explained by the dielectric layer of Li_2O_2 alone. The decrease must therefore reflect a reduction in active surface area. The cathode passivates when the critical thickness of Li_2O_2 is reached and tunneling is no longer possible. In stage 3, the available surface area is not sufficient to support the constant current, and the voltage drops to enable conduction through the blocked parts of the electrode. This is seen as an increase in cathode resistance. When fully discharged, the resistance is too large, and the current cannot be supported within the cut-off limit of 2.2 V. This is in full agreement with observations made by Luntz et al. using flat glassy carbon electrodes in electrolysis cells [63].

Because of discussions in literature on the significance of oxygen diffusion in the electrolyte, it is worth mentioning that the sudden death is not due to pore clogging and

increased oxygen diffusion resistance. In a typical discharge, the average thickness of Li_2O_2 is 0.5 nm - 1 nm based on the BET surface area of XC-72. This means that the porosity and Damköhler number are almost unchanged during the entire discharge, and, as stated by Wang et al. [64], such small changes will not give rise to the sudden death behavior.

4.6 Reaction mechanisms and SEI layer formation during charge

The charge of the Li-O_2 battery is complicated. The DEMS and absorption measurements described in Sections 4.1.2 and 4.1.3 show that both chemical and electrochemical reactions occur during charge and the cyclic voltammogram and differential capacity plot presented in Figures 4.6 and 4.7 both reveal a significant number of reactions. This section will analyze the results further and propose detailed input to the charge mechanism, degradation mechanisms and the potential increase.

4.6.1 Decreasing resistivity of Li_2O_2 in charge mode

It has been reported that the onset potential of Li_2O_2 oxidation on flat glassy carbon electrodes is close to the equilibrium potential and that the charge transfer through the Li_2O_2 decreases as the voltage increases from discharge mode to charge mode [63]. The use of impedance spectroscopy makes it possible to confirm that this is also valid in porous electrodes.

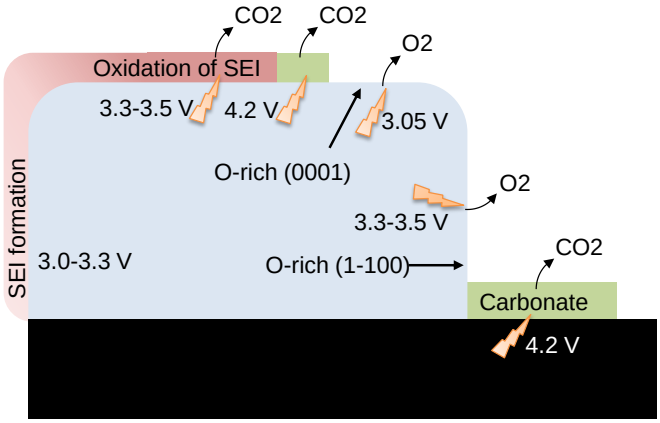

FIGURE 4.13: Sketch of the reactions and SEI formation during charge of the Li-O_2 battery. The potentials in the figure are the proposed onset potentials. Li_2O_2 oxidation occurs at 3.05 V and an SEI layer is formed immediately on the freshly oxidized surface. At 3.3 V – 3.5 V several reactions occur. Among these are gas evolution from the SEI layer and oxidation of other Li_2O_2 surfaces. Reprint from Paper II.

The change in resistivity in charge mode is identified by comparing the impedance at the end of discharge with the resistance in the beginning of the charge. During charge, the polarization resistance was 500 Ω at a current of 250 μA (220 μA/cm^2), which is much lower than the extrapolated value of 3 kΩ at 2.0 V during discharge. Furthermore, it is seen from Figure 4.7b and similar measurements that the charge resistance had only little dependence on the discharge current and depth of discharge, which suggests that the charge is not limited by the same process as the discharge. Luntz et al. have previously explained this by a reduction of the tunneling barrier because of a change in the Fermi energy by experiments on flat glassy carbon electrodes in an electrolysis cell [63].

4.6.2 Identification of Li_2O_2 oxidation at 3.05 V

It is argued that the process identified at 3.05 V is oxidation of Li_2O_2 based on three observations. First, Figure 4.2 and Figure S2 in the Supporting Information of Paper II, show that the e^-/O_2 ratio is between 2.0 (at 2V) and 2.1 (at 3.2 V) in the beginning of the charge, which is exactly – or at least very close to – the expected value for Li_2O_2 oxidation. Second, Figure 4.7b shows how the onset potential of the process at around 3.05 V increases with the depth of discharge and the exposure time at low potentials. To understand the shift, it is noted that DEMS measurements show that the e^-/O_2-ratio is 2.0 during the entire discharge, and McCloskey et al. show that the Li_2O_2 yield is independent of the depth of discharge [52]. This means that the thickness, and thereby the conductivity, of the Li_2O_2 layer is the only parameter expected to change between the measurements, and as the conductivity through the Li_2O_2 layer affects the onset potential of the reaction, it suggests that the reaction is a surface reaction at the Li_2O_2 surface. Third, the onset potential at the investigated current densities (0.1 μA/cm2 real surface area) is 2.9 V – 3.0 V which corresponds well with the onset potential of Li_2O_2 oxidation measured by Viswanathan et al. using flat glassy carbon electrodes.[27]

4.6.3 SEI layer formation

DEMS measurements show that all electrons come from the Li_2O_2 oxidation at the onset of the charge, until 3.1 V. In this interval, it was found that 4.3 % of the Li_2O_2 was oxidized electrochemically (Section 4.1.3) and in Figure 4.3b it is seen that another 4.6 % was removed without gas evolution. Since all electrons are accounted for by the gas evolved, the reaction with no gas evolution must be chemical and it is interpreted as the formation of an SEI layer based on three observations. First, the amount of degradation is close to the amount of electrochemically oxidized Li_2O_2 in the initial part of

the charge, and as this process does not continue, it suggests that an electrochemical oxidation of Li_2O_2 exposes the surface such that the oxidation is followed by a chemical degradation of Li_2O_2, forming an SEI layer. Furthermore, the amount of oxidized and chemically degraded Li_2O_2 both correspond to approximately one monolayer, which suggest that the reaction occur on the entire surface of Li_2O_2. Second, the 60 % decrease in capacitance at 3.1 V suggests a significant deposition at this potential that could be explained by the formation of an SEI layer. Third, the monotonic increase in Li_2O_2 resistance until 3.3 V suggests a decrease of available surface area or an increased electronic transport resistance. Both could be explained by a growing SEI layer.

4.6.4 Electrochemical degradation

Identification of the lowest potential without electrochemical degradation is important to identify a safe-voltage limit. It is proposed that at least one of the three separate processes identified in the differential capacity plot in the voltage range from 3.3 V to 3.5 V is an electrochemical degradation reaction as the e^-/O_2-ratio increases in this range. Two observations suggest that the reaction occurs at 3.3 V, but further investigation is needed to determine the onset potential definitively. First, EIS measurements show that the pseudocapacitance increases and the resistance decreases at 3.3 V. A sudden change like this suggests a new reaction pathway at this potential. Second, isotope measurements presented by McCloskey et al. on an identical system show that CO_2 evolution occurs from the electrolyte-Li_2O_2 interface from 3.3 V.[28] As the CO_2 evolution reaction depends on the potential, it is likely that this reaction is the new reaction pathway seen in the EIS measurements.

At around 3.6 V, the resistance decreases in Figure 4.12b and the pseudocapacitance decreases. As discussed in previous sections, the relationship between impedance and overpotential is not straight forward, but the significant decrease in impedance as the voltage increases, is a strong indication of a shift in equilibrium potential caused by a mixed potential established between different oxidation reactions to maintain the constant current. The theory of a mixed potential is further substantiated by measurements at higher potentials shown in Figure 4.11. The polarization resistance is almost constant throughout the entire charge even though the charging potential increases. As shown by DEMS and absorption measurements, the charging reaction is not a 2 e^-/O_2-process, but rather a 2.5-3 e^-/O_2-process and parasitic electrochemical reactions are thus present during the entire charge. This is in line with previous publications by McCloskey et al. [28, 41, 52, 56], and keeping in mind that the OCV never exceeded 3.2 V during charge, and no significant resistance increase was seen in the impedance spectra, it

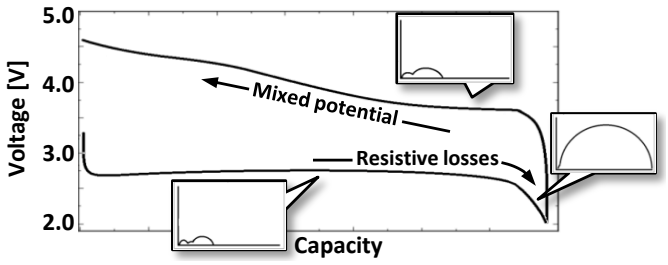

FIGURE 4.14: Illustration of the primary contribution to the voltage changes during discharge and charge based on the discussions in Sections 4.5 and 4.6. Reprint from Paper I.

suggests that a mixed potential between these competing electrochemical reactions was established during charge to support the high current.

4.6.5 Mixed potential

It is noted that these results contradicts the theory proposed by Chen et al. suggesting that the increase in charge overpotential occurs because the Li_2O_2 closest to the electronically conducting part of the cathode oxidizes first [65]. If this was the case, an increase of the charge resistance of at least an order of magnitude would be expected to explain the voltage increase, but the resistance does not increase by more than a factor of 2. Furthermore, after discharging under alternating O_2 isotope atmospheres, Li_2O_2 oxidation was found to preferentially occur at the Li_2O_2-electrolyte interface over the Li_2O_2-cathode interface during the initial stages of charge, as shown in a previous publication [55].

4.7 Summary of the fundamental characterization of overpotentials and degradation

In this chapter, the electrochemistry of the Li-O_2 system with a DME-LiTFSI electrolyte and a XC72 carbon black cathode has been studied using wide a range of physical and electrochemical characterization methods, including XRD, TEM, Li_2O_2 quantification using absorption, DEMS and EIS. Based on these measurements, explanations to some of the fundamental problems of the Li-O_2 system, including the sudden death at the end of discharge and the increase in potential during charge, has been proposed.

It was possible to assign the three identified contributions in the EIS spectra during discharge to either the cathode or the anode. Only one of the two cathode processes depended on the presence of oxygen. This indicates that this contribution was related

to the Li_2O_2 formation. The other contribution was cathode specific and may reflect a degradation reaction related to the PTFE binder. It was shown that the rapid potential change near the end of discharge was due to an increase in polarization resistance, primarily related to the charge transport through the Li_2O_2. This supports previously published work by Luntz et al. [63], which states that the electronic transport through Li_2O_2 at relevant current densities is governed by tunneling.

In the initial part of the charge, it was shown that the impedance was low compared to the end of discharge at sudden death, and that Li_2O_2 is oxidized already at 3.05 V, but that this facile oxidation is limited to approximately one monolayer. Analysis of the chemical degradation and the change in double layer capacitance indicate that the Li_2O_2 surface reacts with the electrolyte to form a SEI layer as soon as the outermost layer is oxidized. The resistance increases as the SEI layer blocks the surface and the voltage increases to maintain the constant current.

Three reactions were identified between 3.3 V and 3.5 V. The interval is dominated by Li_2O_2 oxidation with a small amount of electrochemical degradation and significant chemical degradation of Li_2O_2. It is expected that the reactions in this region are a gas evolving degradation reaction in the Li_2O_2-electrolyte interface and oxidation of another Li_2O_2 crystal plane, possibly the O-rich (1-100) plane, among others.

As charging progressed, the voltage increased significantly, whereas the resistance and OCV were almost unchanged, and DEMS measurements identified the presence of parasitic reactions. This suggests that the electrochemistry changed during charge and that the voltage increase was due to a mixed potential of parasitic reactions and Li_2O_2 oxidation, established to support a constant current. This was further substantiated by a sudden decrease in resistance between 3.5 V and 3.6 V.

Knowing the exact degradation mechanisms is crucial to improve the Li-O_2 system. From the measurements presented in this chapter, the immediate formation of an SEI layer on the oxidized surface in the initial part of the charge is highlighted as a significant problem that needs to be resolved before a viable Li-O_2 battery can be developed, and an analysis of the very first part of the charge might serve as a suitable screening parameter in the search for better electrolytes.

Chapter 5

Screening for new electrolytes

The development of a stable electrolyte is perhaps the greatest challenge of making a reversible Li-O_2 system. Most electrolytes investigated are actually stable until at least 4.6 V in a pristine Li-O_2 battery, but as shown in Paper II and by McCloskey et al. [41], the presence of the discharge product Li_2O_2 enable alternative degradation mechanisms with a lower onset potential. The continuous plating and stripping of lithium on the negative electrode and Li_2O_2 on the positive electrode make the system very exposed to degradation reactions, and a stable, flexible SEI layer that remains unchanged during thousands of cycles is difficult to imagine if the electrolyte reacts with the Li_2O_2. Moreover, a suitable electrolyte for Li-O_2 cells should have low volatility to avoid solvent evaporation, high oxygen solubility and diffusivity to enable sufficient oxygen transport to the air electrode, low viscosity, high conductivity and a wide electrochemical window. Although many solvents have been investigated in this regard, none of them fulfill the above mentioned requirements.

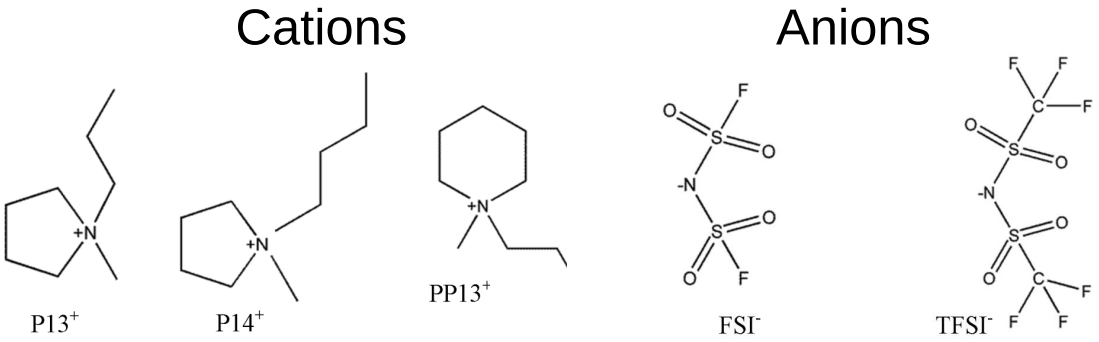

FIGURE 5.1: Schematic diagram of the different cations and anions used to test IL based electrolytes in Li-O_2 batteries. Adapted from Paper IV.

Ionic liquids (ILs) have been proposed by several researchers as suitable in electrolytes for Li-O_2 batteries because of their relatively high electrochemical and chemical stability against $\cdot O_2^-$ radicals [66–76]. Ionic Liquids are a class of molten organic salts which are liquid at temperatures around 100 °C or below. They are generally comprised by an organic cation and an inorganic anion [77–81], and they have stimulated much interest for a variety of chemical, physical and biological processes in past few decades due to their remarkable and unique properties such as negligible volatility, thermal and electrochemical stability, non flammability, tunable viscosity, high ionic conductivity and superior hydrophobicity.

In 2005, Kuboki et al. presented the first results with an IL-based electrolyte in a Li-O_2 system [67], and in the past few years, IL-based electrolytes have received significant attention as safe and environmentally friendly in Li-O_2 systems due to the nonvolatile nature. [67, 69, 72, 82, 83]. Among the most promising ILs are Pyrrolidinium and piperidinium based cations in combination with the bis(trifluoromethanesulfonyl)imide ($TFSI^-$) anion as reported by Lu et al. [84], and these ionic liquids have been the focus of our investigations.

In this study, we investigate the rechargeability in a Li-O_2 cell with ionic liquid electrolytes based on N-alkylmethylpyrrolidinium ($P13^+$ and $P14^+$) and N-alkylmethylpipiridinium ($PP13^+$) cations in combination with the $TFSI^-$ anion prepared as described in Section 3.1.3. An additional number of ILs are included in Paper IV for comparison.

5.1 Investigation of ionic liquids

DEMS measurements were performed as described in Section 3.2 and the gas consumption and gas evolution were quantified using both pressure measurements and mass spectrometry. Currents of 20 μA and 50 μA were applied with lower and upper potential

Solvent	Salt	OER/ORR	$(e^-/O_2)_{dis}$	$(e^-/O_2)_{ch}$	CO_2/ORR	H_2/ORR[b]
P14TFSI	LiTFSI	0.628[a]	2.03	2.75	0.00	0.01
P13TFSI	LiTFSI	0.617[a]	2.00	3.09	0.00	0.01
PP13TFSI	LiTFSI	0.402[a]	2.09	4.03	0.03	0.18
P13FSI	LiFSI	0.193[a]	2.51	3.40	0.04	0.02
DME	LiTFSI	0.796 (0.663[a])	1.99	2.62	0.08	0

TABLE 5.1: Differential Electrochemical Mass Spectrometry (DEMS) results of different ionic liquid and DME based electrolytes. [a]Based on charge to 4.2 V. [b]The H_2 intensities were not calibrated and can only be used to compare H_2 evolution between the different electrolytes.

limits of 2.2 V and 4.2 V, respectively, and the cells were all tested at room temperature (21 °C- 24 °C). From the DEMS measurements of the IL-based electrolytes, the following numbers were determined: $(e^-/O_2)_{dis}$, $(e^-/O_2)_{ch}$, OER/ORR, CO_2/ORR, and H_2/ORR. The numbers are summarized Table 5.1 and the data for the DME-LiTFSI electrolyte presented in Table 4.1 is included for comparison. As discussed in Section 2.1.1, these key characteristics are crucial to determine if a Li-O_2 system is truly reversible [14].

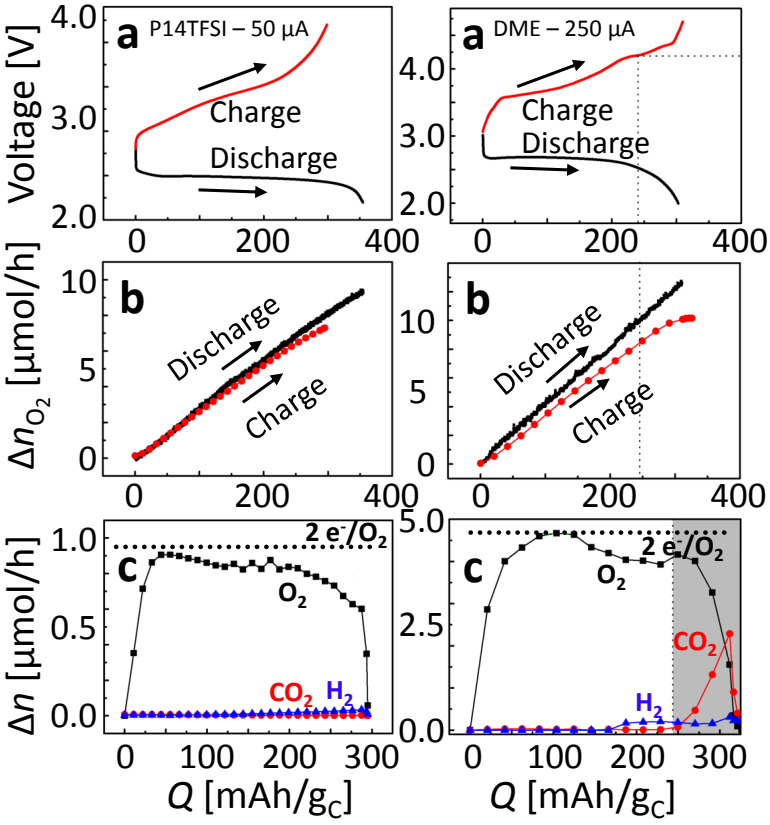

FIGURE 5.2: (a) Galvanostatic discharge-charge curves for cells with P14TFSI (50 μA discharge-charge) and DME (250 μA discharge-charge) based electrolytes. (b) Oxygen consumption (measured using pressure decay) during discharge and evolution (measured using DEMS) during charge. (c) Gas evolution rates for O_2, CO_2, and H_2. Adapted from Paper IV.

Figure 5.2 shows a comparison between the first galvanostatic discharge-charge cycle of a DME-LiTFSI electrolyte and a P14TFSI-LiTFSI electrolyte and three important features are noted. First, the discharge capacity of the two electrolytes are comparable and the difference might be due to a difference in the current density. Second, the charge voltage is not increasing as rapidly in the experiment with P14TFSI electrolyte compared to the one with DME, and more than 15 % of the capacity is charged at a voltage below 3.15 V with P14TFSI compared to only 4.3 % with DME as shown in Section 4.2. Third, both electrolytes show e^-/O_2 ratios close to 2 during both discharge and charge.

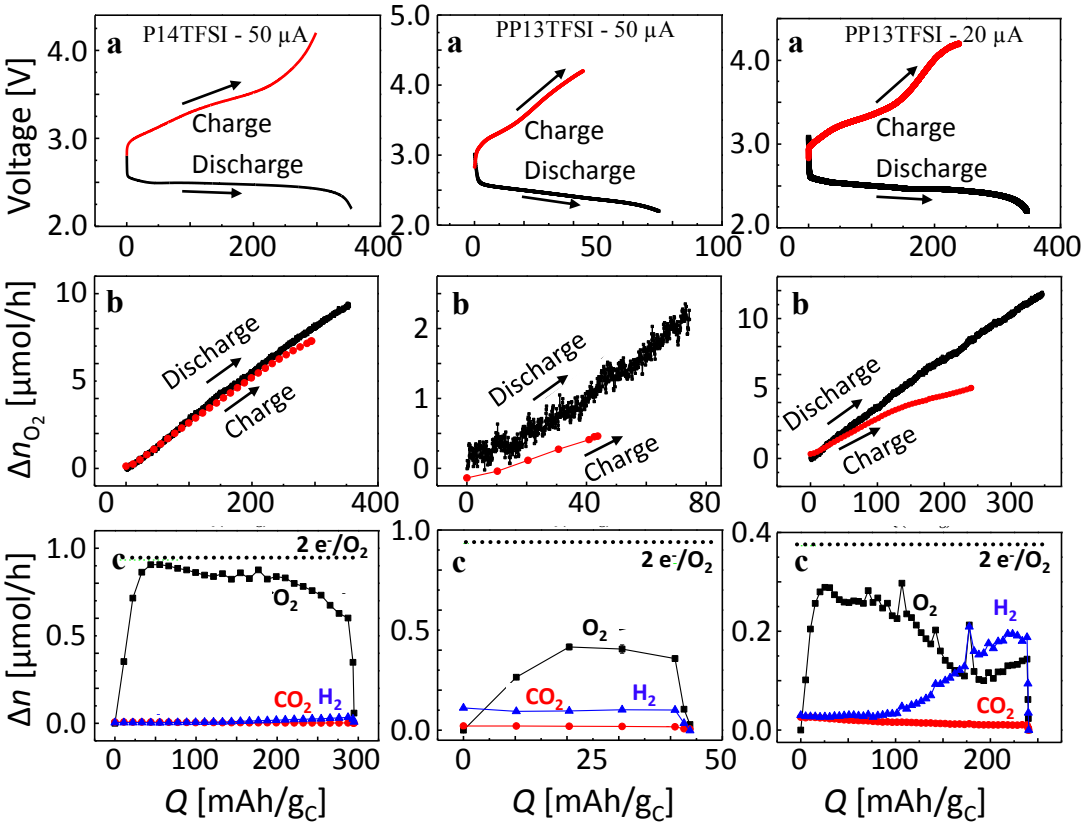

FIGURE 5.3: (a) Galvanostatic discharge-charge curves for cells with P14TFSI (50 μA discharge-charge) and PP13 (20 μA and 50 μA discharge-charge) based electrolytes. (b) Oxygen consumption (measured using pressure decay) during discharge and evolution (measured using DEMS) during charge. (c) Gas evolution rates for O_2, CO_2, and H_2. Adapted from Paper IV.

Figure 5.3 shows a comparison between the first galvanostatic discharge-charge cycle of electrolytes based on P14TFSI and PP13TFSI, respectively. PP13TFSI did not perform as well as P14TFSI. At 50 μA, the battery based on PP13TFSI was not able to sustain the current for long, showing a premature cell death, and only little oxygen was evolved during charge. At a lower current of 20 μA, a capacity similar to P14TFSI at 50 μA was obtained. Although the electron count per oxygen is near 2.09 during discharge, this electrolyte showed poor reversibility with an OER/ORR ratio of 40 % and an $(e^-/O_2)_{ch}$ ratio of 4, which is quite similar to result obtained by McCloskey et al. [56].

Figure 5.4a shows the first galvanostatic discharge-charge cycle curve for electrolytes based on P13TFSI and P13FSI. It is immediately seen that the FSI gives a larger discharge capacity than all of the other electrolytes, but the rechargeable capacity is very low and the DEMS measurements show that the extra capacity is due to a significant electrochemical degradation during discharge. During charge, P13FSI is showing an initial 2 e^-/O_2 ratio, suggesting Li_2O_2 oxidation, but after charging approximately 10 % of the full discharge capacity, the oxygen evolution decreases and the potential increases

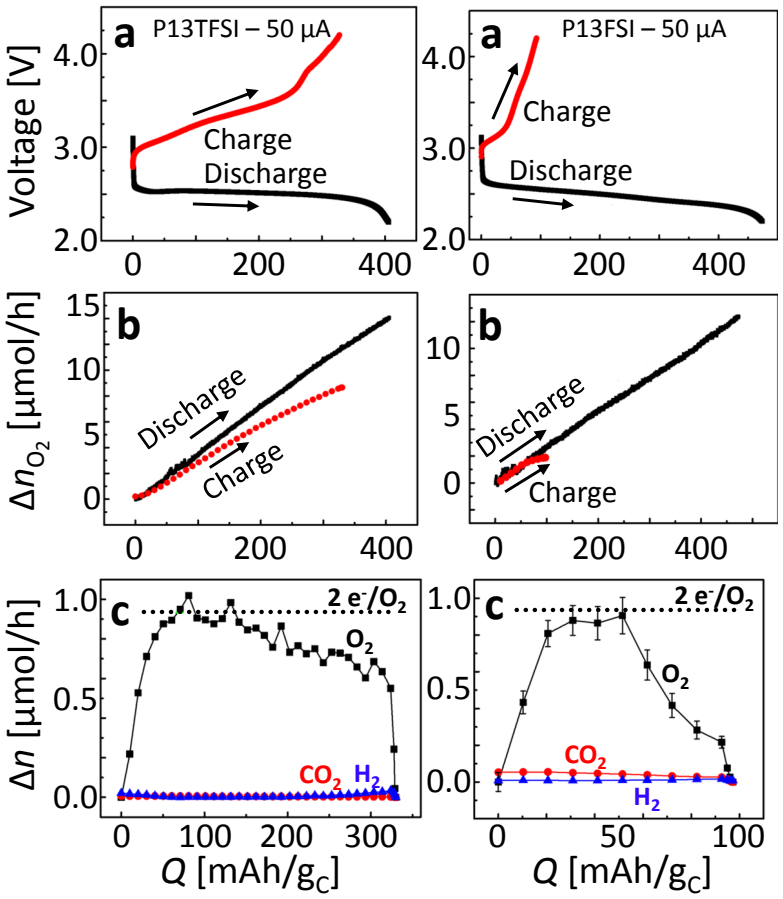

FIGURE 5.4: (a) Galvanostatic discharge-charge curves for cells with P13TFSI (50 μA discharge-charge) and P13FSI (50 μA discharge-charge) based electrolytes. (b) Oxygen consumption (measured using pressure decay) during discharge and evolution (measured using DEMS) during charge. (c) Gas evolution rates for O_2, CO_2, and H_2. Adapted from Paper IV.

rapidly. P13TFSI show a behavior very similar to P14TFSI, but with a slightly higher $(e^-/O_2)_{ch}$ of 3 during charge.

Figure 5.5 shows XRD measurements of discharged cathodes for pure IL and DME based electrolytes. All cells were discharged to 2.2 V at a current of 20 μA. The six major Li_2O_2 peaks are clearly visible in all samples except in the cathode tested with an FSI^- based ionic liquid. Most of the other peaks are from the PTFE binder.

Figure 5.6 shows the e^-/O_2 data through six cycles at 50 μA between 2.2 V and 4.2 V for electrolytes based on P14TFSI and P13TFSI. It is seen that the amount of electrochemical degradation reactions increases during both discharge and charge as the batteries are cycled. This shows that even though the first cycle seems promising, the system is not stable.

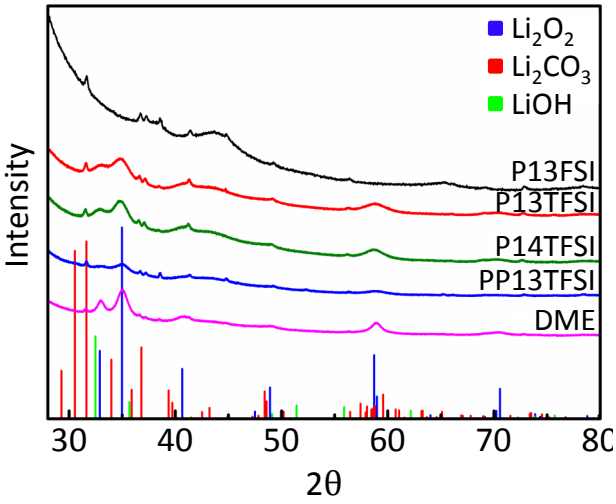

FIGURE 5.5: XRD patterns of discharged XC72 carbon cathodes with various electrolytes. Adapted from Paper IV.

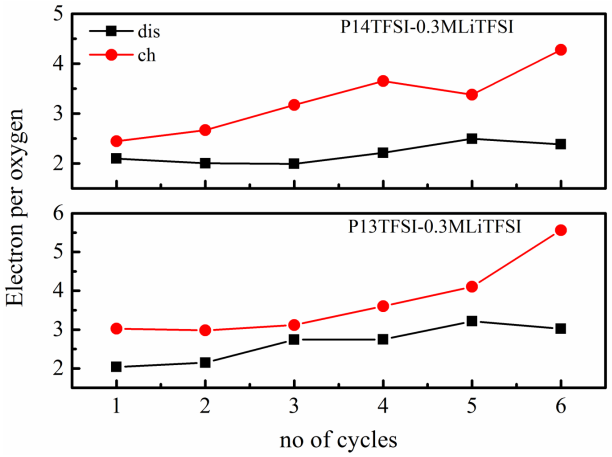

FIGURE 5.6: Cycling behavior of Li-O_2 batteries with P14TFSI and P13TFSI based electrolytes. Adapted from Paper IV.

5.1.1 Comparison between ionic liquid and organic solvent

The measurements presented in Figure 5.2 and in Table 5.1, show that the P14TFSI and DME are relatively close to each other in terms of electrochemical stability and discharge capacity. It is also noted that a larger part of the reaction occur at low potentials using the P14TFSI IL compared to DME. Due to the tunability of ILs, it therefore seems likely that some IL-based electrolytes might be able to compete with organic solvents in terms of stability, but the ILs often have a higher viscosity and a lower oxygen solubility, which limits the discharge current, and this should of course be taken into account as well.

5.1.2 Choice of anion

From the measurements presented in Figure 5.4 and in Table 5.1, it is clearly seen that the $TFSI^-$ anion is much better that the FSI^-. The combination of DEMS and XRD measurements suggests that only a small fraction of the discharge product in cells with FSI^- is Li_2O_2, whereas Li_2O_2 is the primary discharge product using $TFSI^-$. We are currently analyzing the measurements and collecting supporting data to determine the underlying reasons for the difference. So far we are looking primarily at the oxygen solubility, the amount of flourine in the anion and the size of the anion.

5.1.3 Choice of cation

From the measurements presented in Table 5.1, it is seen that all of the electrolytes having a TFSI anion showed an e^-/O_2 ratio of approximately 2 during discharge, but during charge, the different cations resulted in different electrochemistry. The PP13TFSI showed an OER/ORR of 0.40 at 4.2 V, whereas P13TFSI and P14TFSI showed a value of 0.62 - 0.63, which is close to DME at 4.2 V. The amount of electrochemical degradation is also different, from 4.0 e^-/O_2 in PP13TFSI to 2.8 e^-/O_2 in P14TFSI. We are currently analyzing the measurements and collecting supporting data to determine the underlying reasons to why PP13TFSI is less stable during charging than P13TFSI and P14TFSI. One of the major differences may be the concentration of impurities such as water as discussed below. We are also looking into the transport limitation in PP13TFSI indicated by the low capacity at 50 μA.

5.1.4 Impurities

One of the problems with commercially available ILs is the purity. The ILs sometime contain a significant amount of water that is difficult to remove, and which may have a significant impact on the electrolyte stability. In aprotic Li-ion electrolytes like ethylenecarbonate (EC), it has been shown that a change in impurity level from 0.09 % to 0.021 % increased the oxidation potential with 0.6 V from 4.87 V to 5.50 V [85], and it is likely that impurities will have a similar effect on the ionic liquids. From Figure 5.3c it is seen that PP13TFSI is developing a significant amount of H_2 during charge. The values are not calibrated, but it is a clear indication of water in the sample. This could therefore be the reason for the difference between the cations investigated. Looking at the cycling experiment in Figure 5.6, an increase in the e^-/O_2 ratio is observed. In paper V we saw a similar situation where impurities from the first cycle affected the following

cycles. The increase in e^-/O_2 ratio during cycling agree well with results published by Piana et al. [74] using P14TFSI based electrolytes.

5.1.5 Summary

A number of ILs have been tested with DEMS to investigate the electrochemical stability in the Li-O_2 system. It was shown that the extent of rechargeability depends on the choice of cation and anion. Unfortunately, none of the studied IL-based electrolytes behaved as ideal electrolytes in a Li-O_2 battery. It was found that the anion $TFSI^-$ was much more stable in the Li-O_2 system than the FSI^- anion and that ILs based on s pyrrolidium cation and the TFSI anion (P13TFSI and P14TFSI) had better rechargeability below 4.2 V (OER/ORR $> 60\%$) compared to the PP13TFSI based electrolyte, but further investigation is needed to determine whether the difference between the cations is related to the has to do with the type of cation or the level of impurities.

The work clearly showed the benefit of the DEMS technique to qualify the discussion of different electrolytes, as a comparison between the voltage profiles and discharge capacities is often too simplified to distinguish the complicated reaction mechanisms inside the Li-O_2 battery during charge.

Chapter 6

Commercial applications of lithium-air batteries

As it is clear from the results presented in Chapters 4 and 5, significant challenges need to be overcome to enable a commercialization of the Li-O_2 technology. It is, however, relevant to consider how the technology benchmark against competing technologies, if the degradation problem is solved, as this may decide whether it is worth the risk to pursue this technology. A part of this is an economic assessment of the system. Recently, two assessments of a Li-O_2 system have been presented [13, 86]. Both show that Li-O_2 may be significantly better than current state Li-ion batteries on a system level, but that new types of Li-ion batteries under development have similar energy densities and may be associated with less risks of failure in the development phase.

An important input to such calculations is a technical description of the system. This chapter focuses on two technical issues related to a commercialization of the Li-O_2 battery: 1. The air purification system to enable an open Li-air system and 2. The determination of the State-of-Charge in a Li-O_2 battery. The last part is closely related to Paper III. The battery used for calculations in this chapter has an energy content of 100 kWh, which is more than any EV battery on the market today. This size is in agreement with previously published system calculations [13, 86], and further details about the assumptions are found in the Supporting Information of Paper III.

6.1 Impedance-based management of Li-O_2 batteries

A battery management system (BMS) is often needed to ensure safe and reliable performance of any type of battery, and to predict the remaining capacity. The two important

BMS functions are the calculation of the remaining capacity in the battery, the state of charge (SoC), and the health of the battery; generally combining capacity retention on cycling and power capability. The health parameter is referred to as the state of health (SoH). The SoC and SoH is calculated by the BMS to predict the performance under different scenarios, to enable optimized usage of the remaining capacity, and even preventing dangerous situations that may occur if the battery powered device, e.g. an electric vehicle, is suddenly without power. The SoC can be calculated in several ways, with the most simple being a comparison of terminal voltage to previously recorded cycling data of cell voltage and battery capacity. A slightly more complex approach is to continuously monitor and integrate the current over time, also known as coulomb counting. The coulomb counting method accumulates errors if calibration is not performed, as it relies on the accuracy of the measurement and several methods for mitigating this have been proposed for lead-acid and lithium-ion batteries [87]. In Li-O_2 batteries, main electrochemical process is unchanged during discharge and charge (assuming no degradation). This means that the open circuit is constant and does not change with SoC as shown in Figure 4.6a. Furthermore, constant current measurements show a flat discharge plateau in a majority of the discharge period as shown in Figure 4.2. It has also been observed that the current densities have a significant impact on the onset of sudden death and thus also available capacity, due to the increase in required charge transport through the poorly conducting Li_2O_2 layer [88–90]. Since the coulomb counting method relies on a known total capacity to predict sudden death, the method is not well suited for predicting the remaining capacity in these batteries.

This section describes a method to accurately predict the SoC of Li-O_2 batteries using a single frequency EIS measurements to estimate the remaining capacity as well as the degradation of the battery materials. EIS is used in many systems to perform in situ

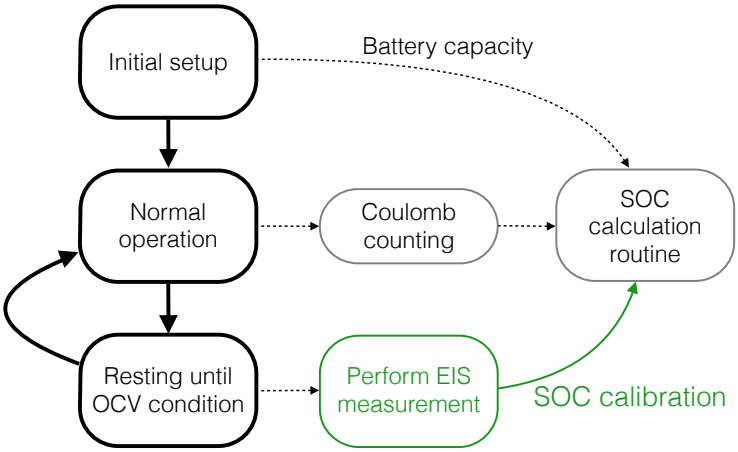

FIGURE 6.1: Working principle of the proposed impedance-based BMS system for Li-O_2 batteries.

determination of certain parameters like degradation of secondary Li-ion batteries [91–93], capacity fading of Li-S batteries [94, 95], and discharge mechanisms for Si-air [96], and the following work shows that EIS will be very suited for battery management of Li-O_2 batteries as well.

6.1.1 The working principle of the method

In Section 4.4 it was shown that the low frequency (<1 Hz) contribution of the impedance is related to the positive electrode and an EIS measurements in this frequency regime hold information about the double layer capacitance of the electrode. The capacitance can be calculated under constant load, but the value depends on the current density due to kinetic effects, and the true value is obtained at OCV. Since the measurements under load introduces new variables, this work focus on measurements at OCV. At OCV, the oxygen reduction reaction and Li_2O_2 oxidation reactions are very slow, and if the EIS excitation signal is sufficiently small, the impedance signal from the positive electrode becomes capacitive at the relevant frequencies (see insert in Figure 6.3). This means that the capacitance can be determined by the simple expression shown in Equation (6.1) [18].

$$C = \frac{-1}{2\pi f \cdot Z_{\text{im}}} \tag{6.1}$$

where f is the AC perturbation frequency and Z_{im} is the imaginary part of the corresponding impedance. It is important that other impedance contributions from processes with similar time constants do not overlap at the frequency used for the calculation. A frequency of 10 mHz was chosen because it was the highest frequency (and hence shortest measurement time) with the main contribution from the positive electrode capacitance.

During discharge, Li_2O_2 is deposited on the carbon surface in the positive electrode and as Li_2O_2 is a dielectric, the capacitance of the surface will change as described in Section 2.2.2, and the proposed SoC estimation is based on following the decrease in capacitance as the Li_2O_2 is deposited. As it will be shown later, the correlation between the capacity and capacitance follow the same trend in all experiments. The trend is an empirical function given by

$$C = C_0 - p_2 \left(1 - \exp\left(\frac{Q}{p_1}\right)\right) \tag{6.2}$$

where C_0 is the initial capacitance, Q is the capacity, and p_1 and p_2 are refined parameters determining the exponential shape.

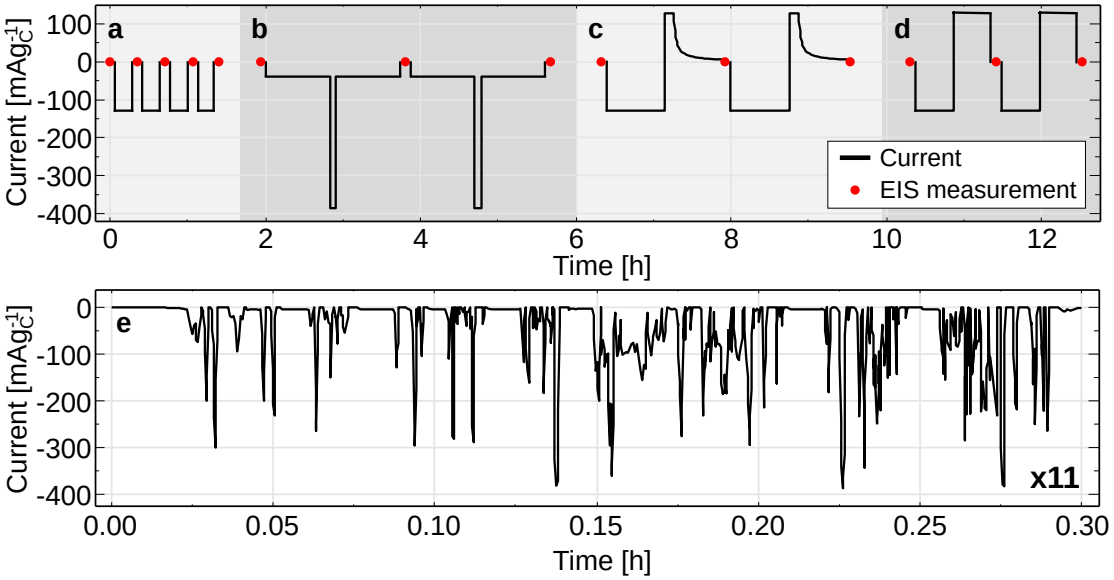

FIGURE 6.2: Load profiles used in the experiments to test the applicability of SoC determination based on the measured capacitance. (a) Discharge of 130 mA/g_C to 2 V interrupted by impedance measurements every 100 mAh/g_C. 13 mA/g_C, 39 mA/g_C and 390 mA/g_C were tested in the same way. (b) staircase discharge profile with 33 mAh/g_C at 39 mA/g_C, 33 mAh/g_C at 390 mA/g_C and 33 mAh/g_C at 39 mA/g_C between each impedance measurement. (c) discharge of 130 mA/g_C to 100 mAh/g_C followed by a 3.2 V voltage-limited charge of 130 mA/g_C to reduce electrochemical decomposition to a minimum. (d) Capacity limited galvanostatic cycling at 130 mA/g_C limited to 65 mAh/g_C. The charge was limited to 4.5 V to avoid severe electrolyte decomposition. (e) Drive cycle from ISEA-RWTH Aachen recorded from a Fiat eCity, scaled to a maximum current density of 390 mA/g_C. Reprint from Paper III.

6.1.2 Testing the method

Figure 6.2 shows the different current densities used to test the methods. The current densities were selected on basis of a future scenario, where electric vehicles will be powered by Li-O_2 batteries as the only source of power. The scaling of the peak and average current densities are based on an electric vehicle with a 100 kWh battery, a sustained high power of 55 kW and a peak power of 105 kW, which matches most electric vehicles today in terms of peak power and is superior in terms of capacity [97]. Details on the calculation are found in the Supporting Information of Paper III.

Figure 6.3a shows the imaginary part of the impedance spectrum at low frequencies during discharge. It is seen that the imaginary impedance is increasing, meaning that the capacitance decreases. The data points at 10 mHz is marked and the corresponding capacitance is listed in the figure. Figure 6.3b shows the calculated capacitances as a function of capacity, and while the potential is almost constant, the capacitance decreases throughout the discharge. At the end of discharge, when the battery reached 2.2 V, the capacitance was 50 % of the initial value.

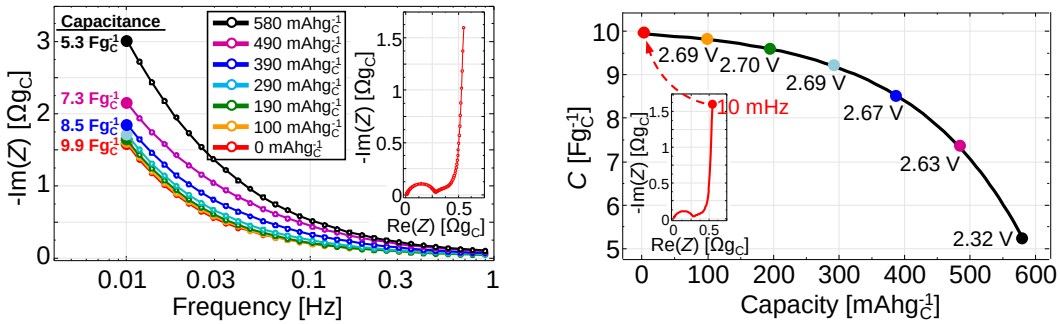

FIGURE 6.3: Left: The imaginary part of the impedance spectrum at low frequencies during discharge. It is seen that the imaginary impedance is increasing, meaning that the capacitance decreases. Right: Capacitance as a function of the capacity for a constant current discharge at 130 mA/g$_C$. Insert shows a Nyquist plot of the impedance measurement. The voltage labels are measured during discharge prior to the impedance measurements. The OCV was 2.83 V during the entire discharge. Reprint from Paper III.

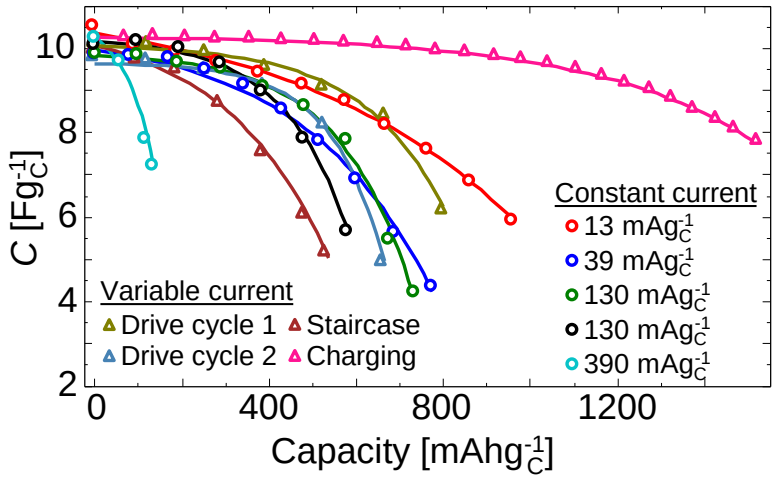

FIGURE 6.4: Overview of the change in capacitance measured at OCV between different types of discharge. Reprint from Paper III.

Figure 6.4 shows the change in capacitance as a function of capacity for all measurements. It is seen that the capacitance decrease is similar in nature for all measurements, but that the capacity of the different batteries vary significantly, up to a factor of 14. The data has been fitted to Equation (6.2) and the fitted parameters are presented in Table 6.1. Three observations are made based on these values: (1) all initial capacitances fall within 10.0 Fg_c^{-1} ± 0.4 Fg_c^{-1}, (2) the trend of the decreasing capacity is very similar for all measurements performed at different current densities varying a factor of 30, and at both dynamic and constant current loads, and (3) all capacitances have decreased to approximately 50 % in the end of discharge, except the high current measurement at 390 mA/g$_C$ and the measurement including charging. Both of these exceptions will be discussed further below.

The purpose of a BMS is to predict the remaining capacity, and in the following we have

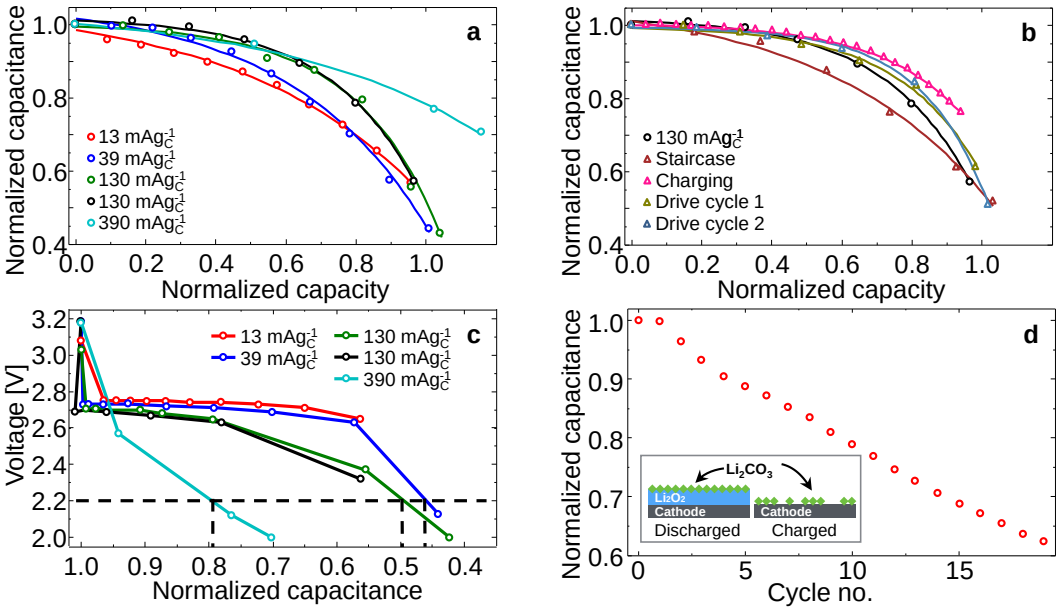

FIGURE 6.5: Results from experiments on Li-O_2 batteries. The data is labeled according to current profiles in Figure 6.2. Capacitance is normalized to the initial value before the discharge, and capacity is normalized to the value at 2.2 V. (a) Constant current load at four current densities: 13 mA/g_C, 39 mA/g_C, 130 mA/g_C, and 390 mA/g_C, (b) dynamic current profiles according to Figure 6.2 and data from a 130 mA/g_C constant current experiment, (c) Discharge voltage and capacitance from constant current experiments, showing the relation between current density and capacitance. (d) cycling experiment over 20 cycles showing decreasing capacitance as a function of cycle number. The insert shows the suggested reason for a decrease in capacitance, due to an accumulation of the degradation product Li_2CO_3 during cycling. Reprint from Paper III.

therefore normalized each discharge capacity to the capacity at 2.2 V, to investigate how well the remaining capacity is predicted by the capacitance. Even though all initial capacitances are very similar, we have chosen to normalize these values also, as this is what would be done in an actual BMS, where the capacitance may vary between batteries and may change over time due to degradation.

Figure 6.5a and Figure 6.5b show the data from Figure 6.4 using this normalization to investigate the dependence between the capacitance and the SoC at the different current profiles seen in Figure 6.2. Figure 6.5c depicts how the voltage during discharge relates to the capacitance for different current densities, and it is evident that the current densities impact the discharge capacity, and thereby the capacitance at 2.2 V. Figure 6.5d shows the normalized capacitance in the fully charged state, as a function of cycle number. Upon cycling, the capacitance decreases almost linearly to approximately 65 % after 20 cycles.

	C_0	p_1	p_2	$Q_{2.2V}$	$\frac{C_{2.2V}}{C_0}$
	Fg_c^{-1}	mAh/g_C	Fg_c^{-1}	mAh/g_C	-
13 mA/g_C	10.3	518	820	1001	53%
39 mA/g_C	10.0	300	467	767	44%
130 mA/g_C	9.83	169	76.9	700	52%
130 mA/g_C	10.1	148	90.9	599	50%
390 mA/g_C	10.2	67	465	117	78%
Staircase	10.1	241	610	519	54%
Charging	10.3	377	44.8	1614	69%
Drive cycle 1	10.0	188	54.9	812	59%
Drive cycle 2	9.64	124	21.8	652	56%

TABLE 6.1: Experimental values and parameters obtained by fitting experimental data to Equation (6.2). C_0 is the initial capacitance, $Q_{2.2V}$ is the discharge capacity at the 2.2 V cut-off, $\frac{C_{2.2V}}{C_0}$ is the fraction of capacitance at the 2.2 V cut-off to the initial capacitance.

6.1.3 State of charge

The constant current experiments presented in Figure 6.3 show how the capacitance changes as a function of capacity. The correlation is decreasing and at the end of discharge the capacitance is 50 % of the initial value. Assuming that the change is due to a uniform layer of Li_2O_2, this corresponds to a layer thickness of ∼5 nm at these current densities, and as discussed in Section 6.1.1, this is in line with the general understanding of the sudden death mechanism [90]. The voltage during discharge is shown in Figure 6.3 as labels on the capacitance data points, and remains unchanged at ∼2.70 V between 100 % and 33 % SoC, whereas the capacitance decreases as the battery is discharged. Seeing that all measurements behave similarly, this shows that the capacitance holds information about the SoC, that is not possible to obtain using voltage based measurements.

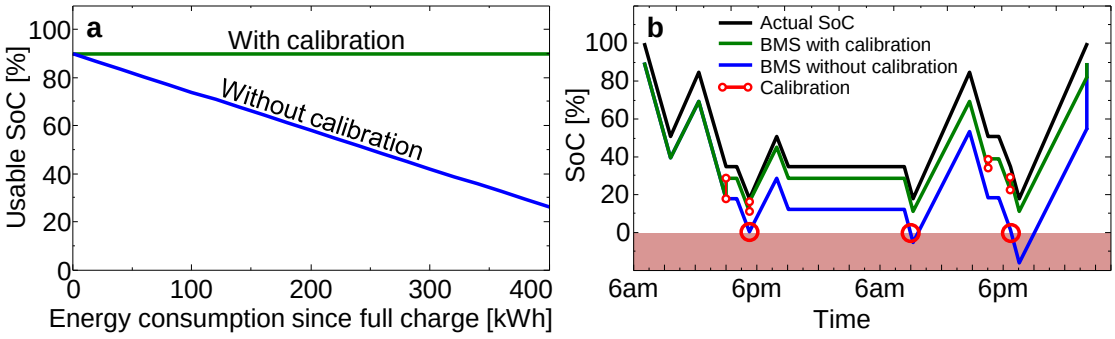

FIGURE 6.6: (a) The combined accumulation of error in the estimation of SoC, including both the coulomb counting error and the needed capacity reserve. (b) Scenario showing the difference in estimation of useable capacity between BMS systems with and without calibration based on capacitance.

The accuracy of the SoC estimation from capacitance is determined by evaluating the uncertainty in the capacitance to capacity correlation from the experiments with the

130 mA/g_C constant current load and the drive cycle load shown in Figure 6.5b. To test the effect of the calibration, we have designed a BMS system based on the following assumptions:

1. Due to high current dependency on capacity, a reserve of 10 % SoC is needed, resulting in 90 % useable capacity.
2. Coulomb counting has a 3 % accumulation of error.
3. The SoC is calibrated at end of full charge.
4. Charging is performed at 10 kW and fast charging is not considered.

If no SoC calibration is performed, the coulomb counting error and the need for a capacity reserve will result in a significant decrease of useable capacity as the battery is discharge and charged. During discharge, the accumulated error corresponds to 3 % and during charge, the error is 13 %, due to the additional need of a 10 % capacity reserve for the following discharge. Figure 6.6a shows the effect of the combined error of 16 % on a 100 kWh battery as a function of energy consumption of up to 400 kWh without fully charging the battery. When the battery is fully charged, a BMS would be able to correct the estimation of useable capacity to the nominal capacity of the battery without the capacitance calibration, and thus reset the useable capacity to 90 %. Without the SoC calibration, the useable SoC could decrease to 26 % over an accumulated energy consumption of 400 kWh, whereas the SoC calibration based on capacitance would be able to keep the SoC estimation at 90 %, thus maximizing the useable capacity.

Since the capacity of future Li-O_2 batteries is expected to increase, we postulate a use-scenario for the batteries based on ∼10 kW charging power available and no need for fast charging with daily use. This scenario is illustrated in Figure 6.6b, where the battery is either discharged, charged or at rest. The calibrations performed in Figure 6.6b enables the BMS to more accurately predict the remaining capacity, whereas the estimated capacity without calibration would become less than zero (shown on the figure as circles when the SoC is crossing the 0 % threshold), warning the vehicle or driver to stop. The capacitance calibration is less accurate in the less critical beginning of discharge, due to the slope of the capacitance correlation to the capacity, and gradually more accurate as the battery is discharged. Figure 6.6b shows that the calibrations performed below 50 % SoC have the possibility to initially correct the SoC by ∼10 %, and when performed multiple times, able to further minimize the uncertainty of the SoC estimation, resulting in periods with an uncertainty of less than 5 % SoC.

6.1.4 Power capability

The current density of 390 mA/g_C is only able to provide 12 % of the capacity compared to the current density of 13 mA/g_C. This indicates that the available capacity depends explicitly on the current density. For correct estimation of the available power, the internal resistance is usually used to predict if the terminal voltage of a battery will exceed the limit during high power demands. For Li-O_2 batteries, this is not possible since the resistance is almost unchanged during the entire discharge as shown in Paper I. Previously, we saw that the capacitance of the 390 mA/g_C experiment did not decrease to ∼50 % of the initial capacitance. If we look at the voltage during the constant current experiments (Figure 6.5c), we see that the high current density experiments (130 mA/g_C and 390 mA/g_C) have significantly higher overpotentials, thus the 2.2 V limit is reached prematurely. From the measurements, it seems that current densities of 390 mA/g_C are only supported at capacitances above 78 % of the initial capacitance, while it is possible to use 130 mA/g_C until a capacitance of 50 %. This shows that the capacitance can also be used to estimate the maximum power that the battery is capable of delivering at the given state.

6.1.5 State of health

The cycling experiment (Figure 6.5d) shows how the capacitance of a fully charged positive electrode decreases as a function of cycle number. From several papers [56, 62, 98, 99] it has been shown that Li_2CO_3 and similar species are accumulating upon charging and are immobilized in the positive electrode (see Figure 6.5d, insert). The presence of Li_2CO_3 in the cathode has two main effects on the battery performance. First, the amount of Li_2CO_3 will increase for each cycle, resulting in a decrease of the available active area for Li_2O_2 deposition. This results in a lower discharge capacity for the battery. Second, the inclusion of Li_2CO_3 in the deposited Li_2O_2 decreases the charge transport through the Li_2O_2, thus increasing the required overpotential [61]. It was shown in Figure 2.6 that even a few angstrom of Li_2CO_3 will decrease the capacitance significantly, and using the capacitance in the fully charged state, it is possible to track the degradation of the positive electrode, and a BMS can use this information to determine the SoH parameter related to capacity retention, and thereby the cycle life of the battery.

6.1.6 Further development of the model

With more knowledge about the system, it is expected that the time at OCV can be reduced significantly and that measurements can be made even while discharging or charging the battery. This could be done by employing impedance measurements in the time domain to calculate the capacitance. In this case, it might even be possible to perform SoC calibrations while driving. Another direction would be to implement an adaptive state estimation algorithm, akin to the work done by Fleischer et al. [100], using the capacitance measurements to improve the calibration uncertainties.

The charging experiment shown in Figure 6.5b has a much larger discharge capacity compared to the other experiments as seen in Table 6.1 (1614 mAh/g_C vs 599 mAh/g_C for the 130 mA/g_C experiment), and we suspect that this is due to the accumulation of Li_2CO_3 and similar species. The reason for the capacitance not decreasing to more than 69% is not fully understood and further studies of cycling effects on Li-O_2 systems is needed.

Many metal-O_2 systems show the same type of discharge and charge curves as the Li-O_2, but further studies on other metal-O_2 systems are needed to conclude if the proposed method is applicable to these systems. A likely candidate for further studies is the Na-O_2 battery, where the discharge product, NaO_2 is considered to have surface conductivity. The conductive nature of the NaO_2 is expected to cause an increase in capacitance as the battery is discharged, reflecting an increase in surface area as the NaO_2 cubes are grown [101].

6.1.7 Summary of impedance based management of Li-O_2 batteries

A method for estimating the remaining capacity, power capability and cycle life of Li-O_2 batteries has been proposed and verified through a number of tests. Experiments showed that the capacitance of the positive electrode decreased exponentially during discharge, and that it was possible to improve the prediction of the remaining battery capacity significantly based on a single frequency measurement of the positive electrode capacitance. In a typical scenario, a single SoC calibration was able to improve the available SoC by more than 10 % of the full battery capacity, by minimizing the uncertainty of the SoC. The capacitance was also used to estimate a degradation of the positive electrode in a Li-O_2 battery cycled 20 times. This makes the method applicable not only for electric vehicles, but for batteries in a large range of electrical devices, as the measurements can be performed when needed, thus maintaining a high level of accuracy for the estimation of remaining capacity and state-of-health. The approach is furthermore expected to be transferable to other metal-O_2 systems.

6.2 Separation of O_2 from air

A true Li-air system rely on the use of ambient air. Dry atmospheric air contains 78% N_2, 20.9% O_2, 0.93% Ar and 400 ppm CO_2, and in addition to this, the air typically contains 1% - 3% H_2O [102]. To develop a true lithium-air battery, it is therefore important to investigate how the non-oxygen gases affect the electrochemistry. Luntz et al. have shown that nitrogen and argon are inactive in the battery, whereas both H_2O and CO_2 have significant impact on the electrochemistry [14]. Meini et al. [103] have shown that even a small amount of H_2O is able to cause a 10-fold increase in discharge capacity. This effect has been investigate further by Aetukuri et al. [58], proposing that water increase the solubility of LiO_2, to enable a solution-mediated growth of toroidal shaped Li_2O_2 particles. While improving the discharge capacity, the presence of water, unfortunately, also speed up the degradation reactions inside the battery [58].

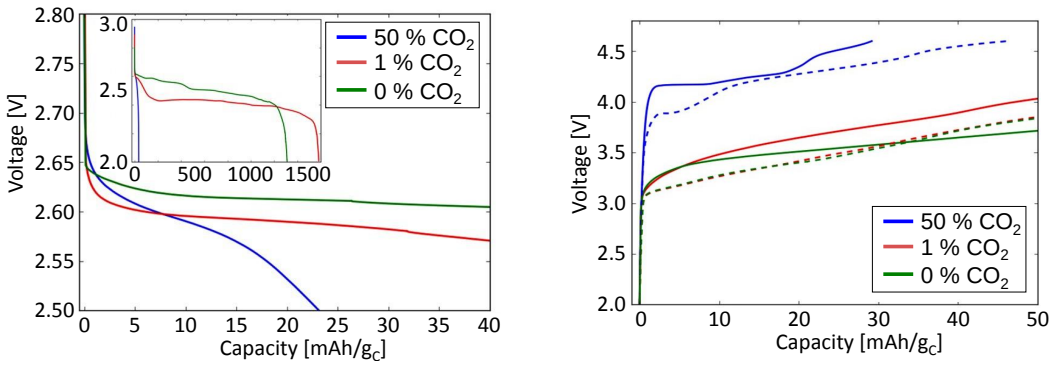

FIGURE 6.7: The effect of adding CO_2 impurities to the oxygen gas during discharge (left) and charge (right). Adding only 1% CO_2 increases the overpotentials significantly during both discharge and charge. Reprint from Paper V.

A similar effect is observed with CO_2 [53, 104, 105]. In correspondence with these observations, Figure 6.7 shows that both the overpotentials and the capacity increase in a mixture of O_2 and CO_2 compared to a system with pure oxygen. If the CO_2 content becomes too high, the discharge capacity decreases significantly. In Paper V and [61], it is suggested that the increase in overpotential is caused by an increased amount of Li_2CO_3-like species in the Li_2O_2, and the higher potentials will lead to further degradation in the battery. The mechanism causing the increase in discharge capacity is not fully understood, but in Paper V, Mekonnen et al. suggest that the formation of Li_2CO_3-like species at the step valley sites of the Li_2O_2 surface will alter the shape and growth directions of the Li_2O_2 in a beneficial way, but as with H_2O, the effect is also expected to increase degradation through cycling. From a current perspective, it is therefore crucial to remove H_2O and CO_2 from the gas stream.

6.2.1 Previous Li-O_2 and Li-air strategies

Several strategies have been pursued to avoid impurities in the batteries. Three of the most investigate strategies are: 1. passive hydrophobic membranes on top of the air electrode, 2. removal of impurities from the gas and 3. on-board oxygen storage. Girishkumar et al. discussed that it is not possible to use hydrophobic membranes, as the O_2 permeability will always be higher than the H_2O permeability [10], and Zhang et al. have tested such a membrane system with limited success [106]. In 2009 Excellatron Solid State LLC filed a patent describing the use of H_2O and CO_2 scrubbers as absorbents [107]. Since then, Bosch and others have proposed methods to reduce moisture from the inlet gas either by using a regenerative dehumidifier based on a desiccant [108–111], or by using a selectively permeable membrane [112], and a regenerative CO_2 absorption system that selectively absorbs CO_2 over O_2 has been described in [113]. The third strategy is having an oxygen reservoir on-board. Bosch, Ford and Tesla have filed patents on this method in different variants. Bosch has suggested an inflatable bladder pumped by the electrochemical reaction itself [114], whereas Ford and Tesla have looked at more traditional systems with an oxygen tank and a compressor [115, 116].

6.2.2 A solution for an open Li-air system

The purpose of this assessment is to determine whether it is possible to make an air purification system that is suitable for use in electric vehicles in terms of weight, volume and energy consumption. Calculations made on a specific system, based, among others, on the strategies mentioned above, is included in Appendix D. The main conclusions are presented below.

The calculations are based on a 100 kWh Li-air battery with an average discharge voltage of 2.65 V that consumes 17 m^3 of oxygen through a full discharge. The scenario is based on a calculation of 100 % humidity at 25 °C and 400 ppm CO_2. In order to dimension the system, a minimum discharge capacity time of 3 hours is assumed, which corresponds to an average speed of 170 km/h, as a total driving range of 500 km is expected from a 100 kWh battery.

The suggested system is cleaning the air in three steps, as sketched in Figure 6.8. First, the air is compressed to 3 bar. This has been shown to increase the performance of the battery [117, 118], and is thus expected to be needed anyway. As the dew-point is almost independent of pressurization, the compression corresponds to a decrease in dew point from 25 °C to 7.9 °C as described in Appendix D. Second, the gas is pre-dried in a semipermeable membrane unit like the Permapure Drier. This decreases the amount

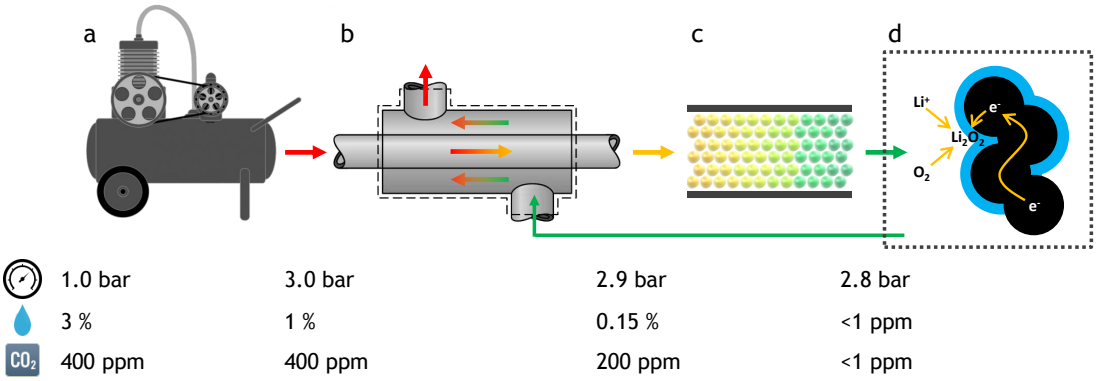

FIGURE 6.8: Schematic illustration of an air cleaning system for Li-air batteries to remove H_2O and CO_2 to below ppm levels. The red color represent air with impurities and the green colors represent the allowed amounts of H_2O and CO_2.

of CO_2 and H_2O significantly, and limits the size and energy consumption of the last step. Third, a system of plug flow reactors with H_2O and CO_2 absorbents is used to reduce the impurity levels below 1 ppm. After this final step, the air is ready to use in the battery. An important part of the cleaning design is to use the dry air from the battery in a counter flow setup in the membrane-based pre-drying step, as this will save a significant amount of energy.

Allowing 1 ppm of impurities in the gas stream, accumulates to a total amount of 40 g H_2O and 100 g CO_2 in a total lifespan of the battery corresponding to a total of 420 full cycle equivalents similar to the calculation performed by Albertus et al. in Ref. [13]. If this is found not to be sufficient, an alkaline guard like Potassium or Sodium can be used as a final cleaning step.

Based on the calculations performed, the system weight will be 20-30 kg in a design based on regeneration during charging. The energy consumption is estimated to be approximately 1 % of the battery capacity during discharge due to a pressure loss in the cleaning system and 4% during charging to heat up the adsorbents to release the captured H_2O and CO_2. The gas compressor itself is not considered in this calculation. Compared to the complications and volume requirements of having an oxygen storage tank, this looks like an attractive option. Concerning the weight, it is also noted that the weight of the oxygen itself in the storage tank is 23 kg in a 100 kWh system.

6.2.3 Summary of separation of O_2 from air

It was shown that it is possible to design a system with a relatively low weight and energy consumption, that is able to remove H_2O and CO_2 to a level below 1 ppm. A

realistic estimate of the price has been left out, as the expected economy of scale of such a system will have a huge effect on the system price.

6.3 Summary of commercial applications of lithium-air batteries

Due to significant challenges related to degradation of the electrodes and electrolyte in Li-O_2 batteries, a commercialization of the technology is not expected soon. If (or when) the battery will be ready to enter the market, this chapter has presented solutions to two challenges that both could have been show-stoppers. First, a method for estimating remaining capacity, power capability and cycle life of Li-O_2 batteries has been proposed and verified through a number of tests. Second, an air purification system with acceptable weight and energy consumption was designed to meet a demand of sub-ppm levels of H_2O and CO_2 as required in an open Li-O_2 system.

Chapter 7

Summary and outlook

In this thesis I have presented the results of my research during the last three years. I have divided the results into three chapters, and a summary of the findings has been given at the end of each chapter. It is not my intention to fully repeat those summaries here, but only to emphasize a few of the most important aspects of the work and briefly discuss the outlook of this thesis.

7.1 Summary of main results

During my PhD project, I have investigated carbon based air-electrodes in Li-O_2 batteries to establish the necessary testing facilities and develop a theoretical framework with DEMS and EIS as the key techniques with the ultimate goal of proposing new materials and screening methods. The main outcome of this work can be summarized as follows:

- During the project I constructed the differential electrochemical mass spectrometer and used it to investigate different systems, including electrolytes based on ionic liquids. It was an important achievement, since the measurement of the oxygen consumed and released is necessary to determine if a Li-O_2 system is reversible.
- The biggest contribution of this work to the field of research is the increased understanding of the electrochemical impedance spectroscopy (EIS) in the Li-O_2 system. Working closely with the research group at IBM Almaden Research Center, it was possible to combine their extensive knowledge of the system with the conducted EIS measurement. Among others, it was possible to use EIS to show that the capacity is also limited by tunneling in porous cathodes, and that the change in double layer capacitance at sudden death corresponds to a Li_2O_2 layer

of approximately 5 nm in porous electrodes, which is in line with flat electrode measurements and DFT calculations.

- Further development of the EIS technique enabled a detailed probing of the impedance during charge and combined with DEMS and other supplementary techniques, it was possible to show that the Li_2O_2 oxidizes at very low potentials (3.05 V) during charge, but that the reaction is blocked by the formation of an SEI layer. The EIS measurements were important to identify the existence of a mixed potential during charge.

- It was possible to use the knowledge obtained working with EIS to develop a new and simple tool for battery management systems to estimate the state of charge and state of health of Li-O_2 batteries.

7.2 Outlook

Having worked within the same field of research in three years naturally brings up many ideas for further research. I have here chosen the six suggestions that I consider most interesting.

1. The ultimate goal of investigating the fundamental electrochemistry with DEMS, EIS and supplementary methods has been to find new materials. I suggest to use the established competences to look for new materials. The search for new electrolytes using DEMS is well documented in Chapter 5, and an additional screening parameter could be to use the capacity in charge below 3.15 V to measure the formation rate of the SEI layer. Cathodes are more complicated as the electrolyte degradation is often dominating, but the use of EIS and differential capacity measurements might reveal reactions at certain potentials, that is only related to electrode degradation, which could then serve as a screening test.

2. Disregarding the stability issues, carbon is indisputably the best cathode material because it is light, conducting and can be made with a very high surface area. Investigations of ALD coating of carbon cathodes with a protective layer might therefore provide the optimal solution.

3. Further development of the EELS/EFTEM method to probe lithium and oxygen on the sub-nanometer scale. TEM studies often presents nice pictures of toroidal shaped particles formed in the presence of water impurities, but no one has probed the thin layers on top of the carbon and this might very well give important inside into the reaction mechanisms and the SEI layer formation among others.

4. The use of the capacitance to determine the state of charge should be investigated further and, if possible, expanded to other metal-air systems. Techniques to reliably

determine the capacitance in the time domain and away from OCV, will strengthen the method significantly.

5. Having the entire framework of DEMS and EIS ready, it would be interesting to look at Na-O_2 and other similar systems to qualify and quantify the discussion. Especially EIS could be useful to describe the differences between Li-O_2 and Na-O_2

6. Finally, the DEMS setup can be used to study many different processes. One option is to investigate high voltage behavior of electrolytes and measure the gas evolution as a function of potential.

Appendix A

Development of the testing equipment

In the project I have been main responsible for building up the basic testing equipment for Li-O_2 batteries. Among others, I have designed and developed

- the differential electrochemical mass spectrometer (DEMS)
- the 2-electrode Swagelok cells
- the equipment used to automatically change gas in the cells from oxygen to argon and vice verse
- the cell holders to mount the Swagelok cells inside the furnace
- the cathode fabrication using an airbrush

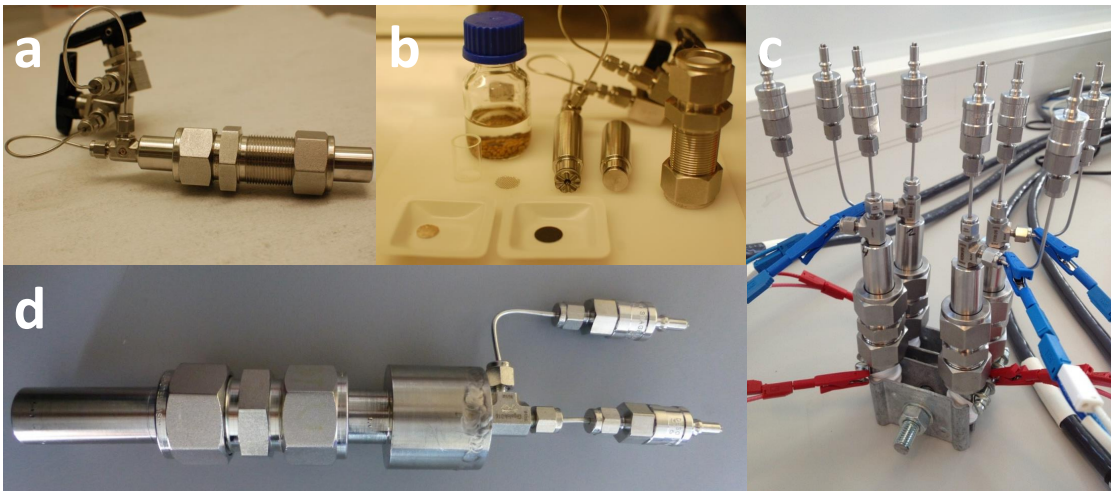

FIGURE A.1: (a)-(b) The initial cell design with manual valves. (c) First Li-O_2 battery pack in the ReLiable project. Tested in 2012 using the second cell design with quick-connect valves. (d) Final cell design with 10 mL volume.

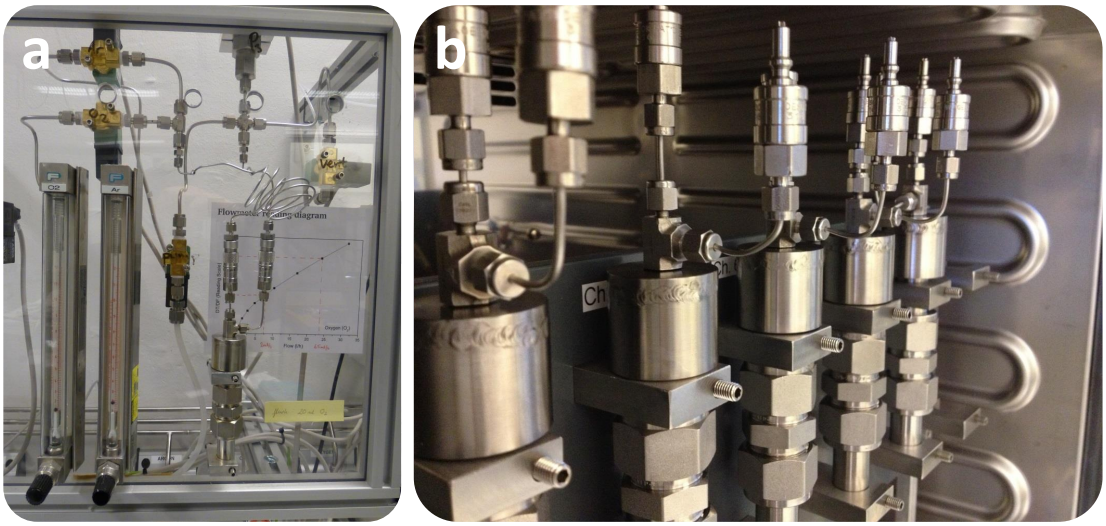

FIGURE A.2: (a) Gas filling and changing system. (b) Five Swagelok cells in the temperature controlled furnace.

Figure A.1 shows three of the four design versions of the Swagelok cell. As it may be seen, we increased the gas volume inside the cells in each generation. As we improved our competences in the preparation of the active materials, our capacity in the cathode increased and we needed a larger gas volume in the cells. In our initial design we had a gas volume of 0.5 mL, which was insufficient to support a full discharge. The volumen was increased to 2 mL, which was still a little too low to be able to neglect the pressure decrease during discharge. The choice of welding a larger volume onto the Swagelok cells was made to ensure that the pressure did not decrease by more than 15 % during discharge, while maintaining the rather compact design.

Figure A.2a shows the Labview controlled gas-change station used to automatically change gas in the cells from oxygen to argon and vice verse. Based on a wide number of experiments, we found this necessary to ensure a consistent gas-change routine in terms of flow time and gas pressure inside the cell after gas-change. In addition to this, the program was designed to prevent a back-flow of ambient air, which ensured that we

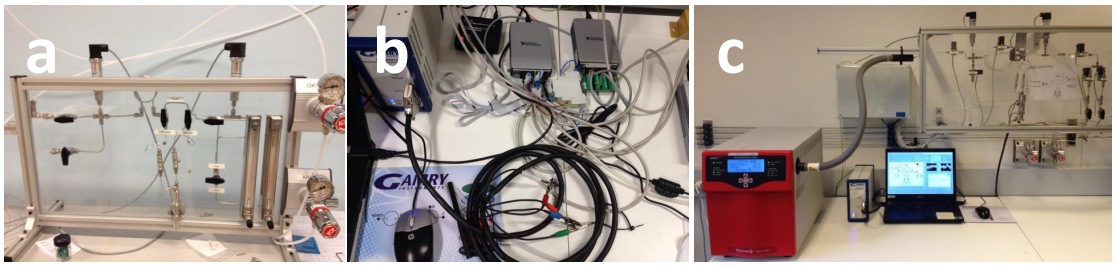

FIGURE A.3: The DEMS setup was constructed in two phases. To gain experience, we constructed a manual DEMS setup to determine appropriate volumes, flushing times etc. After this, we automated the setup in a Labview interface, basically making DEMS measurements a one-click experiment.

always had the pure 6.0 gas available. Figure A.2b shows five Swagelok cell being tested inside the temperature controlled furnace.

Figure A.3a shows the first version of the DEMS setup. It was a manual system designed to gain experience with the method before the more complicated and expensive system was built. I co-supervised Andreas Hansen Poulsen, who did most of the work in a close collaboration with me. Figures A.3b and A.3c show the automatic DEMS system under and after construction. I designed and constructed the setup with invaluable help from research technician Mike Wichmann and student assistant Mathias Kjærgaard Christensen. It was automated by using magnetic valves, an automatic 2-position 6-way valve and a much more advanced Labview interface, controlling the mass spectrometer, potentiostat, magnetic valves and pressure measurements.

Appendix B

Differential electrochemical mass spectrometry - In situ gas analysis

B.1 Initial measurements and design

The first setup in our lab was built in the spring 2012 with manual valves and without automation to enable fast changes as we learned more about the method and the lithium-air system. Andreas Hansen Poulsen was responsible for this development under my supervision. From September 2012 to March 2013, I built a fully automated DEMS setup based on the experiences we learned from the manual setup. This would not have been possible without the invaluable help from Mathias Kjærgaard Christensen who helped me setup the Labview framework and Mike Wichmann, who assembled the pipes and valves.

To ensure a reliable measurement, a wide number of parameters need to be measured and characterized. Some of the most important steps are included below.

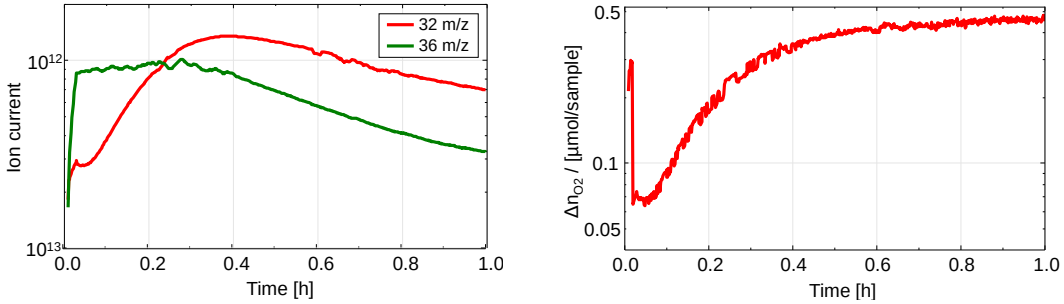

FIGURE B.1: Left: Measurement of ion currents on m/z values of 32 and 36 corresponding to O2 and ^{36}Ar. Right: The ion currents have been used to calculate the molar amount of O_2 in the sampled volume. The time dependence reflect that the gases are not equally distributed in the capillary inlet to the mass spectrometer.

The timing of the measurement of ion currents turned out to be very important. Figure B.1 (left) shows a 1 h measurement with the mass spectrometer of a gas sample in the beginning of the first charge of a Li-O_2 battery. The time axis start just as magnetic valve (1) in Figure 3.5 was opened. It is seen that the ion currents of m/z 32 and 36 behave differently, and as the relative current between these channels are used to calculate the molar amount of gas evolved, it is clear that timing is important. In Figure B.1 (right) the molar amount of O_2 calculated based on the ion currents is shown without the proper calibration. This emphasizes that it is important to fix the time from the magnetic valve (1) opens, to the measurement of ion currents is performed. From these measurements, it was decided to use the data after 10 minutes. Since then, the pumping procedure between each sampling has improved and the measurement is now used after only 2 minutes. Every time this changes, a new calibration of the ion currents is needed.

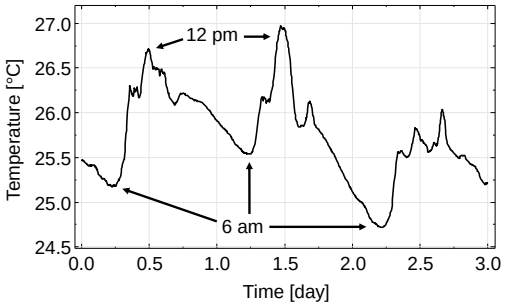

FIGURE B.2: Temperature variations in the room of the DEMS setup.

Temperature Figure B.2 shows the temperature variations in the room in a 3-days period. The temperature varies periodically with a minimum temperature in the morning and a maximum temperature at noon. As the temperature changes affect the pressure inside the DEMS setup, it is important measure the temperature throughout the entire measurement to correct the pressure measurements. Using the ideal gas law, a change in temperature of 2°C from 24.7°C to 26.7°C corresponds to a change in pressure of ((273.15+26.7)/(273.15+24.7)-1)*1.8 bar = 12 mbar. In the DEMS setup this pressure change is equivalent to 0.14 mAh of the $2e^-/O_2$ discharge or charge reaction. For cathodes with a small carbon loading this corresponds to one third of the total capacity.

Calibration of ion current A number of calibration experiments are needed to enable a quantitative translation of M/Z intensities and pressure changes to moles of gas consumed or evolved. We used a 5 % O_2, 5 % CO_2 and 90 % Ar to calibrate the correspondence between the measured intensities of O_2, CO_2 and Ar and the corresponding partial pressures. Using measurements of the intensities after 2 minutes, the following correction factors were obtained:

$$\frac{p_{O_2}}{p_{^{36}Ar}} = 1.273\frac{I_{O_2}}{I_{^{36}Ar}} \tag{B.1}$$

$$\frac{p_{CO_2}}{p_{^{36}Ar}} = 1.152\frac{I_{CO_2}}{I_{^{36}Ar}}, \tag{B.2}$$

By diluting the gas with pure argon, it was shown that this ratio was unchanged in the range 0.1 % to 5 % of O_2 and CO_2.

Volume calibration The internal volumes are important to calculate the molar amount of gas consumed or evolved. Relative volumes in the setup was determined by monitoring the pressure changes of the two pressure transducers as different combinations of valves were opened or closed. The actual volumes were determined by replacing a part of the pipe with two different calibration volumes (500 μL and 1.00 mL) and measuring the effect on the pressure changes as valves were opened or closed.

The two volumes, essential to calculate the molar amounts of gas, were determined to be

$$V_{\text{dis}} = 4.98 \text{ mL} \tag{B.3}$$

$$V_{\text{MS}} = 1.03 \text{ mL} \tag{B.4}$$

where V_{dis} and V_{MS} are specified in Figure 3.6.

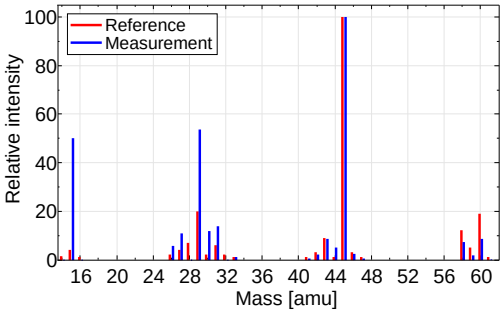

FIGURE B.3: Mass spectrum of 1,2-dimethoxyethane as measured by the mass spectrometer. The measurement is compared with a reference spectrum from NIST Chemistry Webbook [119]

Overlapping peaks in the mass spectrum The electrolyte of our reference system in the ReLiable project is based on DME, which is very volatile. It is therefore important to ensure that the m/z peaks of DME in the mass spectrum does not overlap with the peaks of O_2 and CO_2. Figure B.3 shows a measured and a reference spectrum of DME and it is seen that the contributions at m/z values of 32 (O_2) and 44 (CO_2) are very small.

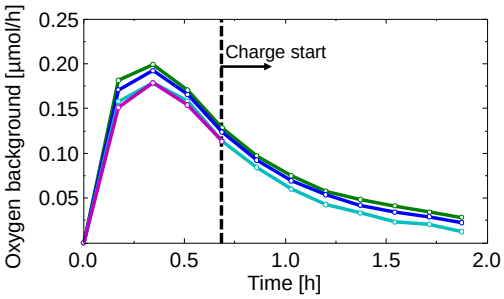

FIGURE B.4: The oxygen background in DEMS measurements as a function of time.

Flushing O_2 out of the system When the DEMS setup is measuring the evolved gas inside the cell, it flushes the cell with argon. Most of the gas in the cell is changed, but not everything. In the beginning of the charge, the cell is initially filled with pure O_2 and even small amounts of O_2 left in the cell will be significant compared to the evolved amount of O_2 during charge. Therefore, the cell needs to be flushed sufficiently.

Figure B.4 shows four measurements of how the amount of oxygen decreases between each measurement after changing the gas to argon. These measurements were made in a dummy cell without O_2 evolution, but the onset time of the charge in the real batteries is shown in the figure. A typical discharge current in the DME-XC72 system is 0.5 mA, which correspond to 9.3 μmole/h. In this case the oxygen left in the system is insignificant, but in measurements with a lower current density, as in the measurements with ionic liquids, described in Chapter 5, the O_2 background must be taken into account.

B.2 Calculations

The key calculations are:

$$\Delta n_{e^-} = \frac{Q}{F} \tag{B.5}$$

$$\Delta n_{O_2} = \frac{\Delta p \cdot V}{R \cdot T}, \tag{B.6}$$

where Δn_{e^-} and Δn_{O_2} are the moles of electrons and oxygen molecules consumed in a given period of time, Q is the integrated charge, $F = 9.65 \cdot 10^4$ C/mole is the Faradays constant, Δp is the gas pressure inside the Swagelok cell, V is the volume shown in red in Figure 3.6 left, R is the gas constant and T is the temperature. As described in Section B.1, the volume has been calibrated to be 4.98 mL, and as most of the volume is in the gas system and not in the Swagelok cell, small differences between the different cells does not affect the measurements. The temperature is measured continuously during the measurement.

$$n_{O_2} = \frac{p_{O_2} \cdot V}{R \cdot T} \tag{B.7}$$

As shown in Section B.1, measurements with a calibration gas with O_2 and CO_2 partial pressures in the range of 0.1% to 5% showed that

$$\frac{p_{O_2}}{p_{^{36}Ar}} = 1.273 \frac{I_{O_2}}{I_{^{36}Ar}} \tag{B.8}$$

$$\frac{p_{CO_2}}{p_{^{36}Ar}} = 1.152 \frac{I_{CO_2}}{I_{^{36}Ar}}, \tag{B.9}$$

and using that $p_{^{36}Ar} = 0.00333 \cdot p_{Ar} = p_{Ar}/300.3$, Equation B.7 can be rewritten as:

$$n_{O_2} = 1.273 \frac{I_{O_2}}{I_{^{36}Ar}} \cdot \frac{p_{^{36}Ar} \cdot V}{R \cdot T} = \frac{1.273}{300.3} \frac{I_{O_2}}{I_{^{36}Ar}} \cdot \frac{p_{Ar} \cdot V}{R \cdot T} \tag{B.10}$$

$$n_{CO_2} = 1.152 \frac{I_{CO_2}}{I_{^{36}Ar}} \cdot \frac{p_{^{36}Ar} \cdot V}{R \cdot T} = \frac{1.152}{300.3} \frac{I_{CO_2}}{I_{^{36}Ar}} \cdot \frac{p_{Ar} \cdot V}{R \cdot T} \tag{B.11}$$

As argon constitutes 99-99.9% of the gas, the p_{Ar} is approximated with the total pressure of the analyzed gas.

B.3 Comparing oxygen consumption with electrochemistry

The DEMS measurement can be used in two modes: Pressure mode and DEMS. Figure B.5 shows measurements using the XC72 reference system using both of these modes for comparison. First of all it is noted that they agree well. The pressure measurements does not have information about which gases are evolved, and is thus only applicable when the main gas evolved is oxygen.

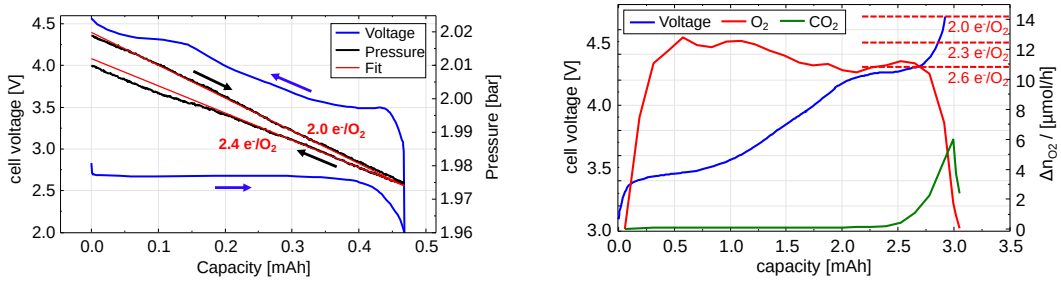

FIGURE B.5: Left: Pressure change in a Li-O_2 battery during discharge and charge. Right: A quantitative analysis of the evolved gases during charge measured by mass spectrometry.

To validate the DEMS setup, a number of measurements have been performed on the reference system for comparison with similar measurements performed by Bryan D. McCloskey et al. at IBM. The measurements are simple charges and discharges like the ones shown in Figure B.5 with current densities of 100-200 mA/g carbon.

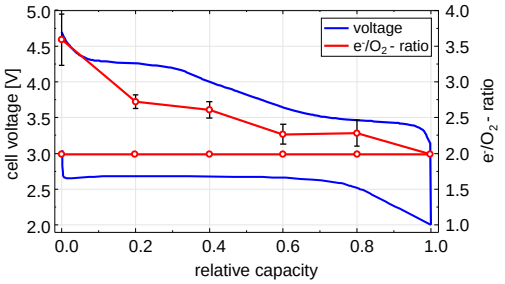

FIGURE B.6: The SOC dependence of the e^-/O_2-ratio. The values are averages of six batteries tested at currents in the range of 100-200 mA/g carbon.

Figure B.6 shows how the e^-/O_2-ratio depends on SoC. The values are averages of six measurements and the error-bars indicate one standard deviation. It is seen that the process is a 2.0 e^-/O_2 process during the entire discharge with very small deviations. During charge, however, the e^-/O_2-ratio increases during the entire charge ending at 3.5 e^-/O_2 at the end of charge. It is also noted that the standard deviation of the e^-/O_2-ratio increases significantly in charge-mode, indicating that the exact electrochemistry may change between measurements depending on small variations in current density

or other parameters. Based on the performed measurements the discharge process is a 1.99 e^-/O_2 with a standard deviation of 0.02 e^-/O_2. The average value during charge is 2.62 e^-/O_2 with a standard deviation of 0.12 e^-/O_2. The OER/ORR ratio is 0.78 with a standard deviation of 0.05. These values are compared with the values reported by McCloskey et al. in [56] in Table B.1, and it is noted that all values are well within one standard deviation.

	OER/ORR	$(e^-/O_2)_{dis}$	$(e^-/O_2)_{cha}$
DTU	0.78 ± 0.05	1.99 ± 0.02	2.62 ± 0.12
IBM, [56]	0.78	2.01	2.59

TABLE B.1: Comparison between DEMS measurements performed at the setup built at DTU and values reported by McCloskey et al. at IBM [56].

Appendix C

Supporting TEM measurements

C.1 Beam damage and observations of lattice fringes in Li_2O_2

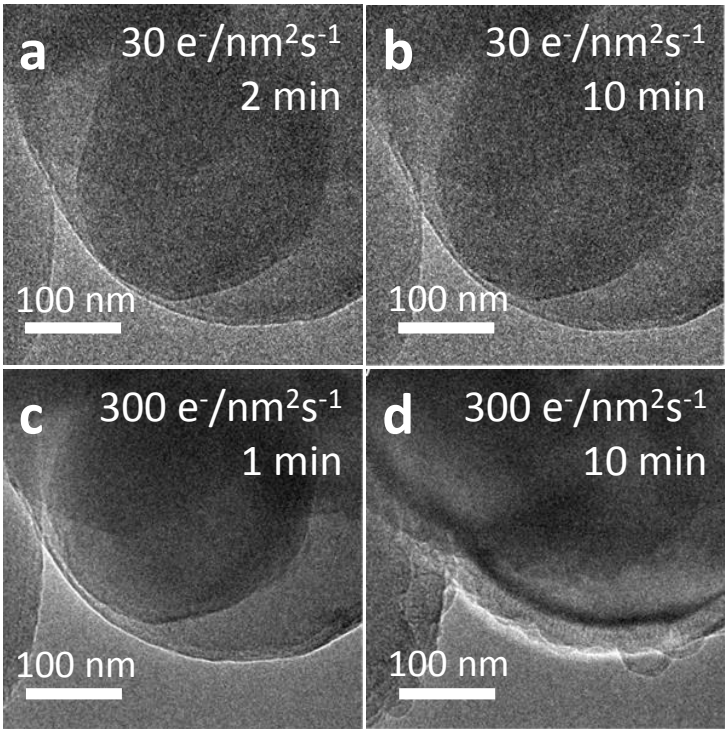

FIGURE C.1: Test of Li_2O_2 beam sensitivity by monitoring visual changes to the particles. The same particle is subjected to (a)-(b) 30 e^-/nm^2s^{-1} in 10 min and then (c)-(d) 300 e^-/nm^2s^{-1} in 10 min. The measurements were performed at Titan microscope operated in TEM-mode at 300kV.

A Li_2O_2 particle subjected to increasing exposure time and dose rate is shown in Figure C.1. It is seen that the particle can be imaged and spectroscopically inspected by TEM-EELS for at least 10 minutes without any visible damage at 300keV using a low electron dose rate of 30 e^-/nm^2s^{-1}. A ten times higher electron dose rate of 300 e^-/nm^2s^{-1}, results in morphological changes. This is on the same order of magnitude as recently reported by Zhong et al. [47] (20 e^-/nm^2s^{-1} at 200 keV) to study Li_2O_2 precipitates.

C.2 Selected area electron diffraction

The cathode used the most in the experiments described in this thesis contains XC72 carbon black and PTFE binder, and, if discharged, it also contains Li_2O_2. As lithium is a very light element, it is important to find a suited strategy to distinguish this from the rest of the cathode. Selected area electron diffraction (SAED) and electron energy loss spectroscopy (EELS) are measured on reference systems to identify the best suited method. The morphology is also useful for quick identification, but it cannot stand

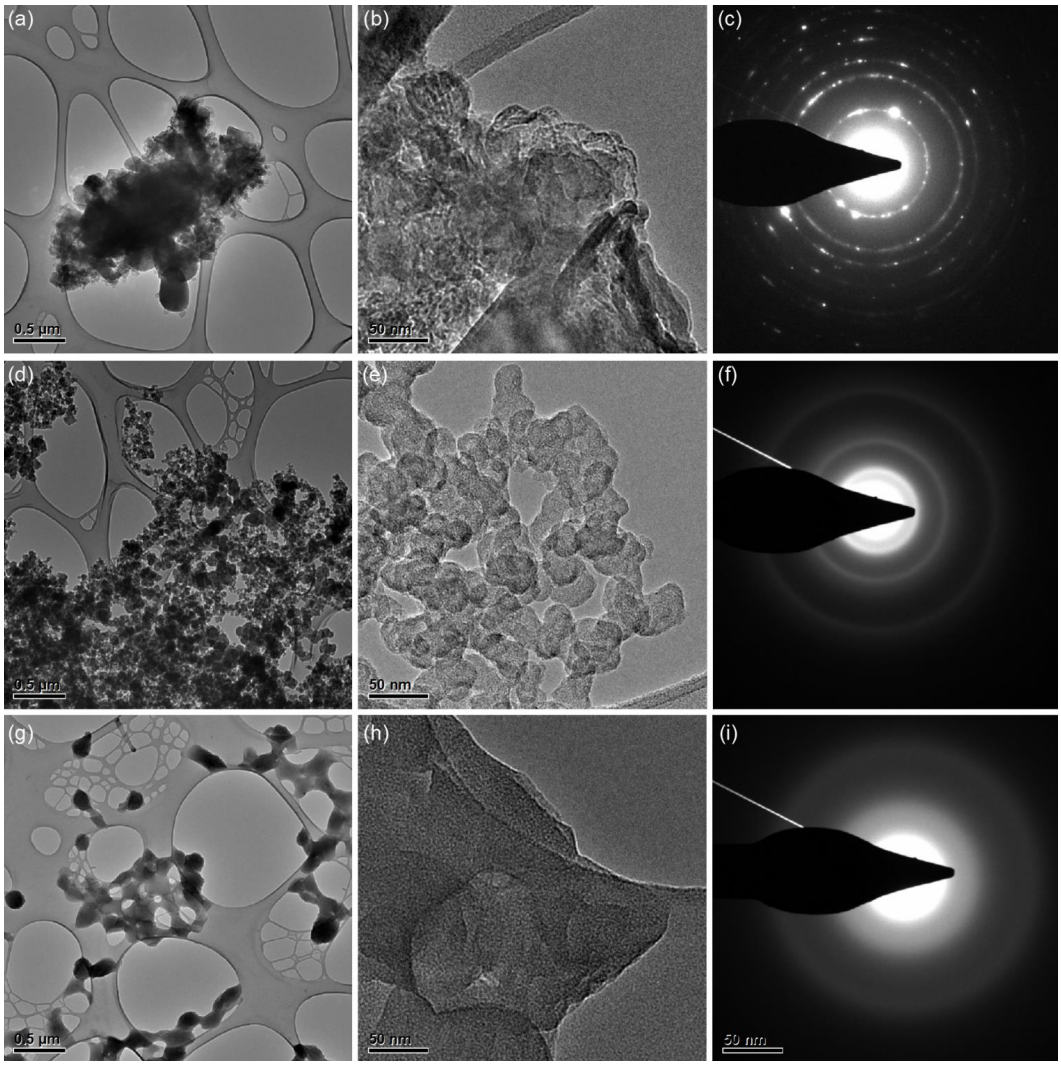

FIGURE C.2: TEM images at two magnifications and selected area diffraction patterns of (a,b,c) Li_2O_2, (d,e,f) XC72 carbon black, and (g,h,i) PTFE binder. The measurement time on Li_2O_2 was kept below 10 min with a doserate of 140 e^-/nm^2s^{-1} to avoid visual structural and crystalline changes. The measurements were performed at CM200 (Haldor Topsøe A/S) in the HR-TEM mode. The beam damage is investigated further in Figure C.1.

alone. The aim of the reference measurements is to test the TEM-EELS technique to study Li_2O_2 precipitates on the nm-scale, i.e. species that may be formed during the discharging of Li-air batteries. In particular, the beam stability of Li_2O_2 material is addressed, and low-loss EELS is used to spectroscopically identify lithium species. The possibilities of imaging crystalline Li_2O_2 at high-resolution, i.e. imaging of lattice fringes and eventually sub-nm surface layers are estimated from a theoretical/practical point of view.

Figure C.2 shows TEM images in two magnifications and SAED patterns for Li_2O_2, carbon XC72 and PTFE binder. The compounds were dispersed on a standard Cu TEM-grid with lacey C-film. The XC72 was ultrasonicated in ethanol for 1 min and

dispersed in ambient conditions, the PTFE was dispersed using an air-brush using the same procedure as cathode fabrication, but without adding carbon to the dispersion, and the Li_2O_2 was crushed and dispersed dry and transferred to the CM200 microscope. The Li_2O_2 was exposed to ambient conditions for less than 2 min.

The samples were examined in CM200 in the HR-TEM mode at different magnification. Approximately 20 agglomerates from each sample were viewed and 5 of the agglomerates were recorded at low magnification (for overview) and two agglomerates were further inspected at higher magnification and by SAED. Electron diffraction patterns were recorded with a fixed camera length of 330 mm, i.e. the same magnification. Figure C.2shows TEM and SAED images of the three samples. The SAED patterns show that PTFE and XC72 are amorphous, whereas the Li_2O_2 particle is polycrystalline.

C.3 Electron energy loss spectroscopy

EELS measurements were performed on commercial Li_2O_2 in the Titan microscope operated in TEM-mode at 300kV at a nominal TEM magnification of SA 6,300x. In addition, a post-magnification was introduced by the GIF (about x15). The length scale of the images is not calibrated, but the image size is estimated. The zero loss peak for the EELS was continuously adjusted to allow an energy resolution of 1.2-1.4 eV measured as the FWHM of the zero loss peak. All EELS data were recorded with a dispersion of 0.2eV/channel and a selected entrance aperture (SEA) of 2 mm inserted. The incident beam dose rate on the sample was measured on the retractable current-readout-stick (viewing stick) inserted in the electron beam. Electron beam dose rates of 30-300 e^-/nm^2s^{-1} were used. Imaging was done prior to and after each EELS acquisition to record eventual visual changes of the sample during EELS acquisition. Also images with and without the selected entrance aperture inserted were recorded to identify the localized sample area giving rise to the EELS signals.

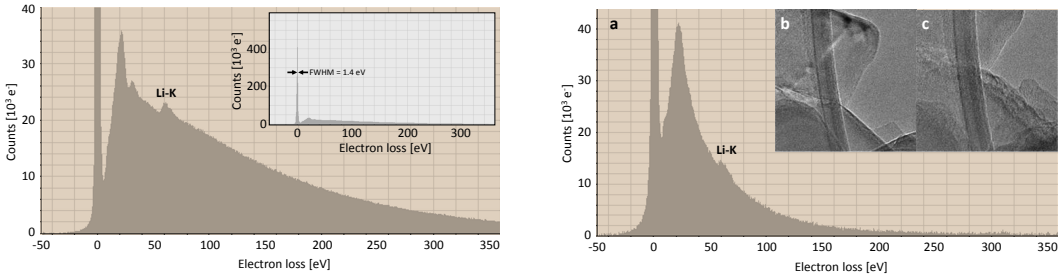

FIGURE C.3: Low-loss TEM-EELS spectrum of commercial Li_2O_2 in an area (a) without lacey-C film and (b) with lacey-C film recorded at a dose rate of 300 e^-/nm^2s^{-1}. The spectra show clear signature of the lithium K-edge (Li-K, near 55eV). A visual damage was observed on the particle at this dose rate. Image size is about 420 nm x 420 nm.

Figure C.3 shows the EELS signal from as-prepared Li_2O_2 sample. The spectrum demonstrates distinctive EELS signatures of lithium such as Li K edge near 55eV in the low loss region, which are not present in EELS from the carbon and/or oxygen, shown in Figure C.4. This verifies the presence of Li. Figure C.3b shows the EELS signal from an area of both carbon-film and lithium-sample. The determination of the crystal phase (e.g. Li_2O_2, Li_2O, or LiO_2) cannot be readily deduced from the present EELS data and complementary techniques such as SAED should be used.

In conclusion, Li_2O_2 precipitates can be imaged and spectroscopically inspected by TEM-EELS for at least 10 minutes without any visible damage at 300keV using a low electron dose rate of 30 e^-/nm^2s^{-1}. A ten times higher electron dose (rate) of 300 e^-/nm^2s^{-1}, results in clearly visually damaged/changed particles during acquisitions. Li and C can readily be identified by EELS on the nm-scale, although a drift stable EELS setup is required due to the weak signals. The oxygen EELS signal was not addressed in this study. Atomic resolution imaging of Li_2O_2 without damaging the structure by the electron beam is lofty as extremely long acquisition times of about 18 minutes are needed (as compared to 1s for typical high resolution imaging).

C.3.1 EELS reference spectra

Figure C.4a shows the electron energy loss spectra (EELS) of the low loss and core loss energy windows for lithium, carbon, and oxygen. For the present study, only the energy losses of 0-300eV were recorded to reveal the zero-loss peak (to determine the energy resolution), the low loss features (plasmonic region, ca. 10-50eV) and core loss of Li-K (55 eV) and C-K (onset at 284eV).

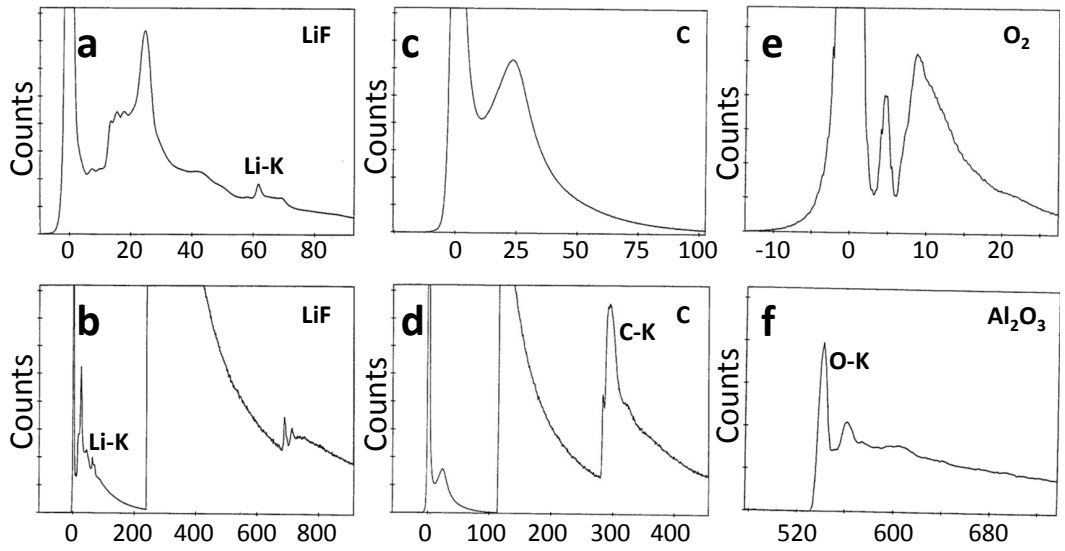

FIGURE C.4: References of electron energy loss spectra. From the EELS atlas.

Appendix D

Calculations used to assess the air purification system of an open Li-O_2 system

D.1 Design frame

To assess the viability of an open system based on known technology, a specific calculation on dimensions and weight of such a system is performed in this section. The key numbers are presented in this section. The design criteria of the filter are

- Energy: 100 kWh
- Discharge potential: 2.65 V
- Minimum discharge time: 3h
- Required purity: <1 ppm H_2O and <1 ppm CO_2

Using these numbers, the total consumption of oxygen in a full discharge is calculated

$$n_{O_2} = \frac{n_{e^-}}{2} = \frac{Q}{2F} = \frac{E}{2UF} = \frac{100 \text{ kWh}}{2 \cdot 2.65 \text{ V} \cdot 96.5 \text{ kC/mole}} = 704 \text{ mole} \tag{D.1}$$

At standard conditions, this correspond to a volume of

$$V_{O_2} = \frac{n_{O_2} RT}{p_{O_2}} = \frac{704 \text{ mole} \cdot 8.314 \text{ J/mole/K} \cdot 298 \text{ K}}{1 \text{ bar}} = 17 \text{ m}^3 \tag{D.2}$$

With 20.9 % oxygen in the air, this corresponds to 82 m^3 air with up to 1.82 kg H_2O (3 %) and 59 g CO_2 (400 ppm).

As discussed in Section 6.2.2, it is reasonable to assume that compression of the gas is needed. If the air is compressed to 3 bar, this corresponds to a decrease in dew point from 25 °C to 7.9 °C or a change in maximum water content from 1.82 kg to 650 g, using the equation of the dew point defined by Buck [120]

$$p_{H_2O} = (1.0007 + 3.46 \cdot 10^{-6} \cdot p_{\text{total}}) \cdot 6.1121 \cdot \exp\left(\frac{17.502 \cdot T}{240.97 + T}\right) \tag{D.3}$$

where p_{H_2O} and p_{total} is the water and total pressure in millibar, and T is the temperature in degrees Celsius.

The best zeolite absorbents reach an absorption capacity of 30% [121], which means that 6.1 kg zeolite could absorb the water from a full discharge, but as it will cost a lot of energy to release the water again, a pre-drying step is added. By using a water permeable Nafion membrane like the Permapure Drier in a counter flow setup with the dry gas from the battery, the energy consumption of the system can be reduced significantly.

D.2 Pre-drying using a membrane system

The relative dimensioning between zeolites and the passive pre-drying unit depends on the need for energy savings. If energy is not a concern, the amount of adsorbents should be increased, whereas the pre-drying unit is better, if energy savings on the regeneration is important. This calculation is based on a Permapure 24" PD-200T, Ø1". Using a maximum discharge time of 3 h, 82 m^3 air corresponds to 460 l/min, and with a maximum flow rate in the Permapure tubes of 40 l/min, 12 pipes are needed. Using the dimensions of the pipes, they can be fiited into a box of 66 cm x 12 cm x 8 cm. The pressure drop can be calculated to be 0.1 bar and the output concentration od H_2O is calculated to be 1550 ppm. As the Permapure dryer is also permeable to CO_2, this concentration is assumed to be halved to 200 ppm.

D.3 Designing the adsorption system

The typical design of an absorption system is a plug-flow reactor. Two considerations are important when designing such a system: capacity and kinetics. The capacity should be sufficient to store all impurities in the inlet gas until regeneration and the kinetics should be fast enough such that impurities are not able to slip through the reactor without being absorbed.

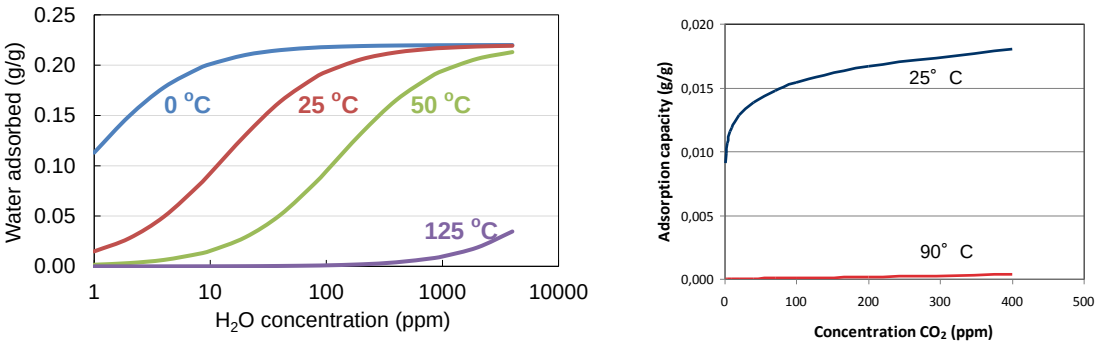

FIGURE D.1: Langmuir isotherm for H_2O adsorption in zeolites and CO_2 adsorption in a solid amine.

The capacity is typically calculated using the Langmuir isotherm, that describes the ability of the material to adsorb a given molecule as a function of pressure and temperature. It is defined as

$$\theta_a = \frac{K p_\mathrm{a}}{K p_\mathrm{a} + 1} \tag{D.4}$$

where θ_a is the fractional occupancy of the adsorption sites, p_a is the partial pressure of the impurity 'a' and K is the equilibrium constant given by $K = k \exp(-\Delta G^{\ominus}/(RT)) =$

$k\exp(-(\Delta H - T\Delta S)/(RT))$. In addition to describing the capacity, the Langmuir isotherm is important to define how easy it is to regenerate the adsorbent by heating. Figure D.1 shows the Langmuir isotherm for a proposed adsorbent for H_2O and one for CO_2. The important thing to note is that the storage capacity of both materials are high at room temperature and decreases significant at 125 °C for the H_2O adsorbent and at 90 °C for the CO_2 adsorbent. This means that heating the adsorbent 100 °C, will release almost all of the adsorbed H_2O and CO_2 molecules.

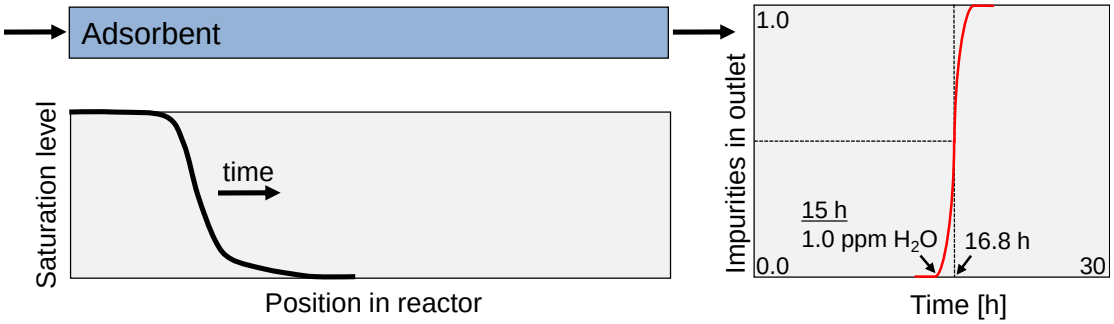

FIGURE D.2: Schematic illustration of a plug flow reactor with an adsorbent. The graph below show the change in impurity concentrations in the adsorbents during operation and the graph to the right is adapted from [122] and show the H_2O concentration in the output stream of a H_2O adsorption reactor as a function of time. The steep transition of ¡1 ppm level to no adsorption, show that the kinetics are very fast.

The kinetics Figure D.2 shows an actual measurement of the water adsorption. The plug flow reactor and saturation profile is sketched in the left part of the figure. As an increasing amount of impurities are adsorbed, the saturation profile moves to the right. When the profile approaches the outlet of the reactor, it is no longer possible to adsorb all molecules. Figure D.2 (right) shows the impurities in the outlet during operation using the zeolite considered as H_2O adsorbent. It is seen that the concentration is below 1 ppm until a total test time of 15 h, and as the full capacity corresponds to 16.8 h, an excess capacity of 12 % is needed to ensure sufficient adsorption.

Calculating the system size Based on the fast kinetics and a capacity of 0.1-0.2 g/g and fast kinetics, an excess capacity of 30 % is chosen with an average capacity utilization of 0.15 g/g. To remove 1550 ppm H_2O and 200 ppm CO_2 from 82 m^3 of air, corresponding to 94 g H_2O and 30 g CO_2, a total of 815 g H_2O adsorbent and 260 g CO_2 adsorbent are needed.

D.4 Energy consumption and weight

Pressure drop The pressure drop in the in the Permapure dryer is 0.2 bar (0.1 bar entering the battery and 0.1 bar exiting the battery. The pressure drop in the plug flow reactors are assumed to be 0.1 bar. A total pressure drop of 0.3 bar in a 82 m^3 of gas corresponds to 2.5 MJ or 0.7 kWh, which is 0.7 % of the total battery capacity.

Heating during regeneration A reasonable measure of the energy required to heat the adsorbents 100 °C is to compare the system with sand. If the system weight is 20 kg, the energy required is approximately 2 MJ. The desorption of H_2O and CO_2 further needs 2.5 MJ and including heating of the gasses and other losses, the energy requirements may be somewhat bigger than during discharge. 4 kWh (or 4 % of the battery capacity) is used to be on the safe side, and it is noted that the exact value is not as important during charge, because the car is connected to the grid.

Weight of the system The permapure dryers can fit into a 6.6 L box which means that the weight is probably 10-15 kg. The active materials in the adsorption system weigh a little more than 1 kg and it is safe to assume that the entire system with heaters do not exceed a weight of 10 kg. The total weight of the system will therefore be 20-30 kg.

List of publications

Paper I

An electrochemical impedance spectroscopy investigation of the overpotentials in Li-O_2 batteries

Jonathan Højberg, Bryan D. McCloskey, Johan Hjelm, Tejs Vegge, Keld Johansen, Poul Norby and Alan C. Luntz

ACS Appl. Mater. Interfaces, 7, 4039–4047 (2015)

Paper II

Reactions and SEI formation during charging of Li-O_2 cells

Jonathan Højberg, Kristian B. Knudsen, Johan Hjelm and Tejs Vegge

ECS Electrochem. Lett., 4, A63–A66 (2015)

Paper III

Impedance-based battery management for metal-O_2 systems

Andreas E. Christensen, Jonathan Højberg, Poul Norby and Tejs Vegge

J. Pow. Sources. *Submitted* (2015)

Paper IV

Rechargeability of ionic liquids in Li-O_2 batteries

Supti Das, Jonathan Højberg, Kristian B. Knudsen, Poul Norby and Tejs Vegge

To be submitted

Paper V

The influence of CO_2 poisoning on overvoltages and discharge capacity in non-aqueous Li-air batteries

Yedilfana S. Mekonnen, Kristian B. Knudsen, Jon S. G. Mýrdal, Reza Younesi, Jonathan Højberg, Johan Hjelm, Poul Norby and Tejs Vegge

J. Chem. Phys., 140 (2014)

ACS APPLIED MATERIALS & INTERFACES

Research Article

www.acsami.org

An Electrochemical Impedance Spectroscopy Investigation of the Overpotentials in Li–O_2 Batteries

Jonathan Højberg,*[,†,‡,§] Bryan D. McCloskey,[†,⊥] Johan Hjelm,[‡] Tejs Vegge,[‡] Keld Johansen,[§] Poul Norby,[‡] and Alan C. Luntz[†,∥]

[†]IBM Almaden Research Center, San Jose, California 95120, United States

[‡]DTU Energy, Frederiksborgvej 399, DK-4000 Roskilde, Denmark

[§]Haldor Topsøe A/S, Nymøllevej 55, DK-2800 Kgs. Lyngby, Denmark

[∥]SUNCAT, SLAC National Accelerator Laboratory, Menlo Park, California 94025, United States

Supporting Information

ABSTRACT: Lithium–O_2 (Li–O_2) batteries are currently limited by a large charge overpotential at practically relevant current densities, and the origin of this overpotential has been heavily debated in the literature. This paper presents a series of electrochemical impedance measurements suggesting that the increase in charge potential is not caused by an increase in the internal resistance. It is proposed that the potential shift is instead dictated by a mixed potential of parasitic reactions and Li_2O_2 oxidation. The measurements also confirm that the rapid potential loss near the end of discharge ("sudden death") is explained by an increase in the charge transport resistance. The findings confirm that our theory and conclusions in ref 1, based on experiments on smooth small-area glassy carbon cathodes, are equally valid in real Li–O_2 batteries with porous cathodes. The parameter variations performed in this paper are used to develop the understanding of the electrochemical impedance, which will be important for further improvement of the Li–air battery.

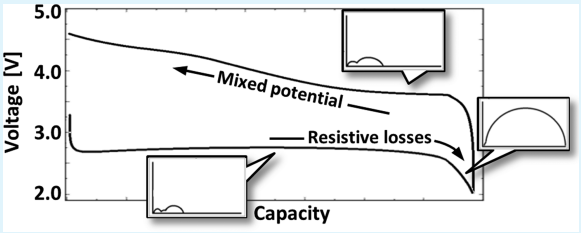

KEYWORDS: *Li–O_2 batteries, electrochemical impedance spectroscopy, overpotential, mixed potential, battery performance*

1. INTRODUCTION

Lithium–air and Li–O_2 batteries have attracted much attention in recent years because of a potentially high specific energy density and low cost. Furthermore, the fundamental electrochemistry has very low reaction barriers, which, in principle, enables a high cycle efficiency. The low reaction barriers have been predicted by Hummelshøj et al.[2,3] using density functional theory (DFT) and proven recently by Viswanathan et al.[4] using experiments on flat glassy carbon cathodes in an electrolysis cell.

However, more realistic batteries with porous electrodes show large overpotentials,[5] which significantly reduces the cycle efficiency. Understanding this is crucial to develop a commercially viable Li–O_2 technology. The origin of the overpotential has been investigated intensively. We have previously used DFT modeling,[2,4] differential electrochemical mass spectrometry (DEMS), and Li_2O_2 titration.[5] In addition to this, and among others, Zhong et al. used in situ transmission electron microscopy (TEM) to study growth mechanisms,[6] and Chen et al. used a redox-mediator to investigate limitations in the electronic conductivity.[7]

In this study, we use electrochemical impedance spectroscopy (EIS) that is often used as a diagnostic tool to identify the underlying mechanisms of the polarization curves in electrochemical systems such as lithium-ion batteries and fuel cells, as it is a powerful tool to obtain noninvasive in situ information on degradation mechanisms and possible bottlenecks in the electrochemical reactions. Very recently, Adams et al. and Landa-Medrano et al. have also used EIS to measure the internal resistances of a Li–O_2 battery using a two-electrode configuration.[8,9] They varied parameters like cathode morphology, oxygen partial pressure, salt concentration, and state-of-charge (SOC), and they succeed in assigning the different impedance contributions to the processes of either the anode or the cathode. The batteries investigated were, however, not characterized by DEMS and Li_2O_2 titration, which are important complementary methods necessary to link EIS results to the fundamental electrochemistry.

In this work, we used an intensely studied and well-characterized in-house reference system used in a number of previous publications.[5,10−15] It consists of an XC-72 carbon black and poly(tetrafluoroethylene) (PTFE) binder cathode, lithium metal anode, and 1 M LiTFSI/1,2-dimethoxyethane electrolyte. A series of electrochemical impedance spectra was measured at different state-of-discharge (SOD), SOC, and at different current densities with a focus on three states of the

Received: November 6, 2014
Accepted: January 27, 2015
Published: January 27, 2015

DOI: 10.1021/am5083254
ACS Appl. Mater. Interfaces 2015, 7, 4039−4047

ACS Applied Materials & Interfaces Research Article

Li−O_2 battery electrochemistry: the discharge plateau, sudden death at the end of discharge, and the initial stage of the charging process.

By combining the measurements with previous results presented by McCloskey and Luntz et al.,[1,4,5] the EIS measurements are related to the measured potential.

We show that the overpotential during discharge is caused by internal resistance and is dominated by the charge transport through the deposited Li_2O_2 at the end of discharge. During charge, however, the potential increase reflects a mixed potential of parasitic reactions and Li_2O_2 oxidation.

2. EXPERIMENTAL SECTION

Most of the experimental setup and procedures have been described in detail previously in ref 11 and are only briefly described here. The cathodes were prepared by air-spraying a carbon/PTFE dispersion onto a 316SS 100 mesh (TWP, Inc., Berkeley, CA). The slurries were prepared by sonicating a carbon black powder (Vulcan XC72, www.fuelcellstore.com) and PTFE (60 wt % dispersion in water, Sigma-Aldrich) in a 3:1 wt/wt ratio in a 20:80 isopropanol/water mixture. A Badger model 350 air sprayer was used to uniformly coat the SS mesh (the SS mesh was rinsed in acetone several times prior to cathode preparation). Prior to cutting 12 mm diameter cathodes from the carbon-coated SS mesh, the mesh was allowed to air-dry for 1 h. All cathodes were dried in vacuum at 120 °C for at least 12 h, washed in pure 1,2-dimethoxyethane (DME) in a glovebox, followed by a second drying under vacuum for 10 min, and then at 200 °C in the glovebox for at least 1 h. A typical carbon loading was two milligrams per cathode.

All solvents and salts in this study were purchased from Novolyte (Purolyte electrolyte grade), stored in an argon glovebox (0.1 ppm of O_2 and H_2O) and used without further purification. The H_2O content of solvents was periodically checked with a Karl Fischer titrator (Metrohm Inc.) and found to be no more than 20 ppm. The measurements were made with an 11 mm diameter lithium metal anode, a 12.5 mm diameter Celgard 2500 separator, a 12 mm diameter cathode, and 60 μL of 1 M bis(trifluoromethane)sulfonimide lithium salt (LiTFSI) dissolved in DME.

The test cell used in this study is shown in Figure S1 in the Supporting Information. The cell components were stacked between SS alloy 20 anode and cathode tips that were hermetically sealed against a quartz tube using compressed Markez O-rings (Marco Rubber). Capillaries were silver soldered into the cathode tip to allow gases to be fed to and swept away from the cell. Gases swept away from the cell could be quantitatively identified using the DEMS setup described in detail in ref 10.

2.1. Electrochemical Impedance Spectroscopy. All electrochemical measurements were made with a BioLogic VMP3 potentiostat. Electrochemical impedance spectra were measured while a current was drawn (GEIS) to investigate the processes under relevant conditions as discussed previously by Adams et al.[8] Impedance was measured at currents between 15 μA (13 μA/cm^2) and 1 mA (0.88 mA/cm^2). Frequencies between 4 mHz and 100 kHz were investigated with 15 points per decade and an alternating current (AC) amplitude of 10% of the direct current (DC) level. This typically gave an AC potential response amplitude of 2−5 mV, which was found to be within the linear regime, while still ensuring a sufficient signal-to-noise ratio.

To distinguish impedance contributions from the anode and the cathode in a two-electrode cell, it is often necessary to vary physical parameters that will affect the two electrodes differently. We used three methods: (i) measuring impedance at open-circuit voltage (OCV) in argon atmosphere to prevent the oxygen reduction/oxidation, (ii) using a symmetrical cell of two predischarged cathodes, and (iii) testing a different cathode (see Figure 4 below and Figures S2 and S3 in the Supporting Information). In the symmetrical cell, the anode/cathode reactions are oxidation/reduction of Li_2O_2, which remove any lithium metal-related contributions from the EIS measurement. Both cathodes in the symmetrical cell initially discharged 0.25 mAh in separate cells before they were combined in a new cell. The cathodes were rinsed with DME after the individual discharge to remove the electrolyte salt before the cathodes were used in the symmetrical cell. The symmetrical cell was tested in O_2 gas and was made without exposing the cathodes to air at any point.

2.2. Modeling Li−O_2 Impedance. The impedance is defined as the derivative of the *iv* curve:

$$Z(i) = \frac{\partial v}{\partial i} = \frac{\partial \eta}{\partial i} \tag{1}$$

where v is the potential, i is the current density, and η is the overpotential. Therefore, the impedance is linked closely to the Tafel plot, which has previously been used to describe reaction mechanisms in Li−O_2 batteries.[4,10,16,17] From the Tafel equation, the overpotential is seen to be proportional to $\log(i)$ at large overpotentials ($|\eta| \gg RT/nF$), but as our batteries contain a porous cathode, this ideal behavior is not applicable. The consequences of a porous electrode have been investigated by Lasia and show that the Tafel slope will increase at higher currents.[18] This is in line with our measurements as well as previous Li−O_2 battery measurements by Viswanathan et al. and Adams et al. on porous electrodes.[4,8] To describe the measurements better

$$\eta = |v - \mathrm{OCV}| = c_1 \cdot i^{c_2} \tag{2}$$

is applied as an empirical model, when eq 1 is used to compare the measured impedance with the overpotential. OCV is the open circuit potential, and c_1 and c_2 are constants. As c_2 is found to be less than 1 in Section 3.4, $Z(i)$ is expected to be larger at small currents according to eq 1.

The measured impedance response can, to a first approximation, be described using an equivalent circuit model consisting of three Voigt elements (parallel connected resistor with a constant phase element (CPE)) connected in series, see Figure S4a in the Supporting Information. The impedance of the Voigt elements is adopted from Hirschorn et al.,[19] and the total impedance, $Z(\omega)$, is thus given by

$$Z(\omega) = R_s + \sum_{i=1,2,3} \frac{R_i}{1 + (j\omega)^{n_i} Q_i R_i} \tag{3}$$

where ω is the angular frequency, and R_i, Q_i, and n_i are parameters in Voigt element i. Even though the model is not anchored in an electrochemical model, it is likely that key physical processes like charge transfer reactions, diffusion, and electronic transport through the Li_2O_2 layer will dominate one or more of the observed features in the spectra. Therefore, parametrization using the simplified model makes it possible to determine the magnitude of these processes, although each feature may contain contributions from multiple physical

DOI: 10.1021/am5083254
ACS Appl. Mater. Interfaces 2015, 7, 4039−4047

ACS Applied Materials & Interfaces Research Article

processes, and anode and cathode processes may overlap to some extent. The sum of the frequency-dependent resistances R_1, R_2, and R_3 is the polarization resistance, R_p. The equivalent circuit fits are made using the scipy optimizer fmin_slsqp using the software package RAVDAV 0.9.7.[20]

The Voigt elements have three parameters: R, Q, and n. R is the DC resistance, and Q and n are parameters of the CPE. If n = 1, the CPE is a capacitor, and even if n is between 0.7 and 1, a pseudocapacitance, C^*, can be calculated. This criterion is met in all measurements presented in this work, except for the very end of the 20 μA discharge presented in Figure 3. As discussed in detail by Jamnik et al.,[21] this capacitance is typically a double-layer capacitance related to the process, and by comparing with reference values, it is possible to estimate the surface area contributing to the process. This can be used to distinguish reactions at the flat lithium anode from reactions in the porous cathode, since the surface areas of these are ~1 cm^2 and 1 m^2, respectively. The capacitance at the lithium metal surface in an organic electrolyte is typically 10−20 $\mu F/cm^2$ as reported by Aurbach et al.,[22,23] and the capacitance of XC72 is 12.6 F/g in an organic aprotic electrolyte as reported by Barbieri et al.[24] From this, it is calculated that the capacitances should be in the range of 10 μF and 25 mF for the anode and cathode, respectively. These values should then be compared with the pseudocapacitance, calculated from the equivalent circuit parameters according to Hirschorn et al.[19]

$$C^* = Q^{1/n}\left(\frac{R_\Omega R}{R_\Omega + R}\right)^{(1-n)/n} \quad (4)$$

where R, Q, and n are fitting parameters from the Voigt elements, and R_Ω is the DC resistance at the investigated frequency. As discussed by Zoltowski et al., the pseudocapacitance of a CPE element is not well-defined,[25] which means that the surface area obtained using C^* might vary slightly from the actual surface area, but the order of magnitude and relative changes are still valid.

The capacitance is expected to change during discharge as the dielectric Li_2O_2 is deposited. The relative permittivity ε_r of Li_2O_2 has been measured to be 30−35 by Gerbig et al. and Dunst et al.[26,27] Using a value of 30 to calculate the capacitance of the Li_2O_2 layer in series with a typical electrode−electrolyte capacitance of 20 mF, a Li_2O_2 layer of 8 nm will halve the cathode capacitance. A similar calculation can be made for the Li_2CO_3 interface layer between the cathode and the Li_2O_2. Using the relative permittivity of Li_2CO_3 of 4.9 measured by Young et al.,[28] the capacitance will be halved with a layer thickness of 1 nm.

The role of oxygen diffusion in the electrolyte has been discussed in several papers.[29−31] To evaluate the significance of diffusion, the Damköhler number, Da, can be used as a quick comparison between the oxygen consumption/evolution with the diffusion rate.[29] Using typical values for our system, Da is 0.3 at a current of 250 μA, which means that the diffusion rate is ~3 times higher than the consumption rate. Oxygen diffusion is therefore not expected to be dominating, but it will have some significance.

Basic requirements for carrying out EIS measurements are that the system is stable, causal, and linear. Among other things, this implies that no (or only a negligible) change in voltage and impedance characteristics is allowed during the measurement period. Methods have been proposed to deal with impedance measurements in nonstationary systems such as a PEM fuel cell with hindered water removal during operation.[32] This approach, however, requires interpolation, which is difficult to apply in this case with a dramatically decreasing cell voltage toward the end of discharge of the battery. Without use of such methods, one can reduce drift problems by decreasing the measurement time or decreasing the change of the system. To do this, we optimized the frequency range and compared impedance spectra from stable low-current measurements (18 $\mu A/cm^2$ cathode) with impedance spectra from measurements at less stable but more realistic current densities (>0.2 mA/cm^2 cathode).

The Kramers−Kronig relation was used to evaluate the causality of all measurements. The largest deviations occur at low frequencies as the electrochemistry changes during the measurement. To minimize this effect, a frequency cutoff level of 5% deviation of the Kramer−Kronig transform was used.

3. RESULTS

All measurements were performed using a system with an XC72 carbon black cathode, DME/LiTFSI electrolyte, and lithium anode. This system has been characterized extensively in previous publications from 2011 to 2013 by McCloskey et al.[5,10−15] The most important methods used in these studies are differential electrochemical mass spectrometry (DEMS), peroxide titration, and X-ray diffraction.

In this work, we used DEMS to quantify gas consumption and release during discharge and charge at all investigated current densities to verify that the measured impedance can be related to previous work. A ratio of 2.0 e^-/O_2 was observed during discharge at all investigated currents between 10 μA (8.8 $\mu A/cm^2$) and 5 mA (4.4 mA/cm^2). During charge, the amount of oxygen released corresponded to 2.5 e^-/O_2 until a potential of 3.7 V. Above this potential, the ratio changed to 3 e^-/O_2. CO_2 was evolved at potentials above 4.2 V.

The OCV was measured as a function of discharge and charge to ensure an accurate determination of the overpotential. A full discharge−charge cycle at 250 μA (220 $\mu A/cm^2$) is seen in Figure 1. The battery was allowed to relax to

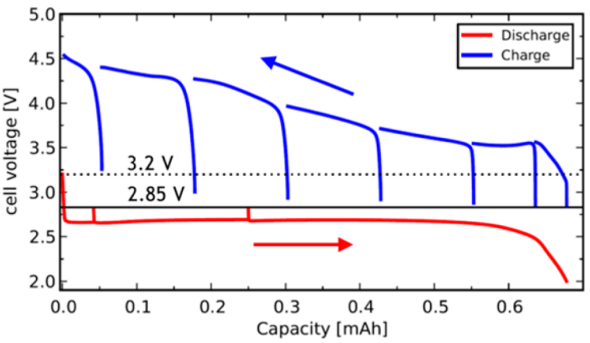

Figure 1. Measurement of OCV through a 250 μA (220 $\mu A/cm2$) discharge and charge. The steep voltage transients occur when the battery is allowed to relax at OCV.

OCV by interruption of the current a number of times during both discharge and charge, which is seen as steep voltage transients in Figure 1. The relaxation criteria were a change in cell voltage of less than 1 mV/h or a relaxation time of 15 h. The initial OCV was 3.2 V. The OCV decreased to 2.85 V after a short period of discharge and stayed at this value during the entire discharge—also after reaching the 2.0 V cutoff at sudden

DOI: 10.1021/am5083254
ACS Appl. Mater. Interfaces 2015, 7, 4039−4047

ACS Applied Materials & Interfaces Research Article

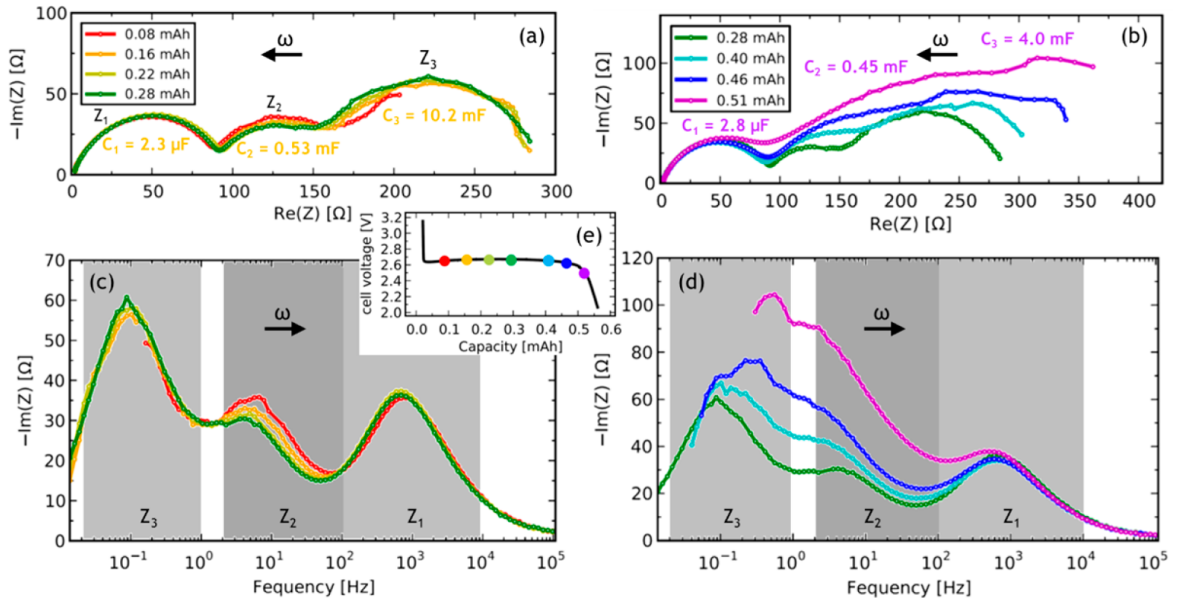

Figure 2. Nyquist plot (a) and (b) and Bode-like plot (c) and (d) of impedance measurements during a 250 μA (220 μA/cm2) constant current discharge. The approximate SODs are shown in (e) and in the legends of (a) and (b). Three processes are identified and named Z_1, Z_2, and Z_3, and the corresponding peak frequencies are within the gray intervals marked in (c) and (d) at all current densities and SODs investigated.

Table 1. Peak Frequencies, Resistances, and Pseudocapacitances from Selected Impedance Fit[a]

	f_1 [Hz]	f_2 [Hz]	f_3 [Hz]	R_1 [Ω]	R_2 [Ω]	R_3 [Ω]	C_1^* [mF]	C_2^* [mF]	C_3^* [mF]
				discharge at 250 μA					
0.16 mAh	733	5.4	93×10^{-3}	96	56	145	2.3×10^{-3}	0.53	10.2
0.51 mAh	605	3.4	184×10^{-3}	94	92	188	2.8×10^{-3}	0.45	4.0
				discharge at 20 μA					
0.5 mAh	470	1.15	5.5×10^{-3}	109	50	1007	3.1×10^{-3}	2.8	19.3
1.9 mAh	464	1.12	9.9×10^{-3}	107	158	2131	3.2×10^{-3}	0.6	2.0
2.3 mAh	479		1.1×10^{-3}	114		14 097	2.9×10^{-3}		0.8
				charge at 250 μA					
0.03 mAh	678	9.6	267×10^{-3}	65	166	497	3.6×10^{-3}	76×10^{-3}	1.0
0.42 mAh	983	14.0	19×10^{-3}	255	105	700	0.6×10^{-3}	99×10^{-3}	9.0

[a]The expected capacitances for the full anode and cathode are 10 μF and 25 mF, respectively. Typical values of n are $n_1 = 0.77$, $n_2 = 0.86$, and $n_3 = 0.78$.

death. During charge, the OCV was 2.85 V, but it increased slightly toward the end of charge where it reached 3.2 V.

3.1. Discharge to Sudden Death at 250 μA. EIS measurements from the first discharge at 250 μA (220 μ/cm^2) are shown in Figure 2a–d. The spectra were measured while drawing a current, which means that the SODs shown in Figure 2 and Table 1 are approximate values. Three arcs are distinguished in the Nyquist plot in Figure 2a. They were almost constant in the first part of the discharge but changed as the potential decreased near the end of discharge. The three identified impedance contributions are labeled Z_1, Z_2, and Z_3, and, on the basis of a fit to the equivalent circuit given in eq 3 and shown in Figure S4a in the Supporting Information, the corresponding peak frequencies, resistances, and pseudocapacitances are calculated. The values from two of these calculations are given in Table 1.

It is seen that R_1 is constant through the discharge, whereas R_2 and R_3 increase and C_3^* decreases. The decrease of C_3^* and increase of R_3 through the discharge could be a blocking of the cathode surface. The magnitudes of the pseudocapacitances indicate that Z_1 originates from an anode process, and Z_2 and Z_3 originate from cathode processes. The cathode blocking and identification of reaction processes in the impedance spectra are discussed further in Section 4.1.

The peak frequencies changed between different current densities and close to sudden death. In all of our measurements, however, f_1 was between 100 Hz and 10 kHz, f_2 was between 2 and 100 Hz, and f_3 was between 20 mHz and 1 Hz. These intervals are shown in Figure 2c,d, and the clear separation helps in identifying the different impedance contributions.

3.2. Discharge to Sudden Death at 20 μA. We decreased the discharge current to 20 μA (18 μA/cm^2) to increase the stability of the system during the impedance measurements, see Figure 3. When comparing this with the previous discharge at 250 μA presented in Figure 2, it is important to note that both the capacity and the polarization resistance, R_p, are significantly larger in the 20 μA discharge.

On the basis of a fit using eq 3, representing the equivalent circuit presented in Figure S4a in the Supporting Information, the resistance and pseudocapacitance parameters of Z_1, Z_2, and

DOI: 10.1021/am5083254
ACS Appl. Mater. Interfaces 2015, 7, 4039–4047

ACS Applied Materials & Interfaces Research Article

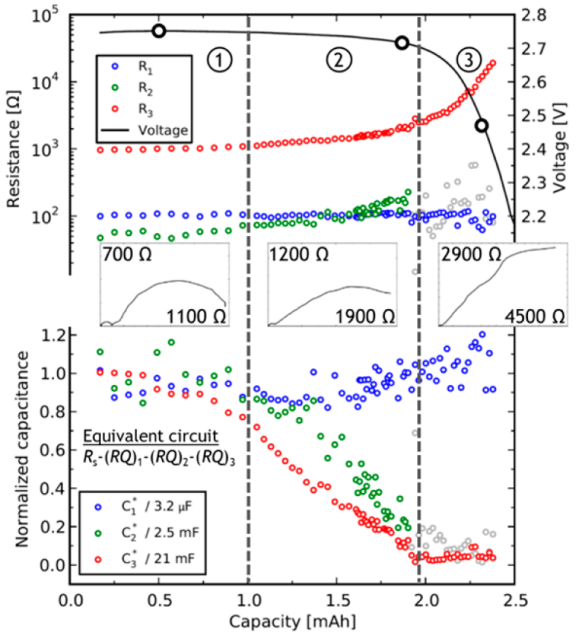

Figure 3. Resistances and normalized pseudocapacitances determined from EIS measurements in a 20 μA (18 μA/cm2) constant current discharge to 2.2 V using eq 3. Nyquist plots are shown at three representative stages, and the corresponding SODs are marked with circles on the voltage profile. R_2 and C_2^* could not be determined well at the end of discharge and are thus greyed out.

Z_3 are presented in Figure 3 and summarized in Table 1. The parameters of Z_1 were constant through the entire discharge, and the change of parameters related to Z_2 and Z_3 are divided into three parts as indicated in Figure 3: (1) At 0−40% SOD, only negligible change was observed, (2) at 40−80% SOD, R_2 and R_3 increased 2−3 times, and C_2^* and C_3^* decreased by 95%, and (3) at 80−100% SOD, R_3 increased exponentially to 14.1 kΩ at 90% SOD (more than 10 times the initial value), the pseudocapacitances stayed at ∼5% of the initial value, and the voltage dropped. Parameters related to Z_2 could not be determined in the last part of the discharge because of an overlap with Z_3.

At 20 μA, the average relative Kramers−Kronig deviation at frequencies from 1 mHz to 10 Hz was typically 0.5% at the plateau, increasing near sudden death to 2% at 2.2 V. The n_3 value got below 0.7 in the end of the discharge to typical values of 0.62. This means that the pseudocapacitance C_3^* is less meaningful to calculate.

3.3. EIS Measurement in Argon. A potentiostatic EIS measurement at OCV with 5 mV amplitude was made on a fresh battery in argon atmosphere before exposure to oxygen to investigate reactions not related to oxygen reduction. The measurement is shown in Figure 4, and clearly, reactions were still taking place in the absence of oxygen, as Z_1 and Z_2 were still present. The low frequency tail could be modeled with a capacitor, C_3, which means that no charge transfer reaction is present for this process. The spectrum was modeled with the equivalent circuit *R-RQ-RQ-RQ-C*, shown in Figure S4c in the Supporting Information. The capacitance C_3 was 18.3 mF, and the pseudocapacitances C_1^* and C_2^* were 1.2 μF and 0.2 mF, respectively. The presence of Z_2 suggests that this process is not related to oxygen reduction.

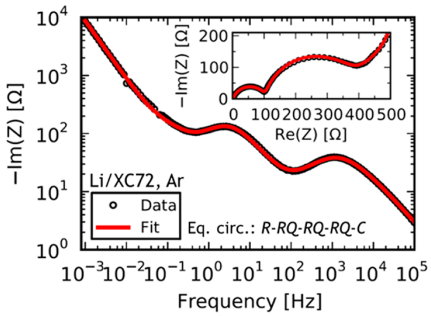

Figure 4. Bode plot and Nyquist plot (inset) of a potentiostatic EIS measurement at OCV in argon atmosphere. The spectrum is modeled with an *R-RQ-RQ-RQ-C* circuit, shown in Figure S4c in the Supporting Information.

3.4. *iv* Curve at the Discharge Plateau. As discussed in Section 2.2, the impedance is the slope of the *iv*-curve at a given current. To obtain a full understanding of the relationship between the impedance and the overpotential, it is necessary to investigate the current dependence of the impedance. We did this by measuring the impedance at the plateau at ∼40% of the total capacity at different current densities and compared this with the corresponding *iv* curve. As the impedance is almost constant in the first part of a discharge, the exact time of measurement was of less importance. To avoid effects of degradation in the battery, each point in the plot was made with a fresh battery. To eliminate variations due to different masses of the cathodes, both currents and impedances were weighed with the mass of carbon.

Figure 5 shows the *iv* curve of the plateau potential as a function of current density (red dots). The values are fitted

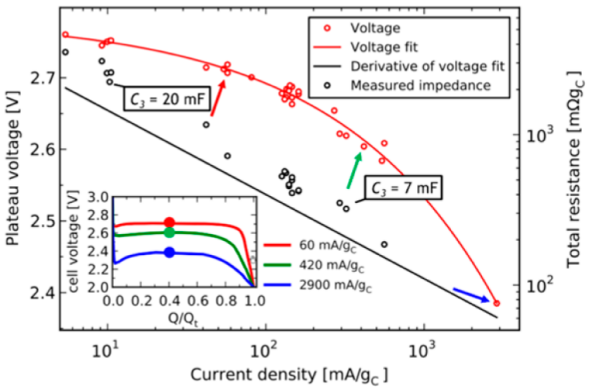

Figure 5. Plateau voltage dependence on current density (red dots) from 10 μA (9 μA/cm2) to 5 mA (4.4 mA/cm2). Equation 2 is fitted to the data (red line), which is then differentiated (black line) and compared with the total resistance (black dots) measured with impedance. Three representative discharge curves show how the plateau voltage is determined. The impedance and current density were weighed by the carbon mass of each electrode.

with eq 2 (red line) with OCV, c_1, and c_2 as fitting parameters. The result is OCV = 2.78 V, c_1 = 12 mV·$(g_C/mA)^{0.44}$ and c_2 = 0.44, which correspond to a Tafel slope of 120 millivolts per decade at 180 mA/g_C. This is in line with previous publications by Viswanathan et al. and Lu et al.[4,17] The *iv* curve fit is differentiated (black line) and compared with the measured

DOI: 10.1021/am5083254
ACS Appl. Mater. Interfaces 2015, 7, 4039−4047

impedance (black dots) in accordance with eq 1. It is seen that the measured impedance followed the same trend, but that it was higher than expected based on the *iv* curve. The reason for this discrepancy is likely related to a chemically induced parasitic side reaction that becomes more pronounced at lower discharge rates. This will be discussed further in Section 4.1.

3.5. Charge at 250 μA. In Figure 6, we present typical EIS measurements during a charge. To limit the complexity of the analysis, impedance measurements are only made at voltages below 4.2 V to avoid the major decomposition reactions observed at higher potentials using DEMS. In this measurement, the 4.2 V limit corresponded to 60% SOC.

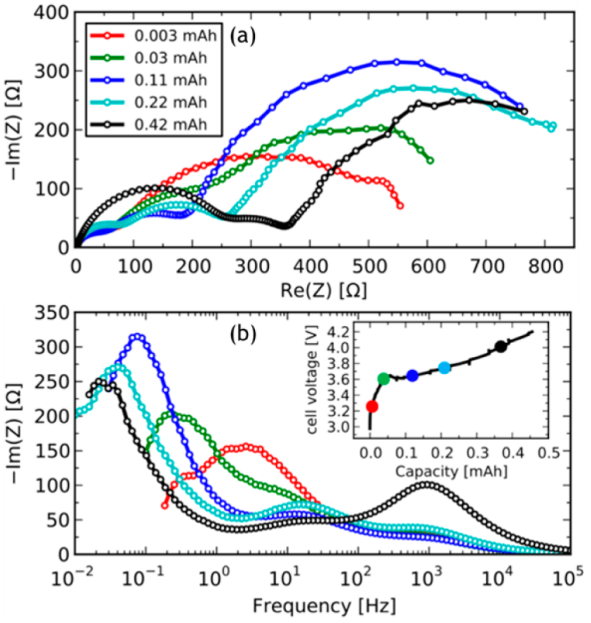

Figure 6. Nyquist (a) and Bode-like (b) plots of EIS measurements made during a 250 μA (220 μA/cm2) constant current charge. The charge followed a discharge similar to that shown in Figure 2 with a discharge resistance extrapolated to 3 kΩ at 2.0 V. The SOCs are shown as circles in the inset graph of the voltage profile. The 0.03 mAh and 0.42 mAh measurement was modeled using eq 3, and the obtained parameters are presented in Table 1

Three impedance contributions are identified. The correlation between the impedance and SOC is more complex than during discharge. The spectrum is dominated by a high- and a low-frequency response similar to Z_1 and Z_3 during discharge. It seems like the frequencies between 1 and 100 Hz are dominated by a mix of different processes appearing at certain SOCs and then disappearing at higher SOC, but further studies are needed to qualify this. The parameters obtained using equivalent circuit fitting on the green (0.03 mAh) and black (0.42 mAh) spectra with eq 3 are given in Table 1. The three contributions are in the same frequency ranges as seen during discharge. The polarization resistance, R_p, was almost constant in the range of 500−1000 Ω, but the peak frequencies and the relative magnitude of the different impedance contributions changed. Looking at the pseudocapacitances, C_1^* decreased from 3.6 μF to 0.6 μF, and C_3^* increased from 1.0 mF to 9.0 mF. This suggests that the active cathode area is increasing and that the active area of the anode is decreasing during charge. It is further noted that C_3^* is almost the same in the end of charge and in the beginning of the discharge (10.2 mF). Finally, it is noted that R_1 was almost constant until 3.7 V, after which it suddenly increased. This supports that the lithium anode surface is deactivated by an accelerated formation of the solid electrolyte interface (SEI) layer − possibly due to oxygen crossover.

4. DISCUSSION

To gain electrochemical knowledge of the fundamental reactions and bottlenecks during discharge and charge of the Li−O_2 battery, a series of electrochemical impedance spectra at different current densities and SOCs has been measured. It was seen that three impedance contributions were present during both discharge and charge, and they are referred to as Z_1, Z_2, and Z_3. The five key findings were that

(i) the impedance did not change at the discharge plateau,
(ii) Z_2 and Z_3 increased near sudden death,
(iii) C_3^* decreased significantly just before sudden death,
(iv) pseudocapacitances related to Z_1, Z_2, and Z_3 were typically 3 μF for C_1^*, 0.1−3 mF for C_2^*, and 1−20 mF for C_3^*, and
(v) the OCV was always 2.85 V during discharge and the initial stages of charge, then slowly increased to 3.2 V at the end of charge.

4.1. Identification of Processes during Discharge. Our results support previous findings by Adams et al. and Landa-Medrano et al. in refs 8 and 9 that Z_1 originates from the anode and that Z_2 and Z_3 originate from the cathode. In addition to this, our results show that Z_3 is a combination of the charge transfer reaction of oxygen reduction and the electronic transport through the Li_2O_2, whereas Z_2 is a cathode-specific process that is not related to the oxygen reduction. The assignment of anode and cathode features in the EIS is substantiated by the following three observations.

First, the full capacitance at the lithium anode surface is expected to be in the range of 10 μF as discussed in Section 2.2, whereas the capacitance of the XC72 electrode is expected to be 25 mF. If only part of an electrode is active during the EIS measurement, the capacitance will be lower. As reported, C_1^* was typically 3 μF, whereas C_2^* and C_3^* were in the range of 0.1−20 mF. Furthermore, the cathode capacitance per active surface area calculated by Adams et al. was in the same range as C_3^*.[8]

Second, the careful parameter study presented by Adams et al. in ref 8 shows that relevant cathode processes have peak frequencies below 10 Hz, which correspond with f_2 and f_3 in our study, whereas the peak frequency of the anode process is ∼1 kHz, which corresponds to f_1 in our study.

Third, Z_1 did not change during discharge, whereas Z_2 and Z_3 increased significantly close to sudden death. Both electrodes changed during the measurement. On the lithium anode, Younesi et al. have previously shown that an SEI layer is forming in a combination of chemical and electrochemical reactions,[33] but as shown by McCloskey et al. this is affecting neither the electrochemistry nor the measured impedance.[4] On the other hand, the cathode is covered with an insulating layer of mainly Li_2O_2 during discharge, and an increase in charge transfer resistance is typically captured in EIS measurements.

Ascribing Z_3 to oxygen reduction and electronic transport through Li_2O_2 is based on two observations: (i) Z_3 is the only process related to oxygen reduction, as both Z_1 and Z_2 are

DOI: 10.1021/am5083254
ACS Appl. Mater. Interfaces 2015, 7, 4039−4047

ACS Applied Materials & Interfaces Research Article

present in argon, and (ii) R_3 was the largest resistance during the entire discharge, both when the cathode was limited by reaction kinetics at the discharge plateau and by electronic conduction at sudden death.

The process related to Z_2 is cathode specific and not related to oxygen reduction, as it was present in argon but almost absent in a measurement with P50 carbon paper, shown in Figure S3 in the Supporting Information. As P50 is binder-free, this could indicate a degradation effect related to the PTFE binder. A little surprising, Z_2 was not present in the symmetrical cell measurement. This could indicate that the parasitic reaction was chemically passivated during handling when assembling the symmetrical cell.

The *iv* curve in Figure 5 was made to ensure that all electrochemical processes were captured in the impedance spectrum. This was indeed the case, since the total impedance could account for the changes in the overpotential. Actually, the measured impedance seemed to overestimate the slope of the *iv* curve, and the reason is most likely a result of lower Li_2O_2 formation yields, and therefore more heterogeneous discharge electrodeposits, at lower current densities as shown in a previous publication.[5] Garcia-Lastra et al. and Mekonnen et al. have shown that an increase of Li_2CO_3-like inclusions in the Li_2O_2 layer can change the electrical conductivity using DFT calculations,[34,35] and such changes would also change the current dependence of the impedance and explain the deviation.

4.2. Analysis of the Overpotential during Discharge. The measurements show that the electrochemistry was unchanged during the entire discharge, and they support the general understanding of tunneling being the dominant charge transport mechanism through the Li_2O_2 layer at relevant current densities and temperatures, which was initially proposed by Albertus et al.[16] and confirmed by Luntz et al.[1] Furthermore, the discharge was initially occurring in the entire cathode, whereas the increasing electronic transport through the growing Li_2O_2 layer passivated large parts of the cathode during discharge.

The tunneling mechanism is supported by two observations. First, the impedance contribution Z_3 related to oxygen reduction and electronic conduction through Li_2O_2 was constant at the discharge plateau and increased rapidly near sudden death, which is characteristic for the tunneling barrier that depends exponentially on the Li_2O_2 layer thickness, and second, the electrochemistry was unchanged during the discharge, as shown by a constant 2 e^-/O_2 process and identification of the same three processes in the impedance spectra at all SODs.

Passivation of the cathode is observed in the pseudocapacitance C_3^*. At 20 μA, the initial value is 21 mF. This is the expected value of the entire cathode, which means that Li_2O_2 deposition is occurring in the entire cathode. The decrease in stage 1, as defined in Figure 3, reflects Li_2O_2 formation, because the introduction of a dielectric material in a capacitor changes the capacitance. In stage 2, the decrease is significant, cannot be explained by the dielectric layer of Li_2O_2 alone, and must therefore reflect a reduction in active surface area. The cathode passivates when the critical thickness of Li_2O_2 is reached and tunneling is no longer possible. In stage 3, the available surface area is not sufficient to support the constant current, and the voltage drops to enable conduction through the blocked parts of the electrode. This is seen as an increase in cathode resistance. When fully discharged, the resistance is too large, and the current cannot be supported within the cutoff limit of 2.2 V. This is in full agreement with observations made by Luntz et al. using flat glassy carbon electrodes in electrolysis cells.[1]

Because of discussions in literature on the significance of oxygen diffusion in the electrolyte, it is worth mentioning that the sudden death is not due to pore clogging and increased oxygen diffusion resistance. In a typical discharge, the average thickness of Li_2O_2 is 0.5−1 nm based on the BET surface area of XC-72. This means that the porosity and Damköhler number are almost unchanged during the entire discharge, and as stated by Wang et al.,[29] such small changes will not give rise to the sudden death behavior.

4.3. Analysis of the Overpotential during Charge. The EIS measurements from the charge confirm that the electrical resistivity through Li_2O_2 decreases in charge mode as proposed by Luntz et al. using flat glassy carbon electrodes[1] and show that the voltage increase during charge is a mixed potential rather than an increase in internal resistance, as McCloskey et al. have also suggested based on modeling.[10]

The change in resistivity in charge mode is identified by comparing the impedance at the end of discharge with the resistance in the beginning of the charge. During charge, the polarization resistance was ∼500 Ω at a current of 250 μA (220 $\mu A/cm^2$), which is much lower than the extrapolated value of 3 kΩ at 2.0 V during discharge. Furthermore, the charge resistance had only little dependence on the discharge current and depth of discharge, which suggests that the charge is not limited by the same process as the discharge. Luntz et al. have previously explained this by a reduction of the tunneling barrier because of a change in the Fermi energy by experiments on flat glassy carbon electrodes in an electrolysis cell.[1]

The mixed potential is identified because the impedance was not increasing as the charging potential increased, which indicates a change of reaction mechanisms. As shown by DEMS and Li_2O_2 titration, the charging reaction is not a 2 e^-/O_2 process but rather a 2.5−3 e^-/O_2 process, and parasitic electrochemical reactions are thus present during the entire charge.[5,10,11,15] Keeping in mind that the OCV never exceeded 3.2 V during charge, and no significant resistance increase was seen in the impedance spectra, it suggests that a mixed potential between these competing electrochemical reactions was established during charge to support the high current.

These results contradict the theory proposed by Chen et al. suggesting that the increase in charge overpotential occurs because the Li_2O_2 closest to the electronically conducting part of the cathode oxidizes first.[7] If this was the case, an increase of the charge resistance of at least an order of magnitude would be expected to explain the voltage increase, but the resistance does not increase by more than a factor of 2. Furthermore, after discharging under alternating O_2 isotope atmospheres, Li_2O_2 oxidation was found to preferentially occur at the Li_2O_2/electrolyte interface over the Li_2O_2/cathode interface during the initial stages of charge, as shown in a previous publication.[14]

Interestingly, R_1 increased four times when the battery reached 4 V, and C_1^* decreased to 20%. This suggests significant anode degradation and is in line with previous work by Younesi et al. showing how the SEI layer changes on the lithium metal during charge of a Li−O_2 battery.[33] At this point it is not possible to determine whether this change is caused by degradation of the anode or an overlapping cathode process, but if the increase is because of anode degradation, this will be important to prevent in a commercial Li−O_2 battery.

DOI: 10.1021/am5083254
ACS Appl. Mater. Interfaces 2015, 7, 4039−4047

5. CONCLUSION

By measuring EIS spectra at different current densities and different SOCs it was possible to assign the three identified contributions to either the cathode or the anode. Only one of the two cathode processes depended on the presence of oxygen. This indicates that this contribution was related to the Li_2O_2 formation. The other contribution was cathode specific and may reflect a degradation reaction related to the PTFE binder.

During discharge, the rapid potential change near the end of discharge was due to an increase in polarization resistance, primarily related to the charge transport through the Li_2O_2. This supports previously published work by Luntz et al. in ref 1, which states that the electronic transport through Li_2O_2 at relevant current densities is governed by tunneling.

In the initial part of the charge, the impedance was low compared to the end of discharge at sudden death. This supports that the electronic conductivity is improved when changing to charge mode, which has also been shown in a previous work on smooth glassy carbon cathodes in an electrolysis cell.[1] During charge, the voltage increased significantly, whereas the resistance and OCV were almost unchanged, and DEMS measurements identified the presence of parasitic reactions. This suggests that the electrochemistry changed during charge and that the voltage increase was due to a mixed potential of parasitic reactions and Li_2O_2 oxidation, established to support a constant current.

■ ASSOCIATED CONTENT

Ⓢ Supporting Information

Schematic illustration of the test cell, equivalent circuit diagrams, and EIS measurements on modified systems that suppress different features in the EIS spectrum made to support the conclusions made in the article. These modifications are (1) using a symmetrical carbon−carbon cell and (2) using a cathode with a different type of carbon. This material is available free of charge via the Internet at http://pubs.acs.org.

■ AUTHOR INFORMATION

Corresponding Author

*E-mail: jhoj@topsoe.dk. Phone: (+45) 27292175. Fax: (+45) 45272999.

Present Address

⊥Bryan D. McCloskey: Department of Chemical and Biomolecular Engineering, University of California and Environmental Energy Technologies Division, Lawrence Berkeley National Laboratory, Berkeley, CA 94720, United States.

Notes

The authors declare no competing financial interest.

■ ACKNOWLEDGMENTS

The authors acknowledge support of this work from the ReLiable project (Project No. 11-116792) funded by the Danish Council for Strategic Research Program Commission on Sustainable Energy and Environment.

■ REFERENCES

(1) Luntz, A. C.; Viswanathan, V.; Voss, J.; Varley, J. B.; Speidel, A.; Nørskov, J. K.; Scheffler, R. Tunneling and Polaron Charge Transport Through Li_2O_2 in Li-O_2 Batteries. *J. Phys. Chem. Lett.* **2013**, *4*, 3494−3499.

(2) Hummelshøj, J. S.; Blomqvist, J.; Datta, S.; Vegge, T.; Rossmeisl, J.; Thygesen, K. S.; Luntz, A. C.; Jacobsen, K. W.; Nørskov, J. K. Communications: Elementary Oxygen Electrode Reactions in the Aprotic Li-Air Battery. *J. Chem. Phys.* **2010**, *132*, 071101−1−071101−4.

(3) Hummelshøj, J. S.; Luntz, A. C.; Nørskov, J. K. Theoretical Evidence for Low Kinetic Overpotentials in Li-O_2 Electrochemistry. *J. Chem. Phys.* **2013**, *138*, 034703−1−034703−12.

(4) Viswanathan, V.; Nørskov, J. K.; Speidel, A.; Scheffler, R.; Gowda, S. R.; Luntz, A. C. Li−O_2 Kinetic Overpotentials: Tafel Plots from Experiment and First-Principles Theory. *J. Phys. Chem. Lett.* **2013**, *4*, 556−560.

(5) McCloskey, B. D.; Valery, A.; Luntz, A. C.; Gowda, S. R.; Wallra, G. M.; Garcia, J. M.; Mori, T.; Krupp, L. E. Combining Accurate O_2 and Li_2O_2 Assays to Separate Discharge and Charge Stability Limitations in Nonaqueous Li-O_2 Batteries. *J. Phys. Chem. Lett.* **2013**, *4*, 2989−2993.

(6) Zhong, L.; Mitchell, R. R.; Liu, Y.; Gallant, B. M.; Thompson, C. V.; Huang, J. Y.; Mao, S. X.; Shao-Horn, Y. In Situ Transmission Electron Microscopy Observations of Electrochemical Oxidation of Li_2O_2. *Nano Lett.* **2013**, *13*, 2209−2214.

(7) Chen, Y.; Freunberger, S. A.; Peng, Z.; Fontaine, O.; Bruce, P. G. Charging a Li-O_2 Battery Using a Redox Mediator. *Nat. Chem.* **2013**, *5*, 489−494.

(8) Adams, J.; Karulkar, M.; Anandan, V. *J.* Evaluation and Electrochemical Analyses of Cathodes for Lithium-Air Batteries. *J. Power Sources* **2013**, *239*, 132−143.

(9) Landa-Medrano, I.; Ruiz de Larramendi, I.; Ortiz-Vitoriano, N.; Pinedo, R.; Ignacio Ruiz de Larramendi, J.; Rojo, T. In Situ Monitoring of Discharge/Charge Processes in Li-O_2 Batteries by Electrochemical Impedance Spectroscopy. *J. Power Sources* **2014**, *249*, 110−117.

(10) McCloskey, B. D.; Speidel, A.; Scheffler, R.; Miller, D.; Viswanathan, V.; Hummelshøj, J. S.; Nørskov, J. K.; Luntz, A. C. Twin Problems of Interfacial Carbonate Formation in Nonaqueous Li-O_2 Batteries. *J. Phys. Chem. Lett.* **2012**, *3*, 997−1001.

(11) McCloskey, B. D.; Bethune, D. S.; Shelby, R. M.; Girishkumar, G.; Luntz, A. C. Solvents' Critical Role in Nonaqueous Lithium-Oxygen Battery Electrochemistry. *J. Phys. Chem. Lett.* **2011**, *2*, 1161−1166.

(12) Gowda, S. R.; Brunet, A.; Wallraff, G. M.; McCloskey, B. D. Implications of CO_2 Contamination in Rechargeable Nonaqueous Li-O_2 Batteries. *J. Phys. Chem. Lett.* **2013**, *4*, 276−279.

(13) McCloskey, B. D.; Scheffler, R.; Speidel, A.; Bethune, D. S.; Shelby, R. M.; Luntz, A. C. On the Efficacy of Electrocatalysis in Nonaqueous Li-O_2 Batteries. *J. Am. Chem. Soc.* **2011**, *133*, 18038−18041.

(14) McCloskey, B. D.; Scheffler, R.; Speidel, A.; Girishkumar, G.; Luntz, A. C. On the Mechanism of Nonaqueous Li-O_2 Electrochemistry on C and Its Kinetic Overpotentials: Some Implications for Li-Air Batteries. *J. Phys. Chem. C* **2012**, *116*, 23897−23905.

(15) McCloskey, B. D.; Luntz, A. C.; Bethune, D. S.; Shelby, R. M.; Mori, T.; Scheffler, R.; Speidel, A.; Sherwood, M. Limitations in Rechargeability of Li-O_2 Batteries and Possible Origins. *J. Phys. Chem. Lett.* **2012**, *3*, 3043−3047.

(16) Albertus, P.; Girishkumar, G.; McCloskey, B. D.; Sánchez-Carrera, R. S.; Kozinsky, B.; Christensen, J.; Luntz, A. C. Identifying Capacity Limitations in the Li/Oxygen Battery Using Experiments and Modeling. *J. Electrochem. Soc.* **2011**, *158*, A343.

(17) Lu, Y.-C.; Gasteiger, H. A.; Shao-Horn, Y. Method Development to Evaluate the Oxygen Reduction Activity of High-Surface-Area Catalysts for Li-Air Batteries. *Electrochem. Solid-State Lett.* **2011**, *14*, A70−A74.

(18) Lasia, A. Impedance of Porous Electrodes. *J. Electroanal. Chem.* **1995**, *397*, 27−33.

(19) Hirschorn, B.; Orazem, M. E.; Tribollet, B.; Vivier, V.; Frateur, I.; Musiani, M. Determination of Effective Capacitance and Film Thickness from Constant-Phase-Element Parameters. *Electrochim. Acta* **2010**, *55*, 6218−6227.

(20) Graves, C. *RAVDAV Data Analysis Software,* Version 0.9.7.

DOI: 10.1021/am5083254
ACS Appl. Mater. Interfaces 2015, 7, 4039−4047

(21) Jamnik, J.; Maier, J. Generalised Equivalent Circuits for Mass and Charge Transport: Chemical Capacitance and Its Implications. *Phys. Chem. Chem. Phys.* **2001**, *3*, 1668−1678.
(22) Aurbach, D.; Weissman, I.; Zaban, A.; Chusid, O. Correlation Between Surface Chemistry, Morphology, Cycling Efficiency and Interfacial Properties of Li Electrodes in Solutions Containing Different Li Salts. *Electrochim. Acta* **1994**, *39*, 51−71.
(23) Aurbach, D.; Zaban, A.; Schechter, A.; Ein-eli, Y.; Zinigrad, E.; Markovsky, B. The Study of Electrolyte Solutions Based on Ethylene and Diethyl Carbonates for Rechargeable Li Batteries. I. Li Metal Anodes. *J. Electrochem. Soc.* **1995**, *142*, 2873−2882.
(24) Barbieri, O.; Hahn, M.; Herzog, a.; Kötz, R. Capacitance Limits of High Surface Area Activated Carbons for Double Layer Capacitors. *Carbon* **2005**, *43*, 1303−1310.
(25) Zoltowski, P. *J.* On the Electrical Capacitance of Interfaces Exhibiting Constant Phase Element Behaviour. *J. Electroanal. Chem.* **1998**, *443*, 149−154.
(26) Gerbig, O.; Merkle, R.; Maier, J. Electron and Ion Transport in Li_2O_2. *Adv. Mater.* **2013**, *25*, 3129−3133.
(27) Dunst, A.; Epp, V.; Hanzu, I.; Freunberger, S. A.; Wilkening, M. Short-Range Li Diffusion vs. Long-Range Ionic Conduction in Nanocrystalline Lithium Peroxide Li_2O_2 - the Discharge Product in Lithium-Air Batteries. *Energy Environ. Sci.* **2014**, *7*, 2739−2752.
(28) Young, K. F.; Frederikse, H. P. R. Compilation of the Static Dielectric Constant of Inorganic Solids. *J. Phys. Chem. Ref. Data* **1973**, *2*, 313.
(29) Wang, Y.; Cho, S. C. Analysis of Air Cathode Perfomance for Lithium-Air Batteries. *J. Electrochem. Soc.* **2013**, *160*, A1847−A1855.
(30) Mehta, M.; Mixon, G.; Zheng, J. . P.; Andrei, P. Analytical Electrochemical Impedance Modeling of Li-Air Batteries under D.C. Discharge. *J. Electrochem. Soc.* **2013**, *160*, A2033−A2045.
(31) Sandhu, S. S.; Fellner, J. P.; Brutchen, G. W. Diffusion-Limited Model for a Lithium/Air Battery with an Organic Electrolyte. *J. Power Sources* **2007**, *164*, 365−371.
(32) Schiller, C. A.; Richter, F.; Gülzow, E.; Wagner, N. Validation and Evaluation of Electrochemical Impedance Spectra of Systems with States that Change with Time. *Phys. Chem. Chem. Phys.* **2001**, *3*, 374−378.
(33) Younesi, R.; Hahlin, M.; Roberts, M.; Edström, K. The SEI Layer Formed on Lithium Metal in the Presence of Oxygen: A Seldom Considered Component in the Development of the Li-O_2 Battery. *J. Power Sources* **2013**, *225*, 40−45.
(34) Garcia-Lastra, J. M.; Myrdal, J. S. G.; Christensen, R.; Thygesen, K. S.; Vegge, T. DFT+U Study of Polaronic Conduction in Li_2O_2 and Li_2CO_3: Implications for Li-Air Batteries. *J. Phys. Chem. C* **2013**, *117*, 5568−5577.
(35) Mekonnen, Y. S.; Knudsen, K. B.; Mýrdal, J. S. G.; Younesi, R.; Højberg, J.; Hjelm, J.; Norby, P.; Vegge, T. Communication: The Influence of CO_2 Poisoning on Overvoltages and Discharge Capacity in Non-aqueous Li-Air Batteries. *J. Chem. Phys.* **2014**, *140*, 121101.

DOI: 10.1021/am5083254
ACS Appl. Mater. Interfaces 2015, 7, 4039−4047

Supporting Information: An Electrochemical Impedance Spectroscopy Investigation of the Overpotentials in Li-O_2 Batteries

Jonathan Højberg[†,‡,§,*], *Bryan D. McCloskey*[†], *Johan Hjelm*[‡], *Tejs Vegge*[‡], *Keld Johansen*[§], *Poul Norby*[‡], *Alan C. Luntz*[†,∥]

[†]IBM Almaden Research Center, San Jose, California 95120, United States

[‡]DTU Energy Conversion, Frederiksborgvej 399, DK-4000 Roskilde, Denmark

[§]Haldor Topsøe A/S, Nymøllevej 55, DK-2800 Kgs. Lyngby, Denmark

[∥]SUNCAT, SLAC National Accelerator Laboratory, Menlo Park, California 94025

*Corresponding author

E-mail: jhoj@topsoe.dk

Tel.: (+45) 27292175

Fax: (+45) 45272999

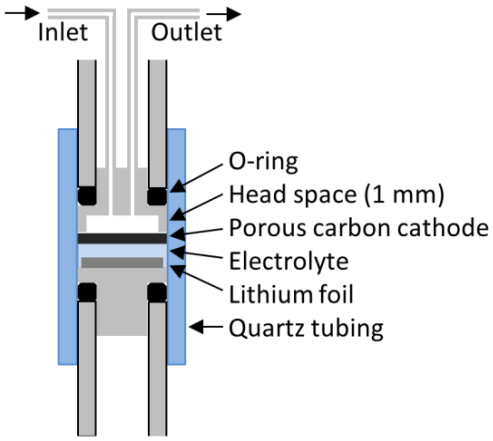

Figure S1. Schematic figure of the test cell used in this study. The inlet and outlet allow gasses to be fed to and swept away from the cell and analyzed in a mass spectrometer.

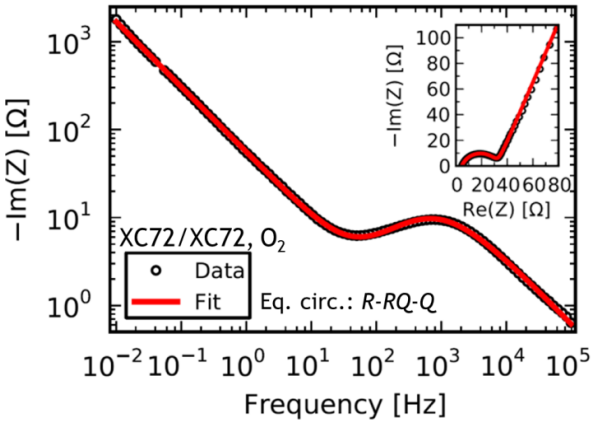

Figure S2. Bode-plot and Nyquist-plot (inset) of a potentiostatic EIS measurement of a symmetrical XC72 cell at 0 V with an ac amplitude of 5 mV. The cell was made of two cathodes that had been discharged in separate cells with a lithium anode at 250 μA (220 μA/cm^2). The spectrum is modeled with a R-RQ-Q circuit, shown in Figure S4b.

A potentiostatic EIS measurement of a symmetrical cell at OCV with 5 mV amplitude was made to eliminate contributions from the lithium anode in the EIS spectrum. The cell was made of two cathodes that had been discharged 1 hour in separate cells with a lithium anode at 250 µA (220 µA/cm^2). The measurement is shown in Figure S2. The spectrum has been modeled with a R-RQ-Q circuit. The CPE element was chosen instead of a capacitor to describe the low frequency tail, because the slope was -0.74 in the Bode plot, rather than -1 in the case of a capacitor. The pseudo-capacitance of the low frequency tail was 2.1 mF and the resistance and pseudo-capacitance of the RQ circuit was 27 Ω and 4.3 µF, respectively.

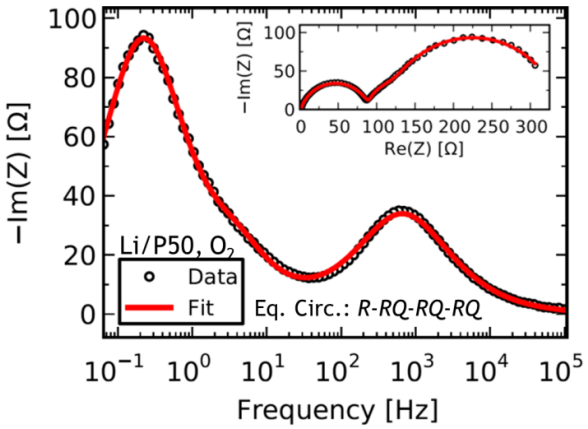

Figure S3. Bode-like plot and Nyquist-plot (inset) of a 250 μA (220 μA/cm^2) discharge GEIS of an AvCarb P50 cathode carbon paper. The spectrum is modeled with a $R\text{-}RQ\text{-}RQ\text{-}RQ$ circuit, shown in Figure S4a.

A GEIS measurement on AvCarb P50 carbon paper prepared as described in Ref. 1 is shown in Figure S3. Both Z_1 and Z_3 have similar parameter values compared to XC72 and Z_2 is very small.

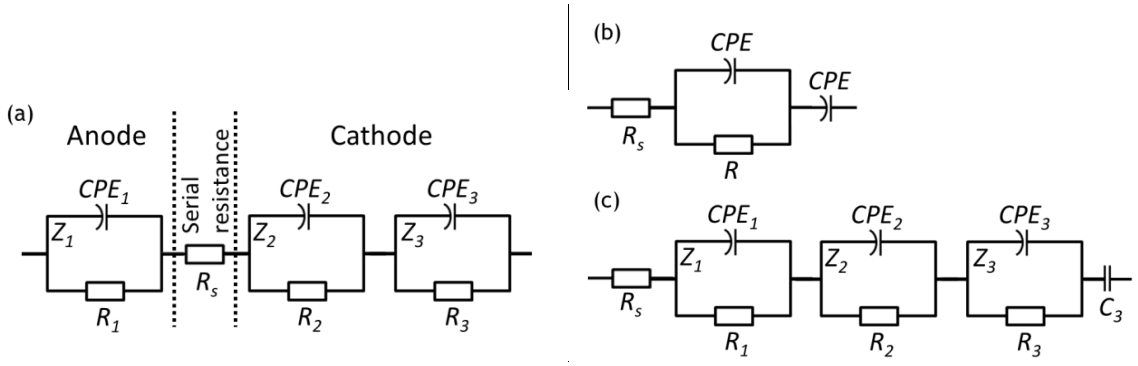

Figure S4. Equivalent circuit diagrams used to model the impedance measurements presented in the paper. The most common element is a Voigt element (parallel connected resistor with a constant phase element, *CPE*). (a) The equivalent circuit used the most. As discussed in the paper, the contributions to the impedance can be attributed to either the anode (Z_1) or the cathode (Z_2 and Z_3). (b) is used to model the data in Figure S2 and (c) is used to model data in Figure 4.

References

(1) McCloskey, B. D.; Scheffler, R.; Speidel, A.; Bethune, D. S.; Shelby, R. M.; Luntz, A. C. On the Efficacy of Electrocatalysis in Nonaqueous Li-O_2 Batteries. *J. Am. Chem. Soc.* **2011**, *133*, 18038–18041.

ECS Electrochemistry Letters, **4** (7) A63-A66 (2015) A63
2162-8726/2015/4(7)/A63/4/$33.00 © The Electrochemical Society

Reactions and SEI Formation during Charging of Li-O_2 Cells

Jonathan Højberg,[a,b,z] Kristian Bastholm Knudsen,[b] Johan Hjelm,[b,*] and Tejs Vegge[b]

[a]*Haldor Topsøe A/S, DK-2800 Kgs Lyngby, Denmark*
[b]*Department of Energy Conversion and Storage, Technical University of Denmark, DK 4000 Roskilde, Denmark*

In this letter we combine detailed electrochemical impedance measurements with quantitative measurements of O_2 evolution and Li_2O_2 oxidation to describe the charge mechanisms during charge of Li-O_2 batteries with porous carbon electrodes. We identify Li_2O_2 oxidation at 3.05 V and an apparent chemical formation of a solid electrolyte interface (SEI) layer as the first monolayer of Li_2O_2 is oxidized, leading to a voltage increase. The first electrochemical degradation reaction is identified between 3.3 V and 3.5 V, and the chemical degradation is limited above 3.5 V, suggesting that a chemically stable SEI layer has been formed.
 [DOI: 10.1149/2.0051507eel]

Manuscript submitted March 31, 2015; revised manuscript received May 4, 2015. Published May 13, 2015.

The non-aqueous Li-O_2 battery has received significant attention in the past years due to its potentially high specific energy and low cost, which makes it ideal for future electric vehicles. The combination of metallic lithium as the negative electrode and reduction of molecular oxygen at the positive electrode enable a theoretical energy density of 3.8 kWh/kg including the weight of lithium and oxygen.

During discharge, oxygen is consumed to form the insoluble Li_2O_2; a high bandgap product that will limit conduction of electrons and holes to the surface when the growing layer reaches a critical thickness.[1,2] Low overpotentials (<0.2 V) have been predicted for discharge and charge using density functional theory,[3–6] and supported experimentally by Luntz et al. using flat glassy carbon electrodes.[2] However, practical batteries with large surface area cathodes display large overpotentials.[7] This decreases the cycle efficiency significantly and open up potential dependent parasitic reactions during charge.[8]

Here, we focus on the initial part of the charge until a potential of 3.6 V to understand why the potential increases as the battery is charged. Understanding and ultimately solving this problem is an important step toward commercialization of the Li-O_2 technology. We have analyzed Li-O_2 batteries identical to a carbon based reference system used in a number of previous publications.[8–12] A differential capacity plot of a galvanostatic charge is used to identify the onset of at least eight electrochemical reactions during a full charge and using differential electrochemical mass spectrometry (DEMS), electrochemical impedance spectroscopy (EIS), and quantitative optical absorption spectroscopy; it was possible to explain why the initial low-overpotential oxidation of Li_2O_2 does not continue and why the voltage increases. The findings are illustrated in Figure 1a.

Experimental

All electrochemical measurements were performed using a 2-electrode Swagelok cell with XC72 carbon black cathodes (Vulcan XC72, Cabotcorp, GA), 1 M LiTFSI (Sigma-Aldrich) in 1,2-dimethoxyethane (BASF) electrolyte, a Whatman glass fiber separator and lithium anode. LiTFSI was dried at 180°C for 12 h and 1,2-dimethoxyethane was dried using 4 Å molecular sieves (Sigma-Aldrich). The carbon cathodes were manufactured by air-spraying a slurry of XC72 Carbon Black and PTFE (60 wt% dispersion in water) in a wt/wt ratio of 3:1 as described in Ref. 8.

Electrochemical impedance spectroscopy (EIS) and galvanostatic discharge-charge curves were measured using Bio-Logic VMP3 and MPG-2 potentiostats. Potentiostatic EIS measurements were performed at different charge potentials, U_{ch}, from 3.1 V to 3.6 V. Frequencies between 20 kHz and 10 mHz were investigated with 15 points per decade and an alternating current (AC) amplitude of 5 mV. All impedance measurements followed the procedure: a) discharge to 2.6 V at 130 mA/g_{carbon} followed by 150 min at 2.6 V, b) charge to U_{ch} at 130 mA/g_{carbon}, and c) continuous EIS measurements at U_{ch} until the current decreased to 13 mA/g_{carbon}. 130 mA/g_{carbon} was chosen because it is within a commercially interesting range and comparable to previous studies.[7–9] The voltage profile is presented in Figure S3 in the Supporting Information.

DEMS measurements were performed at 130–260 mA/g_{carbon} and the gas consumption and gas evolution were quantified using both pressure measurements and mass spectrometry. The applied in-house DEMS setup is similar in design to the setup used by McCloskey et al.[9]

To assess the amount of Li_2O_2 in the air electrode at different stages of charge, we used a spectrophotometric measurement to determine the concentration of a Ti-complex. Li_2O_2 was allowed to react with water to form H_2O_2 that oxidizes $TiOSO_4$ in the solution to form the Ti-complex. The concentration of the Ti-complex was determined by measuring the absorbance at around 408 nm. A detailed description of the method is included in the Supporting Information.

Results and Discussion

Figure 1b shows a typical charge curve, and Figure 2 shows differential capacity plots (dQ/dV) of such curves. The peaks correspond to voltage plateaus in the charge curve and thereby different processes, and from this, eight electrochemical processes can be identified at 3.05 V, 3.3 V, 3.4 V, 3.5 V, 3.85 V, 4.2 V, 4.3 V and 4.5 V. These potentials form the basis of the following discussion. Analyses of 10 charge measurements following a discharge to 2.6 V show a charge capacity below 3.15 V corresponding to 540 ± 80 $\mu mol_{Li_2O_2}/g_{carbon}$. This corresponds to 4.3% of the total discharge capacity or approximately one monolayer as calculated in the Supporting Information.

Quantification of Li_2O_2 and O_2 evolution.— Figure 3a shows the oxygen evolution (blue line) and the Li_2O_2 removal (red line) as the cathode is charged. The oxygen evolution is determined based on the DEMS measurements presented in Figure S1 in the Supporting Information and the Li_2O_2 removal is based on the optical absorption measurements presented in Figure S2 in the Supporting Information. The O_2 evolution and, in particular, the deviation from the theoretical value is in accordance with measurements presented by McCloskey et al.,[7] and suggests the presence of electrochemical degradation reactions, especially at potentials above 3.5 V. The Li_2O_2 is, however, disappearing more rapidly than expected from the electrochemistry, suggesting a significant chemical degradation. Figure 3b shows the amount of chemical and electrochemical reactions in different potential intervals, and it is clear that the chemical degradation is most significant in the potential ranges 2 V–3.1 V and 3.3 V–3.5 V. This effect is somewhat more pronounced than previously reported.[7]

Electrochemical impedance spectroscopy (EIS).— EIS was measured at 11 different potentials during the initial charge from 3.10 V to 3.60 V. Figure S4 in the Supporting Information shows a typical measurement, with the equivalent circuit fit and the determination of the resistance, $R_{Li_2O_2}$, and the pseudocapacitance. Both parameters are related to a combination of the charge transfer through Li_2O_2 and Li_2O_2

*Electrochemical Society Active Member.
[z]E-mail: jhoj@topsoe.dk

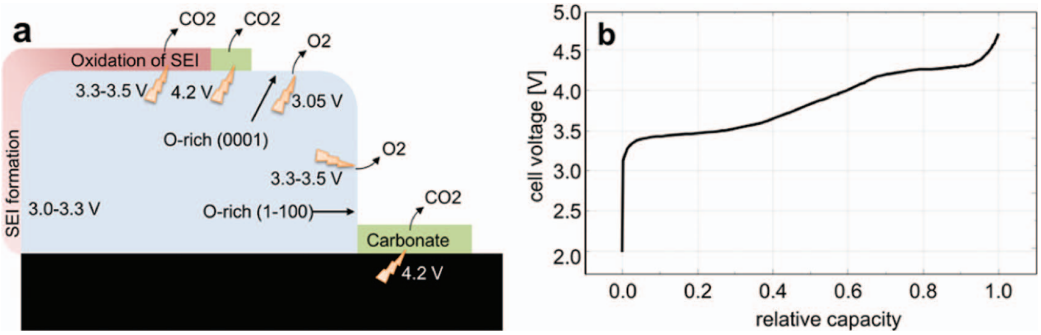

Figure 1. (a) Sketch of the reactions and SEI formation during charge of the Li-O_2 battery as discussed in this letter. The potentials in the figure are the proposed onset potentials. Li_2O_2 oxidation occurs at 3.05 V and an SEI layer is formed immediately on the freshly oxidized surface. At 3.3 V–3.5 V several reactions occur. Among these are gas evolution from the SEI layer and oxidation of other Li_2O_2 surfaces. (b) Charge of a Li-O_2 battery after a discharge to 2.6 V.

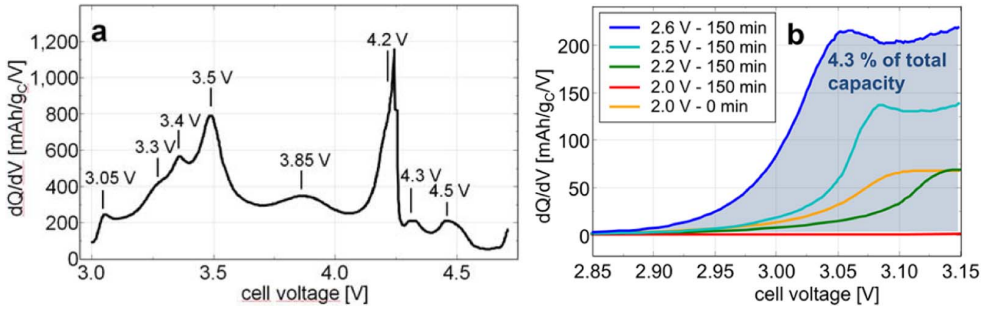

Figure 2. (a) Differential capacity plot (dQ/dV) of a representative battery charge. Each peak represents the onset of an electrochemical reaction. (b) Differential capacity plot of the initial part of the charge following a constant current 130 mA/g_{carbon} discharge to 2.0 V, 2.2 V, 2.5 V or 2.6 V, which was maintained for 150 min before charging. The measurement labeled *2.0 V–0 min* corresponds to charging immediately after discharge to 2.0 V.

oxidation.[8] Figure 4a shows the cathode resistance at selected voltages during charge, as determined by EIS. It is seen that the resistance increases from 3.10 V to 3.30 V, decreases at 3.33 V, increases until 3.50 V, and decreases again at 3.60 V. The resistance and corresponding pseudocapacitances at the marked cross section at 65 mA/g_{carbon} are shown in Figure 4b for all 11 potentials. Both the resistance and the pseudocapacitance change stepwise as a function of potential. The resistance increases monotonic until 2.27 V, then it drops and continue a second monotonic increase from 3.33 V to 3.50 V after which it drops. The pseudocapacitance is high at 3.10 V, decreases at 3.20 V, increases at 3.33 V and decreases again at 3.60 V. When keeping the potential at 3.10 V, it was observed that the capacitance decreased 60% from 0.7 mF/g_{carbon} at 130 mA/g_{carbon} to 0.28 mF/g_{carbon} at 13 mA/g_{carbon}. During the measurement, the current decreases and Li_2O_2 is removed. Both changes are expected to increase the capacitance, and the decreasing capacitance therefore clearly suggests that compounds are deposited during this initial charge, which is in line with the absorption measurements.

Identification of Li_2O_2 oxidation at 3.05 V.— We argue that the process identified at 3.05 V is oxidation of Li_2O_2 based on three observations. First, Figure S1 in the Supporting Information, shows that the e^-/O_2 ratio is between 2.0 (at 2 V) and 2.1 (at 3.2 V) in the beginning of the charge, which is exactly – or at least very close to – the expected value for Li_2O_2 oxidation. Second, Figure 2b shows how the onset potential of the process at around 3.05 V increases with the depth of discharge and the exposure time at low potentials. To understand this shift, it is noted that DEMS measurements show that the e^-/O_2 ratio is 2.0 during the entire discharge, and McCloskey et al. show that the Li_2O_2 yield is independent of the depth of discharge.[7] This means that the thickness, and thereby the conductivity, of the Li_2O_2 layer is the only parameter expected to change between the

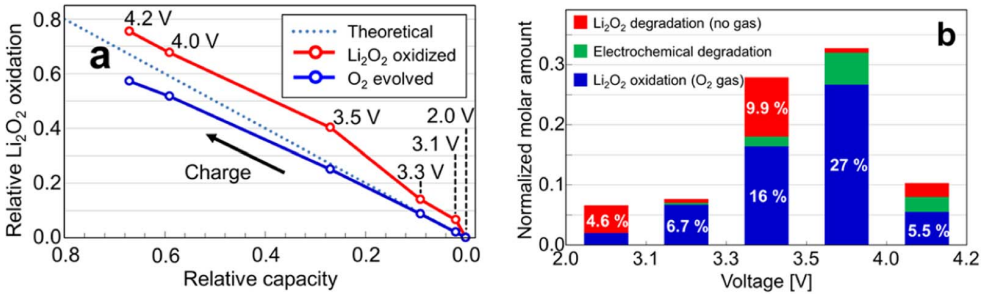

Figure 3. (a) Measurement of O_2 evolution using DEMS (blue) and Li_2O_2 removal (either chemical or electrochemical) determined spectrophotometrically (red). The dotted line corresponds to a pure electrochemical 2 e^-/O_2 oxidation of Li_2O_2 without any chemical degradation. (b) The amount of Li_2O_2 oxidation with and without gas evolution and electrochemical degradation in different potential intervals during charge. Values are normalized such that the sum of the electrochemical reactions (blue and green) equals the relative change in capacity in each interval and sum up to 1 for a full charge.

ECS Electrochemistry Letters, **4** (7) A63-A66 (2015) A65

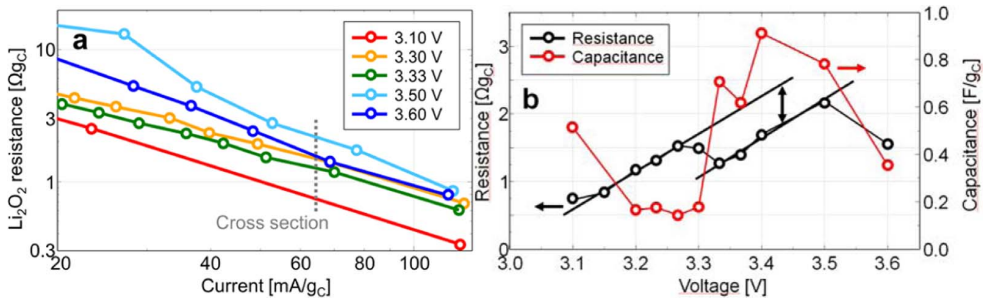

Figure 4. (a) The resistance related to the charge transfer through Li_2O_2 and Li_2O_2 oxidation measured at different potentials determined using EIS. The current decreases during the measurement. (b) Resistance and capacitance values at different potentials during charge. Guide lines have been inserted to illustrate the monotonic increases in the resistance.

measurements, and as the conductivity through the Li_2O_2 layer affects the onset potential of the reaction, it suggests that the reaction occurs at the Li_2O_2 surface. Third, the onset potential at the investigated current densities (~0.1 μA/cm^2 real surface area) is 2.9 V–3.0 V which corresponds well with the onset potential of Li_2O_2 oxidation measured by Viswanathan et al. using flat glassy carbon electrodes.[13]

SEI layer formation.— DEMS measurements show that all electrons come from the Li_2O_2 oxidation at the onset of the charge, until 3.1 V. In this interval, it was found from Figure 2b that 4.3% of the Li_2O_2 was oxidized electrochemically and in Figure 3b it is seen that another 4.6% was removed without gas evolution. Since all electrons are accounted for by the gas evolved, the reaction with no gas evolution must be chemical and it is interpreted as the formation of an SEI layer based on three observations. First, the amount of Li_2O_2 degradation is close to the amount of electrochemically oxidized Li_2O_2 in the initial part of the charge, and as the oxidation does not continue, it suggests that the electrochemical oxidation of Li_2O_2 exposes the surface such that the oxidation is followed by a chemical degradation of Li_2O_2, forming an SEI layer. Furthermore, the amount of oxidized and chemically degraded Li_2O_2 both correspond to approximately one monolayer, which suggest that the reaction occur on the entire surface of Li_2O_2. Second, the 60% decrease in capacitance at 3.1 V suggests a significant deposition of a dielectric compound that could be explained by the formation of an SEI layer. Third, the monotonic increase in Li_2O_2 resistance until 3.3 V suggests a decrease of available surface area or an increased electronic transport resistance. Both options could be explained by a growing SEI layer.

Electrochemical degradation.— Identification of the lowest potential without electrochemical degradation is important to identify a safe-voltage limit. We propose that at least one of the three separate processes identified in the differential capacity plot in the voltage range from 3.3 V to 3.5 V is an electrochemical degradation reaction as the e^-/O_2 ratio increases in this range. Two observations suggest that the reaction occurs at 3.3 V, but further investigation is needed to determine the onset potential definitively. First, EIS measurements show that the pseudocapacitance increases and the resistance decreases at 3.3 V. A sudden change like this suggests a new reaction pathway at this potential. Second, isotope measurements presented by McCloskey et al. using an identical system show that CO_2 evolution occurs from the electrolyte-Li_2O_2 interface from 3.3 V.[9] As the CO_2 evolution reaction depends on the potential, it is likely that this reaction is the new reaction pathway seen in the EIS measurements. To explain that three processes are identified in this voltage range, it is noted that DFT calculations from different groups show that onset potentials in this range could also be oxidation of another Li_2O_2 crystal plane like the oxygen rich (1–100) surface.[14,15]

Charge above 3.5 V.— At around 3.6 V, the resistance and the pseudocapacitance decrease again. The correspondence between impedance and overpotential is not straight forward, but the significant decrease in impedance as the voltage increases, is a strong indication of a shift in equilibrium potential caused by a mixed potential established between different oxidation reactions to maintain the constant current. The theory of a mixed a potential is further substantiated by measurements at higher potentials shown in a previous publication.[8]

Summary

The main results of this work are shown in Figure 1a. We have showed that Li_2O_2 is oxidized already at 3.05 V in porous carbon cathodes, but that this facile oxidation is limited to approximately one monolayer. Analysis of the chemical degradation and the change in double layer capacitance indicate that the Li_2O_2 surface reacts with the electrolyte to form a SEI layer as soon as the outermost layer is oxidized. The resistance increases as the SEI layer blocks the surface and the voltage increases to maintain the constant current.

Three reactions were identified between 3.3 V and 3.5 V. The interval is dominated by Li_2O_2 oxidation with a small amount of electrochemical degradation and significant chemical degradation of Li_2O_2. It is expected that the reactions in this region are a gas evolving degradation reaction in the Li_2O_2-electrolyte interface and oxidation of another Li_2O_2 crystal plane, possibly the O-rich (1–100) plane, among others. Above 3.5 V the chemical and electrochemical reactions become more complicated and a shift in equilibrium potential due to the establishment of a mixed potential is indicated as previously reported,[8] but further work would be needed to understand and distinguish these reactions fully.

In conclusion, the immediate formation of an SEI layer on the oxidized Li_2O_2 surface in the initial part of the charge is a significant problem that needs to be resolved before a viable Li-O_2 battery can be developed and an analysis of the very first part of the charge might serve as a suitable screening parameter in the search for better electrolytes.

Acknowledgments

The authors acknowledge support from the ReLiable project funded by the Danish Council for Strategic Research – Programme Commission on Sustainable Energy and Environment (project #11-116792).

References

1. V. Viswanathan, K. S. Thygesen, J. S. Hummelshøj, J. K. Nørskov, G. Girishkumar, B. D. McCloskey, and A. C. Luntz, *J. Chem. Phys.*, **135**, 214704 (2011).
2. A. C. Luntz, V. Viswanathan, J. Voss, J. B. Varley, A. Speidel, J. K. Nørskov, and R. Scheffler, *J. Phys. Chem. Lett.*, **4**, 3494 (2013).
3. J. S. Hummelshøj, J. Blomqvist, S. Datta, T. Vegge, J. Rossmeisl, K. S. Thygesen, A. C. Luntz, K. W. Jacobsen, and J. K. Nørskov, *J. Chem. Phys.*, **132**, 071101 (2010).
4. J. S. Hummelshøj, A. C. Luntz, and J. K. Nørskov, *J. Chem. Phys.*, **138**, 034703 (2013).
5. J. Chen, J. S. Hummelshøj, K. S. Thygesen, J. S. G. Myrdal, J. K. Nørskov, and T. Vegge, *Catal. Today*, **165**, 2 (2011).
6. D. J. Siegel and M. D. Radin, *Energy Environ. Sci.*, **6**, 2370 (2013).

7. B. D. McCloskey, A. Valery, A. C. Luntz, S. R. Gowda, G. M. Wallra, J. M. Garcia, T. Mori, and L. E. Krupp, *J. Phys. Chem. Lett.*, **4**, 2989 (2013).
8. J. Højberg, B. D. McCloskey, J. Hjelm, T. Vegge, K. Johansen, P. Norby, and A. C. Luntz, *ACS Appl. Mater. Interfaces*, **7**, 4039 (2015).
9. B. D. McCloskey, A. Speidel, R. Scheffler, D. Miller, V. Viswanathan, J. S. Hummelshøj, J. K. Nørskov, and A. C. Luntz, *J. Phys. Chem. Lett.*, **3**, 997 (2012).
10. B. D. McCloskey, D. S. Bethune, R. M. Shelby, G. Girishkumar, and A. C. Luntz, *J. Phys. Chem. Lett.*, **2**, 1161 (2011).
11. S. R. Gowda, A. Brunet, G. M. Wallraff, and B. D. McCloskey, *J. Phys. Chem. Lett.*, **4**, 276 (2013).
12. B. D. McCloskey, R. Scheffler, A. Speidel, D. S. Bethune, R. M. Shelby, and A. C. Luntz, *J. Am. Chem. Soc.*, **133**, 18038 (2011).
13. V. Viswanathan, J. K. Nørskov, A. Speidel, R. Scheffler, S. R. Gowda, and A. C. Luntz, *J. Phys. Chem. Lett.*, **4**, 556 (2013).
14. M. D. Radin, F. Tian, and D. J. Siegel, *J. Mater. Sci.*, **47**, 17 (2012).
15. J. S. G. Myrdal and T. Vegge, *Rsc Adv.*, **4**, 15671 (2014).

Supporting Information: Reactions and SEI formation during charging of Li-O_2 cells

Jonathan Højberg[1,2,*], Kristian Bastholm Knudsen[2], Johan Hjelm[2], Tejs Vegge[2]

[1]Haldor Topsøe A/S, Nymøllevej 55, DK-2800 Kgs Lyngby, Denmark

[2]Department of Energy Conversion and Storage, Technical University of Denmark, Frederiksborgvej 399, DK-4000 Roskilde, Denmark

*Corresponding author

E-mail: jhoj@topsoe.dk

Tel.: (+45) 27292175

Fax: (+45) 45272999

DEMS measurements

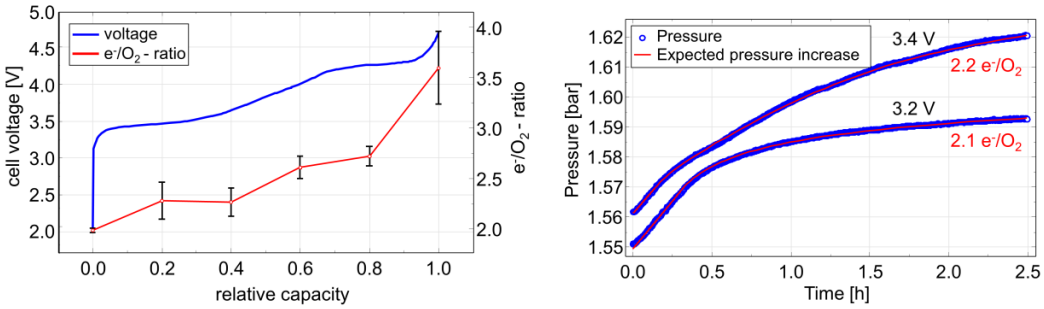

Figure S1. Left: Charge of a Li-O_2 battery after a discharge to 2.6 V. The e^-/O_2 ratio was calculated using an average of six DEMS measurements. The errorbars indicate one standard deviation. Right: Headspace pressure increase during charge at 130 mA/g_{carbon} constant current charge until a potential U_{ch} (noted in the figure) is reached. The charging is continued potentiostatic at U_{ch}, resulting in a decreasing current with time.

Calculation of monolayers

It is not possible to estimate the thickness of the Li_2O_2 layer, because the full BET area may not reflect the accessible surface area, as the use of binder has been shown to block the micropores of the carbon electrode.[1,2] Another approach is to use that it is generally accepted that the sudden death occur as the insulating Li_2O_2 layer reaches a thickness of ~5 nm at relevant current densities, and, using this thickness, the initial oxidation of 4.3 % correspond to a removal of 2.1 Å Li_2O_2. This is approximately one monolayer of Li_2O_2.

Chemical quantification of Li_2O_2

After electrochemical test of a Li-O_2 battery, the cell was purged with argon and transferred to a glovebox. The cell was carefully disassembled and the cathode was extracted. Each cathode was washed with 1,2-dimethoxyethane (BASF) dried using 4 Å molecular sieves (Sigma-Aldrich), and the cathodes were subsequently dried in vacuum. The cathodes were taken from the glovebox and immediately put into a 4 mL 0.063-0.07 % $TiOSO_4$ aqueous solution and the colored oxidized Ti-complex was seen immediately. The reactions occurring are listed in (S1) and (S2).[3]

$$Li_2O_2 + 2H_2O \rightarrow 2LiOH + H_2O_2 \qquad \text{(S1)}$$

$$Ti(IV)OSO_4 + H_2O_2 + 2H_2O \rightarrow 4H^+ + H_2Ti(VI)O_4 + OSO_4^{4-} \qquad \text{(S2)}$$

$H_2Ti(VI)O_4$ absorbs strongly at 408 nm. The solutions were left to react for 15-30 min and to remove carbon particles, which otherwise would interfere with the spectrophotometric measurement, samples were centrifuged and the supernatant was extracted yielding a clear colored liquid that was characterized using a Shimadzu UV-3600 PharmaSpec with 1 nm resolution and medium scan in absorbance mode.

The results from the absorption measurements are illustrated in Figure S2.

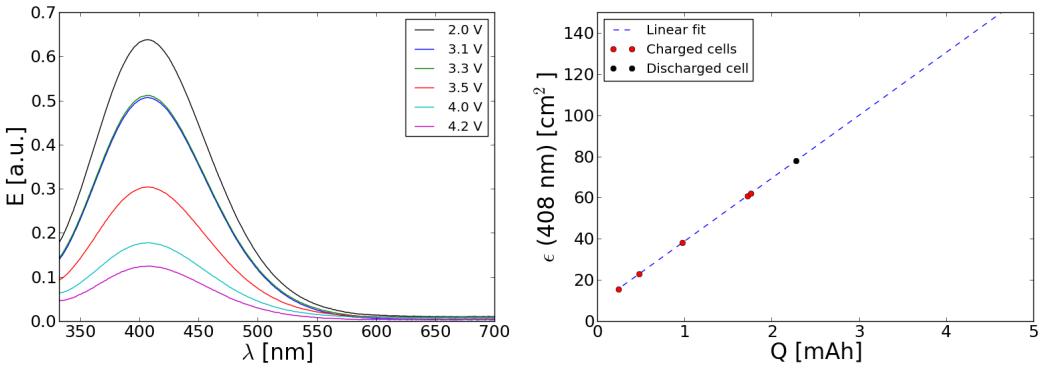

Figure S2. Optical absorption spectroscopy for the washed Li_2O_2 coated electrodes. Left: The extinction of the $H_2Ti(VI)O_4$ complex in aqueous solutions illustrating the amount of detected Li_2O_2. Right: Lambert-Beer type

calibration curve used to determine the amount of Li_2O_2 in the cathodes. The curve is made by measuring the absorbance of solutions with a known amount of peroxide. In the graph, the amount of Li_2O_2 is represented by a capacity equivalent.

The chemical quantification of Li_2O_2 using the Ti-complex presumes that Li_2O_2 reacts with water forming LiOH and H_2O_2. Another reaction is, however, possible

$$Li_2O_2 + H_2O \rightarrow ½O_2 + 2LiOH \quad \text{(S3)}$$

If this reaction takes place, the amount of Li_2O_2 would be underestimated, since the Ti() complex is only oxidized by H_2O_2 that is not formed during this reaction.

Experimentally we did not observe any O_2 evolution from cathodes submerged in H_2O and previous McCloskey et al. used a similar method to convert Li_2O_2 and LiO_2 from identical cathodes into H_2O_2, and detailed tests of the method showed that all Li_2O_2 was converted to H_2O_2.[4]

Electrochemical impedance spectroscopy

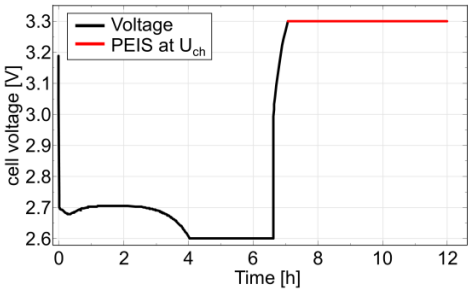

Figure S3. Typical voltage profile used to measure the impedance at specific potentials during charge. All impedance measurements follow the procedure: a) discharge to 2.6 V at 130 mA/g_{carbon} followed by 150 min at 2.6 V, b) charge to U_{ch} at 130 mA/g_{carbon}, and c) continuous EIS measurements at U_{ch} until the current decreased to 13 mA/g_{carbon}. The voltage profile show a measurement with U_{ch} = 3.30 V.

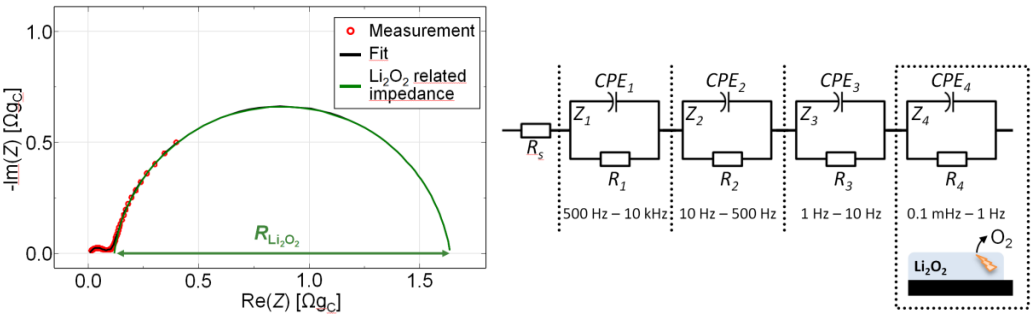

Figure S4. Left: Typical EIS measurement performed at a constant potential U_{ch}. The spectrum is dominated by the low frequency arc that has been shown to relate to the Li_2O_2 reduction during discharge and Li_2O_2 oxidation during charge.[5] Right: The equivalent circuit used to describe the impedance during charge. The allowed peak-frequency intervals of all processes are listed in the figure. As previously shown, Z_4 is related to the oxygen oxidation and double layer capacitance of the cathode.[5]

As discussed in a previous publication, the pseudocapacitance C^* is calculated using[5]

$$\boldsymbol{C^* = Q^{1/n}\left(\frac{R_\Omega R}{R_\Omega + R}\right)^{(1-n)/n}},$$

where R, Q and n are fitting parameters from the Voigt elements, and R_Ω is the DC resistance at the investigated frequency.

References

1. S. Meini, M. Piana, H. Beyer, J. Schwammlein, and H. A. Gasteiger, *J. Electrochem. Soc.*, **159**, A2135–A2142 (2012).

2. R. Younesi, N. Ingh, S. Urbonaite, and K. Edström, in *ECS transaction*,, p. 121–127 (2010).

3. G. Eisenberg, *Ind. Eng. Chem. Anal. Ed.*, **15**, 327–328 (1943).

4. B. D. McCloskey, A. Valery, A. C. Luntz, S. R. Gowda, G. M. Wallra, J. M. Garcia, T. Mori, and L. E. Krupp, *J. Phys. Chem. Lett.*, **4**, 2989–2993 (2013).

5. J. Højberg, B. D. McCloskey, J. Hjelm, T. Vegge, K. Johansen, P. Norby, and A. C. Luntz, *ACS Appl. Mater. Interfaces*, **7**, 4039–4047 (2015).

Impedance-based Battery Management for Metal-O_2 Systems

Andreas E. Christensen[a,c,*], Jonathan Højberg[b,c], Poul Norby[c], Tejs Vegge[c]

[a] *Lithium Balance A/S, Baldershøj 26C, 2635 Ishøj, Denmark*
[b] *Haldor Topsøe A/S, Nymøllevej 55, 2800 Kgs. Lyngby, Denmark*
[c] *DTU Energy, Frederiksborgvej 399, 4000 Roskilde, Denmark*

Abstract

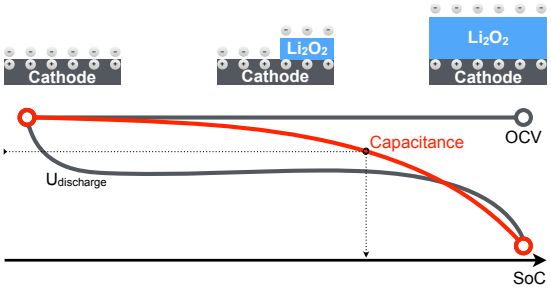

Li-O_2 batteries have received wide attention as an enabling technology for a mass-market entry of electric vehicles due to a potential capacity much higher than current Li-ion technology. In electric vehicles, reliable estimation of the state-of-charge (SoC) is crucial to determine the remaining capacity, but Li-O_2 batteries are very different to Li-ion batteries, and current SoC-estimation methods prove insufficient. In Li-O_2 batteries, the capacity is highly dependent on the discharge rate, since different current densities enable different growth mechanisms of Li_2O_2, and an on-board calibration of the SoC is therefore needed. Such a calibration is typically performed by measuring the open-circuit voltage (OCV), but as the OCV of the Li-O_2 battery does not change as a function of capacity, this method cannot be used. In this manuscript, we propose a method, based on a single-frequency electrochemical impedance measurement, to estimate the remaining capacity and assess the state-of-health by calculating the capacitance of the positive electrode where the discharge products are formed. The results show that the capacitance is a good measure of the remaining capacity and that the SoC estimation can be improved significantly by the calibration.

Highlights

– *A new method to estimate capacity and degradation in metal-O2 batteries is proposed*
– *The method uses impedance measurement to determine the positive electrode capacitance*
– *Extensive testing on Li-O2 batteries show a decreasing capacitance during discharge*
– *The proposed method is able to reduce the SoC estimation uncertainty to less than 10 %*

Keywords: Battery management, Metal-O_2, Li-O_2, Impedance spectroscopy, SoC, State-of-health

1. Introduction

The continued research in improving the performance of batteries for portable devices and electric vehicles has led to an increasing interest in metal-O_2 battery technologies such as Li-O_2, Al-O_2, Mg-O_2, and Na-O_2 [1, 2], because these technologies offer specific energies that are much higher than the battery technology powering today's devices. For electric vehicles, the Li-O_2 battery technology has the potential of increasing the driving range by up to 4 times, compared to the electric vehicles on the market in 2014 [3]. To ensure safe and reliable performance from any battery, and to predict remaining capacity, a battery management system (BMS) is needed. The two important BMS functionalities are the calculation of the remaining capacity in the batteries, the state-of-charge (SoC), and the health of the battery; generally combining capacity retention

*Corresponding author. Tel.: +45 5851 5104 Fax.: +45 5851 5098
Email address: andreas@lithiumbalance.com (Andreas E. Christensen)

on cycling and power capability. The health parameter is referred to as the state-of-health (SoH). The SoC and SoH is calculated by the BMS to predict the performance under different scenarios, to enable optimised usage of the remaining capacity, and even preventing dangerous situations that may occur if the battery powered device, e.g. an electric vehicle, is suddenly without power. The SoC can be calculated in numerous ways, with the most simple being a comparison of terminal voltage to previously recorded cycling data of cell voltage and battery capacity. A slightly more complex approach is to continuously monitor and integrate the current over time, also known as coulomb counting [4]. The coulomb counting method accumulates errors if calibration is not performed, as it relies on the accuracy of the measurement and several methods for mitigating this have been proposed for lead-acid and lithium-ion batteries [5]. Common for the secondary metal-O_2 technologies is that the main electrochemical process is unchanged during discharge and charge (assuming no degradation). This means that the open circuit voltage (OCV) does not change as a function of SoC. Furthermore, constant current measurements show a flat discharge plateau in a majority of the discharge period. This has been shown for Li-O_2 and Na-O_2 batteries [6, 7], as well as for Mg-O_2 and Al-O_2 [8, 9]. Taking the well studied Li-O_2 battery as an example, the dominating process during discharge is reduction of oxygen to deposit Li_2O_2 on top of an existing Li_2O_2 layer [10]. Initially Li_2O_2 is deposited on the pristine positive electrode and later the process changes to Li_2O_2 depositing on Li_2O_2. As this process continues during the entire discharge, both OCV and discharge potential is constant until the end of discharge, where other processes become limiting, resulting in a rapid voltage drop referred to as "sudden death". It has also been observed that the current densities have a significant impact on the onset of sudden death and thus available capacity, due to the increase in required electron transport through the poorly conducting Li_2O_2 layer [11, 12, 13]. Since the coulomb counting method relies on a known total capacity to predict sudden death, the method is not well suited for predicting the remaining capacity in these batteries.

New methods have to be developed to overcome the constant OCV and flat discharge plateau that otherwise would complicate accurate online prediction of remaining capacity in Li-O_2 batteries. In the following, we propose a method to accurately predict the SoC of Li-O_2 batteries using a single frequency impedance measurements to estimate the remaining capacity as well as the degradation of the battery materials. Since the method is not limited to Li-O_2, we will also discuss the applicability in other metal-O_2 systems.

2. Experimental

Electrochemical measurements were performed on Li-O_2 batteries using 2-electrode Swagelok cells that were assembled inside an Ar-filled glovebox (<3 ppm O_2 and H_2O). The batteries used an XC72 carbon black positive electrode (Vulcan XC72, Cabotcorp, GA), and 1 M LiTFSI (99.95 % Sigma-Aldrich) in 1,2-dimethoxyethane (BASF) electrolyte was used with a Whatman GF/A glass fiber separator (Whatman) and lithium anode (HongKong Wisdom Tech Company). The carbon electrodes were made by air-spraying a slurry of XC72 Carbon Black and PTFE (60 wt% dispersion in water) in a wt/wt ratio of 3:1 as described in Mekonnen et al. [14]. All experiments were performed in a temperature controlled environment at 25 °C. Electrochemical impedance spectroscopy (EIS) and discharge-charge curves were measured using Bio-Logic VMP3 and MPG2 potentiostats. Impedance measurements were performed throughout a number of different current profiles. All reported impedance measurements were performed at OCV after at least 3 h rest. The full impedance spectra included frequencies between 20 kHz and 10 mHz with 15 points per decade and an alternating current (AC) amplitude of 10 mV (potentiostatic mode) or a current density of 13 mA g_c^{-1} (galvanostatic mode). In measurements replicating an actual BMS system, only one frequency (10 mHz) was investigated in order to establish a fast and simple assessment. The validity of using only this single frequency was confirmed by comparison with a full spectrum. For all experiments on Li-O_2 batteries, the discharge capacity was calculated as the capacity between fully charged and the the onset of sudden death; indicated by the voltage decreasing to 2.2 V. The current densities were calculated based on the carbon-loading of the electrodes, which typically was ~6.5 mg cm^{-2} for an electrode with a diameter of 10 mm.

2.1. Impedance analysis

EIS is used in many systems to perform in situ determination of certain parameters like degradation of secondary Li-ion batteries [15, 16, 17], capacity fading of Li-S batteries [18], and discharge mechanisms for Si-air [19]. In Li-O_2 batteries, it has previously been shown that the low frequency (<1 Hz) contribution of the impedance is related to the positive electrode [20, 21, 22]. EIS measurements in this frequency

regime gives a capacitance value that relates to the double layer capacitance of the electrode [20]. The best measurements of this value is performed at OCV, as this gives a uniform distribution of charged species in the entire electrode, but our initial experiments showed that it is also possible to measure the capacitance under constant load. Because the measurements under load introduces new variables, we are focusing on measurements at OCV in this manuscript. At OCV, the oxygen reduction reaction and Li_2O_2 oxidation reactions are very slow, and if the EIS excitation signal is sufficiently small, the impedance signal from the positive electrode becomes capacitive at the relevant frequencies (see insert in Figure 2). This means that the capacitance can be determined by the simple expression shown in Equation 1 [23].

$$C = \frac{-1}{2\pi f \cdot Z_{im}} \tag{1}$$

where f is the AC perturbation frequency and Z_{im} is the imaginary part of the corresponding impedance. It is important that other impedance contributions from processes with similar time constants do not overlap at the frequency used for the calculation. A frequency of 10 mHz was chosen because it was the highest frequency (and hence shortest measurement time) with the main contribution from the positive electrode capacitance.

2.2. Relating capacitance to the discharge processes

The capacitance of the positive electrode is determined by the electrochemical double layer capacitance that reflects the ability of the system to store electrical charge by rearranging the charges in the carbon (electrons) and in the electrolyte (ions). The value is proportional to the surface area and depends on the choice of electrolyte, the concentration of charged species in the electrolyte (salt concentration) and deposits on the carbon surface. For a Li-O_2 battery, Li_2O_2 is deposited on the surface during discharge and as Li_2O_2 is a dielectric, the capacitance of the surface will change. The capacitance of XC72 is 12.6 F g_c^{-1} in an organic aprotic electrolyte as reported by Barbieri et al., which corresponds to 5.4 μF cm^{-2}, using a measured BET area of 235 m^2 g^{-1} [24]. The capacitance of the Li_2O_2 layer is calculated using Equation 2.

$$C = \epsilon_r \epsilon_0 \frac{A}{d} \tag{2}$$

where ϵ_r is the relative permittivity, ϵ_0 is the vacuum permittivity, A is the area of the layer and d is the thickness of the layer. The relative permittivity of Li_2O_2 has been determined to be 35 by Gerbig et al. [25], and using these values it can be calculated that going from a pristine carbon surface without Li_2O_2 to ~6 nm of Li_2O_2 will halve the capacitance (a detailed description of this is found in Supporting Information S1). The proposed SoC estimation is based on analysis of the decrease in capacitance as the Li_2O_2 is deposited.

As it will be shown later, the correlation between the capacity and capacitance is following the same trend for all the performed Li-O_2 experiments and that trend can be described by the simple functional form in Equation 3.

$$C = C_0 - p_2\left(1 - \exp\left(\frac{Q}{p_1}\right)\right) \tag{3}$$

where C_0 is the initial capacitance, Q is the capacity, and p_1 and p_2 are refined parameters determining the exponential shape.

2.3. Scaling the current density

The experiments are divided into two categories, (i) constant current discharges at different current densities, and (ii) dynamic current densities with different profiles. Figure 1 shows the applied techniques. Current densities are selected on basis of a future scenario, where electric vehicles will be powered by metal-O_2 batteries as the sole source of power. The scaling of the peak and average current densities are based on an electric vehicle with a 100 kWh battery, a sustained high power of 55 kW and a peak power of 105 kW, which matches most electric vehicles today in terms of peak power and is superior in terms of capacity [27]. See Supporting Information S2 for details.

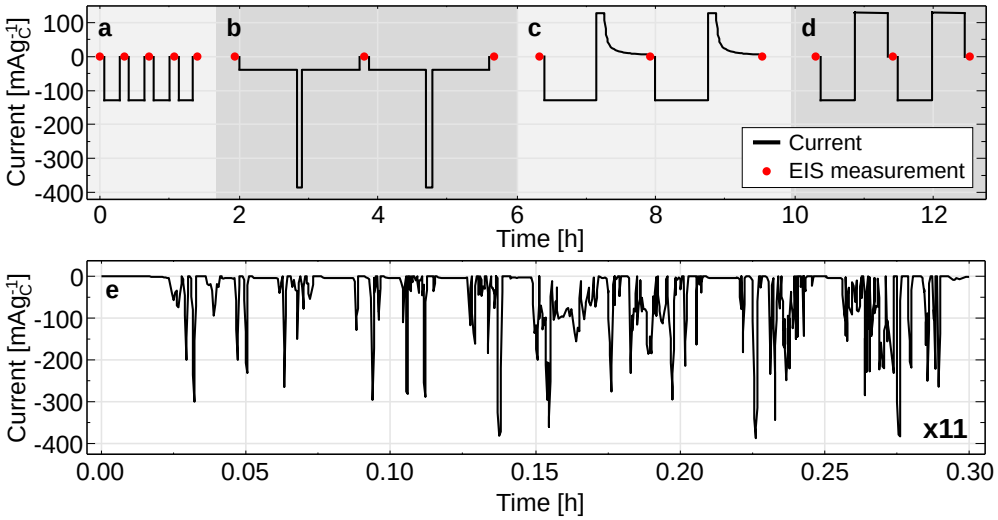

Figure 1: Current profiles used in the experiments. (a) discharge at 130 mA g_c^{-1} to 2.0 V interrupted by impedance measurements every 100 mAh g_c^{-1}. 13 mA g_c^{-1}, 39 mA g_c^{-1}, and 390 mA g_c^{-1} were tested in similar manner. (b) staircase discharge profile with 33 mAh g_c^{-1} at 39 mA g_c^{-1}, 33 mAh g_c^{-1} at 390 mA g_c^{-1} and 33 mAh g_c^{-1} at 39 mA g_c^{-1} between each impedance measurement. (c) discharge of 130 mA g_c^{-1} for 100 mAh g_c^{-1} with 3.20 V voltage-limited charge at 130 mA g_c^{-1} to reduce electrochemical decomposition to a minimum. (d) capacity limited galvanostatic cycling at 130 mA g_c^{-1} limited to 65 mAh g_c^{-1}. The charge was limited to 4.5 V to avoid severe electrolyte decomposition. (e) drive cycle from ISEA-RWTH Aachen recorded from a Fiat 500 eCity [26], scaled to a maximum of 390 mA g_c^{-1} (55 kW).

3. Results

To investigate the correlation of the capacitance during discharge and charge to the SoC, SoH and power capability of the Li-O_2 battery, we have performed a number of experiments based on the current profiles listed in Figure 1. All experiments with Li-O_2 batteries show a decrease in the capacitance as the battery is discharged.

Figure 2 shows the capacitance decrease as a function of capacity and it is clear how the capacitance changes even though the voltage is unchanged. The capacitance is calculated according to Equation 1 and the insert in Figure 2 shows how the impedance measurement is related to the capacitance. For every data point, a unique impedance measurement was made and the capacitance was determined. At the end of discharge, when the battery reached sudden death, the capacitance was 50 % of the initial value.

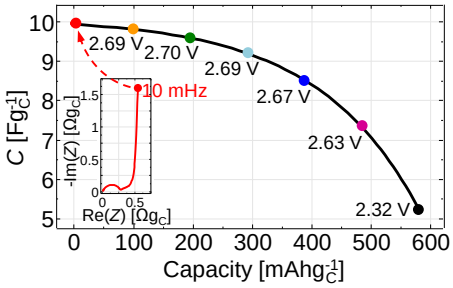

Figure 2: Capacitance as a function of the capacity for a constant current discharge at 130 mA g_c^{-1}. Insert shows a Nyquist plot of the impedance measurement, where the capacity data is highlighted. The voltage labels are measured during discharge prior to the impedance measurements. The OCV was 2.83 V during the entire discharge.

Figure 3a and Figure 3b show additional measurements of the dependence between the capacitance and the SoC at the different current profiles seen in Figure 1. When testing Li-O_2 batteries using different current profiles, the capacity varies significantly. From Table 1 it is seen that the discharge capacity can vary up to a factor of ~14 between the conducted measurements. The purpose of a BMS is to predict the remaining capacity, and in the following we have therefore normalised each discharge capacity to the capacity at 2.2 V, to investigate how well the remaining capacity is predicted by the capacitance. Even though all initial capacitances are very similar, we have chosen to normalise this value also, as this is what would be done in an actual BMS, where the capacitance may vary between batteries and may change over time due to degradation. The original data is pre-

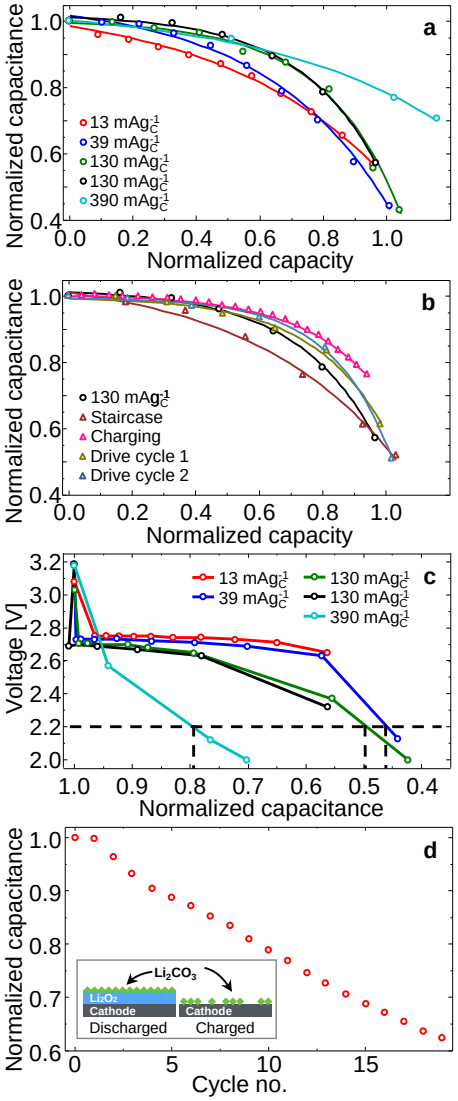

Figure 3: Results from experiments on Li-O_2 batteries, data labeled according to current profiles in Figure 1. Capacitance is normalised to the initial value before discharge, and capacity is normalised to the value at 2.2 V. (a) constant current at four current densities: 13 mA g_c^{-1}, 39 mA g_c^{-1}, 130 mA g_c^{-1}, and 390 mA g_c^{-1}, (b) dynamic current profiles according to Figure 1 and data from a 130 mA g_c^{-1} constant current experiment to make comparison easier, (c) discharge voltage and capacitance from constant current experiments, showing the relation between current density and capacitance. (d) cycling experiment over 20 cycles showing decreasing capacitance as a function of cycle number, insert showing possible degradation mechanism by Li_2CO_3 accumulation.

sented in Supporting Information S3. All measurements have been fitted to Equation 3 and it is seen that they all follow the same trend. Table 1 shows the experimental values and derived parameters, and three observations are made: (i) all initial capacitances fall within 10.0 F g_c^{-1} ± 0.4 F g_c^{-1}, (ii) the trend of the decreasing capacity is very similar for all measurements performed at current densities varying a factor of 30, and at both dynamic and constant current experiments, and (iii) all capacitances have decreased to approximately 50 % in the end of discharge, except the high current measurement at 390 mA g_c^{-1} and the measurement including charging; Both these exceptions will be discussed further below.

Figure 3c depicts how the voltage during discharge relates to the capacitance for different current densities, and it is evident that the current densities impact the discharge capacity, and thereby the capacitance at 2.2 V. Figure 3d shows the normalised capacitance in the fully charged state, as a function of cycle number. Upon cycling, the capacitance decreases almost linearly to approximately 65 % after 20 cycles.

	C_0	p_1	p_2	$Q_{2.2V}$	$\frac{C_{2.2V}}{C_0}$
	F g_c^{-1}	mAh g_c^{-1}	F g_c^{-1}	mAh g_c^{-1}	-
13 mA g_c^{-1}	10.3	518	820	1001	53%
39 mA g_c^{-1}	10.0	300	467	767	44%
130 mA g_c^{-1}	9.83	169	76.9	700	52%
130 mA g_c^{-1}	10.1	148	90.9	599	50%
390 mA g_c^{-1}	10.2	67	465	117	78%
Staircase	10.1	241	610	519	54%
Charging	10.3	377	44.8	1614	69%
Drive cycle 1	10.0	188	54.9	812	59%
Drive cycle 2	9.64	124	21.8	652	56%

Table 1: Experimental values and parameters obtained by fitting experimental data to Equation 3. C_0 is the initial capacitance, $Q_{2.2V}$ is the discharge capacity at the 2.2 V cut-off, $\frac{C_{2.2V}}{C_0}$ is the fraction of capacitance at the 2.2 V cut-off to the initial capacitance.

4. Discussion

In the following, we show the correlation between the capacitance and the capacity, which qualifies the method for further studies targeting commercial use in a Li-O_2 BMS.

4.1. State-of-charge

The constant current experiments presented in Figure 2 show how the capacitance changes as a function of capacity. The correlation is decreasing and at the end of discharge the capacitance is 50 % of the initial value, which is in very good agreement with the estimates based on Equation 2. Assuming that the change

is due to a uniform layer of Li_2O_2, this corresponds to a layer thickness of ~6 nm at these current densities, and as discussed in Section 2.2, this is in line with the general understanding of the sudden death mechanism [13]. The voltage during discharge is shown in Figure 2 as labels on the capacitance data points, and remains unchanged at ~2.70 V between 100 % and 33 % SoC, whereas the capacitance decreases as the battery is discharged. Seeing that all measurements behave similarly, this shows that the capacitance holds information about the SoC, that is not possible to obtain using voltage based measurements.

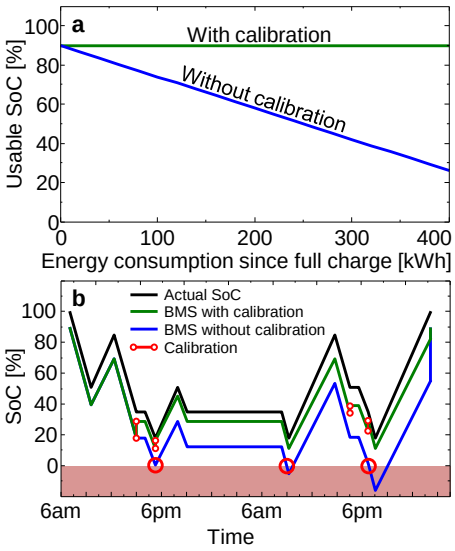

Figure 4: (a) Effect of error accumulation in coulomb counting and capacity reserve, without reaching a full charge. (b) Scenario showing difference in estimation of useable capacity between a BMS using calibration based on capacitance, and no calibration other than full-charge correction, shown as a vertical line at the end. The circles at 0 % SoC highlights places were the capacitance calibration would enable further discharging of the battery.

To estimate the error of the SoC estimation based on capacitance measurements, the two drive cycle measurements and the measurement at 130 mA g_c^{-1} in Figure 3b are used to give a minimum relative capacity based on a given capacitance. The points of calibration used in the drive scenario are presented in Supporting Information S4, Table S2.

To test the effect of the calibration, we have designed a BMS system based on the following assumptions:

1. Due to high current dependency on capacity, a reserve of ~10 % SoC is needed, resulting in 90 % useable capacity.
2. Coulomb counting has a ~3 % accumulation of error.
3. The SoC is calibrated at end of full charge.
4. Fast charging is not considered, charging performed at ~10 kW.

If no SoC calibration is performed, the coulomb counting error and the need for a capacity reserve will result in a signicant decrease of useable capacity as the battery is discharge and charged. During discharge, the accumulated error corresponds to 3 % and during charge, the error is 13 %, due to the additional need of a 10 % capacity reserve for the following discharge. Figure 4a shows the effect of the combined error of 16 % on a 100 kWh battery as a function of energy consumption of up to 400 kWh without fully charging the battery. When the battery is fully charged, a BMS would be able to correct the estimation of useable capacity to the nominal capacity of the battery without the capacitance calibration, and thus reset the useable capacity to 90 %. Without the SoC calibration, the useable SoC could decrease to 26 % over an accumulated energy consumption of 400 kWh, whereas the SoC calibration based on capacitance would be able to keep the SoC estimation at 90 %, thus maximising the useable capacity.

Since the capacity of future metal-O_2 batteries is expected to increase, we postulate a use-scenario for the batteries based on ~10 kW charging power available and no need for fast charging with daily use. This scenario is illustrated in Figure 4b, where the battery is respectively discharged, charged or at rest. The calibrations performed in Figure 4b enables the BMS to more accurately predict the remaining capacity, whereas the estimated capacity without calibration would become less than zero (shown on the figure as circles when the SoC is crossing the 0 % threshold), warning the vehicle or driver to stop. The capacitance calibration is less accurate in the less critical beginning of discharge, due to the slope of the capacitance correlation to the capacity, and gradually more accurate as the battery is discharged. Figure 4b shows that the calibrations performed below 50 % SoC have the possibility to initially correct the SoC to an uncertainty of less than ~10 %, and when performed multiple times, able to further minimise the uncertainty of the SoC estimation, resulting in periods with an uncertainty of less than 5 % SoC.

4.2. Power capability

The current density of 390 mA g_c^{-1} is only able to provide 12 % of the capacity compared to the current density of 13 mA g_c^{-1}. This indicates that the available capacity depends explicitly on the current density. For correct estimation of the available power, the internal resistance is usually used to predict if the terminal voltage of a battery will exceed the limit during high

power demands. For Li-O_2 batteries, this is not possible since the resistance is almost unchanged during the entire discharge [20]. Previously, we saw that the capacitance of the 390 mA g_c^{-1} experiment did not decrease to ~50 % of the initial capacitance. If we look at the voltage during the constant current experiments (Figure 3c), we see that the high current density experiments (130 mA g_c^{-1} and 390 mA g_c^{-1}) have significantly higher overpotentials, thus the 2.2 V limit is reached prematurely. From the measurements, it seems that current densities of 390 mA g_c^{-1} are only supported at capacitances above 78 % of the initial capacitance, while it is possible to use 130 mA g_c^{-1} until a capacitance of 50 %. This shows that the capacitance can also be used to estimate the maximum power that the battery is capable of delivering at the given state.

4.3. State-of-health

The cycling experiment (Figure 3d) shows how the capacitance of a fully charged positive electrode decreases as a function of cycle number. From several papers [14, 28, 29, 30] it has been shown that Li_2CO_3 and similar species are accumulating upon charging and are immobilised in the positive electrode (see Figure 3d, insert). The presence of Li_2CO_3 in the cathode has two main effects on the battery performance. First, the amount of Li_2CO_3 will increase for each cycle, resulting in a decrease of the available active area for Li_2O_2 deposition. This results in a lower discharge capacity for the battery. Second, the inclusion of Li_2CO_3 in the deposited Li_2O_2 decreases the charge transport through the Li_2O_2, thus increasing the required overpotential [31]. It has previously been shown that even a few angstrom of Li_2CO_3 will decrease the capacitance significantly [20], and using the capacitance in the fully charged state, it is possible to track the degradation of the positive electrode, and a BMS can use the information to determine the SoH parameter related to capacity retention, and thereby the cycle life of the battery.

4.4. Further development of the model

With more knowledge about the system, it is expected that the time at OCV can be reduced significantly and that measurements can be made even while discharging or charging the battery. This could be done by employing impedance measurements in the time domain to calculate the capacitance. In this case, it might even be possible to perform SoC calibrations while driving. Another direction would be to implement an adaptive state estimation algorithm, akin to the work done by Fleischer et al. [26], using the capacitance measurements to improve the calibration uncertainties.

The charging experiment shown in Figure 3b has a much larger discharge capacity compared to the other experiments (Table 1: 1614 mAh g_c^{-1} vs 599 mAh g_c^{-1} for the 130 mA g_c^{-1} experiment), and we suspect that this is due to the accumulation of Li_2CO_3 and similar species. The reason for the capacitance not decreasing to more than 69% is not fully understood and further studies of cycling effects on Li-O_2 systems is needed.

Since the capacitance is expectedly one of the only parameters changing during large parts of the discharge, it is likely that the proposed method will be an important part of any metal-O_2 BMS. Many metal-O_2 systems show the same type of discharge and charge curves as the Li-O_2, but further studies on other metal-O_2 systems are needed to conclude if the proposed method is applicable to these systems. A likely candidate for further studies is the Na-O_2 battery, where the discharge product, NaO_2 is considered to have surface conductivity. The conductive nature of the NaO_2 is expected to cause an increase in capacitance as the battery is discharged, reflecting an increase in surface area as the NaO_2 cubes are grown [32].

5. Conclusion

A method for estimating remaining capacity, power capability and cycle life of metal-O_2 batteries has been proposed. The method was verified using Li-O_2 batteries, and the approach is expected to be transferrable to other metal-O_2 systems. Experiments showed that the capacitance of the positive electrode decreased exponentially during discharge, and that it was possible to improve the prediction the remaining battery capacity significantly based on a single frequency measurement of the positive electrode capacitance. In a typical scenario, a single SoC calibration is able to improve the available SoC by more than 10 % of the full battery capacity, by minimising the uncertainty of the SoC. The capacitance was also used to estimate a degradation of the positive electrode in a Li-O_2 batteries cycled over 20 times. This makes the method applicable not only for electric vehicles, but for batteries in a large range of electrical devices, as the measurements can be performed when needed, thus maintaining a high level of accuracy for the estimation of remaining capacity and state-of-health.

6. Acknowledgements

The authors acknowledge support of this work from the ReLiable project (Project No. 11-116792) funded

by the Danish Council for Strategic Research Program Commission on Sustainable Energy and Environment.

References

[1] M. M. Thackeray, C. Wolverton, E. D. Isaacs, Electrical energy storage for transportationapproaching the limits of, and going beyond, lithium-ion batteries, Energy & Environmental Science 5 (7) (2012) 7854. doi:10.1039/c2ee21892e.

[2] F. Cheng, J. Chen, Metalair batteries: from oxygen reduction electrochemistry to cathode catalysts, Chemical Society Reviews 41 (6) (2012) 2172. doi:10.1039/c1cs15228a.

[3] K. G. Gallagher, S. Goebel, T. Greszler, M. Mathias, W. Oelerich, D. Eroglu, V. Srinivasan, Quantifying the promise of lithiumair batteries for electric vehicles, Energy & Environmental Science 7 (2014) 1555. doi:10.1039/c3ee43870h.

[4] S. Piller, M. Perrin, A. Jossen, Methods for state-of-charge determination and their applications, Journal of Power Sources 96 (1) (2001) 113–120. doi:10.1016/S0378-7753(01)00560-2.

[5] K. S. Ng, C. S. Moo, Y. P. Chen, Y. C. Hsieh, Enhanced coulomb counting method for estimating state-of-charge and state-of-health of lithium-ion batteries, Applied Energy 86 (9) (2009) 1506–1511. doi:10.1016/j.apenergy.2008.11.021.

[6] P. Hartmann, C. L. Bender, M. Vračar, A. K. Dürr, A. Garsuch, J. Janek, P. Adelhelm, A rechargeable room-temperature sodium superoxide (NaO2) battery., Nature materials 12 (3) (2013) 228–32. doi:10.1038/nmat3486.

[7] B. D. McCloskey, J. M. Garcia, A. C. Luntz, Chemical and Electrochemical Differences in Nonaqueous LiO 2 and NaO 2 Batteries, The Journal of Physical Chemistry Letters 5 (7) (2014) 1230–1235. doi:10.1021/jz500494s.

[8] T. Shiga, Y. Hase, Y. Kato, M. Inoue, K. Takechi, A rechargeable non-aqueous MgO2 battery, Chemical Communications 49 (80) (2013) 9152–9154.

[9] R. Revel, T. Audichon, S. Gonzalez, Non-aqueous aluminium-air battery based on ionic liquid electrolyte, Journal of Power Sources 272 (c) (2014) 415–421.

[10] J. S. Hummelshø j, J. Blomqvist, S. Datta, T. Vegge, J. Rossmeisl, K. S. Thygesen, Communications : Elementary oxygen electrode reactions in the aprotic Li- air battery Communications : Elementary oxygen electrode reactions in the aprotic Li-air battery, The Journal of Chemical Physics 071101 (7) (2010) –. doi:10.1063/1.3298994.

[11] J. Chen, J. S. Hummelshø j, K. S. Thygesen, J. S. G. Myrdal, J. K. Nø rskov, T. Vegge, The role of transition metal interfaces on the electronic transport in lithium-air batteries, Catalysis Today 165 (1) (2011) 2–9. doi:10.1016/j.cattod.2010.12.022.

[12] M. D. Radin, D. J. Siegel, Charge transport in lithium peroxide: relevance for rechargeable metalair batteries, Energy & Environmental Science 6 (8) (2013) 2370. arXiv:1305.2904, doi:10.1039/c3ee41632a.

[13] V. Viswanathan, K. S. Thygesen, J. S. Hummelshj, J. K. Nrskov, G. Girishkumar, B. D. McCloskey, a. C. Luntz, Electrical conductivity in Li 2O 2 and its role in determining capacity limitations in non-aqueous Li-O 2 batteries, Journal of Chemical Physics 135 (21) (2011) 214704. doi:10.1063/1.3663385.

[14] Y. S. Mekonnen, K. B. Knudsen, J. S. G. Mýrdal, R. Younesi, J. Hø jberg, J. Hjelm, P. Norby, T. Vegge, Communication: The influence of CO2 poisoning on overvoltages and discharge capacity in non-aqueous Li-Air batteries, Journal of Chemical Physics 140 (12) (2014) 121101. doi:10.1063/1.4869212.

[15] F. Huet, A review of impedance measurements for determination of the state-of-charge or state-of-health of secondary batteries, Journal of Power Sources 70 (1998) 59–69. doi:10.1016/S0378-7753(97)02665-7.

[16] M. H. Hung, C. H. Lin, L. C. Lee, C. M. Wang, State-of-charge and state-of-health estimation for lithium-ion batteries based on dynamic impedance technique, Journal of Power Sources 268 (2014) 861–873. doi:10.1016/j.jpowsour.2014.06.083.

[17] S. Rodrigues, N. Munichandraiah, a. K. Shukla, Review of state-of-charge indication of batteries by means of a.c. impedance measurements, Journal of Power Sources 87 (1) (2000) 12–20. doi:10.1016/S0378-7753(99)00351-1.

[18] Z. Deng, Z. Zhang, Y. Lai, J. Liu, J. Li, Y. Liu, Electrochemical Impedance Spectroscopy Study of a Lithium/Sulfur Battery: Modeling and Analysis of Capacity Fading, Journal of the Electrochemical Society 160 (4) (2013) A553–A558. doi:10.1149/2.026304jes.

[19] G. Cohn, R. a. Eichel, Y. Ein-Eli, Supplement: New insight into the discharge mechanism of silicon-air batteries using electrochemical impedance spectroscopy., Physical chemistry chemical physics : PCCP 15 (9) (2013) 3256–63. doi:10.1039/c2cp43870d.

[20] J. Hø jberg, B. D. McCloskey, J. Hjelm, T. Vegge, K. Johansen, P. Norby, A. C. Luntz, An Electrochemical Impedance Spectroscopy Investigation of the Overpotentials in LiO 2 Batteries, ACS Applied Materials & Interfaces 7 (7) (2015) 150211151515002. doi:10.1021/am5083254.

[21] I. Landa-Medrano, I. Ruiz De Larramendi, N. Ortiz-Vitoriano, R. Pinedo, J. Ignacio Ruiz De Larramendi, T. Rojo, In situ monitoring of discharge/charge processes in Li-O2 batteries by electrochemical impedance spectroscopy, Journal of Power Sources 249 (c) (2014) 110–117. doi:10.1016/j.jpowsour.2013.10.077.

[22] J. Adams, M. Karulkar, V. Anandan, Evaluation and electrochemical analyses of cathodes for lithium-air batteries, Journal of Power Sources 239 (0) (2013) 132–143. doi:10.1016/j.jpowsour.2013.03.140.

[23] M. Orazem, B. Tribollet, Electrochemical impedance spectroscopy, John Wiley & Sons, 2008.

[24] Barbieri, Hahn, Herzog, Kotz, Capacitance limits of high surface area activated carbons for double layer capacitors, Carbon 43 (6) (2005) 1303–1310. doi:10.1016/j.carbon.2005.01.001.

[25] O. Gerbig, R. Merkle, J. Maier, Electron and ion transport in Li2O2, Advanced Materials 25 (2013) 3129–3133. doi:10.1002/adma.201300264.

[26] C. Fleischer, W. Waag, H. M. Heyn, D. U. Sauer, On-line adaptive battery impedance parameter and state estimation considering physical principles in reduced order equivalent circuit battery models: Part 2. Parameter and state estimation, Journal of Power Sources 262 (2014) 457–482. doi:10.1016/j.jpowsour.2014.03.046.

[27] Compare Electric Vehicles Side-by-Side, (accessed 2015-03-19).
URL http://www.fueleconomy.gov/feg/evsbs.shtml

[28] B. D. McCloskey, D. S. Bethune, R. M. Shelby, T. Mori, R. Scheffler, A. Speidel, M. Sherwood, a. C. Luntz, Limitations in Rechargeability of Li-O2Batteries and Possible Origins, The Journal of Physical Chemistry Letters 3 (2012) 3043–3047. doi:10.1021/jz301359t.

[29] M. M. Ottakam Thotiyl, S. a. Freunberger, Z. Peng, P. G. Bruce, The carbon electrode in nonaqueous Li-O2 cells, Journal of the American Chemical Society 135 (1) (2013) 494–500. doi:10.1021/ja310258x.

[30] B. M. Gallant, R. R. Mitchell, D. G. Kwabi, J. Zhou, L. Zuin,

C. V. Thompson, Y. Shao-Horn, Chemical and Morphological Changes of LiO2 Battery Electrodes upon Cycling, The Journal of Physical Chemistry C 116 (2012) 20800–20805. arXiv:10.1021/jp308093b, doi:10.1021/jp308093b.

[31] J. M. Garcia-Lastra, J. S. G. Myrdal, R. Christensen, K. S. Thygesen, T. Vegge, DFT+U study of polaronic conduction in Li2O2 and Li2CO3: Implications for Li-air batteries, Journal of Physical Chemistry C 117 (11) (2013) 5568–5577. doi:10.1021/jp3107809.

[32] P. Hartmann, C. L. Bender, J. Sann, A. K. Dürr, M. Jansen, J. Janek, P. Adelhelm, A comprehensive study on the cell chemistry of the sodium superoxide (NaO2) battery., Physical chemistry chemical physics : PCCP 15 (28) (2013) 11661–72. doi:10.1039/c3cp50930c.

Supporting Information: Impedance-based Battery Management for Metal-O_2 Systems

Andreas E. Christensen[a,c,*], Jonathan Højberg[b,c], Poul Norby[c], Tejs Vegge[c]

[a] *Lithium Balance A/S, Baldershøj 26C, 2635 Ishøj, Denmark*
[b] *Haldor Topsøe A/S, Nymøllevej 55, 2800 Kgs. Lyngby, Denmark*
[c] *DTU Energy, Frederiksborgvej 399, 4000 Roskilde, Denmark*

S1. Li_2O_2 capacitance

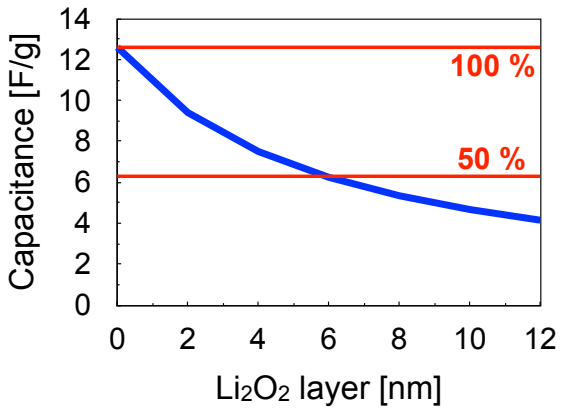

Figure S1: Calculation of capacitance depending on Li_2O_2 layer thickness, showing where capacitance is 50 % of the initial 12.6 F g_c^{-1}

The calculation of capacitance is based on a simple model with two capacitances: the capacitance of the pristine carbon electrode, and the capacitance of the Li_2O_2 layer deposited on the carbon electrode. Equation 2 in the manuscript and a calculation of two capacitances in series is used to calculate the total capacitance depending on the Li_2O_2 layer thickness. The final formula is:

$$C_{total}(d) = \left(\frac{1}{\epsilon_r \epsilon_0 A/d} + \frac{1}{C_{\mathrm{XC72}}} \right)^{-1} \tag{1}$$

Where ϵ_r is the relative permittivity, ϵ_0 is the vacuum permittivity, A is the area of the layer, d is the thickness of the Li_2O_2 layer, and C_{XC72} is the capacitance of XC72 in an aprotic electrolyte. For the case where $d = 0$ only the capacitance of XC72 is used, all other calculations use: $\epsilon_r = 35$ [1], $\epsilon_0 = 8.9 \cdot 10^{-12}$, $A = 235$ m^2 g^{-1}, and $C_{\mathrm{XC72}} = 12.6$ F g_c^{-1} [2].

*Corresponding author.
Email address: andreas@lithiumbalance.com (Andreas E. Christensen)

S2. Scaling of current densities

Target energy kWh	$V_{discharge}$ V	$Q_{2.2V}$ mAh g_c^{-1}	m_c kg	I_{high} mA g_c^{-1}	P_{high} kW	I_{peak} mA g_c^{-1}	P_{peak} kW
100	2.65	700	53.9	390	55.7	736	105.2

Table S1: Calculation based on target energy of 100 kWh.

The current densities are calculated based on a target energy of 100 kWh, a discharge voltage plateau of 2.65 V, and a capacity of 700 mAh g_c^{-1}. Peak power of 105 kW corresponds to expected peak motor power for electric vehicles, based on comparison of 8 vehicles, model year 2013 [3].

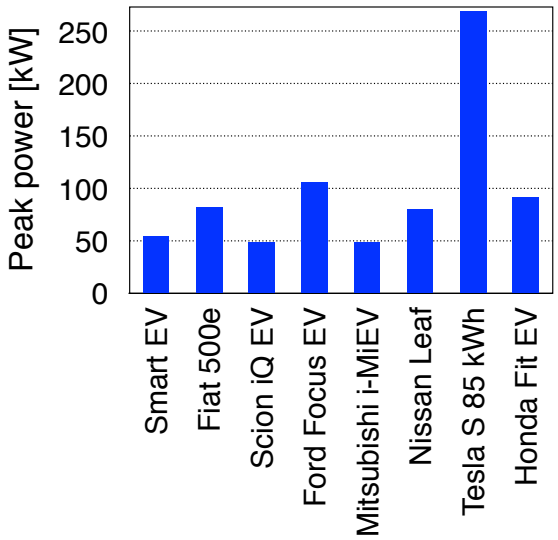

Figure S2: Comparison of peak motor power for selected electric vehicles, model year 2013.

S3. Original capacitance data

Capacitance data before normalisation, from all experiments.

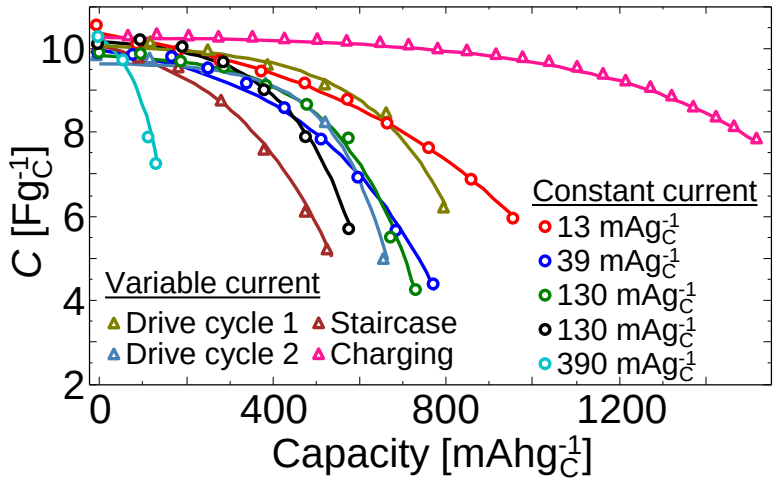

Figure S3: Capacitance data from all Li_2O_2 experiments.

S4. SoC estimation error

To estimate the error of the SoC estimation based on capacitance measurements, the two drive cycle measurements and the measurement at 130 mA g_c^{-1} in Figure 3b in the manuscript are used to give a minimum relative capacity based on a given capacitance. The points of calibration used in the drive scenario are presented in Table S2.

Actual capacity	Capacitance	Minimum capacity
100%	100%	79%
85%	99%	69%
68%	98%	62%
51%	94%	39%
35%	90%	29%
18%	83%	18%
1%	61%	1%

Table S2: Calibration data.

It is clearly seen that the capacity is not estimated well in the beginning of the discharge, but in this regime coulomb counting will be sufficient. In the end of the discharge, where the exact knowledge of the remaining capacity is much more important, the estimation is, however, much more accurate. This enables a precise determination of the SoC and thereby a better utilisation of the battery capacity as shown in Figure 4 in the manuscript.

References

[1] O. Gerbig, R. Merkle, J. Maier, Electron and ion transport in Li2O2, Advanced Materials 25 (2013) 3129–3133. doi:10.1002/adma.201300264.

[2] Barbieri, Hahn, Herzog, Kotz, Capacitance limits of high surface area activated carbons for double layer capacitors, Carbon 43 (6) (2005) 1303–1310. doi:10.1016/j.carbon.2005.01.001.

[3] Compare Electric Vehicles Side-by-Side, (accessed 2015-03-19).
URL http://www.fueleconomy.gov/feg/evsbs.shtml

Rechargeability/Reversibility of Ionic Liquids in Li-O_2 Battery/Cells

Supti Das[1], Jonathan Højberg[1,2], ……

[1] Department of Energy Conversion and Storage, Technical University of Denmark, Frederiksborgvej *399, DK-4000 Roskilde, Denmark*

[2]Haldor Topsøe A/S, Nymøllevej 55, DK-2800 Kgs. Lyngby, Denmark

Abstract

Keywords:

1. Introduction

A quest of alternative energy storage systems has led to significant attention towards Li-air (or Li-O_2) battery during the past decade.[1-6] Exceptionally high theoretical energy density comparable to gasoline makes Li-O_2 battery more appealing than other types of metal-ion or metal-air battery systems. But there are many challenges that are essential to overcome in order to bring this technology into practical and commercially viable applications. In the Li-O_2 battery, oxygen is reduced during discharge to form Li_2O_2 at the air electrode while the lithium electrode is oxidized. During charge, Li_2O_2 is oxidized at the air electrode and lithium is plated on the lithium electrode. To ensure full rechargeability, it is important that the reaction is completely reversible with an insignificant loss in degradation reactions. The development of an electrolyte with sufficient stability towards Li_2O_2 and intermediate reaction products like the superoxide radical has been described as the biggest challenge in the development of the Li-O_2 system,[6] and, so far, no stable electrolytes have been identified.[1, 7-9] Moreover a suitable electrolyte for Li−O_2 cells should also have superior anodic stability; low volatility to avoid solvent evaporation in open cell system; high oxygen solubility and diffusivity to enable sufficient oxygen transport to the air electrode to support the required currents; low viscosity; high conductivity and a wide electrochemical window. Although many solvents have been investigated in this regard, none of them fulfill the above mentioned requirements. Ionic liquids (ILs) have been proposed by several researchers as suitable

electrolyte because of their relatively high electrochemical and chemical stability against $O_2\cdot$ radicals.[3-4, 10-18]

Ionic Liquids (ILs), generally comprised by an organic cations and inorganic anions, are a class of molten organic salts which are fluids at temperatures around 100 °C or below.[19-23] They have stimulated much interest for a variety of chemical, physical and biological processes in past few decades due to their remarkable and unique properties such as negligible volatility, thermal & electrochemical stability, non flammability, tunable viscosity, high ionic conductivity and superior hydrophobicity. Recently ILs have received significant attention as safe and environmentally friendly electrolytes in electrochemical devices such as Li-O_2 battery due to the nonvolatile nature.[4, 11, 18, 24-25] Another interesting fact about these ILs is that the physicochemical properties can be tuned just by varying the combinations of cations and anions. However, one should take into account that not all ILs are suitable as electrolyte. As an example, ILs based on imidazolium families is unstable against peroxide radical attack.[26] On the other hand pyrrolidinium and piperidinium based cations with combination of bis(trifluoromethanesulfonyl)imide ($TFSI^-$) anion has been reported to meet the criteria of good electrolytes.[2] There are many discussions in literature regarding the use of ionic liquid-based electrolytes in Li-oxygen cells. Bresser *et al.*[27] have recently reviewed the utilization of ionic liquids in Li-O_2 battery. The first report on ionic liquid as electrolye in Li-air battery was published by Kuboki *et al*. in 2005.[4] In their study hydrophobic Imidazolium based ionic liquids were investigated as electrolyte solvent in primary lithium-O_2 and lithium-air cells. Mizuno *et al.*[28] studied the applicability of N-methyl-N-propyl piperidinium bis(trifluoromethanesulfonyl)imide (PP13TFSI) as electrolyte solvent for lithium-O_2 batteries, where they found retention of reversible capacity about 60% of the initial capacity after 30 cycles. Recently Monaco *et al.*[14] reported the use of N-butyl-N-methylpyrrolidinium bis-(tri fluoromethane sulfonyl) imide–lithium-bis-(trifluoromethane-sulfonyl) imide (P14TFSI-LiTFSI, 9:1) as electrolyte in a novel Li-O_2 flow cell configuration by circulating the oxygen-saturated electrolyte through the cell. In a more recent study, Elia *et al*.[11] have demonstrated the reversibility of, P14TFSI−LiTFSI) electrolyte with energy efficiency in the order of 82%, by using capacity-limited

galvanostatic cycling. In another report the stability of P14TFSI−LiTFSI electrolytes was investigated by Piana *et al.*[15] in a different Li-O_2 cell configurations. They showed that P14TFSI gets reduced on metallic lithium but it works well in specially designed configuration. They also mentioned that poor cyclability in the particular cell design might be due to the insufficient long-term stability against the attack of $O_2\cdot^-$. Based on these new promising results, the research in developing stable IL based electrolytes increases in order to develop a reversible Li-O_2 battery for energy storage devices.

In our study, we investigate the rechargeability in a Li-O_2 cell with ionic liquid electrolytes based on five different cations and two different anions as shown in Figure 1. The main focus is N-alkylmethylpyrrolidinium ($P13^+$ and $P14^+$) and N-alkylmethylpipiridinium ($PP13^+$) based cations in combination with the $TFSI^-$ anion, and other IL based electrolytes will be used primarily for comparison. As mentioned before, these ILs have shown promising results as stable electrolytes in Li-O_2 battery, and we analyse the stability further using Differential Electrochemical Mass Spectrometry (DEMS) to quantitatively assess the amount of oxygen consumed during discharge (ORR) and the types and amount of gas evolved during charge (OER). Complementary measurements with the bis(trifluoromethanesulfonyl)imide (FSI^-) anion, or a cation based on either imidazolium or quaternary ammonium are used to describe the desired features of an IL-based electrolyte for Li-O_2 batteries.

2. Experimental materials and methods

The ILs used in this study are: N-methyl-N-propylpyrrolidinium bis(trifluoromethanesulfonyl) imide (P_{13}TFSI, purity 99.9 %, Solvionic), N-methyl-N-propylpyrrolidinium bis(fluorosulfonyl) imide (P_{13}FSI, purity 99.9 %, Solvionic), N-methyl-N-propylpiperidinium bis(trifluoromethanesulfonyl) imide (PP_{13}TFSI, purity 99.9 %, Solvionic), N,N-Diethyl-N-methyl-N-propylammonium bis(fluorosulfonyl)imide(N_{1223}FSI, purity 99.9 %, Solvionic), 1-butyl-2,3-dimethyllimidazolium bis(trifluoromethanesulfonyl)imide (BdImTFSI, purity 99.9 %, Solvionic), N-methyl-N-butylpyrrolidinium bis(trifluoromethanesulfonyl) imide (P_{14}TFSI, purity 98.5 %, Sigma-Aldrich). All ILs were used as received from suppliers. Lithium bis(trifluoromethanesulfonyl) imide (LiTFSI, purity

99.9 %, Sigma-Aldrich), was preheated at 180 °C and Lithium bis(fluorosulfonyl) imide (LiFSI, purity 99.9 %, Suzhou Fluolyte) was preheated at 80 °C prior to preparing the electrolye. The 0.3 M LiX-IL (X=TFSI, FSI) electrolytes were prepared by adding the appropriate amount of salt and ionic liquid and stirring over night at room temperature in order to get homogenous electrolyte solution.

Homemade carbon cathodes were manufactured by air-spraying a slurry of XC72 carbon black (Vulcan XC72, Cabotcorp, GA) and PTFE (60 wt% dispersion in water, Sigma-Aldrich) in a wt/wt ratio of 3:1 onto a 316SS stainless steel 150 mesh (Westcoast, Denmark) as described in.[8] After air-drying for at least one hour, the coated SS mesh was cut in 10 mm diameter cathodes. The cathodes were rinsed carefully. First, an acetone and isopropanol wash removed any loose particles and secondly, the cathodes were in vacuum for at least 30 minutes at room temperature followed by at least 12 h at 200 °C inside a glove box. A homebuild airtight swagelok Li-O_2 cell was used for all studies. The cell was assembled with lithium as anode (HongKong Wisdom Tech Company), Whatmann glass fibre separators and XC72 cathode. ~60 µl of electrolyte was used for each experiment.

The presence of crystalline products on electrodes after first cycle (for discharge and charge, separately) was analyzed using a Regaku Advance X-ray Diffractometer (2θ = 20-80°) working with Cu-Kα radiation (λ =0.15418 nm). For this purpose, cathode materials were scratched from the electrode after disassembling inside the glove box and inserted into a 0.7mm diameter capillary. The capillary was sealed with glue and measured in the diffractometer.

DEMS measurements were performed at currents of 20 µA and 50 µA and the gas consumption and gas evolution were quantified using both pressure measurements and mass spectrometry. The applied in-house DEMS setup is similar in design to the setup used by McCloskey *et al.*.[29] From the DEMS measurements it is possible to determine the e^-/O_2 ratio during both discharge and charge, the amount of oxygen consumed (ORR) compared to the oxygen evolved (OER) and the amount of CO_2 and H_2 evolved. These key characteristics are crucial to determine if a Li-O_2 system is truly reversible [30] and Table 1 summarizes this information from all investigated electrolytes.

The concentration and diffusion of oxygen, denoted as $[O_2]$ and D_{O2}, respectively, in the RTILs were determined by a chronoamperometric technique adapted from Shoup and Szabo.[31-32] Prior to this, the ionic liquid was saturated with O_2 for 12 h. A 33 µm glassy-carbon (GC) microdisc electrode (Bio-Logic) was polished using 0.05 µm Al_2O_3 (Buehler). The electrochemical determinations were conducted using a minimal amount of the IL (a few drops) in a borosilicate glass vial that prior to each experiment had been cleaned in boiling HNO_3 (Sigma-Aldrich) and then heated to a 120 ^oC and brought into a glovebox where the IL was added. The glass vial was taken out of the glovebox and rapidly put under an O_2 with a Pt wire acting as both pseudo-reference- and counter electrode. The chronoampero metric experiments were performed using a Bio-Logic VMP3 potentiostat, with a sample time of 0.01 s, by stepping the potential from a voltage from zero current, held for 30 s, to a chosen potential after the reduction of oxygen, measured for 5 s, that was identified by previous cyclic voltammograms.

3. Results and Discussions:

Molecular formulas of the ionic liquid cations and anions investigated in this study are shown in Figure 1. DEMS results for $(e^-/O_2)_{dis}$, $(e^-/O_2)_{ch}$, OER/ORR, CO_2/ORR, and H_2/ORR for all studied IL based electrolytes and the DME based electrolyte are summarized Table 1.

Figure 2(A) shows the first galvanostatic discharge-charge cycle curve for electrolytes based on P13TFSI and P13FSI in Li-oxygen cells at room temperature. The cells were discharged at 50µA to a voltage cutoff of 2.2 V and charged to 4.2V at the same current. Figure 2(B) presents the total gas (O_2) consumed during discharge (ORR) and gas evolved during charge (OER). The value of the ratio (OER/ORR) should be exactly 1 if the cell is fully rechargeable. The measurement shows that P13TFSI and P13FSI are only ~60 % and ~20 % rechargeable at potentials below 4.2 V. Figure 2(C) shows DEMS measurements during charge. Oxygen (m/z = 32) is identified as the main gaseous charging product in both the electrolytes. For P13TFSI, the initial O_2 evolution rate is close to 2 e^-/O_2, which is consistent with Li_2O_2 oxidation. But as charging continues, the oxygen evolution rate gradually decreases to 3 e^-/O_2. P13FSI is also showing an initial 2 e^-/O_2 ratio, suggesting Li_2O_2 oxidation, but

after charging approximately 10 % of the full discharge capacity, the oxygen evolution decreases and the potential increases rapidly.

Results for cells with P14TFSI and PP13TFSI based electrolytes are displayed in Figure 3. The oxygen gas evolution rate of P14TFSI was close to $2e^-/O_2$ throughout most of the charging process and decreased slightly at the end of charge. PP13TFSI, on the other hand, did not perform well. At 50 µA, the battery was not able to sustain the current for long and only little oxygen was evolved. At a lower current of 20 µA, a capacity similar to P14TFSI (measured at 50 µA) was obtained. This measurement showed poor reversibility with an OER/ORR ratio of 40%, which is quite similar with the result by McCloskey *et al.*[1] Although the electron count per oxygen is ~2.09 during discharge, the charge reveal significant electrochemical degradation corresponding to more than half of measured the current.

XRD results of discharged cathodes for pure ionic liquids and DME based electrolyte was depicted in Figure 4. All cells were discharged to 2.2 V at a current of 20 µA. Li_2O_2 crystalline phases were observed in the all discharged cathodes except the electrolytes with FSI^- based ionic liquids (e.g. P13FSI, N1223FSI; Figure 4, Figure S3). This indicates that no detectable Li_2O_2 or other crystalline products are formed during discharge. Although the presence of Li_2CO_3 phases was observed from XRD but we could not see any CO_2 gas evolved till 4.2V in DEMS.

Figure 5 shows the e^-/O_2 data through six cycles for electrolytes based on P14TFSI and P13TFSI. It is seen that the amount of electrochemical degradation reactions increases during both discharge and charge as the batteries are cycled which shows that even though the first cycle seems promising, the system is not stable.

Discussion of P13FSI and P13TFSI

DEMS result in Figure 2 clearly indicates some parasitical electrochemistry attributed to oxidation/degradation of the electrolyte or to the oxidation electrolyte degradation products.[1] Here we should mention that the error bar in O_2 evolution rate in case of P13FSI-0.3MLiFSI is related to the background correction. DEMS result clearly shows the difference in performance in Li-O_2 cell just by

changing the anion. Hence the stability could be because of different structure of those two anions. Literature shows [33] that O_2-solubility of IL might be enhanced by choosing a suitable anion although oxygen mobility may decrease. Monaco *et al.*[33] demonstrated in this study that the reason for the increase in O_2-solubility is the increase in fluorine content in the anion part. Other reason of the improvement in O_2-solubility could be attributed to the increase in the size of anions.[34] Our solubility measurement using the method described above also show higher O_2 solubility in $TFSI^-$ based IL than FSI^- one (Table 2) which suggest better reversibility in P13TFSI based electrolytes due to better O_2 stability of TFSI- anion.

Discussion of P14TFSI and PP13TFSI

It might be interesting to look into oxygen evolution rate behavior during charge of piperidinium (PP13TFSI) based electrolytes at different current density. Here oxygen evolved at a rate higher than 2 (e^-/O_2) (~3) at the beginning but it decreases gradually to ~4 electron processes at low current (20μA) while at relatively higher current (50μA) it is showing value ~4 throughout the charging process. This clearly indicates other chemical/electrochemical reactions are taking part extensively and this electrolyte is not stable in Li-O_2 cell.

The stability of P14TFSI based electrolytes are extensively studied recently by Piana *et al*. in different Li-O_2 cell configurations.[15] They observed decomposition of P14TFSI via reduction on metallic lithium when they assemble cell with pure lithium as anode and vulcan XC72 carbon as cathode. They found alkene and amines as the degradation products, detected by OEMS and 1H-NMR experiments. We too used the similar type cell configuration and the DEMS result show only ~ 62% reversibility in the first cycle. That indicates some other electrochemistry are taking part during discharge and charge but we could not detect any alkene or amine in DEMS.

General discussion

The same result for DME and other ionic liquid based electrolyte compositions are presented in the Supporting Information (Figures S1, S2). Significantly small parasitical reactions are observed in case of P13TFSI, P14TFSI and PP13TFSI where the $(e^-/O_2)_{dis}$ are fairly near 2 while the value is really high in case of BdImTFSI, P13FSI and N1223FSI based electrolytes (Table1). For comparison, 1MLiTFSI - DME based electrolytes also display quite high degree of reversibility with the $(e^-/O_2)_{dis}$ value very near to 2 (table1 and SI). In general all electrolytes show much higher $(e^-/O2)_{ch}$ ($\gg$ 2.0) values which implies that some parasitical electrochemistry always occurs during the charging process. The other gas evolved (e.g., CO_2, H_2) during the cell operation for all electrolytes was very low (below detection level) except for the electrolyte based on PP13TFSI ionic liquid. We have observed substantial amounts of H_2 (~27 %, although non calibrated*) in pipiredinium based electrolytes from DEMS study. Also we have detected trace amount of water in PP13TFSI and BdImTFSI ionic liquids while conducting the solubility measurement.

Although P13TFSI and P14TFSI have been observed to be the best interms of stability in Li-O_2 cells but we could see that these are not sufficient for long term stability purpose (Figure 5). An increase in the e^-/O_2 ratio during cycling agrees well with results published by McCloskey *et al.* in DME based electrolytes and Piana *et al*. in P14TFSI based electrolytes.

4. Conclusions

We have demonstrated using DEMS that the extent of rechargeability is much dependent on the choice of cation and anion. Unfortunately none of the studied ionic liquid based electrolytes could behave as true ideal electrolytes in Li-O_2 battery. Although the pyrrolidium-cation and TFSI-anion (P13TFSI, P14TFSI) based ionic liquids have better rechargrability (OER/ORR>60%) than pyrrolidium-cation and FSI-anion based ionic liquids; still these are quite far for fulfilling the requirement of perfect electrolytes. Other electrolytes based on piperidinium, imidazoliun and quaternary ammonium are unstable in Li-O_2 battery.

Acknowledgements

The authors acknowledge support the ReLiable project funded by the Danish Council for Strategic Research – Programme Commission on Sustainable Energy and Environment (project #11-116792).

References

1. McCloskey, B.; Bethune, D.; Shelby, R.; Mori, T.; Scheffler, R.; Speidel, A.; Sherwood, M.; Luntz, A., Limitations in Rechargeability of Li-O2 Batteries and Possible Origins. *J. Phys. Chem. Lett.* **2012**, *3*, 3043-3047.

2. Lu, J.; Li, L.; Park, J.-B.; Sun, Y.-K.; Wu, F.; Amine, K., Aprotic and Aqueous Li–O2 Batteries. *Chem. Rev.* **2014**, *114*, 5611-5640.

3. Katayama, Y.; Sekiguchi, K.; Yamagata, M.; Miura, T., Electrochemical Behavior of Oxygen/Superoxide Ion Couple in 1-Butyl-1-Methylpyrrolidinium Bis (Trifluoromethylsulfonyl) Imide Room-Temperature Molten Salt. *J. Electrochem. Soc.* **2005**, *152*, E247-E250.

4. Kuboki, T.; Okuyama, T.; Ohsaki, T.; Takami, N., Lithium-Air Batteries Using Hydrophobic Room Temperature Ionic Liquid Electrolyte. *J. Power Sources* **2005**, *146*, 766-769.

5. Ogasawara, T.; Débart, A.; Holzapfel, M.; Novák, P.; Bruce, P. G., Rechargeable Li2o2 Electrode for Lithium Batteries. *J. Am. Chem. Soc.* **2006**, *128*, 1390-1393.

6. McCloskey, B.; Bethune, D.; Shelby, R.; Girishkumar, G.; Luntz, A., Solvents' Critical Role in Nonaqueous Lithium–Oxygen Battery Electrochemistry. *J. Phys. Chem. Lett.* **2011**, *2*, 1161-1166.

7. Mekonnen, Y. S.; Knudsen, K. B.; Mýrdal, J. S. G.; Younesi, R.; Højberg, J.; Hjelm, J.; Norby, P.; Vegge, T., Communication: The Influence of Co2 Poisoning on Overvoltages and Discharge Capacity in Non-Aqueous Li-Air Batteries. *J. Chem. Phys.* **2014**, *140*, 121101.

8. Højberg, J.; McCloskey, B. D.; Hjelm, J.; Vegge, T.; Johansen, K.; Norby, P.; Luntz, A. C., An Electrochemical Impedance Spectroscopy Investigation of the Overpotentials in Li–O2 Batteries. *ACS Appl. mater. Inter.* **2015**, *7*, 4039-4047.

9. Younesi, R.; Urbonaite, S.; Edström, K.; Hahlin, M., The Cathode Surface Composition of a Cycled Li–O2 Battery: A Photoelectron Spectroscopy Study. *J. Phys. Chem. C* **2012**, *116*, 20673-20680.

10. Balaish, M.; Kraytsberg, A.; Ein-Eli, Y., A Critical Review on Lithium–Air Battery Electrolytes. *Phys. Chem. Chem. Phys.* **2014**, *16*, 2801-2822.

11. Elia, G. A.; Hassoun, J.; Kwak, W.-J.; Sun, Y.-K.; Scrosati, B.; Mueller, F.; Bresser, D.; Passerini, S.; Oberhumer, P.; Tsiouvaras, N., An Advanced Lithium–Air Battery Exploiting an Ionic Liquid-Based Electrolyte. *Nano Lett.* **2014**, *14*, 6572-6577.

12. Ara, M.; Meng, T.; Nazri, G.-A.; Salley, S. O.; Ng, K. S., Ternary Imidazolium-Pyrrolidinium-Based Ionic Liquid Electrolytes for Rechargeable Li-O2 Batteries. *J. Electrochem. Soc.* **2014**, *161*, A1969-A1975.

13. Allen, C. J.; Mukerjee, S.; Plichta, E. J.; Hendrickson, M. A.; Abraham, K., Oxygen Electrode Rechargeability in an Ionic Liquid for the Li–Air Battery. *J. Phys. Chem. Lett.* **2011**, *2*, 2420-2424.

14. Monaco, S.; Soavi, F.; Mastragostino, M., Role of Oxygen Mass Transport in Rechargeable Li/O2 Batteries Operating with Ionic Liquids. *J. Phys. Chem. Lett.* **2013**, *4*, 1379-1382.

15. Piana, M.; Wandt, J.; Meini, S.; Buchberger, I.; Tsiouvaras, N.; Gasteiger, H. A., Stability of a Pyrrolidinium-Based Ionic Liquid in Li-O2 Cells. *J. Electrochem. Soc.* **2014**, *161*, A1992-A2001.

16. Soavi, F.; Monaco, S.; Mastragostino, M., Catalyst-Free Porous Carbon Cathode and Ionic Liquid for High Efficiency, Rechargeable Li/O 2 Battery. *J. Power Sources* **2013**, *224*, 115-119.

17. Allen, C. J.; Hwang, J.; Kautz, R.; Mukerjee, S.; Plichta, E. J.; Hendrickson, M. A.; Abraham, K., Oxygen Reduction Reactions in Ionic Liquids and the Formulation of a General Orr Mechanism for Li–Air Batteries. *J. Phys. Chem. C* **2012**, *116*, 20755-20764.

18. Lewandowski, A.; Świderska-Mocek, A., Ionic Liquids as Electrolytes for Li-Ion Batteries—an Overview of Electrochemical Studies. *J. Power Sources* **2009**, *194*, 601-609.

19. Galiński, M.; Lewandowski, A.; Stępniak, I., Ionic Liquids as Electrolytes. *Electrochim. Acta* **2006**, *51*, 5567-5580.

20. Fukaya, Y.; Ohno, H., Hydrophobic and Polar Ionic Liquids. *Phys. Chem. Chem. Phys.* **2013**, *15*, 4066-4072.

21. MacFarlane, D.; Meakin, P.; Sun, J.; Amini, N.; Forsyth, M., Pyrrolidinium Imides: A New Family of Molten Salts and Conductive Plastic Crystal Phases. *J. Phys. Chem. B* **1999**, *103*, 4164-4170.

22. Forsyth, C.; MacFarlane, D.; Golding, J.; Huang, J.; Sun, J.; Forsyth, M., Structural Characterization of Novel Ionic Materials Incorporating the Bis (Trifluoromethanesulfonyl) Amide Anion. *Chem. Mater.* **2002**, *14*, 2103-2108.

23. Golding, J.; Hamid, N.; MacFarlane, D.; Forsyth, M.; Forsyth, C.; Collins, C.; Huang, J., N-Methyl-N-Alkylpyrrolidinium Hexafluorophosphate Salts: Novel Molten Salts and Plastic Crystal Phases. *Chem. Mater.* **2001**, *13*, 558-564.

24. Grande, L.; Paillard, E.; Kim, G.-T.; Monaco, S.; Passerini, S., Ionic Liquid Electrolytes for Li–Air Batteries: Lithium Metal Cycling. *Int. J. Mol. Sci.* **2014**, *15*, 8122-8137.

25. Kar, M.; Simons, T. J.; Forsyth, M.; MacFarlane, D. R., Ionic Liquid Electrolytes as a Platform for Rechargeable Metal–Air Batteries: A Perspective. *Phys. Chem. Chem. Phys.* **2014**, *16*, 18658-18674.

26. Hayyan, M.; Mjalli, F. S.; Hashim, M. A.; AlNashef, I. M., An Investigation of the Reaction between 1-Butyl-3-Methylimidazolium Trifluoromethanesulfonate and Superoxide Ion. *J. Mol. Liq.* **2013**, *181*, 44-50.

27. Bresser, D.; Paillard, E.; Passerini, S., Ionic Liquid-Based Electrolytes for Li Metal/Air Batteries: A Review of Materials and the New 'Labohr' Flow Cell Concept. *J. Electrochem. Sci. Tech.* **2014**, *5*, 37-44.

28. Mizuno, F.; Takechi, K.; Higashi, S.; Shiga, T.; Shiotsuki, T.; Takazawa, N.; Sakurabayashi, Y.; Okazaki, S.; Nitta, I.; Kodama, T., Cathode Reaction Mechanism of Non-Aqueous Li–O 2 Batteries with Highly Oxygen Radical Stable Electrolyte Solvent. *J. Power Sources* **2013**, *228*, 47-56.

29. McCloskey, B. D.; Speidel, A.; Scheffler, R.; Miller, D. C.; Viswanathan, V.; Hummelshøj, J. S.; Nørskov, J. K.; Luntz, A. C., Twin Problems of Interfacial Carbonate Formation in Nonaqueous Li–O2 Batteries. *J. Phys. Chem. Lett.* **2012**, *3*, 997-1001.

30. Luntz, A. C.; McCloskey, B. D., Nonaqueous Li–Air Batteries: A Status Report. *Chem. Rev.* **2014**, *114*, 11721-11750.

31. Shoup, D.; Szabo, A., Chronoamperometric Current at Finite Disk Electrodes. *J. Electroanal. Chem. Inter. Electrochem.* **1982**, *140*, 237-245.

32. Xiong, L.; Aldous, L.; Henstridge, M. C.; Compton, R. G., Investigation of the Optimal Transient Times for Chronoamperometric Analysis of Diffusion Coefficients and Concentrations in Non-Aqueous Solvents and Ionic Liquids. *Anal. Method* **2012**, *4*, 371-376.

33. Monaco, S.; Arangio, A. M.; Soavi, F.; Mastragostino, M.; Paillard, E.; Passerini, S., An Electrochemical Study of Oxygen Reduction in Pyrrolidinium-Based Ionic Liquids for Lithium/Oxygen Batteries. *Electrochim. Acta* **2012**, *83*, 94-104.

34. Hu, Y.-F.; Liu, Z.-C.; Xu, C.-M.; Zhang, X.-M., The Molecular Characteristics Dominating the Solubility of Gases in Ionic Liquids. *Chem. Soc. Rev.* **2011**, *40*, 3802-3823.

Figure Captions

Table 1: Differential Electrochemical Mass Spectrometry (DEMS) result of different liquid and DME based electrolytes.

Figure 1: Schematic diagram of different cations and anions of ionic liquid used in this study.

Figure 2: (A) Galvanostatic discharge−charge curves for cells utilizing P13TFSI-0.3MLiTFSI and P13FSI-0.3MLiFSI. (B) Oxygen consumption (measured using pressure decay) during discharge and evolution (measured using DEMS) during charge. (c) Gas evolution rates for O_2, CO_2, and H_2.

Figure 3: (A) Galvanostatic discharge−charge curves for cells employing P14TFSI-0.3MLiTFSI (50µA discharge-charge) and PP13TFSI-0.3MLiTFSI (50µA and 20µA discharge-charge). (B) Oxygen consumption (measured using pressure decay) during discharge and evolution (measured using DEMS) during charge and (c) Gas evolution rates for O_2, CO_2, and H_2.

Figure 4: XRD patterns of discharged XC72 carbon cathodes of various electrolytes.

Figure 5: Cycling behavior of P14TFSI and P13TFSI based electrolytes.

Table 2: The concentration [O_2] and diffusion of oxygen, DO_2, in the RTILs.

Manuscript Figures

Table 1: Differential Electrochemical Mass Spectrometry (DEMS) result of different ionic liquid and DME based electrolytes (* indicates non calibrated data).

Cathode	Solvent	Salt	OER/ORR	(e^-/O_2)dis	(e^-/O_2)ch	CO_2/ORR	H_2/ORR*
XC72	P13TFSI	LiTFSI	0.6173 (±0.081)	2.0048 (±0.1413)	3.0914 (±0.2717)	0.00493 (±0.0011)	0.0103 (±0.0018)
	P14TFSI	LiTFSI	0.6284 (±0.1368)	2.0309 (±0.1271)	2.7495 (±0.4071)	0.00415	0.01438
	PP13TFSI	LiTFSI	0.40214 (±0.1236)	2.093 (±0.049)	4.025 (±0.078)	0.0316 (±0.0011)	0.18 (±0.086)
	BdImTFSI	LiTFSI	0.45 (±0.15)	2.144 (±0.1077)	8.264	0.0155 (±0.0098)	0.008 (±0.0068)
	P13FSI	LiFSI	0.1929 (±0.0042)	2.51 (±0.098)	3.404	0.044 (±0.032)	0.015 (±0.011)
	N1223FSI	LiFSI	0.1888 (±0.0569)	2.45 (±0.117)	4.059	0.0046 (±0.0018)	0.0026 (±0.0008)
	DME	LiTFSI	0.796 (±0.01)	1.897158 (±0.0468)		0.079475	0.027453

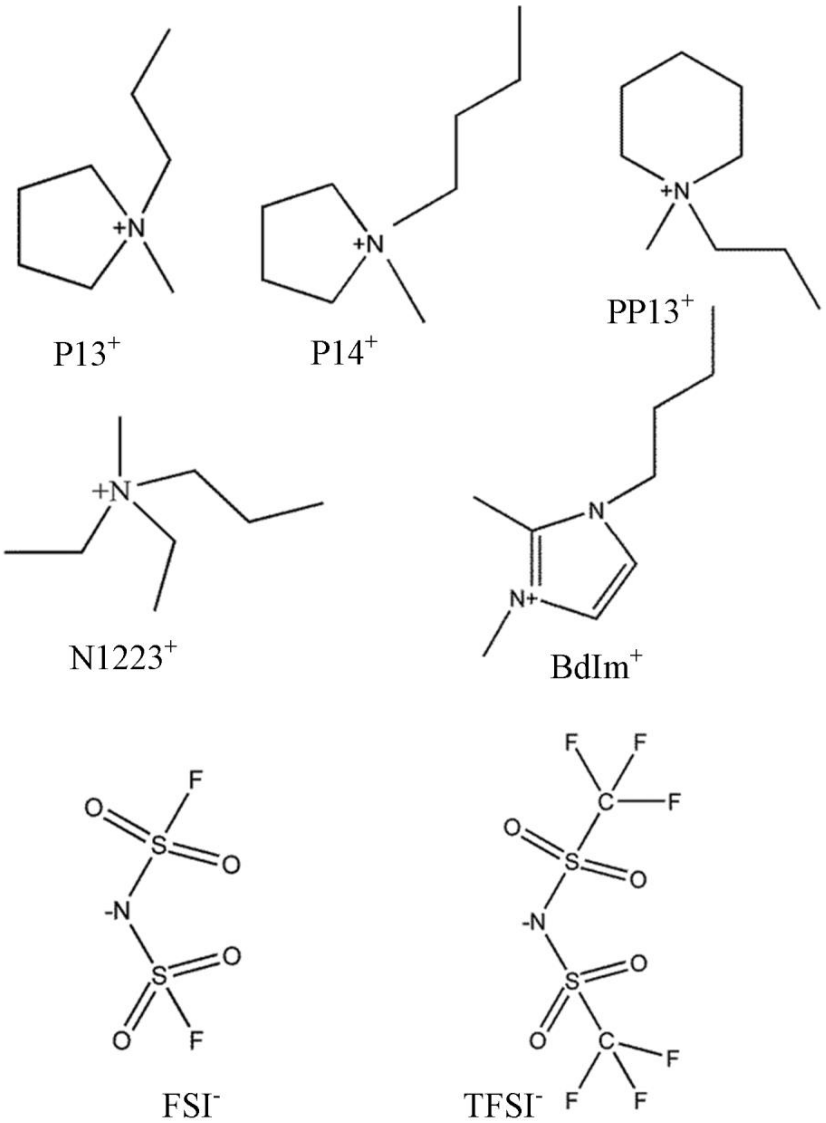

Figure 1: Schematic diagram of different cations and anions of ionic liquid used in this study.

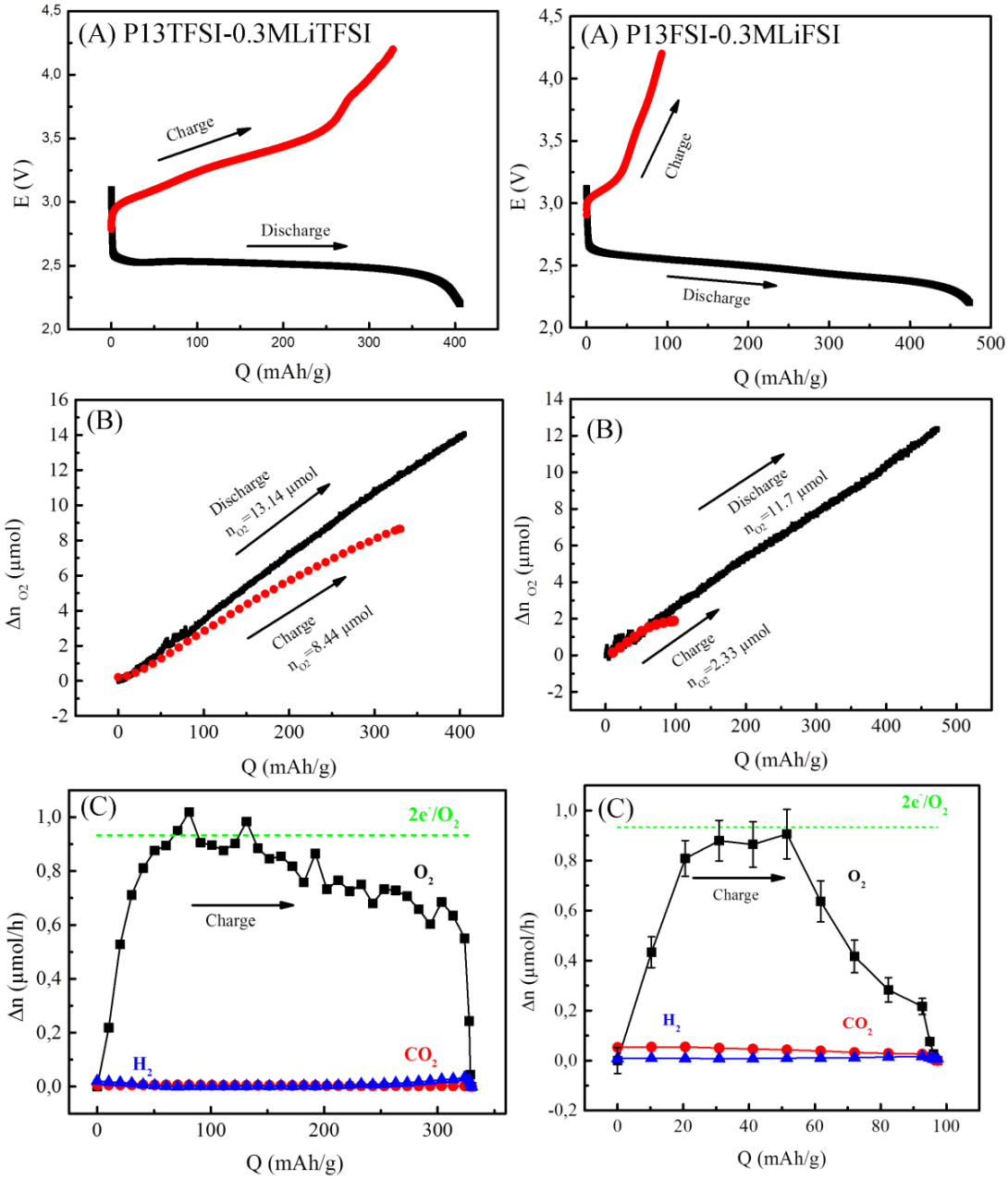

Figure 2: (A) Galvanostatic discharge−charge curves for cells utilizing P13TFSI-0.3MLiTFSI LiTFSI and P13FSI-0.3MLiFSI (both at 50µA discharge-charge). (B) Oxygen consumption (measured using pressure decay) during discharge and evolution (measured using DEMS) during charge. (c) Gas evolution rates for O_2, CO_2, and H_2.

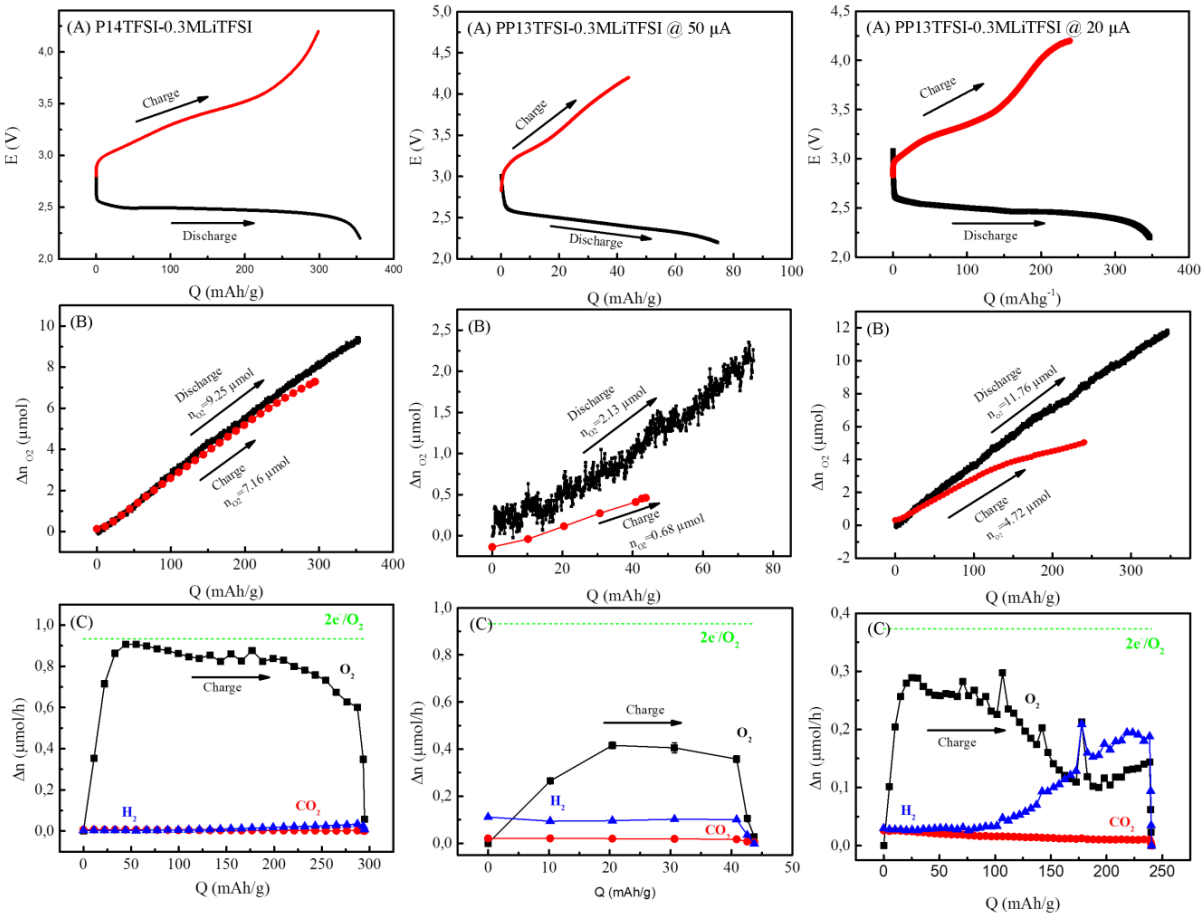

Figure 3: (A) Galvanostatic discharge−charge curves for cells employing P14TFSI-0.3MLiTFSI (50µA discharge-charge) and PP13TFSI-0.3MLiTFSI (50µA and 20µA discharge-charge). (B) Oxygen consumption (measured using pressure decay) during discharge and evolution (measured using DEMS) during charge and (c) Gas evolution rates for O_2, CO_2, and H_2.

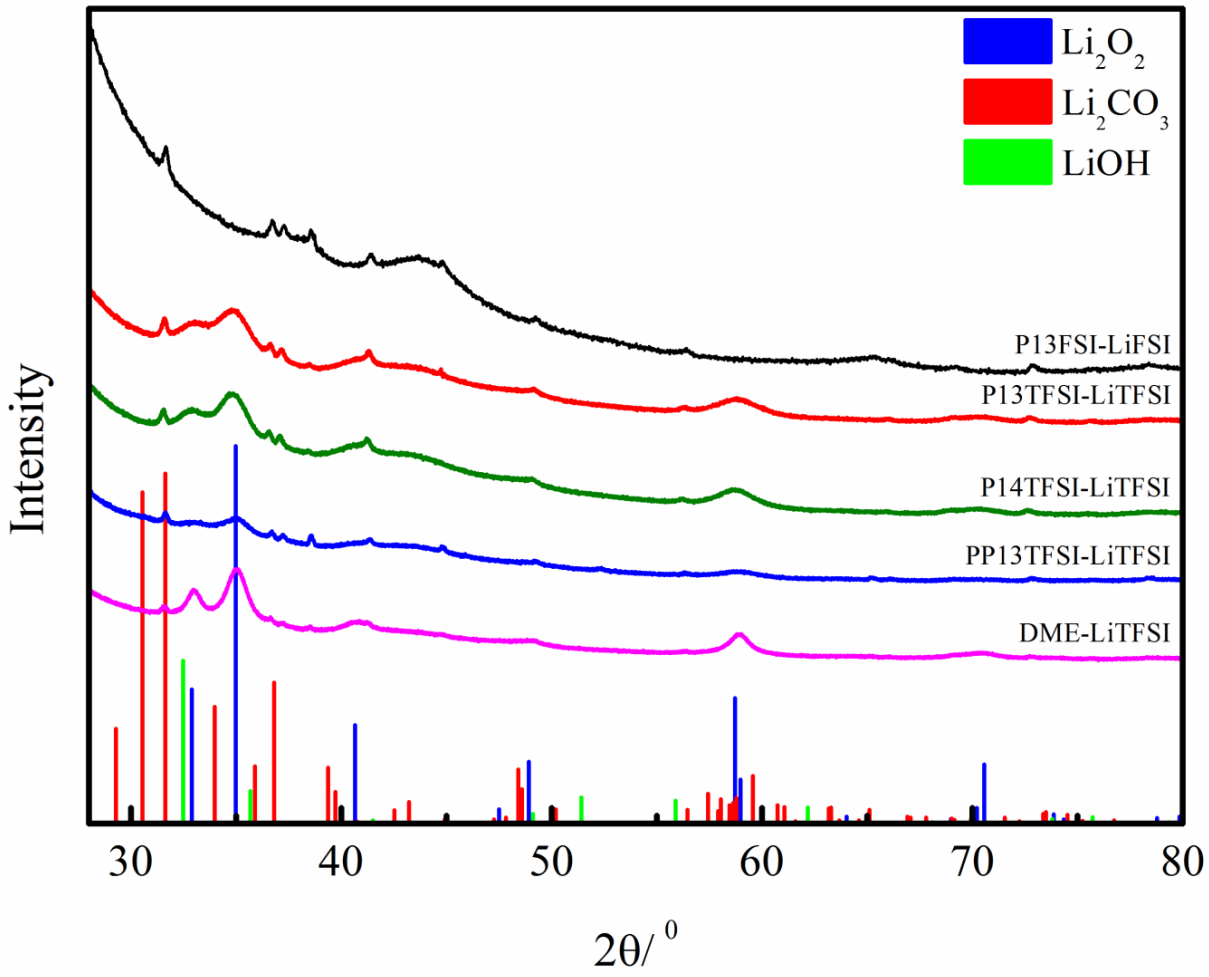

Figure 4: XRD patterns of discharged XC72 carbon cathodes of various electrolytes.

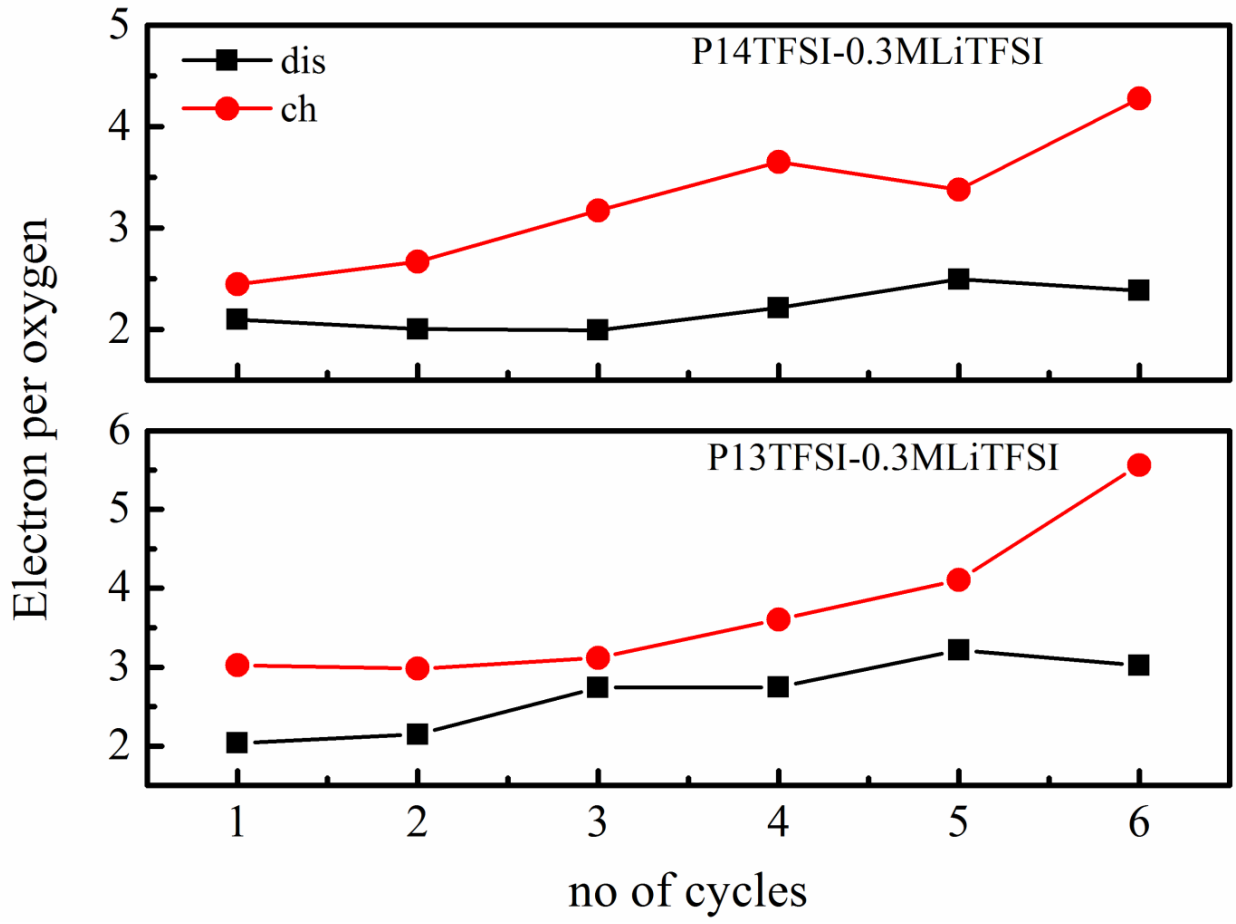

Figure 5: Cycling behavior of P14TFSI and P13TFSI based electrolytes.

IL	**D_{O2} [cm^2/s]**	**[O_2] [mM]**	**η [mPa·s]**
P13FSI	2.57e-6	8.17	52.70
P13TFSI	9.17e-7	11.71	71.23
PP13TFSI	1.78e-6	10.58	151
BdIm-TFSI	1.22e-6	18.81	115.22
P14TFSI	(1.8 ±0.2) e-6	14	89*
N1223FSI	1.22e-6	7.71	

Table 2: The concentration [O_2] and diffusion of oxygen, DO_2, in the RTILs.

Supporting information

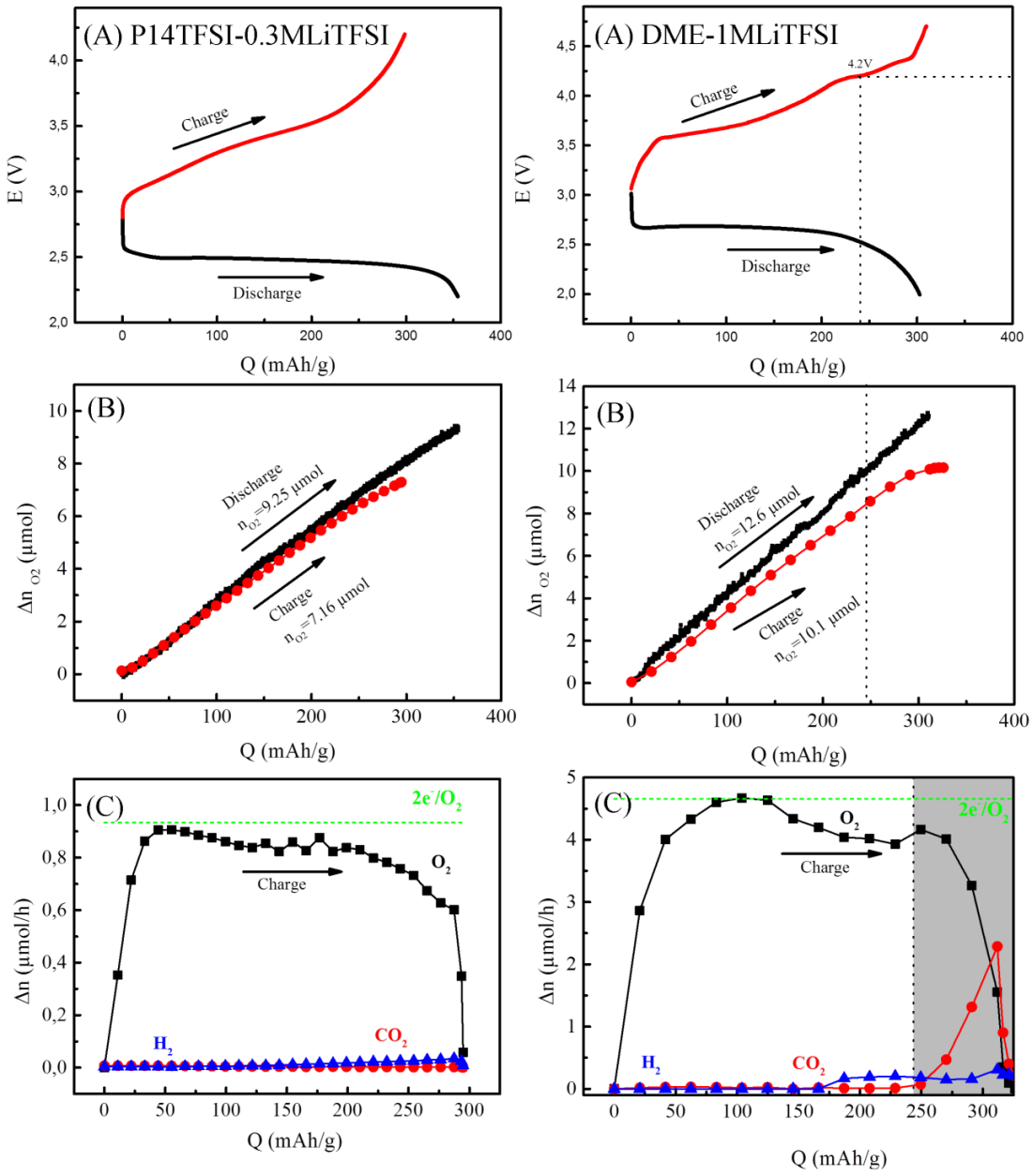
(A) P14TFSI-0.3MLiTFSI
Charge
Discharge
E (V)
Q (mAh/g)
(A) DME-1MLiTFSI
4.2V
Charge
Discharge
E (V)
Q (mAh/g)
(B)
Discharge
n_{O2}=9.25 µmol
Charge
n_{O2}=7.16 µmol
Δn $_{O2}$ (µmol)
Q (mAh/g)
(B)
Discharge
n_{O2}=12.6 µmol
Charge
n_{O2}=10.1 µmol
Δn $_{O2}$ (µmol)
Q (mAh/g)
(C)
2e$^-$/O_2
O_2
Charge
H_2
CO_2
Δn (µmol/h)
Q (mAh/g)
(C)
O_2
2e$^-$/O_2
Charge
H_2
CO_2
Δn (µmol/h)
Q (mAh/g)

Figure S1:

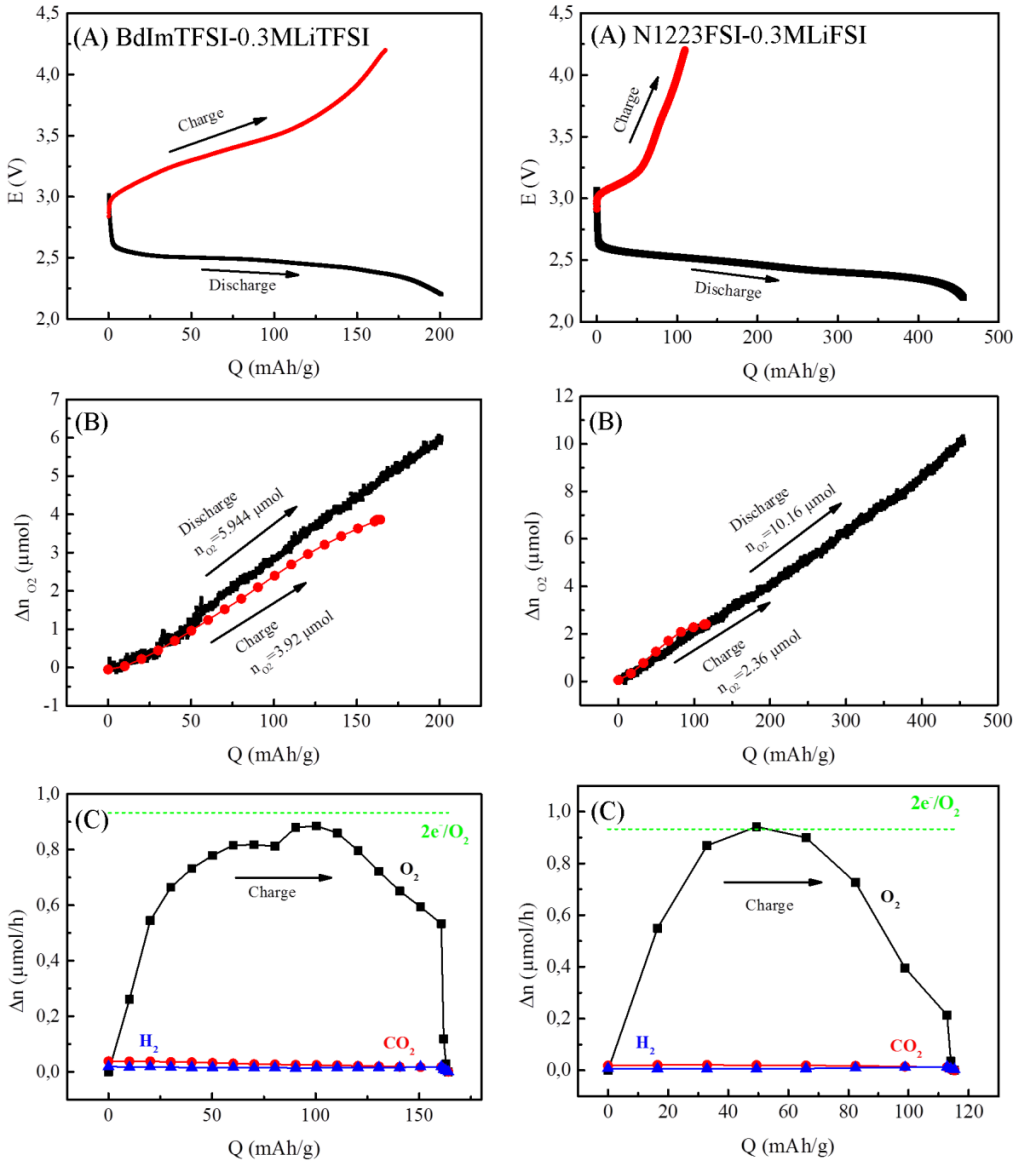
(A) BdImTFSI-0.3MLiTFSI
Charge
Discharge
E (V)
Q (mAh/g)
(A) N1223FSI-0.3MLiFSI
Charge
Discharge
E (V)
Q (mAh/g)
(B)
Discharge
n_{O2}=5.944 µmol
Charge
n_{O2}=3.92 µmol
Δn $_{O2}$ (µmol)
Q (mAh/g)
(B)
Discharge
n_{O2}=10.16 µmol
Charge
n_{O2}=2.36 µmol
Δn $_{O2}$ (µmol)
Q (mAh/g)
(C)
2e$^-$/O_2
O_2
Charge
H_2
CO_2
Δn (µmol/h)
Q (mAh/g)
(C)
2e$^-$/O_2
O_2
Charge
H_2
CO_2
Δn (µmol/h)
Q (mAh/g)

Figure S2:

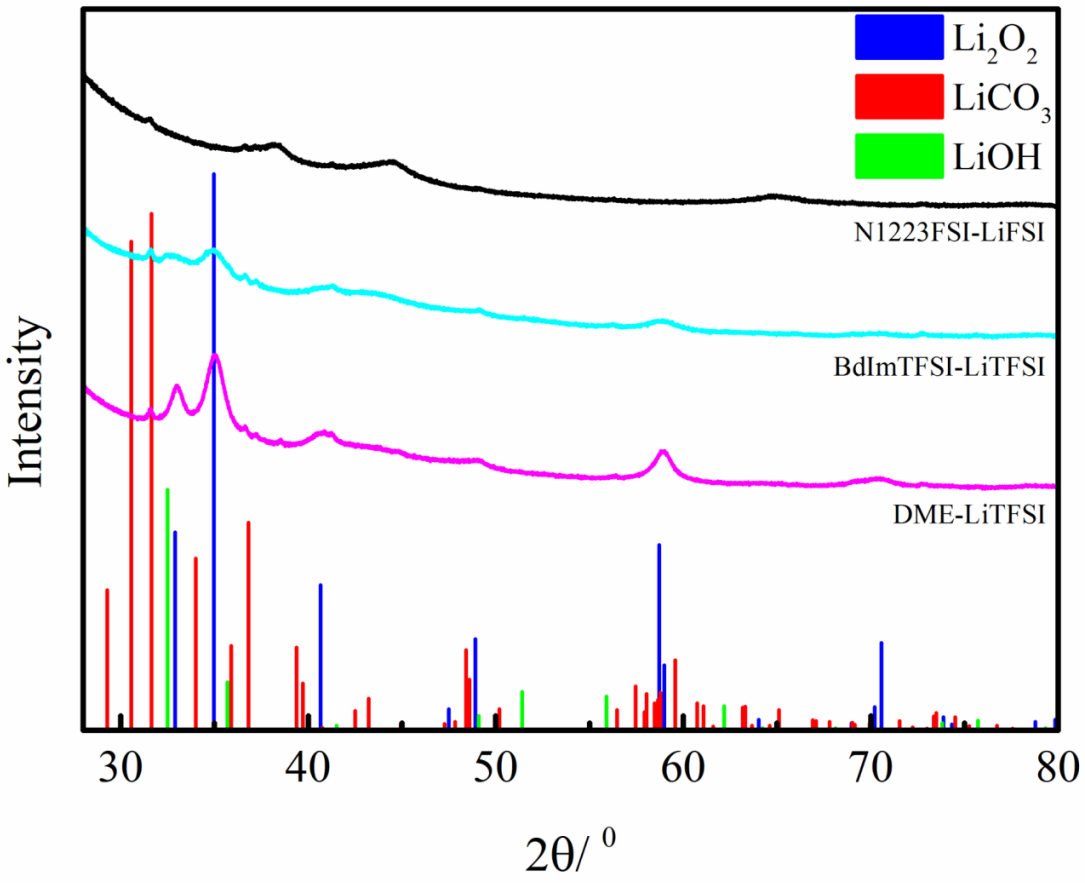
Li2O2
LiCO3
LiOH
N1223FSI-LiFSI
BdImTFSI-LiTFSI
DME-LiTFSI
Intensity
30
40
50
60
70
80
2θ/ 0

Figure S3:

FigureS4: solubility data

THE JOURNAL OF CHEMICAL PHYSICS **140**, 121101 (2014)

Communication: The influence of CO_2 poisoning on overvoltages and discharge capacity in non-aqueous Li-Air batteries

Yedilfana S. Mekonnen,[1,2] Kristian B. Knudsen,[1] Jon S. G. Mýrdal,[1] Reza Younesi,[1] Jonathan Højberg,[1] Johan Hjelm,[1] Poul Norby,[1] and Tejs Vegge[1,a)]

[1]*Department of Energy Conversion and Storage, Technical University of Denmark, Frederiksborgvej 399, DK-4000 Roskilde, Denmark*

[2]*Center for Atomic-scale Materials Design, Technical University of Denmark, DK-2800 Lyngby, Denmark*

(Received 31 January 2014; accepted 11 March 2014; published online 24 March 2014)

The effects of Li_2CO_3 like species originating from reactions between CO_2 and Li_2O_2 at the cathode of non-aqueous Li-air batteries were studied by density functional theory (DFT) and galvanostatic charge-discharge measurements. Adsorption energies of CO_2 at various nucleation sites on a stepped $(1\bar{1}00)$ Li_2O_2 surface were determined and even a low concentration of CO_2 effectively blocks the step nucleation site and alters the Li_2O_2 shape due to Li_2CO_3 formation. Nudged elastic band calculations show that once CO_2 is adsorbed on a step valley site, it is effectively unable to diffuse and impacts the Li_2O_2 growth mechanism, capacity, and overvoltages. The charging processes are strongly influenced by CO_2 contamination, and exhibit increased overvoltages and increased capacity, as a result of poisoning of nucleation sites: this effect is predicted from DFT calculations and observed experimentally already at 1% CO_2. Large capacity losses and overvoltages are seen at higher CO_2 concentrations. © *2014 AIP Publishing LLC*. [http://dx.doi.org/10.1063/1.4869212]

I. INTRODUCTION

As energy storage needs are growing rapidly, there is also an increase in research into high energy density materials for energy storage. Significant attention has been given to metal-air batteries, particularly Li-air batteries, as future environmentally friendly high energy density storage for vehicles, where the capacity offered by existing Li-ion technology is too low to solve the increasing demands on batteries.[1] The Li-O_2 couple is particularly attractive and could have ∼5–10 times greater specific energies than currently available Li-ion batteries, though there are severe scientific and technical challenges that need to be addressed.[2,3] Such as a clear understanding of the Li_2O_2 growth mechanisms, transport processes, interfacial phenomena, air impurities, and stability of the key components are vital parts of non-aqueous rechargeable Li-air cell research.[4]

As first reported by Abraham and Jiang in 1996, the Li-O_2 battery with aprotic solvent is shown to be rechargeable, when Li_2O_2 is formed during discharge at the cathode.[5] Detailed understanding of the Li_2O_2 growth mechanism is important to solve the problem associated with the practical limitations of the battery. Previous theoretical works by Hummelshøj *et al.*[6] and Radin *et al.*[7,8] showed that steps on a reconstructed $(1\bar{1}00)$surface could act as nucleation sites for low discharge overvoltage and facets such as (0001), $(1\bar{1}00)$, and $(11\bar{2}0)$ have similar surface energies. Hummelshøj *et al.*[9] have also shown that surfaces are potential dependent and vary during discharge and charge. According to G_0W_0 calculations, both Li_2O_2 and Li_2CO_3 are insulating materials with wide band gap of 4.9 and 8.8 eV, respectively.[10–12] Therefore, as these materials deposit at the cathode surface during discharge they will limit the electronic conduction and lead to sudden death during discharge within 5–10 nm thick Li_2O_2 deposits.[13,14] However, recent DFT calculations found that hole and electron polaronic transports at the surface and in bulk Li_2O_2 and Li_2CO_3 can take place. Using a PBE+U (Hubbard-corrected Perdew–Burke–Ernzerhof) exchange correlation functional, Garcia-Lastra *et al.*[11] revealed that the hole polarons have higher mobility than electron polarons and Li_2CO_3 exhibits lower conduction than Li_2O_2. Recent works by Luntz *et al.* have shown that hole tunneling should dominate and polaronic transport is only expected to be significant in Li_2O_2 at elevated temperatures and low current densities.[15,16]

Li_2CO_3 like crystalline species are formed by parasitic side reactions between the Li_2O_2 or LiO_2 and carbon sources from air impurities such as CO and CO_2 gases,[17] the graphite itself, or the decomposition of aprotic electrolytes. Younesi *et al.*[18,34] reported the degradation of various electrolytes by Li_2O_2 and documented Li_2CO_3 as a decomposition product from aprotic electrolytes. Likewise, McCloskey *et al.*[3] have shown that carbonates accumulate at the C-Li_2O_2 and Li_2O_2-electrolyte interfaces and are responsible for a large potential increase during recharge and a huge decrease in exchange current density. This makes growth of Li_2O_2 on Li_2CO_3 an equally important process to investigate, but this is beyond the scope of this communication. As reported by Siegfried *et al.*[19] and Myrdal and Vegge[20] adsorption of sulfur containing compounds on oxide surfaces could also control the electrochemical growth mechanism. Adsorbed species at surfaces can potentially block the nucleation sites, and therefore, alter the growth directions, overvoltages, and capacities.

In this communication, we address the influence of CO_2 contamination on the Li_2O_2 growth mechanism, discharge/charge overvoltages, and capacity in non-aqueous

a)E-mail: teve@dtu.dk

TABLE I. Adsorption energies of CO_2 in the gas phase at $(1\bar{1}00)$ Li_2O_2 surface.

Species	Sites	Adsorption energy (eV)
CO_2	Step valley	−0.73
	Terrace valley	−0.21
	Step ridge	−0.02

Li-air batteries using density functional theory (DFT) and galvanostatic measurements. Among other air contaminants, CO_2 is the most critical subject due to its high solubility in aprotic electrolytes and high reactivity with Li_2O_2 to form an insulating material Li_2CO_3.

II. COMPUTATIONAL RESULTS AND ANALYSIS

DFT[21–23] as implemented in the GPAW (grid-based projector-augmented wave method) code[24] is used to perform the presented calculations through the atomic simulation environment (ASE).[25] GPAW is built on real space grids and non-valence electrons are described by PAW (projector augmented-wave method).[26,27] Electron exchange and correlation is approximated by the revised Perdew–Burke–Ernzerhof (RPBE) functional.[28] The stepped $(1\bar{1}00)$ Li_2O_2 surface with a super cell consisting of a 56–64 atoms slab with a 18 Å vacuum layer between periodic images along the z-axis, see Fig. S1 in the supplementary material.[35] Since the oxygen rich (0001) facet will also be exposed, in particular under charging conditions,[9] and subsequent investigations should be performed to analyze the detailed mechanisms of CO_2 bonding to this facet. Recent computational DFT results for SO_2 adsorption on stepped (0001) and $(1\bar{1}00)$ surfaces do, however, show preferential bonding to the $(1\bar{1}00)$ facets,[20] which is investigated here. The k-points are sampled with a (4,4,1) Monkhorst-Pack mesh and 0.15 grid points is used. Atomic energy optimization calculations are performed until all forces are less than 0.01 eV/Å. Energy barriers are calculated by the climbing image nudged elastic band (CINEB) method.[29–31]

Adsorption energies of CO_2 at various nucleation sites on a stepped $(1\bar{1}00)$ Li_2O_2 surface were determined, see Table I. CO_2 binds preferentially at the step valley site and weakly binds at the step ridge site. NEB calculations show that once CO_2 is adsorbed at step valley site, it is bound by barriers upwards of 3 eV, see Fig. S2 in the supplementary material,[35] since the CO_2 molecule is required to desorb from the surface prior to re-adsorbing at the step site. The detailed nature of a conversion of adsorbed CO_2 to Li_2CO_3 warrants further investigations, but we find the adsorption of a single CO_2 molecule forms a $Li_{\sim 3}CO_3$-type complex (Fig. 1(b)), which could act as a nucleation site for further growth of Li_2CO_3.

The computational lithium electrode approach is used in the free energy calculations.[6,32] Defined as, U = 0, when bulk Li anode and Li ions in solution ($Li^+ + e^-$) are at equilibrium. The free energy change of the reaction is shifted by $-neU$ at an applied bias, where n is the number of transferred electrons; other assumptions are listed in the supplementary material.[35] As reported by Hummelshøj *et al.*, kinks and steps sites of the stepped $(1\bar{1}00)$ Li_2O_2 surface are favorable nucleation sites for a low overvoltage Li_2O_2 growth mechanism. The influence of CO_2 poisoning on the Li_2O_2 growth mechanism is studied while CO_2 is already adsorbed at step valley site (Fig. 1(b)).

The free energy diagram in Fig. 2 shows a four steps, two formula units Li_2O_2 growth mechanism on the stepped $(1\bar{1}00)$ Li_2O_2 surface with and without CO_2. The first step in the presence of CO_2 is adsorption of LiO_2 species (Fig. 1(c)), and which reduces the binding energy by 0.44 V compared to the pure discharge. The next step is the addition of a second LiO_2 species (Fig. 1(d)), which is the potential limiting charge step that raises the binding energy by 0.20 V compared to pure Li_2O_2. This is followed by subsequent additions of two Li (Figs. 1(e) and 1(f)) with relatively small binding energies with respect to a pure discharge. In the pure O_2 discharge mechanism, unlike in the presence of CO_2, addition of the first Li is the limiting charge potential step. The $2Li_2O_2$ growth at the step surface effectively displaces CO_2 from the step to the less stable terrace site.

Hummelshøj *et al.* have reported that the pure Li_2O_2 growth mechanism follows a 4 steps reaction mechanism, where all reaction steps are electrochemical, similar to what is seen in the presence of CO_2. The equilibrium potential can be obtained as $U_0 = -\Delta G/2e$. The effective equilibrium potential on a pure surface becomes 2.73 V (experimental value, $U_{0,Exp} = 2.85$ V), while in the presence of CO_2, this is effectively reduced to 2.53 V for the first cycle due to the shift in binding energy of CO_2 from a step valley to terrace site. As a result, discharge at other facets may become activate.[9] At neutral bias all reaction steps are downhill, but at an applied potential, the free energy difference changes for each step calculated as

$$\Delta G_{i,U} = \Delta G_i - eU. \quad (1)$$

The lowest free energy step, $\Delta G_{i,min}$, along the reaction path becomes uphill first at an applied potential called limited discharge potential, $U_{discharge}$, while the largest free energy step, $\Delta G_{i,max}$, that is last to become downhill for the reversed reaction at an applied potential called limited charge potential, U_{charge}, obtained as

$$U_{discharge} = \min[-\Delta G_i/e] \text{ and } U_{charge} = \max[-\Delta G_i/e]. \quad (2)$$

In the presence (absence) of a single CO_2 molecule, this discharge occurs as described in Fig. 1, resulting in $U_{discharge}$ = 2.21 V (2.66 V), and U_{charge} = 2.97 V (2.81 V) and the discharge and charge overvoltages in the presence (absence) of CO_2 are $\eta_{discharge} = 0.31$ V (0.07 V), and $\eta_{charge} = 0.44$ V (0.08 V). The calculated 0.44 V overvoltage for charge corresponds to low CO_2 concentrations, where only a single CO_2 molecule is adsorbed on the Li_2O_2 step forming a $Li_{\sim 3}CO_3$ type complex (see Fig. 1). Here, the charging process follows the same reaction steps as the discharge, but in reverse (from right to left in Fig. 2), i.e., the first two steps are desorption of two Li and followed by desorption of 2 LiO_2 species: in total desorbing 2 Li_2O_2 units from the surface and returning to the configuration in Fig. 1(b). Quantitative agreement with

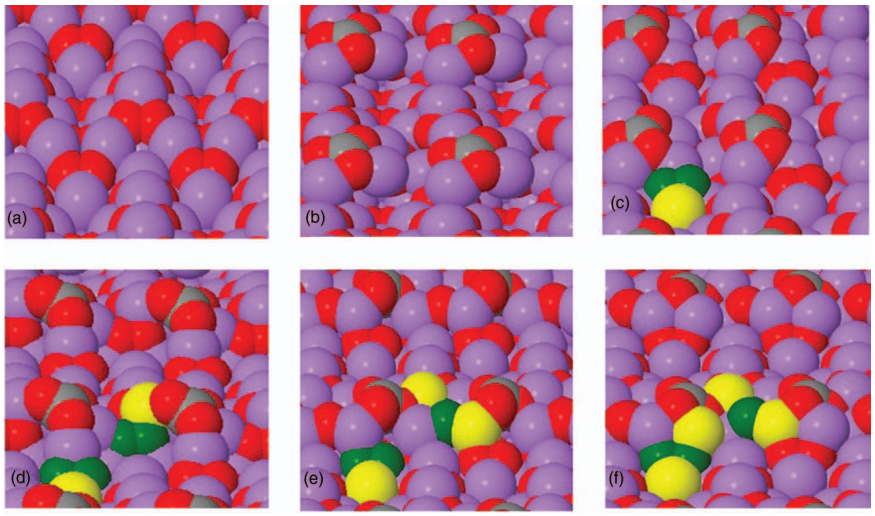

FIG. 1. Stepped Li_2O_2 ($1\bar{1}00$) surface before and after adsorption of CO_2 and 4 steps Li_2O_2 growth pathways during discharge. (a) Pure stepped Li_2O_2 surface. (b) CO_2 adsorbs to step valley site forming a $Li_{\sim 3}CO_3$ type complex. (c) 1st LiO_2 adsorbs. (d) 2nd LiO_2 adsorbs. (e) 1st Li. (f) 2nd Li adsorbs to the surface completing growth of 2 Li_2O_2 formula units. Atoms labeled as: C (gray), Li (purple), and O (red). Deposited atoms shown as: Li (yellow) and O (green).

experimental overvoltages can therefore only be expected for low concentrations of CO_2 (e.g., 1%). For higher CO_2 concentrations, the formation of crystalline Li_2CO_3 would be expected, resulting in significantly larger overvoltages.[3]

III. EXPERIMENTAL RESULTS AND ANALYSIS

Li-air batteries were constructed using a Swagelok design and assembled inside an Ar-filled glovebox ($\leq$3 ppm O_2 and H_2O). Each battery contained a 200 μl 1 M LiTFSI (99.95%, Sigma-Aldrich) and 1,2-dimethoxymethane, DME, (H_2O < 20 ppm, BASF) electrolyte. Cathodes consisted of P50 AvCarb carbon paper (Fuel cell store), which were sonicated using 2-propanol (99.5%, Sigma-Aldrich) and acetone ($\geq$99.8%, Sigma-Aldrich), introduced into a glovebox where they were rinsed with DME before drying in vacuum at 80 °C for 12 h. Cathodes were supported by a 316 steel mesh. A

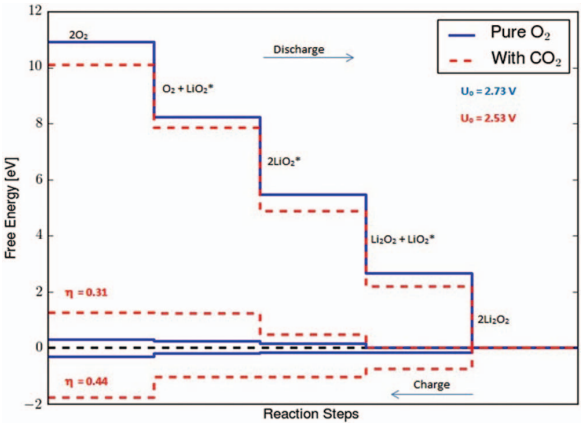

FIG. 2. Calculated free energy diagrams for a four steps discharge mechanism on a stepped ($1\bar{1}00$)Li_2O_2 surface with and without adsorbed CO_2.

10 mm diameter lithium foil (99.9%, Sigma-Aldrich) was used as anode. Two Celgard separators 2500 (Celgard) were placed in between the two electrodes. The separators were sonicated in EtOH (99.9%, Sigma-Aldrich), transferred to a glovebox, and rinsed with DME before drying in vacuum at 80 °C for 12 h. Experiments were performed using a Bio-Logic VMP3 Multichannel galvanostat (Bio-Logic, Claix, France). Batteries were operated in two galvanostatic modes: First, at 100 μA (127.3 μA/cm^2) where cells were discharged to 2 V and charged to 4.6 V vs. Li^+/Li. Second, at 50 μA (63.6 μA/cm^2) using the same potential limits.

To investigate the effect of gaseous CO_2, the assembled cells were purged with three different atmospheres: 0/100 CO_2/O_2, 1/99 CO_2/O_2, and 50/50 CO_2/O_2. Three individual batteries were assembled and investigated for each atmosphere and each curve presented in Figs. 3 and 4 is therefore an average of three cells with the equal atmosphere as shown in Fig. S3 in the supplementary material.[35] The lowest discharge capacity was observed for the 50% CO_2 cells and is likely caused by the high concentration of electrochemically inactive CO_2. A similar effect was observed, by Gowda *et al.*[17] for a pure CO_2 cell, where the cell potential immediately dropped. It should however be noted that Takechi *et al.*[33] observed, quite to the contrary of our observations, higher discharge capacities up to 70% CO_2 with respect to pure O_2 cells. Interestingly, a higher discharge capacity was observed for the 1% CO_2 cells in respect to the pure O_2 cells as shown in Fig. 3 (inset). A possible explanation is the dissolution of Li_2CO_3 species in DME and/or, as also suggested by Gowda *et al.*, or a change in deposition morphology compared to that deposited in the pure O_2 cells as suggested by Myrdal and Vegge.[20] Such morphological changes could increase the total electrodeposited layer and lead to higher capacities.

All CO_2 cells have higher discharge overvoltages compared to cells with pure O_2 at a discharge rate of 127.3 μA/cm^2, which may be caused by the blocking of the

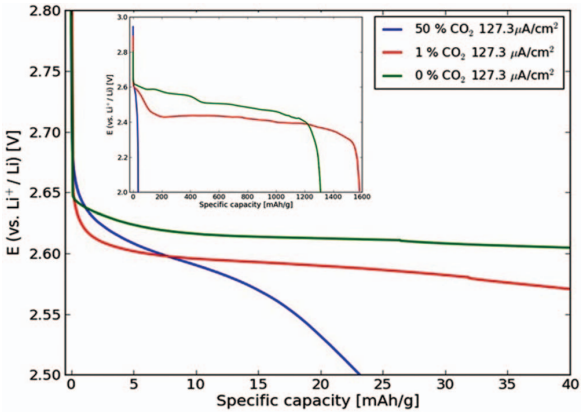

FIG. 3. Galvanostatic discharge profiles at 127.3 μA/cm^2 discharge at three different atmospheres: 50% CO_2, 1% CO_2, and 0% CO_2. Inset shows the increase in discharge capacity in 1% CO_2.

active nucleation sites by solubilized CO_2, forcing the reactions to follow pathways with higher overvoltages. This effect can even be seen at 1% CO_2, as illustrated in Fig. 3 above. The charge capacity, as seen in Fig. 4 and Fig. S4 in the supplementary material,[35] is very dependent on the CO_2 concentration, with high concentrations limiting charge capacity and thereby the cell reversibly. The 50% CO_2 cells reach the lower potential limit (2.0 V) early, at approximately 35 mAh/g, while 1% CO_2 cells and pure O_2 cells continued until capacities in the range 1150–1600 mAh/g were reached depending on current density. The low charge capacity at high CO_2 contaminations should be attributed to the poor Li-CO_2 electrochemistry, also reported by Gowda *et al.* The charging overvoltages are a function of both current density and the level of CO_2 contamination. While there is no significant difference in overvoltages between cells charge at 127.3 and 63.6 μA/cm^2 for 50% CO_2 cells, which again can be attributed to the poor Li-CO_2 electrochemistry. At 127.3 μA/cm^2, there is an increase in overvoltage of about 0.4 and 0.3 V for 1% CO_2 cells and 0% CO_2 cells, respectively. The general increase in overvoltages with increasing current density can be explained by the Butler-Volmer model, while the larger overvoltage for the 1% CO_2 cells than 0% CO_2 cells is expectedly caused by the formation and oxidation of the carbonate like species (Fig. 1(b)). A second charge at 63.6 μA/cm^2 shows identical results for 1% and 0% CO_2. This can be ascribed to the evolution of CO_2 observed during the initial charge cycle, where CO_2 is released at 4.5 V, as shown in Fig. S5 in the supplementary material,[35] resulting in residual CO_2 in the electrolyte causing blocking of the step sites in subsequent charging experiments.

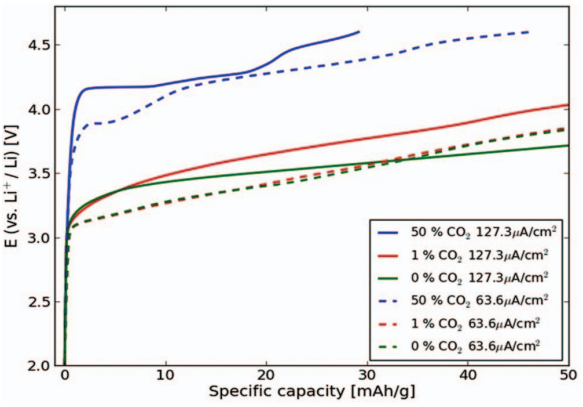

FIG. 4. Galvanostatic charge profiles at 127.3 (solid) and 63.6 (dotted) μA/cm^2 at three different atmospheres: 50% CO_2, 1% CO_2, and 0% CO_2.

IV. CONCLUSIONS

Influences of CO_2 poisoning at a stepped (1$\bar{1}$00) Li_2O_2 surface in non-aqueous Li-air battery were studied using DFT calculations and cells were characterized by electrochemical charge-discharge measurements. CO_2 preferentially binds at step valley site at the Li_2O_2 surface and the Li_2O_2 growth mechanism consists of four electrochemical steps, following the same sequence for both pure and contaminated systems. Accordingly, the first step of the growth mechanism is the adsorption of two LiO_2 species and followed by addition of two Li to form 2 Li_2O_2 at the cathode surface. For charge in the low CO_2 limit, a similar reaction will occur, but in reverse order.

Low concentrations of CO_2 (1%) effectively block the surface-active nucleation sites and alter the shape and growth directions of Li_2O_2 on the surface; resulting in an increased capacity of the battery at the expense of an increase in the overvoltage in the presence of CO_2. A similar behavior is seen in pure oxygen following charging to 4.5 V, resulting from decomposition reactions. The effective discharge potential is reduced by 0.20 V on a stepped (1$\bar{1}$00) Li_2O_2 surface, shifting the reaction to alternate nucleation sites. In general, the DFT calculations and experimental results show that the recharging process is strongly influenced by CO_2 contamination, and exhibits significantly increased charging overvoltage, which is observed already with 1% CO_2 contamination, while at 50% CO_2 a large capacity loss is also seen.

ACKNOWLEDGMENTS

The authors acknowledge support of this work from the ReLiable project (Project No. 11-116792) funded by the Danish Council for Strategic Research Programme Commission on Sustainable Energy and Environment.

[1]D. Linden and T. Reddy, *Hand Book of Batteries*, 3rd ed. (McGraw Hill, New York, 2001).
[2]T. Ogasawara, A. Débart, M. Holzapfel, P. Novák, and P. G. Bruce, J. Am. Chem. Soc. **128**, 1390 (2006).
[3]B. D. McCloskey, A. Speidel, R. Scheffler, D. C. Miller, V. Viswanathan, J. S. Hummelshøj, J. K. Nørskov, and A. C. Luntz, J. Phys. Chem. Lett. **3**, 997 (2012).
[4]G. Girishkumar, B. D. McCloskey, A. C. Luntz, S. Swanson, and W. Wilcke, J. Phys. Chem. Lett. **1**, 2193 (2010).
[5]K. M. Abraham and Z. Jiang, J. Electrochem. Soc. **143**, 1 (1996).
[6]J. S. Hummelshøj, J. Blomqvist, S. Datta, T. Vegge, J. Rossmeisl, K. S. Thygesen, A. C. Luntz, K. W. Jacobsen, and J. K. Nørskov, J. Chem. Phys. **132**, 071101 (2010).
[7]M. D. Radin, J. F. Rodriguez, F. Tian, and D. J. Siegel, J. Am. Chem. Soc. **134**, 1093 (2011).

[8]M. D. Radin, F. Tian, and D. J. Siegel, J. Mat. Sci. **47**, 7564 (2012).
[9]J. S. Hummelshøj, A. C. Luntz, and J. K. Nørskov, J. Chem. Phys. **138**, 034703 (2013).
[10]P. Albertus, G. Girishkumar, B. D. McCloskey, R. S. Sanchez-Carrera, B. Kozinsky, J. Christensen, and A. C. Luntz, J. Electrochem. Soc. **158**(3), A343 (2011).
[11]J. M. Garcia-Lastra, J. S. G. Myrdal, K. S. Thygesen, and T. Vegge, J. Phys. Chem. C **117**, 5568 (2013).
[12]J. M. Garcia-Lastra, J. D. Bass, and K. S. Thygesen, J. Chem. Phys. **135**, 121101 (2011).
[13]V. Viswanathan, K. S. Thygesen, J. S. Hummelshøj, J. K. Nørskov, G. Girishkumar, B. D. McCloskey, and A. C. Luntz, J. Chem. Phys. **135**, 214704 (2011).
[14]J. Chen, J. S. Hummelshøj, K. S. Thygesen, J. S. G. Myrdal, J. K. Nørskov, and T. Vegge, Catal. Today **165**, 2 (2011).
[15]J. B. Varley, V. Viswanathan, J. K. Nørskov, and A. C. Luntz, Energy Environ. Sci. **7**, 720 (2014).
[16]A. C. Luntz, V. Viswanathan, J. Voss, J. B. Varley, J. K. Nørskov, R. Scheffler, and A. Speidel, J. Phys. Chem. Lett. **4**, 3494 (2013).
[17]S. R. Gowda, A. Brunet, G. M. Wallraff, and B. D. McCloskey, J. Phys. Chem. Lett. **4**, 276 (2013).
[18]R. Younesi, M. Hahlin, F. Björefors, P. Johansson, and K. Edström, Chem. Mater. **25**, 77 (2013).
[19]M. J. Siegfried and K. S. Choi, Adv. Mat. **16**, 1743 (2004).
[20]J. S. G. Myrdal and T. Vegge, "DFT study of selective poisoning of Li-Air batteries for increased discharge capacity," RSC Adv. (to be published).
[21]P. Hohenberg and W. Kohn, Phys. Rev. **136**, B864 (1964).
[22]W. Kohn and L. Sham, Phys. Rev. **140**, A1133 (1965).
[23]J. J. Mortensen, L. B. Hansen, and K. W. Jacobsen, Phys. Rev. B **71**, 035109 (2005).
[24]J. Enkovaara, C. Rostgaard, J. J. Mortensen, J. Chen, M. Dulak, L. Ferrighi, J. Gavnholt, C. Glinsvad, V. Haikola, H. A. Hansen, H. H. Kristoffersen, M. Kuisma, A. H. Larsen, L. Lehtovaara, M. Ljungberg, O. Lopez-Acevedo, P. G. Moses, J. Ojanen, T. Olsen, V. Petzold, N. A. Romero, J. Stausholm-Moller, M. Strange, G. A. Tritsaris, M. Vanin, M. Walter, B. Hammer, H. Hakkinen, G. K. H. Madsen, R. M. Nieminen, J. K. Nørskov, M. Puska, T. T. Rantala, J. Schiøtz, K. S. Thygesen, and K. W. Jacobsen, J. Phys. Condens. Matter **22**, 253202 (2010).
[25]S. R. Bahn and K. W. Jacobsen, Comput. Sci. Eng. **4**, 56 (2002).
[26]P. E. Blöchl, Phys. Rev. **50**, 17953 (1994).
[27]P. E. Blöchl, C. J. Först, and J. Schimpl, Bull. Mater. Sci. **26**, 33 (2003).
[28]B. Hammer, L. B. Hansen, and J. K. Nørskov, Phys. Rev. B **59**, 7413 (1999).
[29]H. Jonsson, G. Mills, and K. W. Jacobsen, *Classical and Quantum Dynamics in Condensed Phase Systems*, edited by B. J. Berne, G. Cicotti, and D. F. Coker (World Scientific, 1998).
[30]G. Henkelman and H. Jónsson, J. Chem. Phys. **113**, 9978 (2000).
[31]G. Henkelman, B. Uberuaga, and H. A. Jónsson, J. Chem. Phys. **113**, 9901 (2000).
[32]J. K. Nørskov, J. Rossmeisl, A. Logadottir, L. Lindqvist, J. R. Kitchin, T. Bligaard, and H. Jonsson, J. Phys. Chem. B **108**, 17886 (2004).
[33]K. Takechi, T. Shiga, and T. Asaoka, Chem. Commun. **47**, 3463 (2011).
[34]R. Younesi, P. Norby, and T. Vegge, ECS Electrochem. Lett. **3**, A15 (2014).
[35]See supplementary material at http://dx.doi.org/10.1063/1.4869212 for Figs. S1–S5.

Bibliography

[1] REN21. Renewables 2014: Global Status Report - Key Findings. *Production*, pages 1–13, 2014. doi: ISBN9783981593426.

[2] IEA. World Energy Outlook 2014, 2014. doi: 10.1787/weo-2014-en.

[3] IPCC. Summary for Policymakers. In *Climate Change 2013: The Physical Science Basis. Contribution of Working Group I to the Fifth Assessment Report of the Intergovernmental Panel on Climate Change*, page 33. 2013. ISBN 9781107661820. doi: 10.1017/CBO9781107415324.

[4] International Energy Agengy. 2014 Key World Energy Statistics, 2014. URL http://www.iea.org/publications/freepublications/publication/KeyWorld2014.pdf.

[5] M.Stanley Whittingham. Chemistry of intercalation compounds: Metal guests in chalcogenide hosts, 1978. ISSN 00796786. doi: 10.1016/0079-6786(78)90003-1.

[6] K. Mizushima, P. C. Jones, P. Wiseman, and John B. Goodenough. LixCoO2 (0¡x¡1): A new cathode material for batteries of high energy density, 1981. ISSN 01672738. doi: 10.1016/0167-2738(81)90077-1.

[7] International Energy Agency (IEA). Technology roadmap: Electric and plug-in hybrid electric vehicles. *International Energy Agency, Tech. Rep*, (June):52, 2011. doi: 10.1109/IEMBS.2004.1403974.

[8] USCAR. Goals for Advanced Batteries for EVs (2013) United States Council for Automotive Research document, 2013. URL www.uscar.org/commands/files_download.php?files_id=27.

[9] K. M. Abraham and Z. Jiang. A Polymer Electrolyte-Based Rechargeable Lithium/Oxygen Battery. *Journal of The Electrochemical Society*, 143(1):1–5, 1996. doi: 10.1149/1.1836378.

[10] G. Girishkumar, Bryan D. McCloskey, Alan C. Luntz, S. Swanson, and W. Wilcke. Lithium-Air Battery: Promise and Challenges. *Journal of Physical Chemistry Letters*, 1(14):2193–2203, 2010. doi: 10.1021/jz1005384.

[11] Jang-Soo Lee, Sun Tai Kim, Ruiguo Cao, Nam-Soon Choi, Meilin Liu, Kyu Tae Lee, and Jaephil Cho. Metal-Air Batteries: Metal-Air Batteries with High Energy Density: Li-Air versus Zn-Air. *Advanced Energy Materials*, 1(1):2–2, 2011. doi: 10.1002/aenm.201190001.

[12] Takeshi Ogasawara, Aurélie Débart, Michael Holzapfel, Petr Novák, and Peter G. Bruce. Rechargeable Li2O2 Electrode for Lithium Batteries. *Journal of the American Chemical Society*, 128(4):1390–1393, 2006. doi: 10.1021/ja056811q.

[13] Nobuyuki Imanishi, Alan C. Luntz, and Peter G. Bruce. *The Lithium Air Battery: Fundamentals*. 2014. ISBN 9781489980618. doi: 10.1007/978-1-4899-8062-5.

[14] Alan C. Luntz and Bryan D. McCloskey. Nonaqueous Li-Air Batteries : A Status Report. *Chemical Reviews*, 114:11721–11750, 2014.

[15] Stefano Meini, M. Piana, H. Beyer, J. Schwammlein, and Hubert A. Gasteiger. Effect of Carbon Surface Area on First Discharge Capacity of Li-O2 Cathodes and Cycle-Life Behavior in Ether-Based Electrolytes. *Journal of the Electrochemical Society*, 159(12):A2135–A2142, October 2012. doi: 10.1149/2.011301jes.

[16] Reza Younesi, Neelam Ingh, Sigita Urbonaite, and Kristina Edström. The Effect of Pore Size on the Performance of the Li-O. In *ECS transaction*, pages 121–127, 2010. doi: 10.1149/1.3414010.

[17] Allen J. Bard and Larry R. Faulkner. *Electrochemical Methods - Fundamentals and Applications*. 2001. ISBN 0471043729.

[18] Mark E. Orazem and Bernard Tribollet. *Electrochemical Impedance Spectroscopy*. The Electrochemical Society, 2008. ISBN 9780470041406.

[19] James Adams, Mohan Karulkar, and Venkataramani Anandan. Evaluation and electrochemical analyses of cathodes for lithium-air batteries. *Journal of Power Sources*, 239:132–143, 2013. doi: 10.1016/j.jpowsour.2013.03.140.

[20] Imanol Landa-Medrano, Idoia Ruiz de Larramendi, Nagore Ortiz-Vitoriano, Ricardo Pinedo, José Ignacio Ruiz de Larramendi, and Teófilo Rojo. In situ monitoring of discharge/charge processes in Li-O2 batteries by electrochemical impedance spectroscopy. *Journal of Power Sources*, 249:110–117, March 2014. doi: 10.1016/j.jpowsour.2013.10.077.

[21] Ingo Bardenhagen, Olga Yezerska, Matthias Augustin, Daniela Fenske, Arne Wittstock, and Marcus Bäumer. In situ Investigation of Pore Clogging During Discharge of a Li/O2 Battery by Electrochemical Impedance Spectroscopy. *Journal of Power Sources*, 278:255–264, December 2014. doi: 10.1016/j.jpowsour.2014.12.076.

[22] M. Eswaran, N. Munichandraiah, and L. G. Scanlon. High Capacity Li-O2 Cell and Electrochemical Impedance Spectroscopy Study. *Electrochemical and Solid-State Letters*, 13(9):A121–A124, 2010. doi: 10.1149/1.3447867.

[23] Mojtaba Mirzaeian and Peter J. Hall. Characterizing capacity loss of lithium oxygen batteries by impedance spectroscopy. *Journal of Power Sources*, 195(19): 6817 – 6824, 2010. doi: 10.1016/j.jpowsour.2010.04.064.

[24] Ruben Nelson, Mark H. Weatherspoon, Jamie Gomez, Egwu E. Kalu, and Jim P. Zheng. Investigation of a Li-O2 cell featuring a binder-free cathode via impedance spectroscopy and equivalent circuit model analysis. *Electrochemistry Communications*, 34:77–80, September 2013. doi: 10.1016/j.elecom.2013.04.021.

[25] Ali Rinaldi, Olivia Wijaya, Harry E. Hoster, and Denis Y W Yu. History effects in lithium-oxygen batteries: How initial seeding influences the discharge capacity. *ChemSusChem*, 7:1283–1288, 2014. doi: 10.1002/cssc.201300986.

[26] M. Mehta, G. Mixon, J. .P. Zheng, and P. Andrei. Analytical Electrochemical Impedance Modeling of Li-Air Batteries under D.C. Discharge. *Journal of the Electrochemical Society*, 160(11):A2033–A2045, September 2013. doi: 10.1149/2.046311jes.

[27] Venkat Viswanathan, Jens K. Nø rskov, Angela Speidel, Rouven Scheffler, Sanketh R. Gowda, and Alan C. Luntz. Li-O2 Kinetic Overpotentials Tafel Plots from Experiment and First-Principles Theory. *Journal of Physical Chemistry Letters*, 4:556–560, 2013.

[28] Bryan D. McCloskey, Angela Speidel, Rouven Scheffler, D. Miller, Venkat Viswanathan, Jens S. Hummelshø j, Jens K. Nø rskov, and Alan C. Luntz. Twin Problems of Interfacial Carbonate Formation in Nonaqueous Li-O2 Batteries. *The Journal of Physical Chemistry Letters*, 3:997–1001, 2012.

[29] Paul Albertus, G. Girishkumar, Bryan D. McCloskey, Roel S. Sánchez-Carrera, Boris Kozinsky, Jake Christensen, and Alan C. Luntz. Identifying Capacity Limitations in the Li/Oxygen Battery Using Experiments and Modeling. *Journal of The Electrochemical Society*, 158(3):A343, 2011. doi: 10.1149/1.3527055.

[30] Yi-Chun Lu, Hubert A. Gasteiger, and Yang Shao-Horn. Method Development to Evaluate the Oxygen Reduction Activity of High-Surface-Area Catalysts for Li-Air Batteries. *Electrochemical and Solid-State Letters*, 14(5):A70–A74, 2011. doi: 10.1149/1.3555071.

[31] Andrzej Lasia. Impedance of porous electrodes. *Journal of Electroanalytical Chemistry*, 397(1-2):27–33, November 1995. doi: 10.1016/0022-0728(95)04177-5.

[32] Bryan Hirschorn, Mark E. Orazem, Bernard Tribollet, Vincent Vivier, Isabelle Frateur, and Marco Musiani. Determination of effective capacitance and film thickness from constant-phase-element parameters. *Electrochimica Acta*, 55(21): 6218–6227, August 2010. doi: 10.1016/j.electacta.2009.10.065.

[33] J. Jamnik and J. Maier. Generalised equivalent circuits for mass and charge transport: chemical capacitance and its implications. *Physical Chemistry Chemical Physics*, 3(9):1668–1678, 2001. doi: 10.1039/b100180i.

[34] Piotr Zoltowski. On the electrical capacitance of interfaces exhibiting constant phase element behaviour. *Journal of Electroanalytical Chemistry*, 443(1):149–154, February 1998. doi: 10.1016/S0022-0728(97)00490-7.

[35] Doron Aurbach, I. Weissman, A. Zaban, and O. Chusid. Correlation between surface chemistry, morphology, cycling efficiency and interfacial properties of Li electrodes in solutions containing different Li salts. *Electrochimica Acta*, 39(1): 51–71, 1994.

[36] Doron Aurbach, Arie Zaban, Alexander Schechter, Yair Ein-eli, Ella Zinigrad, and Boris Markovsky. The Study of Electrolyte Solutions Based on Ethylene and Diethyl Carbonates for Rechargeable Li Batteries. I. Li metal Anodes. *Journal of The Electrochemical Society*, 142(9):2873–2882, 1995.

[37] O. Barbieri, M. Hahn, a. Herzog, and R. Kötz. Capacitance limits of high surface area activated carbons for double layer capacitors. *Carbon*, 43(6):1303–1310, May 2005. doi: 10.1016/j.carbon.2005.01.001.

[38] Oliver Gerbig, Rotraut Merkle, and Joachim Maier. Electron and Ion Transport In Li2O2. *Advanced materials*, 25(22):3129–3133, May 2013. doi: 10.1002/adma.201300264.

[39] A. Dunst, V. Epp, I. Hanzu, S. A. Freunberger, and M. Wilkening. Short-range Li diffusion vs. long-range ionic conduction in nanocrystalline lithium peroxide Li2O2 - the discharge product in lithium-air batteries. *Energy & Environmental Science*, 7:2739–2752, 2014. doi: 10.1039/c4ee00496e.

[40] K. F. Young and H. P. R. Frederikse. Compilation of the Static Dielectric Constant of Inorganic Solids. *Journal of Physical and Chemical Reference Data*, 2(2):313, 1973. doi: 10.1063/1.3253121.

[41] Bryan D. McCloskey, Donald S. Bethune, Robert M. Shelby, G. Girishkumar, and Alan C. Luntz. Solvents' Critical Role in Nonaqueous Lithium-Oxygen Battery Electrochemistry. *Journal of Physical Chemistry Letters*, 2(10):1161–1166, 2011. doi: 10.1021/jz200352v.

[42] Stanley Bruckenstein and R. Rao Gadde. Use of a Porous Electrode for in Situ Mass Spectrometric Determination of Volatile Electrode Reaction Products. *Journal of the American Chemical Society*, 93(3):793–794, 1971.

[43] Yi-Chun Lu, David G. Kwabi, Koffi P. C. Yao, Jonathon R. Harding, Jigang Zhou, Lucia Zuin, and Yang Shao-Horn. The discharge rate capability of rechargeable Li-O2 batteries. *Energy and Environmental Science*, 4(8):2999–3007, 2011. doi: 10.1039/C1EE01500A.

[44] Yi-Chun Lu, Zhichuan Xu, Hubert A. Gasteiger, Shuo Chen, Kimberly Hamad-Schifferli, and Yang Shao-Horn. Platinum-Gold Nanoparticles: A Highly Active Bifunctional Electrocatalyst for Rechargeable Lithium-Air Batteries. *Journal of the American Chemical Society*, 132:12170–12171, 2010. doi: 10.1021/ja1036572.

[45] Robert R. Mitchell, Betar M. Gallant, Carl V. Thompson, and Yang Shao-Horn. All-carbon-nanofiber electrodes for high-energy rechargeable Li-O2 batteries. *Energy and Environmental Science*, 4(8):2952–2958, 2011.

[46] Robert R. Mitchell, Betar M. Gallant, Yang Shao-horn, and Carl V. Thompson. Mechanisms of Morphological Evolution of Li2O2 Particles During Electrochemical Growth. *The Journal of Physical Chemistry Letters*, 4:1060–1064, 2013.

[47] Li Zhong, Robert R. Mitchell, Yang Liu, Betar M Gallant, Carl V Thompson, Jian Yu Huang, Scott X Mao, and Yang Shao-Horn. In situ transmission electron microscopy observations of electrochemical oxidation of Li2O2. *Nano letters*, 13 (5):2209–14, May 2013. doi: 10.1021/nl400731w.

[48] Yin Yang, Qian Sun, Yue-Sheng Li, Hong Li, and Zheng-Wen Fu. Nanostructured Diamond Like Carbon Thin Film Electrodes for Lithium Air Batteries. *Journal of The Electrochemical Society*, 158(10):B1211, 2011. doi: 10.1149/1.3623431.

[49] Yin Yang, Qian Sun, Yue-Sheng Li, Hong Li, and Zheng-Wen Fu. A CoOx/carbon double-layer thin film air electrode for nonaqueous Li-air batteries. *Journal of Power Sources*, 223:312–318, February 2013. doi: 10.1016/j.jpowsour.2012.09.052.

[50] Hun-Gi Jung, Hee-Soo Kim, Jin-Bum Park, In-Hwan Oh, Jusef Hassoun, Chong Seung Yoon, Bruno Scrosati, and Yang-Kook Sun. A transmission electron microscopy study of the electrochemical process of lithium-oxygen cells. *Nano letters*, 12(8):4333–5, August 2012. doi: 10.1021/nl302066d.

[51] Christopher Graves. RAVDAV data analysis software, version 0.9.7, 2012.

[52] Bryan D. McCloskey, Alexia Valery, Alan C. Luntz, Sanketh R. Gowda, Gregory M. Wallra, Jeannette M. Garcia, Takashi Mori, and Leslie E. Krupp. Combining Accurate O2 and Li2O2 Assays to Separate Discharge and Charge Stability Limitations in Nonaqueous Li-O2 Batteries. *The Journal of Physical Chemistry Letters*, 4:2989–2993, 2013.

[53] Sanketh R. Gowda, A. Brunet, G. M. Wallraff, and Bryan D. McCloskey. Implications of CO2 Contamination in Rechargeable Nonaqueous Li-O2 Batteries. *The Journal of Physical Chemistry Letters*, 4:276–279, 2013.

[54] Bryan D. McCloskey, Rouven Scheffler, Angela Speidel, Donald S. Bethune, Robert M. Shelby, and Alan C. Luntz. On the Efficacy of Electrocatalysis in Nonaqueous Li-O2 Batteries. *Journal of American Chemical Society*, 133(45): 18038–18041, 2011. doi: 10.1021/ja207229n.

[55] Bryan D. McCloskey, Rouven Scheffler, Angela Speidel, G. Girishkumar, and Alan C. Luntz. On the Mechanism of Nonaqueous Li-O 2 Electrochemistry on C and Its Kinetic Overpotentials : Some Implications for Li-Air Batteries. *The Journal of Physical Chemistry C*, 116:23897–23905, 2012.

[56] Bryan D. McCloskey, Alan C. Luntz, Donald S. Bethune, Robert M. Shelby, T. Mori, Rouven Scheffler, Angela Speidel, and M. Sherwood. Limitations in Rechargeability of Li-O2 Batteries and Possible Origins. *The Journal of Physical Chemistry Letters*, 3:3043–3047, 2012.

[57] Mie Mø ller Storm, Rune E. Johnsen, Reza Younesi, and Poul Norby. Capillary based Li–air batteries for in situ synchrotron X-ray powder diffraction studies. *J. Mater. Chem. A*, 3:3113–3119, 2015. doi: 10.1039/C4TA04291C.

[58] Nagaphani B. Aetukuri, Bryan D. McCloskey, Jeannette M. García, Leslie E. Krupp, Venkatasubramanian Viswanathan, and Alan C. Luntz. Solvating additives drive solution-mediated electrochemistry and enhance toroid growth in non-aqueous Li–O2 batteries. *Nature Chemistry*, (January), 2014. doi: 10.1038/nchem.2132.

[59] Feng Wang, Jason Graetz, M. Sergio Moreno, Chao Ma, Lijun Wu, Vyacheslav Volkov, and Yimei Zhu. Chemical distribution and bonding of lithium in intercalated graphite: Identification with optimized electron energy loss spectroscopy. *ACS Nano*, 5:1190–1197, 2011. doi: 10.1021/nn1028168.

[60] Reza Younesi, Maria Hahlin, Matthew Roberts, and Kristina Edström. The SEI Layer Formed on Lithium Metal in the Presence of Oxygen: A Seldom Considered Component in the Development of the Li-O2 battery. *Journal of Power Sources*, 225:40–45, October 2013. doi: 10.1016/j.jpowsour.2012.10.011.

[61] Juan Maria Garcia-Lastra, Jon S.G. Myrdal, Rune Christensen, Kristian S. Thygesen, and Tejs Vegge. DFT+U Study of Polaronic Conduction in Li2O2 and Li2CO3: Implications for Li-Air Batteries. *The Journal of Physical Chemistry C*, 117(11):5568–5577, March 2013. doi: 10.1021/jp3107809.

[62] Yedilfana S. Mekonnen, Kristian B. Knudsen, Jon S G Mýrdal, Reza Younesi, Jonathan Hø jberg, Johan Hjelm, Poul Norby, and Tejs Vegge. Communication: The influence of CO2 poisoning on overvoltages and discharge capacity in non-aqueous Li-Air batteries. *Journal of Chemical Physics*, 2014. doi: 10.1063/1.4869212.

[63] Alan C. Luntz, Venkat Viswanathan, J. Voss, J. B. Varley, Angela Speidel, Jens K. Nø rskov, and Rouven Scheffler. Tunneling and Polaron Charge Transport through Li2O2 in Li-O2 Batteries. *The Journal of Physical Chemistry Letters*, 4:3494–3499, 2013.

[64] Y. Wang and S. C. Cho. Analysis of Air Cathode Perfomance for Lithium-Air Batteries. *Journal of the Electrochemical Society*, 160(10):A1847–A1855, August 2013. doi: 10.1149/2.092310jes.

[65] Yuhui Chen, Stefan A. Freunberger, Zhangquan Peng, Olivier Fontaine, and Peter G. Bruce. Charging a Li-O2 battery using a redox mediator. *Nature chemistry*, 5(June):489–494, 2013. doi: 10.1038/NCHEM.1646.

[66] Yasushi Katayama, Kaori Sekiguchi, Masaki Yamagata, and Takashi Miura. Electrochemical Behavior of Oxygen/Superoxide Ion Couple in 1-Butyl-1-methylpyrrolidinium Bis(trifluoromethylsulfonyl)imide Room-Temperature Molten Salt. *Journal of The Electrochemical Society*, 152:E247, 2005. doi: 10.1149/1.1946530.

[67] Takashi Kuboki, Tetsuo Okuyama, Takahisa Ohsaki, and Norio Takami. Lithium-air batteries using hydrophobic room temperature ionic liquid electrolyte. *Journal of Power Sources*, 146(1-2):766–769, 2005. doi: 10.1016/j.jpowsour.2005.03.082.

[68] Moran Balaish, Alexander Kraytsberg, and Yair Ein-Eli. A critical review on lithium-air battery electrolytes. *Physical chemistry chemical physics : PCCP*, 16: 2801–22, 2014. doi: 10.1039/c3cp54165g.

[69] G A Elia, J Hassoun, W.-J. Kwak, Y.-K. Sun, B Scrosati, F Mueller, D Bresser, S Passerini, P Oberhumer, N Tsiouvaras, and J Reiter. An Advanced Lithium–Air Battery Exploiting an Ionic Liquid-Based Electrolyte. *Nano Letters*, 14:6572–6577, 2014. doi: 10.1021/nl5031985.

[70] M. Ara, T. Meng, G.-a. Nazri, S. O. Salley, and K. Y. Simon Ng. Ternary Imidazolium-Pyrrolidinium-Based Ionic Liquid Electrolytes for Rechargeable Li-O2 Batteries. *Journal of the Electrochemical Society*, 161(14):A1969–A1975, 2014. doi: 10.1149/2.0031414jes.

[71] Chris J. Allen, Sanjeev Mukerjee, Edward J. Plichta, Mary A. Hendrickson, and K. M. Abraham. Oxygen Electrode Rechargeability in an Ionic Liquid for the Li-Air Battery. *Journal of Physical Chemistry Letters*, 2(19):2420–2424, 2011. doi: 10.1021/jz201070t.

[72] Andrzej Lewandowski and Agnieszka Świderska Mocek. Ionic liquids as electrolytes for Li-ion batteries-An overview of electrochemical studies. *Journal of Power Sources*, 194:601–609, 2009. doi: 10.1016/j.jpowsour.2009.06.089.

[73] Simone Monaco, Francesca Soavi, and Marina Mastragostino. Role of oxygen mass transport in rechargeable Li/O2 batteries operating with ionic liquids. *Journal of Physical Chemistry Letters*, 4:1379–1382, 2013. doi: 10.1021/jz4006256.

[74] Michele Piana, Johannes Wandt, Stefano Meini, Irmgard Buchberger, Nikolaos Tsiouvaras, and Hubert A Gasteiger. Stability of a Pyrrolidinium-Based Ionic Liquid in Li-O2 Cells. *Journal of the Electrochemical Society*, 161(14):1992–2001, 2014. doi: 10.1149/2.1131412jes.

[75] Francesca Soavi, Simone Monaco, and Marina Mastragostino. Catalyst-free porous carbon cathode and ionic liquid for high efficiency, rechargeable Li/O2 battery. *Journal of Power Sources*, 224(2013):115–119, 2013. doi: 10.1016/j.jpowsour.2012.09.095.

[76] Chris J. Allen, Jaehee Hwang, Roger Kautz, Sanjeev Mukerjee, Edward J. Plichta, Mary a. Hendrickson, and K. M. Abraham. Oxygen Reduction Reactions in Ionic Liquids and the Formulation of a General ORR Mechanism for Li–Air Batteries. *The Journal of Physical Chemistry C*, 116(39):20755–20764, October 2012. doi: 10.1021/jp306718v.

[77] Maciej Galiński, Andrzej Lewandowski, and Izabela Stepniak. Ionic liquids as electrolytes. *Electrochimica Acta*, 51:5567–5580, 2006. doi: 10.1016/j.electacta.2006.03.016.

[78] Y Fukaya and H Ohno. Hydrophobic and polar ionic liquids. *Phys Chem Chem Phys*, 15:4066–4072, 2013. doi: 10.1039/c3cp44214d.

[79] Dr MacFarlane and P Meakin. Pyrrolidinium imides: a new family of molten salts and conductive plastic crystal phases. *The Journal of ...*, 103:4164–4170, 1999. doi: 10.1021/jp984145s.

[80] C. M. Forsyth, E. D. MacFarlane, J. J. Golding, J Huang, J Sun, and M Forsyth. Structural characterization of novel ionic materials incorporating the bis(trifluoromethanesulfonyl)amide anion. *Chemistry of Materials*, 14(7):2103–2108, 2002. doi: 10.1021/cm0107777.

[81] J. Golding, N. Hamid, D. R. MacFarlane, M. Forsyth, C. Forsyth, C. Collins, and J. Huang. N-methyl-N-alkylpyrrolidinium hexafluorophosphate salts: Novel molten salts and plastic crystal phases. *Chemistry of Materials*, 13(9):558–564, 2001. doi: 10.1021/cm000625w.

[82] Lorenzo Grande, Elie Paillard, Guk Tae Kim, Simone Monaco, and Stefano Passerini. Ionic liquid electrolytes for Li-air batteries: Lithium metal cycling. *International Journal of Molecular Sciences*, 15:8122–8137, 2014. doi: 10.3390/ijms15058122.

[83] Mega Kar, Tristan J Simons, Maria Forsyth, and Douglas R MacFarlane. Ionic liquid electrolytes as a platform for rechargeable metal-air batteries: a perspective. *Phys. Chem. Chem. Phys.*, 16:–, 2014. doi: 10.1039/C4CP02533D.

[84] Jun Lu, Li Li, Jin-Bum Park, Yang-Kook Sun, Feng Wu, and Khalil Amine. Aprotic and aqueous Li-O2 batteries. *Chemical reviews*, 114:5611–40, 2014. doi: 10.1021/cr400573b.

[85] Masaki Yoshio, Ralph J. Brodd, and Akiya Kozawa. *Lithium-Ion Batteries*. Springer New York, New York, NY, 2009. ISBN 978-0-387-34444-7. doi: 10.1007/978-0-387-34445-4.

[86] Kevin G. Gallagher, Steven Goebel, Thomas Greszler, Mark Mathias, Wolfgang Oelerich, Damla Eroglu, and Venkat Srinivasan. Quantifying the promise of lithium–air batteries for electric vehicles. *Energy & Environmental Science*, 7:1555, 2014. doi: 10.1039/c3ee43870h.

[87] Kong Soon Ng, Chin Sien Moo, Yi Ping Chen, and Yao Ching Hsieh. Enhanced coulomb counting method for estimating state-of-charge and state-of-health of lithium-ion batteries. *Applied Energy*, 86(9):1506–1511, 2009. doi: 10.1016/j.apenergy.2008.11.021.

[88] Jingzhe Chen, Jens S. Hummelshø j, Kristian S. Thygesen, Jon S.G. Myrdal, Jens K. Nø rskov, and Tejs Vegge. The role of transition metal interfaces on the electronic transport in lithium-air batteries. *Catalysis Today*, 165(1):2–9, 2011. doi: 10.1016/j.cattod.2010.12.022.

[89] Maxwell D Radin and Donald J Siegel. Charge transport in lithium peroxide: relevance for rechargeable metal–air batteries. *Energy & Environmental Science*, 6(8):2370, 2013. doi: 10.1039/c3ee41632a.

[90] Venkat Viswanathan, K. S. Thygesen, Jens S. Hummelshø j, Jens K. Nø rskov, G. Girishkumar, Bryan D. McCloskey, and Alan C. Luntz. Electrical conductivity in Li2O2 and its role in determining capacity limitations in non-aqueous Li-O2 batteries. *The Journal of chemical physics*, 135(21):214704, December 2011. doi: 10.1063/1.3663385.

[91] F Huet. A review of impedance measurements for determination of the state-of-charge or state-of-health of secondary batteries. *Journal of Power Sources*, 70: 59–69, 1998.

[92] Min-hsuan Hung, Chang-hua Lin, Liang-cheng Lee, and Chien-ming Wang. State-of-charge and state-of-health estimation for lithium-ion batteries based on dynamic impedance technique. *Journal of Power Sources*, 268:861–873, 2014. doi: 10.1016/j.jpowsour.2014.06.083.

[93] Shalini Rodrigues, N Munichandraiah, and A K Shukla. Review of state-of-charge indication of batteries by means of a.c. impedance measurements. *Journal of Power Sources*, 87(1):12–20, 2000. doi: 10.1016/S0378-7753(99)00351-1.

[94] Zhaofeng Deng, Zhian Zhang, Yanqing Lai, Jin Liu, Jie Li, and Yexiang Liu. Electrochemical Impedance Spectroscopy Study of a Lithium/Sulfur Battery: Modeling and Analysis of Capacity Fading. *Journal of the Electrochemical Society*, 160 (4):A553–A558, January 2013. doi: 10.1149/2.026304jes.

[95] Holger Blanke, Oliver Bohlen, Stephan Buller, Rik W. De Doncker, Birger Fricke, Abderrezak Hammouche, Dirk Linzen, Marc Thele, and Dirk Uwe Sauer. Impedance measurements on lead–acid batteries for state-of-charge, state-of-health and cranking capability prognosis in electric and hybrid electric vehicles.

Journal of Power Sources, 144(2):418–425, June 2005. doi: 10.1016/j.jpowsour.2004.10.028.

[96] Gil Cohn, Rüdiger A Eichel, and Yair Ein-Eli. New insight into the discharge mechanism of silicon-air batteries using electrochemical impedance spectroscopy. *Physical chemistry chemical physics*, 15(9):3256–63, March 2013. doi: 10.1039/c2cp43870d.

[97] Compare Electric Vehicles Side-by-Side. URL http://www.fueleconomy.gov/feg/evsbs.shtml.

[98] Muhammed M Ottakam Thotiyl, Stefan A. Freunberger, Zhangquan Peng, and Peter G. Bruce. The carbon electrode in nonaqueous Li-O2 cells. *Journal of the American Chemical Society*, 135(1):494–500, January 2013. doi: 10.1021/ja310258x.

[99] Betar M. Gallant, Robert R. Mitchell, David G. Kwabi, Jigang Zhou, Lucia Zuin, Carl V. Thompson, and Yang Shao-Horn. Chemical and Morphological Changes of Li-O2 Battery Electrodes upon Cycling. *The Journal of Physical Chemistry C*, 116:20800–20805, 2012.

[100] Christian Fleischer, Wladislaw Waag, Hans Martin Heyn, and Dirk Uwe Sauer. On-line adaptive battery impedance parameter and state estimation considering physical principles in reduced order equivalent circuit battery models: Part 1. Requirements, critical review of methods and modeling. *Journal of Power Sources*, 260:276–291, 2014. doi: 10.1016/j.jpowsour.2014.01.129.

[101] Pascal Hartmann, Conrad L Bender, Joachim Sann, Anna Katharina Dürr, Martin Jansen, Jürgen Janek, and Philipp Adelhelm. A comprehensive study on the cell chemistry of the sodium superoxide (NaO2) battery. *Physical chemistry chemical physics : PCCP*, 15(28):11661–72, June 2013. doi: 10.1039/c3cp50930c.

[102] World Meteorological Organization. *Technical Regulations. Volume I - General Meteorological Standards and Recommended Practices*. World Meteorological Organization, Geneva, 2011 edition, 2012. ISBN 9789263100498.

[103] Stefano Meini, Michele Piana, Nikolaos Tsiouvaras, Arnd Garsuch, and Hubert a. Gasteiger. The Effect of Water on the Discharge Capacity of a Non-Catalyzed Carbon Cathode for Li-O2 Batteries. *Electrochemical and Solid-State Letters*, 15 (4):A45, 2012. doi: 10.1149/2.005204esl.

[104] Kensuke Takechi, Tohru Shiga, and Takahiko Asaoka. A Li–O2/CO2 battery. *Chemical Communications*, 47(12):3463–3465, February 2011. doi: 10.1039/C0CC05176D.

[105] Hyung-Kyu Lim, Hee-Dae Lim, Kyu-Young Park, Dong-Hwa Seo, Hyeokjo Gwon, Jihyun Hong, William a Goddard, Hyungjun Kim, and Kisuk Kang. Toward a Lithium-"Air" Battery: The Effect of CO2 on the Chemistry of a Lithium-Oxygen Cell. *Journal of the American Chemical Society*, 135(26):9733–42, July 2013. doi: 10.1021/ja4016765.

[106] Jian Zhang, Wu Xu, Xiaohong Li, and Wei Liu. Air Dehydration Membranes for Nonaqueous Lithium–Air Batteries. *Journal of The Electrochemical Society*, 157 (8):A940–A946, 2010. doi: 10.1149/1.3430093.

[107] L G Johnson. Oxygen battery system, September 2009. URL https://www.google.dk/patents/US20090239132.

[108] R Hilse, M Schiemann, H G Schweiger, and S D Tillmann. Battery system for use in electrochemical energy generating, storing or consuming apparatus, has drying unit and housing with opening for exchange of gas between housing inner space, housing outer space and drying unit, January 2011. URL https://www.google.dk/patents/DE102009032463A1?cl=en.

[109] M Heger, H Thomas, D J Morton, and I Rottler. Battery system for e.g. hybrid car, has air interchange device that allows exchange of air between interior of battery housing and exterior environment to prevent or minimize ingress of water from exterior environment into interior, October 2012. URL https://www.google.dk/patents/DE102011015925A1?cl=en.

[110] A Gleiter. Vorrichtung zur Reduzierung von Feuchtigkeit in einem Innenraum eines Gehäuses einer Energieeinheit A device for reducing moisture in an internal space of a housing of a power unit, July 2014. URL https://www.google.dk/patents/DE102013200796A1?cl=en.

[111] D G Duff, J C Weintraub, and G Arcenio. Battery pack dehumidifier with active reactivation system, December 2012. URL https://www.google.dk/patents/EP2533325A1?cl=en.

[112] Paul Albertus, John F. Christensen, and Boris Kozinsky. Metal/oxygen battery with an oxygen supply system, January 2014. URL https://www.google.dk/patents/WO2014018842A1?cl=en.

[113] K Noda and T Tomita. Metal-air battery system including co2 selective absorber and operating method therefor, May 2013. URL https://www.google.dk/patents/US20130106359.

[114] Paul Albertus, John F. Christensen, Timm Lohmann, Roel S. Sanchez-Carrera, and Boris Kozinsky. Metal/Air Battery with Electrochemical Oxygen Compression, December 2013. URL https://www.google.dk/patents/US20130344401.

[115] A Pulskamp, A R Drews, J Yang, S Hirano, and M A Tamor. Metal Oxygen Battery Containing Oxygen Storage Materials, June 2011. URL https://www.google.dk/patents/US20110143228.

[116] W A Hermann and J B Straubel. Control, Collection and Use of Metal-Air Battery Pack Effluent, February 2012. URL https://www.google.dk/patents/US20120041628.

[117] G HÜBNER and A K Speidel. Lithium-air battery with high oxygen saturation, February 2012. URL https://www.google.dk/patents/WO2012016606A1?cl=en.

[118] Paul Albertus, John Christensen, Timm Lohmann, and Boris Kozinsky. Metal/oxygen battery with oxygen pressure management, August 2014. URL https://www.google.dk/patents/US20140234730.

[119] P J Linstrom and W G Mallard. NIST Chemistry WebBook, 2011. ISSN 0009-4978. doi: 10.5860/CHOICE.35-2709. URL http://webbook.nist.gov/chemistry/.

[120] Arden L. Buck. New Equations for Computing Vapor Pressure and Enhancement Factor, 1981. ISSN 0021-8952. doi: 10.1175/1520-0450(1981)020⟨1527:NEFCVP⟩2.0.CO;2.

[121] Zeolite Store, 2015. URL http://www.zeolitestore.com/en/zeolites.

[122] Alan L Myers and Sir. Gas Separation by Zeolites. *Handbook of Zeolite Science and Technology*, 2003. doi: 10.1201/9780203911167.ch22.